Advanced Integrated Power Generation Centre for Future More-Electric Aircraft

Xiaoyu Lang (BEng, MSc)

Thesis submitted to the University of Nottingham
for the degree of Doctor of Philosophy

June 2021

Acknowledgements

First and foremost, I am extremely grateful to my supervisors, Prof. Serhiy Bozhko, Dr. Tao Yang and Prof. Patrick Wheeler for their invaluable advice, continuous support, and patience during my PhD study in the past four years. It would be impossible for me to undertake this PhD without their constant guidance.

I would like to thank Prof. Pericle Zanchetta for reviewing my annual reports and acting as my internal examiner. Special thanks are also given to Dr. Patrick Norman for sparing time to be my examiner and making insightful comments on improving the Thesis.

Millions of thanks to all my friends and colleagues for a cherished time spent together in the ATC and PEMC group. I have broadened my visions and leant many things from them. And I hope they too from me. Special thanks to Dr. Zhen Huang, Dr. Zhenyu Wang, Dr. Chen Li, Dr. Cheng Wang, Dr. Hossein Balaghi Enalou, Dr. Seang Shen Yeoh, Mr. Yuzheng Chen, Tim (Dr. Linglin Chen), Mr. Feng Guo and Bob (Dr. Ponggorn Kulsangcharoen). Without them my PhD would not have been achievable.

Thanks to the China Scholarship Council to fund me the living expenses in the past years.

My sincere gratitude also goes out to my family and my girlfriend for supporting me throughout the way. They have raised me and taught me. Without their tremendous understanding and encouragement, it would be very hard for me to complete my study.

Xiaoyu Lang
Nottingham, UK, 2021

Abstract

The More-Electric Aircraft (MEA) concept is a major trend in aircraft electrical power system engineering and results in an increase in onboard electrical loads and electrical power demand. On an aircraft the jet engine acts as the prime power source, providing to the onboard systems pneumatic power, hydraulic power, mechanical power and electrical power. As the aerospace industry is moving towards the MEA paradigm, many functions which are conventionally driven by pneumatic, hydraulic and mechanical power systems are being replaced by their electrical counterparts. However, due to the power off-take limit from the high-pressure (HP) spool, extra power is considered to be extracted from the low-pressure (LP) spool of an engine through the coupled generators. Increased number of generators and power electronic penetration renders a higher requirement to the power generation centre (PGC) in a more electric engine in terms of controllability, stability, fault tolerance, and power flow flexibility.

In recent years, a dual-channel single DC bus PGC was developed for the MEA application. Two electrical machines are coupled to the HP and LP spools of the engine respectively, and each of them is independently regulated by an AC/DC power converter. The DC outputs of the converters are parallel connected to supply a common DC bus. Theoretical analysis and experimental results of relevant research confirm the superiority of the PGC in efficiency and power sharing between sources. However, the PGC suffers from three critical drawbacks: 1) poor fault tolerance to the main rectifier failure; 2) power losses caused by the significant de-fluxing current in the HP generator at high-speed settings, and 3) the incapability to achieve engine and HVDC grid stability optimization in the high-power settings of the engine.

To address these drawbacks, an advanced power generation centre (APGC) with an AC/AC bridging converter is proposed in this Thesis. The bridging converter is introduced to make the APGC much more flexible than the PGC in terms of managing the power flow and the generators control. Compared with the PGC, the APGC allows post-fault operation and supplies uninterruptible power to the downstream loads in the case of main rectifier failure. It also allows the permanent magnet synchronous machine-based HP generator to operate at a high speed without field-weakening operation, which significantly reduces the stator currents

and power losses in the HP generator and power converters. Moreover, due to establishing a power exchange path between the HP and LP power generation channels, the stability of the onboard HVDC grid and the engine can be enhanced simultaneously in the high-power settings of the engine.

System configuration, control schemes in normal and post-fault operation modes, power losses and stability with different power sharing ratios between sources of the APGC have been thoroughly analysed in this Thesis. Theoretical findings of the APGC support the above-mentioned improvements over the PGC. The technical results and simulations are supported by Matlab/Simulink based models and validated by experimental work on an engine emulator system and a downscaled lab prototype of the APGC.

List of Publications

The contents presented in this Thesis have been published or under peer-review in the following journal articles and conference proceedings:

Journal Articles

[J1] **X. Lang**, T. Yang, Z. Wang, C. Wang, S. Bozhko and P. Wheeler, "Fault Tolerant Control of Advanced Power Generation Center for More-Electric Aircraft Applications," in *IEEE Transactions on Transportation Electrification*, early access, June, 2021. doi: 10.1109/TTE.2021.3093506

[J2] **X. Lang**, T. Yang, Z. Huang, C. Wang, Z. Wang, S. Bozhko and P. Wheeler, "Stability Improvement of Onboard HVDC Grid and Engine Using an Advanced Power Generation Center for the More-Electric Aircraft," in *IEEE Transactions on Transportation Electrification*, early access, July, 2021. doi: 10.1109/TTE.2021.3095256

[J3] **X. Lang**, T. Yang, C. Li, H. B. Enalou, S. Bozhko and P. Wheeler, "A Dual-Channel-Enhanced Power Generation Architecture With Back-to-Back Converter for MEA Application," in *IEEE Transactions on Industry Applications*, vol. 56, no. 3, pp. 3006-3019, May-June 2020. doi: 10.1109/TIA.2020.2974145

[J4] **X. Lang**, T. Yang, C. Li, S. Yeoh, S. Bozhko, and P. Wheeler, " An Enhanced Feedforward Flux Weakening Control for High-Speed Permanent Magnet Machine Drive Applications," *IET Power Electronics*, 00: 1-15. (2021) doi: 10.1049/pel2.12170.

[J5] H. Enalou, **X. Lang**, M. Rashed and S. Bozhko, "Time-Scaled Emulation of Electric Power Transfer in the More Electric Engine," in *IEEE Transactions on Transportation Electrification*, vol. 6, no. 4, pp. 1679-1694, Dec. 2020.

[J6] **X. Lang**, T. Yang, Z. Huang, Z. Wang, S. Bozhko, and P. Wheeler, " Instantaneous Power Control within an Advanced Power Generation Center for More-Electric Aircraft Applications," in *IEEE Transactions on Transportation Electrification*, **major revision**.

Conference Papers

[C1] **X. Lang**, T. Yang, H. B. Enalou, C. Li, S. Bozhko, and P. Wheeler, “A dual-channel enhanced power generation architecture with back-to-back converter for MEA application," in *Proc. IEEE Int. Electr. Mach. Drives Conf.*, San Diego, CA, USA, May 2019, pp. 1392–1397.

[C2] **X. Lang**, T. Yang, H. B. Enalou, P. Wheeler and S. Bozhko, "A power generation center with back-to-back converter considering post-fault operation for MEA Application," in *22nd Int. Conf. on Electron. Mach. Syst. (ICEMS)*, Harbin, China, Aug. 2019, pp. 1–6.

[C3] **X. Lang**, T. Yang, H. B. Enalou, S. Bozhko, and P. Wheeler, "An enhanced power generation centre for more electric aircraft applications," in *IEEE Int. Conf. Elect. Syst. Aircr. Railway Ship Propulsion Road Vehicles Internat. Transp. Electrific. Conf.*, 2018, pp. 1–6.

Table of Content

List of Figures

List of Tables

List of Acronyms

AC	Alternative Current
AEGART	Aircraft Electrical Generation Active Rectifier Technology
AFE	Active Front End
APU	Auxiliary Power Unit
APGC	Advanced Power Generation Centre
AR	Active Rectifier
BTB	Back-to-back Converter
CCL	Constant Current Load
CIL	Constant Impedance Load
CPL	Constant Power Load
CPO	Coordinated Power Offtake
CSD	Constant Speed Drive
DC	Direct Current
DSP	Digital Signal Processor
ECS	Environmental Control System
EHA	Electro-hydrostatic Actuator
EMF	Electromotive Force
EMA	Electro-mechanical Actuator
EPS	Electrical Power System
EPT	Electric Power Transfer
EPT	Electrical Power Transfer
ESS	Energy Storage System
FPGA	Field Programmable Gate Array
FW	Field Weakening
HP	High Pressure
HPC	High-pressure Compressor
HPT	High-pressure Turbine
HPG	High-pressure Generator
HPS	High-pressure Spool
HVDC	High-voltage Direct Current

IGBT	Insulated Gate Bipolar Transistor
INR	Incremental Negative Resistance
IM	Induction Machine
IPM	Interior Permanent Magnet
LP	Low Pressure
LPC	Low-pressure Compressor
LPT	Low-pressure Turbine
LPG	Low-pressure Generator
LPS	Low-pressure Spool
MCPEC	Modular Cell Power Electronics Converter
MEA	More-electric Aircraft
PCE	Power Coupling Effect
PGC	Power Generation Centre
PMM	Permanent Magnet Machine
PMSG	Permanent Magnet Synchronous Generator
PWM	Pulse Width Modulation
RHP	Right Half Plane
SG	Starter/Generator
SMPMM	Surface Mounted Permanent Magnet Machine
SRM	Switched Reluctance Machine
SVPWM	Space-vector Pulse Width Modulation
THD	Total Harmonic Distortion
VF	Variable Frequency
VSC	Voltage Source Converter
VSCF	Variable Speed Constant Frequency
VSVF	Variable Speed Variable Frequency
WIPS	Wings Ice Protection System

List of Symbols

C_{HP}	Capacitances of the DC capacitor of the HPR
C_{LP}	Capacitances of the DC capacitor of the LPR
C_{mb}	Capacitances of the DC capacitor of the global main DC bus
g_{LP}	The droop gain for the LPR
g_{HP}	The droop gain for the HPR
i_{aBTBL}	The *a*-phase current of the BTB_L converter
i_{BTB}	The DC current on the DC-link within the BTB converter
i_{aLP}	The *a*-phase current of the LPG
i_{dc}	The total DC current from the rectifiers
i_{dcLP}	The DC current of the LP rectifier
i_{dcHP}	The DC current of the HP rectifier
i_{dBTBL}	*d*-axis current of the BTB_L converter
i_{dHPR}	*d*-axis current of the HPR
i_{qBTBL}	*q*-axis current of the BTB_L converter
i_{qHPR}	*q*-axis current of the HPR
$I_{\max}$	The current limitation of the generator's currents.
$K_{i\mathrm{P}}$	The proportional gain of the current loop controller.
$K_{i\mathrm{I}}$	The integral gain of the current loop controller.
K_{FWp}	The proportional gain of the FW controller.
K_{FWi}	The integral gain of the FW controller.
L_1	The inductance of the inductor deployed at the front end of the BTB_L converter
L_2	The inductance of the inductor deployed at the front end of the HPR
L_d	Stator inductance of the generator in the *d*-axis.

L_q	Stator inductance of the generator in the q-axis
m	A control gain which is also the magnitude ratio between i_{aLP} and i_{aBTBL}
p	The pole pairs of the generator
P_t	Total load power
P_{BTB}	Power of the BTB converter channel
P_{HPR}	Deliver power of the HPR
P_{LPR}	Deliver power of the LPR
P_{HPG}	Deliver power of the HPG
P_{LPG}	Deliver power of the LPG
R_s	Stator resistance of the generator
v_{BTB}	The DC-link voltage within the BTB converter
v_{dBTBL}	d-axis voltage of the BTB_L converter
v_{qBTBL}	q-axis voltage of the BTB_L converter
v_{dc}	The main DC bus voltage
$\overline{v}_{dc}$	The DC bus voltage at a steady-state operating point
$V_{c\max}$	The value of voltage limitation
Z_s	Source impedance
Z_L	Load impedance
ψ_m	Rotor flux linkage of the generator
ζ	Damping ratio
ω_n	Natural frequency
ω_{eLP}	The electrical angular speed of the LPG
ω_{eHP}	The electrical angular speed of the HPG

Chapter 1. Introduction

1.1 More-Electric Aircraft Concept

In the past decades, aircraft have been used as a convenient way of travel. They allow long-distance, high-speed travel, and in some cases, become a fuel-efficient method of transportation. The entire aerospace industry is on average growing at a fast rate. For example, for the turboprops market, in 2010 there were 2,080 aircrafts with turboprops in service. By 2030, a total of 2,440 new aircrafts with turboprops will be delivered and the total number will increase to 3,295 [1].

However, the impact of aircraft on the environment and climate goes beyond fuel efficiency considerations. In the fiercely competitive market of aviation, low-cost airlines are reducing the profitability of airline seat mileage, so there is an urgent need for technologies to reduce environmental impact and reduce the operating costs of civil aircraft. For the aerospace industry, a major threat is that if future emissions cannot be reduced, severe sanctions may be imposed, thereby pushing up ticket prices and reducing air travel miles compared with other means of transportation (such as railways). Energy efficiency, lower CO_2 and NO_x emissions, and low noise have become critical issues as those factors threaten the quality of life for our future generations.

Based on this background, the aerospace industry is paying more attention to efficient and environmentally friendly solutions. Due to the rapid development of electrical and electronic engineering solutions, the current trend is to shift to More-Electric Aircraft (MEA) [2]. The MEA concept could potentially lead to a significant reduction in fossil fuel consumption and pollutant emissions, as electrification technology has accelerated the paradigm shift to more sustainable air travel.

1.2 Advantages of More-Electric Aircraft

The MEA brings increased efficiency while reducing greenhouse gas emission (CO_2, NOx, etc.). Electrification of aircraft will reduce fossil fuel consumption as systems are powered by a network of highly efficient electric components with a lower system weight.

Figure 1.1 shows that electrical power system has been increasing in capacity after each new generation of both single and double-aisle planes. Modern advancements in design and materials have allowed turbofans to produce more thrust and provide more power to downstream loads. While wiring and electronics become more complex, air ducts, hydraulic and pneumatic piping are all removed from the airframe in a MEA. Electrical systems can be lighter and easier to maintain than their conventional counterparts [3].

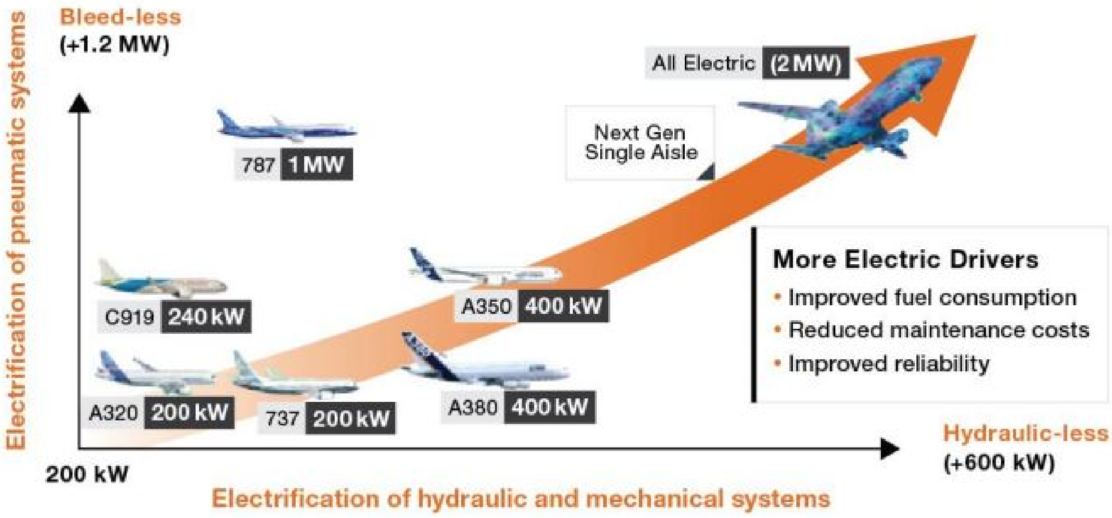

Figure 1.1. Power demand in modern aircraft.

A major component of all aircraft in the modern era is the propulsion system. In the majority of conventional aircraft, the propulsion system uses a jet engine. It works by burning jet fuel such as kerosene in air to release hot accelerated exhaust gases. The gases fulfil the following two functions:

- Firstly, the gas is passed through turbines which powers the shaft. The shaft connects to a gearbox which connects to many systems on the aircraft in a conventional aircraft. These systems include 1) electrical systems, which help power the instruments and avionics of the aircraft. 2) hydraulic systems, which provides power to other subsystems such as the landing gear [4]. 3) mechanical systems, which drive fuel pumps on the engines. 4) bleed air from the compressor at the front of the engine is used in the pneumatic system, which runs the environmental control system (ECS). The systems on a typical conventional aircraft are shown in Figure 1.2.

- Secondly, the accelerated exhaust gases are passed through a diverging duct before exiting the engine at high speed, providing thrust for the aircraft.

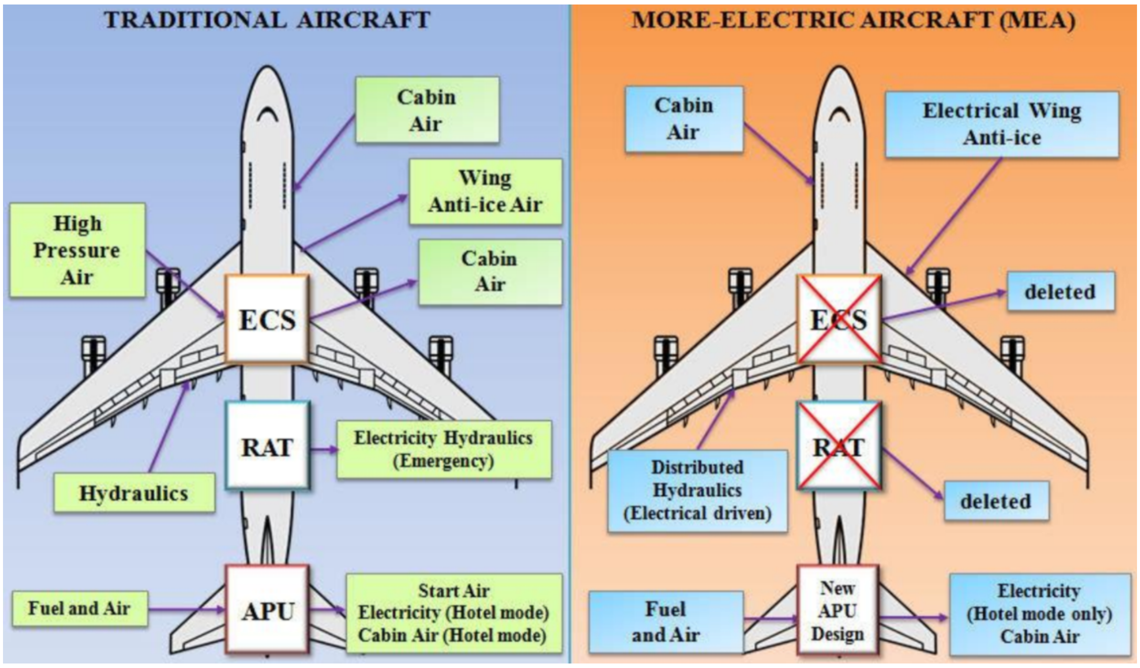

Figure 1.2. The comparison of conventional and MEA systems.

In the MEA, the conventional power systems are changed. In aircraft such as the Boeing 787, a hybrid combination has been adopted to increase fuel efficiency. Additionally, the gearbox of the aircraft is modified to have larger electrical generators, creating an expanded electrical network. To further compare the differences between conventional aircraft and a MEA, two subsystems are selected and compared: The Wing Ice Protection System (WIPS) and hydraulic actuation system.

1.2.1 Wing Ice Protection Systems

Normally, flying an aircraft at high altitudes with considerably low ambient temperatures can lead to ice building up on the control surfaces and wings of the aircraft. This directly influences aircraft performance, resulting in the need for anti-icing and de-icing methods. Anti-icing equipment is turned on before entering icing conditions and is designed to prevent ice from forming. De-icing equipment is designed to remove ice after it begins to accumulate on the airframe [4].

Ice building up on the wings directly impacts aircraft efficiency by increasing the weight of the aircraft, changing the way air flows around the aerofoil and increasing drag. The airflow around wings is the most important aspect of a plane as it determines whether or not the aircraft will stall or fly. Ice building up on the wing area results in an earlier separation point, creating a wake, as shown in Figure 1.3. Furthermore, ice on the leading edge adds to the shape of the aerofoil, disrupting the smooth flow over and under the wing, all of which impacts the efficiency of the wing [5].

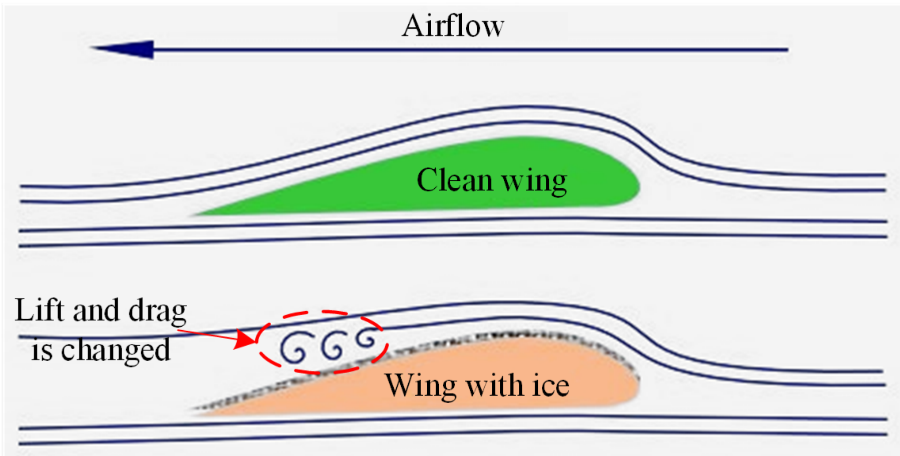

Figure 1.3. The impact of ice on airflow around a wing.

For the conventional aircraft, as shown in Figure 1.4, the cross-section shows how the bleed air is distributed under the external surface of the leading edge of a P-3K Orion wing [4]. This method of de-icing can only operate when the engines are running. It is also proportional to the total engine output, as at lower thrust there will be less airflow. Ice sensors in the nose of the fuselage are used to detect when the valves should open to release the bleed air, as having them always on is inefficient. Ice can only form above and below certain altitudes, hence, de-icing is not required at all times. This conventional method reduces engine efficiency as bleed air is taken from the compressor stage of the turbofan, which otherwise can be used to propel the aircraft.

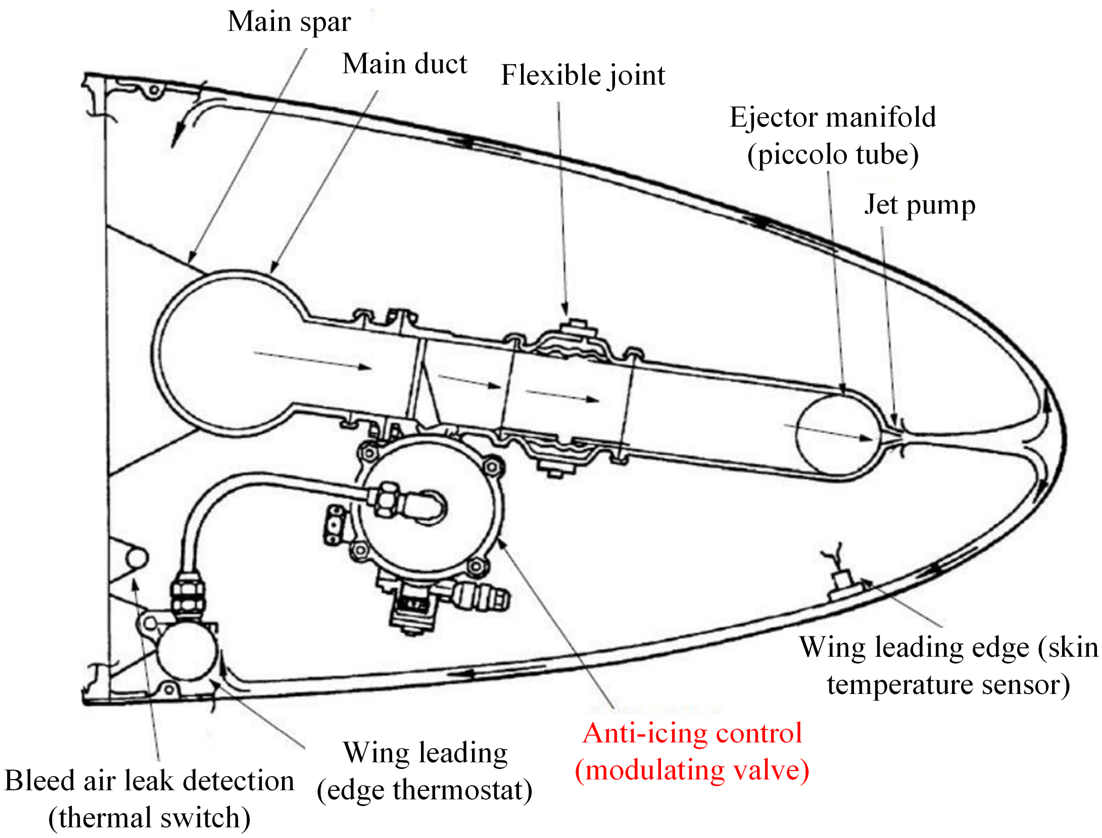

Figure 1.4. Cross-section of the P-3K Orion wing leading edge.

In a MEA such as the Boeing 787, an electro-thermal heating system is used to protect the aircraft wing from ice. Heating blankets are built into the interior of the leading edge of the slats. These heat blankets are metallic conductors with independent zone heating control which are placed between heat resistant insulators. When required, the blankets can be heated either simultaneously for anti-icing protection or sequentially for de-icing purposes. The power from the generators is transferred to a power distribution system and then on to the WIPS [5]. Other examples of electric de-icing systems include electric boots attached to the leading edge of the wing on small aircraft which have heating elements running through them. If required, the boots produce a current which passes through them, increasing the temperature of the front of the wing and removing the ice. Figure 1.5 shows a WIPS model consisting of seven independently controlled electric elements that are embedded with a four-layer composite panel [5].

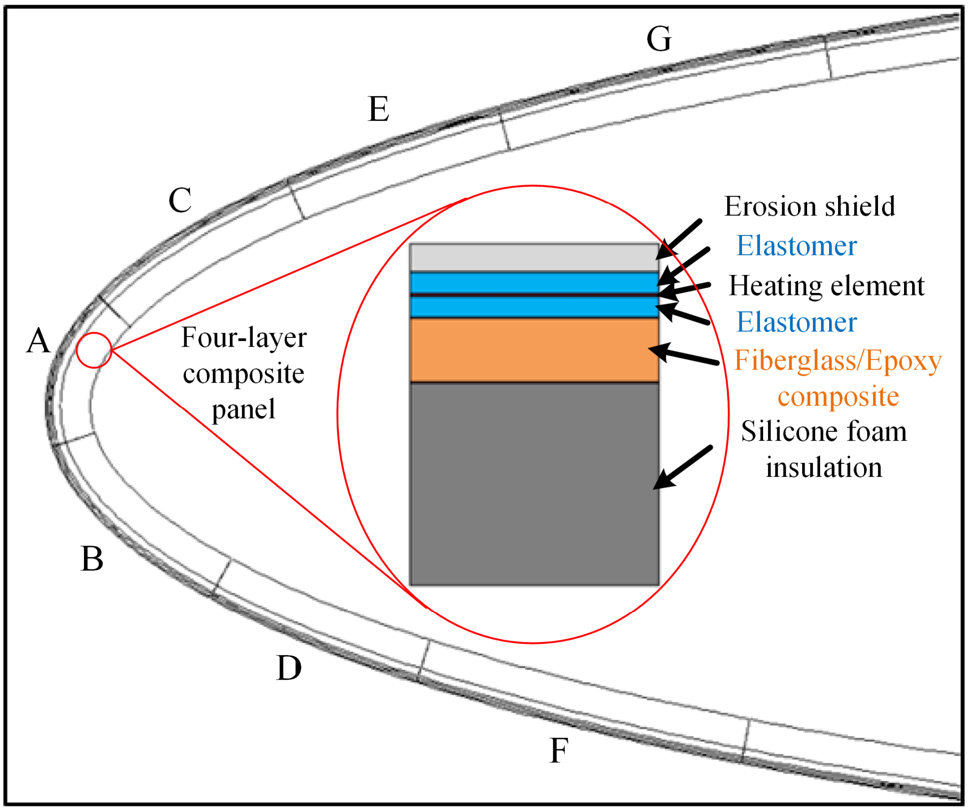

Figure 1.5. The electro-thermal WIPS.

1.2.2 Hydraulic Actuation Systems

Another subsystem for comparison is the hydraulic actuation system. In a conventional aircraft, power is delivered from the engines through gearbox-mounted pumps to hydraulic actuators. Hydraulic actuators are used for various functions, such as primary flight controls, rudders elevators, and ailerons. They are also used in secondary controls, such as flaps, slats, speed brakes, trim and etc [6]. The hydraulic systems in planes need a large amount of tubing. It is also costly and has the risk of leakage.

The current trend is to replace hydraulic systems with electro-hydraulic actuators (EHAs) or electromechanical actuators (EMAs) to reduce the reliance on hydraulics. Diagrams of EHA and EMA are shown in Figure 1.6. An EHA includes a reversible hydraulic pump, hydraulic cylinder and hydraulic oil tank. EHAs eliminate external hydraulic sources and pipes. Therefore, at system level, EHA is considered advantageous in weight, size, reliability, and cost [6]. Currently, EHAs are used in Boeing 787 for the main hydraulic system. EMA does not use any hydraulic power but uses a gearbox and mechanical system to convert rotary motion into linear motion [7]. Therefore, EMA is more effective than EHA and a better choice for leak-free operation. However, EMA is vulnerable to mechanical jamming.

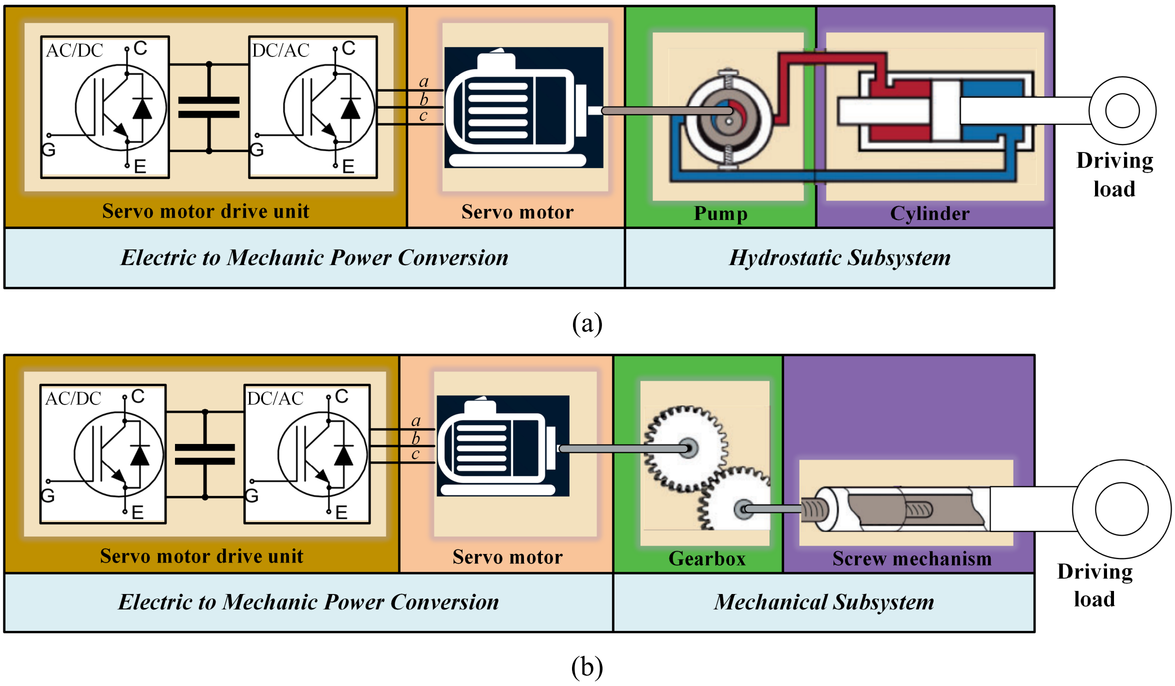

Figure 1.6. Structures of EMA and EHA system. (a) EMA system. (b) EHA system.

1.3 Challenges of Electrical Power System for Moving Towards MEA

Due to the increased electrification of various systems onboard MEA, there is an increase in the electric loading which should be covered by jet engines. This trend also complicates the onboard electrical power system and power generation centre (PGC) [9]. Conventionally, electrical power is extracted from the engine high-pressure shaft (HPS) [6]. However, extracting power only from HPS is not enough to meet the requirements in MEA as the load increases. Moreover, it could have a negative impact on the performance of the engine, such as compressor surge [11]. In [12], [13], it has been shown that there is a limit on the amount of power off-take from the HPS. If the power extracted exceeds the limit, the engine may surge and stall. This issue can be addressed either by increasing the speed of HPS or bypass excess air to the fan discharge duct, whereas those measurements will lead to excessive fuel usage [14]. Another way to extract more power is to offtake some power from the LP spool of engine, but this will lead to a revised PGC architecture inside a more electric engine.

The MEA places more requirements on aircraft PGCs in terms of reliability, fault tolerance, power management, and stability [15]. Therefore, innovations in power generation, distribution, processing and management systems are required. With the increase in the number of power electronic driven loads, MEAs with classic AC networks include a number of AC/DC rectifiers to replace the traditional autotransformer-rectifier units. A systematic solution to reduce the overall weight is the high-voltage direct current (HVDC) network, which consists of generators, rectifier units, filters, and generator control units. Studies have been conducted, especially in the framework of the More Open Electrical Technology (MOET) EU project [17], proving the controllability and efficiency of a 270V HVDC network [18]-[21]. The HVDC network will also facilitate the integration of generators, loads, and maybe consistent with regenerative loads [22], [23].

Different system configurations have been proposed within a HVDC structure, such as single bus, multiple bus, and ring bus. Because of the simplicity, as shown in Figure 1.7, the single bus PGC architecture with various types of loads is one of the promising candidates for future MEA, where the dual-engine driven generators provide power to a single DC bus through individual active rectifiers (ARs).

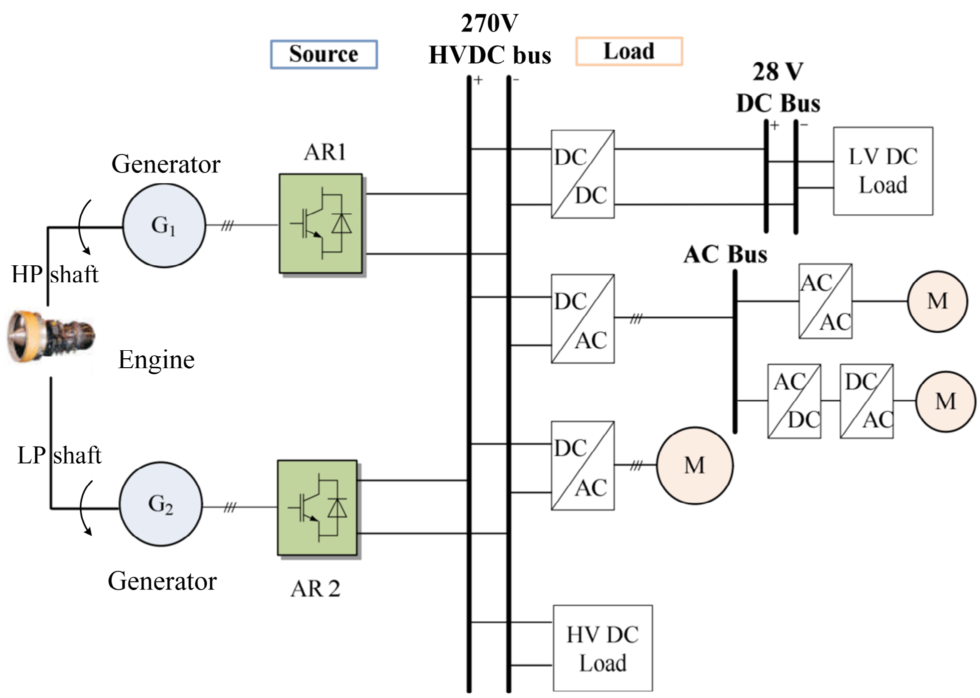

Figure 1.7. Dual-channel power generation centre with a single HVDC bus power distribution system.

Although the PGC shown in Figure 1.7 utilizes energy sources in parallel which improves system redundancy, the following challenges still need to be considered and addressed:

- Appropriate power sharing control between different sources.
- A robust DC bus voltage control and disturbance rejection capability.
- Fault tolerant control in case of rectifier failure scenario.
- High power quality with limited total harmonic distortion (THD).
- Sufficient stability margin and efficiency for both HVDC grid and engine.

These challenges are further discussed below.

1.3.1 Load Power Sharing

For a twin-shaft engine, the low-pressure turbine (LPT) drives the fan and low-pressure compressor (LPC) via the LP shaft, and the high-pressure turbine (HPT) drives the axial and radial high-pressure compressor (HPCs) via HP shaft. The schematic diagram is shown in Figure 1.8. Traditionally, an electrical generator is driven by a gearbox linked to the HPS of the engine. This is due to the desirable HPS characteristics, such as high and relatively constant speed, which enables engineers to decrease the size and weight of the coupled generator. Nevertheless, extracting the high amount of power from the HPS could have a negative impact on the performance of the engine system [12]. An alternative way is to use the LPS as an additional power source, i.e., using the LPS to drive another electrical generator. The engine is connected to dual generators via the LPS and HPS [25]. In such a multi-source multi-load power system, appropriate load power sharing is important for optimizing engine and HVDC grid performance.

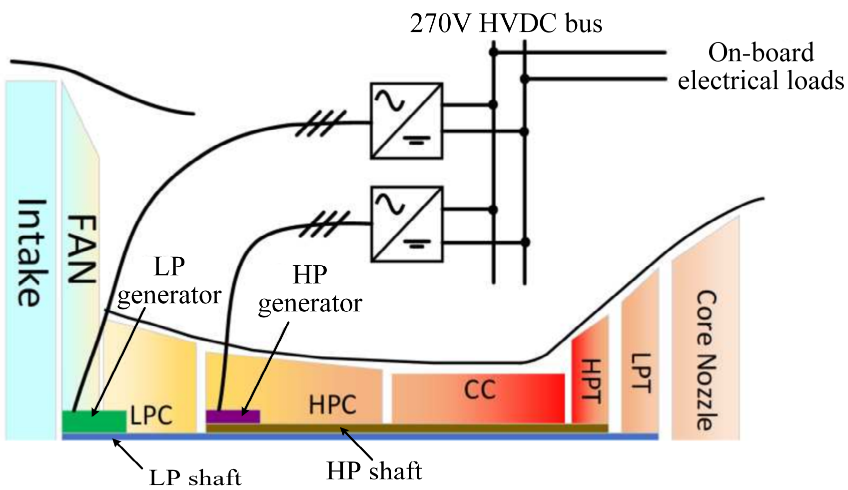

Figure 1.8. Diagram of a twin-spool, high bypass ratio turbofan engine with a single HVDC bus PGC [11].

1.3.2 Fault Tolerance of The Single Bus PGC

Another critical constraint of the architecture in Figure 1.7 is the poor fault tolerance capability in terms of power conversion. In traction and power generation related systems, power converters are identified as the most vulnerable parts [26]. If contingency such as open-circuit fault occurs to the low-pressure channel or high-pressure channel active rectifiers in Figure 1.7 due to gate-driver fault or cycling high currents [27], the faulty rectifier needs to be stopped and disconnected from the DC grid to prevent cascading the problem, for example: damaging the connected generator [28]. However, the associated generators cannot be shut down suddenly as they are connected to the aircraft engine, which has a significant inertia. Moreover, even if the generators are stopped smoothly, these generators are no longer available for the electrical loads. This will undermine the power generation capability and thus limit large-scale applications of onboard electrical equipment. Furthermore, suddenly losing one generator may lead to severe system instability at high load power scenarios. Consequently, the architecture of the PGC shown in Figure 1.7 should be revised to improve the fault tolerance capability. System reconfiguration and associated fault tolerant control should also be developed to deal with the post-fault operation.

1.3.3 DC Bus Voltage Control

For multiple power sources and multiple converters operating in parallel, at least one converter is responsible for regulating the DC bus voltage, and all other converters can operate in active power control mode. However, after one or more converter fails, the remaining converters should share the resulting power in an appropriate proportion. Therefore, it is preferable that all converters operate in DC link voltage control mode instead of strictly following their individual active power references. Hence, a cooperative voltage control amongst all power sources is required.

Moreover, another issue is the DC bus regulation during transient states with load switching. For example, pulsed power loads, such as onboard radars, demand high pulse power. These loads pose a significant disturbance to the HVDC grid [30]. These loads also have impact on other electrical loads on the same DC bus [28]. Therefore, the voltage control should provide fast and robust control performance against disturbance from onboard loads.

1.3.4 Stability Improvement of HVDC Grid and Engine

For the PGC in Figure 1.7, electrical power of the HPR is extracted from the mechanical power of the HPS; and the electrical power of the LPR comes from the mechanical power of the LPS. The feature that electrical power is coupled to the mechanical power is defined as Power Coupling Effect (PCE), which is

HP Channel*: Electrical Power of the HP Rectifier=Mechanical Power of the HP spool*

LP Channel*: Electrical Power of the LP Rectifier=Mechanical Power of the LP spool*

This PCE is a barrier to achieve the stability optimization for both HVDC gird and engine. To maintain the stability of HVDC gird, this Thesis will prove that the LPR should feed more power than the HPR to the DC bus. Due to the PCE, this means that more mechanical power should be extracted from the LPS than the HPS. However, from the analysis of turbofan compressor maps, for engine stability, in the high-power scenarios such as top of climbing and maximum take-off, more power should be extracted from the HPS than the LPS to avoid the overspeed of HPS. Apparently, the PGC with PCE in Figure 1.7 cannot handle this conflict. Revisions should be applied to the PGC to enhance the stability of both HVDC grid and engine simultaneously.

1.4 Aims and Objectives

Following an overview of opportunities and challenges of the single bus PGC architecture for applications in future MEA, this work aims to develop an advanced PGC (APGC) architecture that provides desirable load power sharing between the HP and LP generators, establishes a power exchange path between the engine HP and LP spools, improves the system fault tolerance, efficiency, as well as improves stability of both onboard EPS network and the engine.

The specific objectives to achieve are presented as follows:

1. To investigate the PGC concept as shown in Figure 1.7 and to design a control system to enable the two generators to supply power to the loads over the entire operational range.

2. To propose an APGC topology with a bridging converter capable of implementing a power transfer between the engine shafts.
3. To investigate the bridging converter topology based on back-to-back (BTB) structure and to propose suitable control schemes to regulate the DC bus voltage, generators operation mode and power flow through the BTB converter channel.
4. To investigate the APGC fault scenarios, including faults of one of the channel rectifiers. In this case, the BTB converter can provide an additional power flow path for the post-fault operation of the APGC. This will require consideration of the system reconfiguration and suitable fault-mode control schemes to ensure a smooth transition from the healthy state to the post-fault operation state.
5. To study the BTB converter operation as a bridge for power flow exchange between the engine HP and LP spools to improve the engine efficiency and surge margin. As our previous work [11], [12] show, increasing mechanical power extraction from the HPS compared to the LPS is beneficial for the engine efficiency and stability. Meanwhile, the EPS stability improves if more power comes from the LP channel [29]. A detailed stability analysis needs to be carried out as the theoretical ground for setting power sharing ratios.

1.5 Academic Contributions and Novelty of the Thesis

In this Thesis, a novel power generation centre architecture which features twin spool power offtake and single DC bus is proposed and thoroughly studied. Compared with other state-of-the-art PGCs, the studied one integrates a back-to-back (BTB) converter which establishes an electrical power path between the LP channel and HP channel. The academic contributions of this study can be summarised as follows:

- The typically used field-weakening operation for the HPG is eliminated. The benefits are that the stator currents flowing in the HPG and HPR are greatly reduced, which improves the power generation efficiency.
- System fault tolerance capability to the main rectifier failure is enhanced. With the aid of the proposed system reconfiguration and power flow control, the two generators can supply uninterruptable power to the downstream loads even with one main rectifier shutdown.

- An intrinsic power coupling effect (PCE) which hinders system stability improvement in the conventional single DC bus architecture is identified. In the proposed architecture, the PCE is removed and stability of both the HVDC grid and engine is simultaneously improved at high-power high-thrust settings of engine.
- A DC equivalent circuit and its impedance is proposed. This equivalent circuit and impedance can be used to evaluate the HVDC grid stability with multiple sources and droop control.
- Coordinated control strategies in both healthy state and postfault operation state are developed for the system which realize multiple functions including main DC bus voltage control, power sharing, power flow control of the BTB channel, and stator currents regulation of the generators. This could be of interest for researchers who are studying similar systems with multiple power converters in interaction.

1.6 Structure of the Thesis

The remainder of this Thesis is organized as follows:

Chapter 2 reviews the electrical power system of a MEA, including systems of power generation and distribution. The electrical starter/generator system and possible electrical machine candidates is also discussed. The characteristics of the PGC with parallel generation channels are considered. The proposed APGC integrated with a BTB converter is introduced.

Chapter 3 investigates the dual-channel single bus PGC shown in Figure 1.7 in terms of two modes, coordinated power offtake mode and power-transfer mode. In most time, the two electrical machines operate as generators. While at certain engine operation mode, in order to save fuel and enlarge compressor surge margin, some amount of power can be transferred from the LPS to the HPS, or vice versa. The overall electrical characteristics are analysed in small signal manner. Adaptive control parameters are set to guarantee a consistent control bandwidth at various operating points, i.e., DC bus voltage and load power. A droop control method is adopted to achieve power sharing. The benefits for the engine in power-transfer mode are verified.

Chapter 4 describes the proposed APGC with a BTB converter. Control design for all power converters is carried out based on the developed analytical models. Various functionalities are covered by the controllers, including DC bus voltage control, generator's current control, power flow control of the BTB converter and internal DC-link voltage control of the BTB converter. Design criteria for passive filters are derived. The APGC is built and verified in Matlab/Simulink. One of the core features, which is the elimination of field-weakening operation and hence decreasing the stator current of the HP generator is confirmed. Power losses reduction due to less stator current of the HP generator is verified for the APGC than the PGC.

Chapter 5 deals with the fault tolerance improvement with the APGC. Compared with the PGC shown in Figure 1.7, the proposed APGC can allow operation of generators with one of rectifiers shutdown through the system reconfiguration and using the BTB converter as an additional electrical power path. Appropriate control schemes are developed for the APGC in both healthy and faulty conditions. To avoid the abrupt change of generator currents during the transition from healthy to post-fault operation state, initialization strategies are proposed to properly initialize the *dq*-axes voltage commands in controllers.

Chapter 6 deals with the stability improvement of onboard HVDC grid and engine. A HVDC grid equivalent circuit is built. By analysing this equivalent circuit, it reveals that the LPR should supply more power than the HPR for enhancing the HVDC grid stability. However, it shows that in the maximum take-off mode, more power needs to be extracted from the HPS than the LPS of the engine to avoid the overspeed of the HPS and potential instability. Simulation is carried out, proving that the proposed APGC can improve the stability of both engine and HVDC network.

Chapter 7 reports the experimental verifications of the theoretical results from the previous chapters. The experimental rig and lab prototype setup are explained in detail. Experimental results are shown to support the analytical results and simulation results of previous chapters.

Chapter 8 summarizes the research results and contributions of the Thesis and points out considerations for future work.

Chapter 2. Electrical Power Generation and Distribution Systems within the MEA

2.1 Introduction

The increase of electrical power demand onboard future aircraft imposes challenges for designing appropriate power generation and distribution systems. In this chapter, a potential electric power system of MEA is considered, including various solutions for power generation and distribution. The electrical starter/generator and possible electrical machine candidates are discussed. The single DC bus PGC with two parallel generation channels is discussed in detail.

2.2 Overview of Power Generation

In large commercial aircraft, each engine usually powers one electrical generator. Depending on the type of aircraft, each engine can be connected to more than one backup generator to help meet redundancy requirements. Another source of power on aircraft is the auxiliary power unit (APU), which is essentially a small gas turbine-driven generator. The APU usually provides power when the aircraft is parked or taxiing on ground. It can also provide power in the air in an emergency [6]. There are also batteries on the aircraft that are used to provide backup power for critical equipment in the cockpit and other important functions (such as emergency lighting in the aisle) [31].

Historically, at times when aircraft started to use electric flight control equipment, DC motors were introduced as generators. The DC generators are self-excited or separately excited and can contain electromagnets, which generate electricity when driven by an aircraft engine. The DC power is transmitted to the load through the commutator [32].

As the electrical power demand increased, the aircraft power generation systems evolved from DC to AC generators [32]. In the 1960s, AC 115V at 400 Hz constant frequency (CF) systems were used, as in A320 and A330. With this structure, AC generators are mechanically coupled with engine shaft through a gearbox, which maintains a relatively constant mechanical speed. As a result, the electric frequency of AC bus is also fixed [9]. However, the gearbox itself is very expensive and it performs some critical functions, resulting in a very complex structure. This leads to frequent maintenance to ensure reliability, and failure may cause delays in planned flights. This limitation drives the need to look into alternative topologies which do not require the constant speed drive gearbox for onboard power generation.

A variable-speed constant-frequency (VSCF) solution has appeared since the 2000s [34]. Power electronic converters are employed in this architecture serving as interface between generators, bus, and loads. Due to the characteristic of variable frequency, some electrical loads operating at fixed frequencies (such as pumps driven by induction motors) have been replaced by power electronic controlled loads to be compatible with the wild frequency system (360 Hz to 900 Hz).

The power generation solutions for some recent aircraft are listed in Table 2-1. In the following subsections, the architectures of the power generation systems and their operating principles will be reviewed. The core equipment for power generation, i.e., the starter/generator, will also be discussed.

Table 2-1. Power generation systems for some recent aircrafts [33]

Type of power generation	Civil aircrafts	Power ratings
CF	A340	4×90 kVA
	B737NG	2×90 kVA
	B717	2×40 kVA
VF	A380	4×150 kVA
	B787	4×250 kVA
	Global Ex	4×40 kVA
VSCF (115V at 400Hz)	B777	2×120 kVA
	MD-90	2×75 kVA

2.2.1 Constant Generator Speed Constant Frequency

Traditional aircraft uses complex mechanical gearboxes to keep the mechanical speed of generators constant, so the electrical frequency remains constant (usually at 400 Hz). The architecture is shown in Figure 2.1. The mechanical gearbox is denoted as constant speed drive (CSD). It provides a constant output speed, but the input engine shaft speed can vary according to the engine's operation. However, the complexity of this mechanical CSD, the cost for maintenance and low reliability are of significant concern.

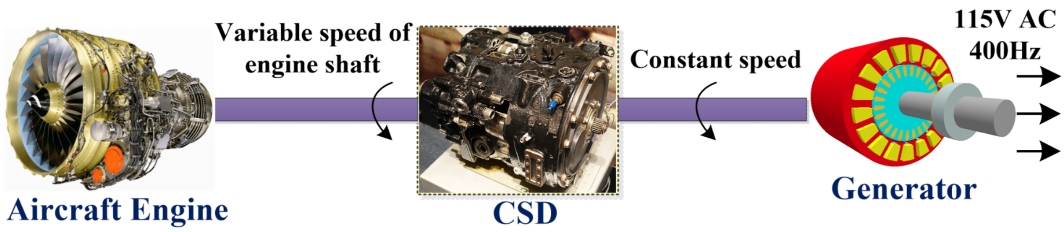

Figure 2.1. Constant frequency power generation system with a CSD.

2.2.2 Variable Generator Speed Constant Frequency

The variable speed constant frequency (VSCF) solution is similar to the CF in that a three-phase AC power source with a constant frequency is generated regardless of the engine shaft speed. The difference is that a power electronic converter is used to regulate the output. This is beneficial for improving efficiency because the bulky hydraulic-mechanical CSD is replaced by power electronic converters. Figure 2.2(a) shows a diode rectifier used to convert the AC output of the generator into DC. Then, an inverter is used to convert the DC power into a fixed frequency AC feeding the main bus. This forms a back-to-back configuration which has been used on B777 as a 20kVA backup power generation system [32]. As there is an additional DC link, it is possible for powering high-voltage loads and charging the onboard batteries through DC/DC converters. In addition to the back-to-back structure, cyclo-converters or matrix converters can also be used to produce a fixed frequency AC supply for the aircraft's power system. This configuration is shown in Figure 2.2(b).

In this VSCF power generation system, no gearbox is required between the gas turbine shaft and the generator. However, the disadvantage is that the power converter must handle all the generated power, so it must have a high-power rating and high reliability. In such a system, the reliable and efficient power electronic converters are a concern.

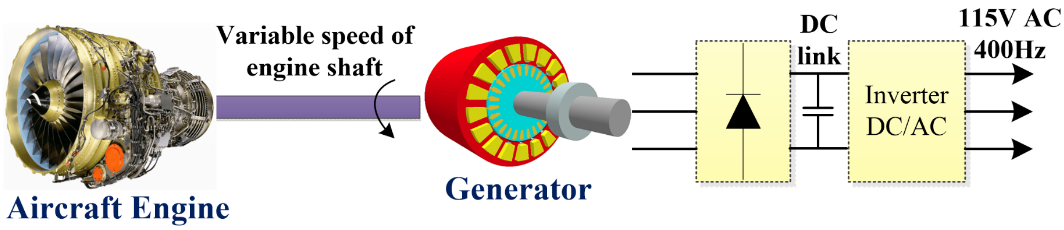

(a)

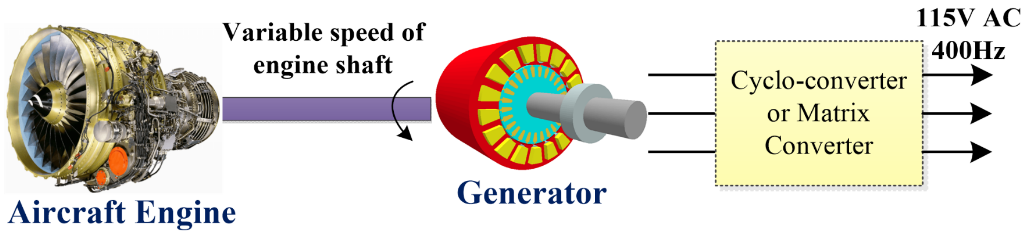

(b)

Figure 2.2. Variable speed constant frequency with a) diode rectifier. b) matrix converter or cyclo-converter.

2.2.3 Variable Speed Variable Frequency

Another solution for power generation is variable speed variable frequency (VSVF), also known as "frequency-wild" systems. These solutions have attracted a lot of attention in the research of future aircraft power generation systems. The key advantage is the direct connection between the generator output and the power system, which provides a simple and potentially reliable configuration. The disadvantage is that almost all aircraft loads will need local power converters for control, because some loads cannot directly use variable frequency power. As shown in Figure 2.3, the generator is connected to the engine shaft and outputs three-phase variable frequency power between 300Hz and 900Hz depending on the engine speed [34].

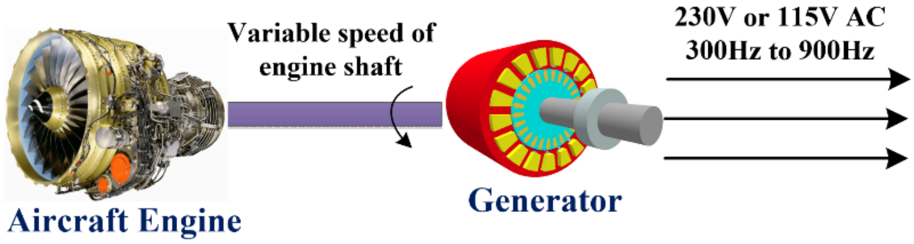

Figure 2.3. Variable speed variable frequency (VSVF) system.

This VSVF architecture has been applied in aircrafts such as the B787 and A380. In these aircraft, the voltage is adjusted to 115V (A380) or 230V AC (B787). The wide variable frequency range affects aircraft loads that are sensitive to frequency, such as AC motors. When powered directly by AC grid, the motor speed depends on the frequency of the AC grid. This may lead to inconsistent performance when using these motors. Local power converters can be used to address this problem as well as implementing more advanced control techniques for these motors [32].

2.2.4 DC Power Generation

The DC power generation system uses a DC generator to generate a DC voltage to power the on-board loads. There are generally two DC buses, one is 28 VDC for low-power loads, and the other is 270 VDC or 540VDC for high-power loads [2]. The DC generator is controlled to provide a constant DC voltage, even under variable engine speed and load power. This control also needs to meet the aerospace standards such as MIL-STD-704F [35] to ensure compatibility between the aircraft power system and other loads.

In some DC power generation systems, the high voltage DC is converted into 115VAC at 400Hz or 28VDC to meet the needs of specific loads, as shown in Figure 2.4. The F-22 and F-35 aircraft manufactured by Lockheed Martin use these DC power generation configurations. It is considered more efficient than traditional power generation methods, because the number of required power conversion stages are significantly reduced [32].

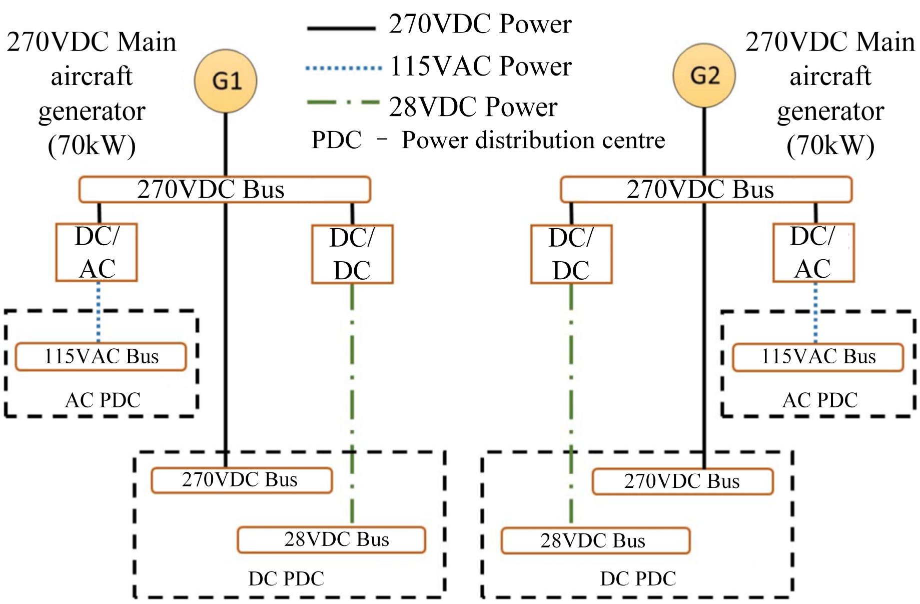

Figure 2.4. Power generation and distribution system in Lockheed Martin F-22.

2.2.5 Electrical Machines for Starter/Generator Applications

In order to reduce the number of components, volume and weight of aircraft systems, thereby potentially improving overall reliability and efficiency, many traditionally independent functions are integrated in the MEA concept. The starter/generator (SG) is an example, which includes both the main engine start and power generation functions.

In the start phase the SG performs as a motor, cranking the innermost compressor stage and enables the coupled compressors to deliver the required air flow into the combustion chamber. Once the required conditions are met, an ignition command is issued and fuel is injected into the combustion chamber, so that combustion occurs, and hot gases begin to flow through the turbine. Therefore, the turbine will generate torque to drive the mechanically coupled compressor stage. When the core shaft speed reaches the self-sustaining speed, the starter is cut-out [36]. In the generator mode, the engine acts as a source of mechanical power, and the SG converts mechanical power of engine shaft into electrical power to feed onboard loads.

In order to reduce the weight and volume of the system, usually the engine shaft with highest possible speed is selected to couple the SG. Therefore, the SG coupled with the HP spool is preferred. Considering the harsh environmental conditions and high temperatures may push most materials to their limits, more innovations are needed in the design of materials and thermal management systems [5]. Various types of electrical machines have been considered for aircraft power generation, including the wound field synchronous machine, induction machine (IM), switched reluctance machine, and permanent magnet machine (PMM) [39].

Wound Field Synchronous Machine (WFSM)

The WFSM machine topology is shown in Figure 2.5. It is often considered for future MEA applications because of their advantages in field regulation, mature technology and possible direct connection to the distribution network. However, compared to other electrical machine topologies, their complex rotor components (with wound field coils and rotating rectifier) present limitations. Therefore, WFSM is regarded as a sub-optimal option.

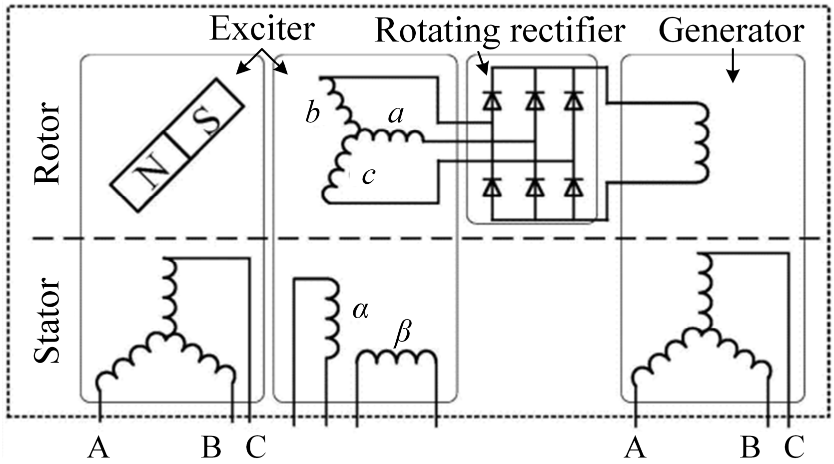

Figure 2.5. Diagram of three-stage wound-field synchronous machine [2].

Induction Machine

Induction machine (IM) presents characteristics including high robustness, fault tolerance, low cost, and tolerance to high operating temperatures. The schematic diagram of IM is shown in Figure 2.6. In [40] an IM-based AC/DC hybrid electric power generation system for a MEA was proposed, addressing the problem of excessive fault current due to the uncontrollable PM excitation in PMM-based generation system. Reference [41] proposed a direct-flux vector control scheme of a six-phase IM. The overload and post-fault operations capabilities have been verified. However, the IM suffers problems such as low power density, large end windings and excitation problems at high speeds, which need to be addressed for the MEA applications.

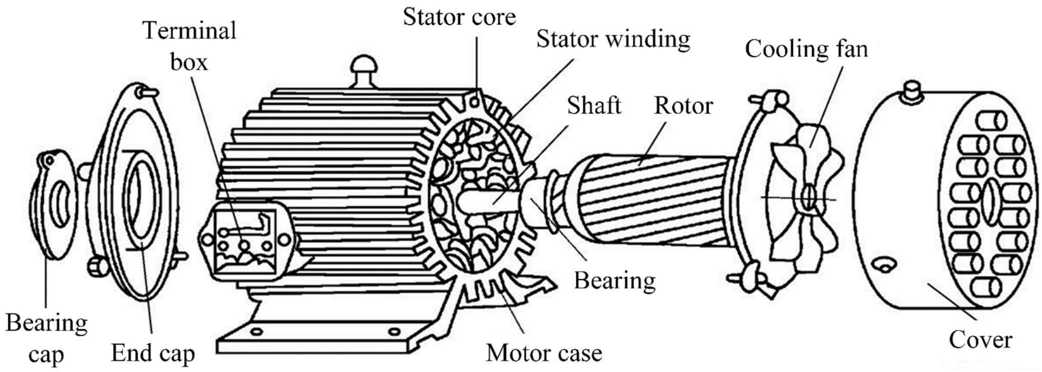

Figure 2.6. Diagram of the induction machine [42].

Switched Reluctance Machine

The switched reluctance machine (SRM)-based starter/generator system features high fault tolerance, wide speed range, and immunity to harsh environments. These features match with the requirements of aircraft applications. The structure of SRM is shown in Figure 2.7. In [43], a 250kW SRM was tested. The machine can operate in the starter and generator mode up to 13.5krpm. Dynamic load impact/dispatch of up to 102.5kW was performed with successful DC bus voltage regulation. However, SRM has inherent drawbacks of high torque ripple and limited power density. The torque ripple and resultant acoustic noise restrict the usage of SRM in MEA applications.

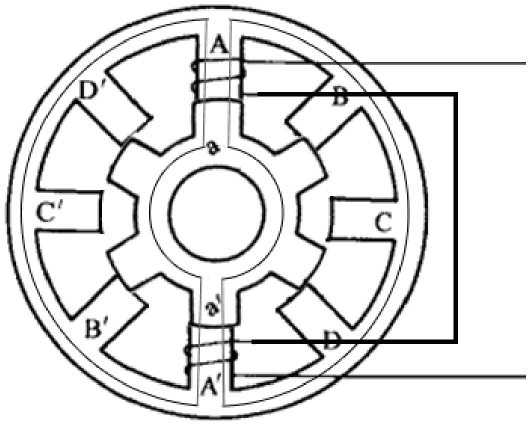

Figure 2.7. Structure of stator and rotor of the switched reluctance machine [43].

Permanent Magnet Machine

Permanent magnet machine (PMM) has taken a dominant position in the traction motor market for electric vehicle and hybrid electric vehicle. They can be designed to operate over a wide speed range and have excellent torque density and power density. The structure of stator of PMM is the same as that of IM. For the rotor side, permanent magnets are embedded in or mounted on the steel rotor to create a constant magnetic field. In [37], a surface-mounted 45kVA, 32krpm PMM machine was reported for SG application. It is interfaced with the DC bus through a neutral point clamped (NPC) three-level converter. Experimental results show excellent power generation and control performance. In [44], an interior PM (IPM) synchronous motor is used as a SG and a field-weakening strategy is developed to exploit its power generation capability in the high-speed region.

The qualitative comparison of different types of electrical machines for SG application is presented in Table 2-2. Due to the advantages of high efficiency, high power density, well-established control strategies, and ease of field weakening operation, the PMM-based PGC is studied in this Thesis.

Table 2-2. Pros and cons of different electrical machines for SG application

	Advantages	Disadvantages
Induction machine	• Robust rotor structure. • Singly excited. • Tolerance to high temperature. • Converter is easily available.	• Large end windings incur weight and reliability issue. • Low power density and power factor.
Switched reluctance machine	• Simple and robust rotor. • Suitable for wide speed operation. • Singly excited with excellent fault tolerance behaviour.	• Significant torque ripples. • High winding losses. • Low power density than PMM because of no stored energy.
Permanent magnet machine	• High power density and high efficiency. • Very good power factor. • Converter is easily available.	• Poor tolerance to high operating temperature. • Poor stator winding short circuit behaviour.

2.2.6 "Aircraft Electrical Generation with Active Rectification Technology"- AEGART Project

The "Aircraft Electrical Generation with Active Rectification Technology" (AEGART) project undertaken by the University of Nottingham is part of the Clean Sky JTI program [45]. The project studied potential SG topology candidates. Due to the advantages of PMM, a surface mounted PMM (SMPMM) powered by a three-level active rectifier was selected. The high-speed SG test rig and three-level power converter are shown in Figure 2.8.

The SMPMM was designed to achieve the torque-speed characteristics shown by the black solid line in Figure 2.9. It can be seen that in the starter mode, the SG covers all the envelope of engine torque-speed characteristics, ensuing a safe and quick engine start [44]. In the starter mode, the SG provides constant torque. The SMPMM outputs maximum torque to meet the torque requirements of the engine within the defined ambient temperature range. When operating in the generator mode, the SG outputs constant power. Given that SG operates as a generator during most of the average flight time, the AEGART machine has been optimized for operation within the speed range shown in Figure 2.9. More details of the design of this AEGART machine can be found in [46].

(a)

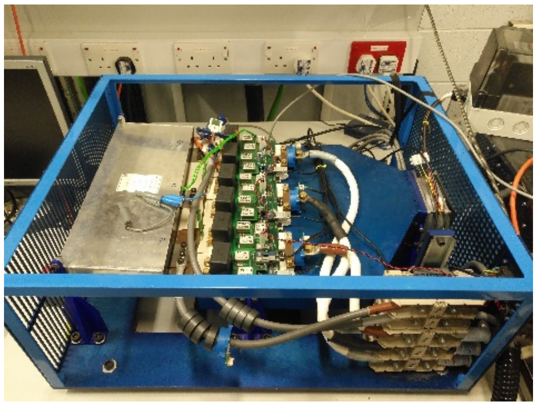

(b)

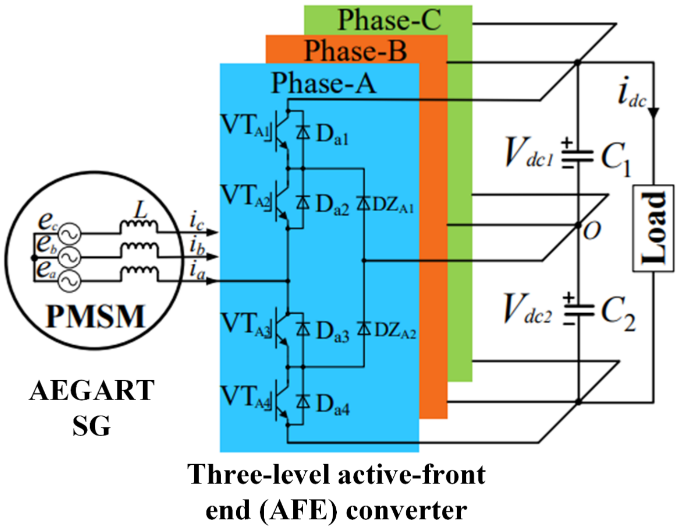

(c)

Figure 2.8. Prototype of the AEGART project at the University of Nottingham. (a) SG high-speed drive system. (b) Three-level power converter. (c) electrical topology of the AEGART SG and the AFE [47].

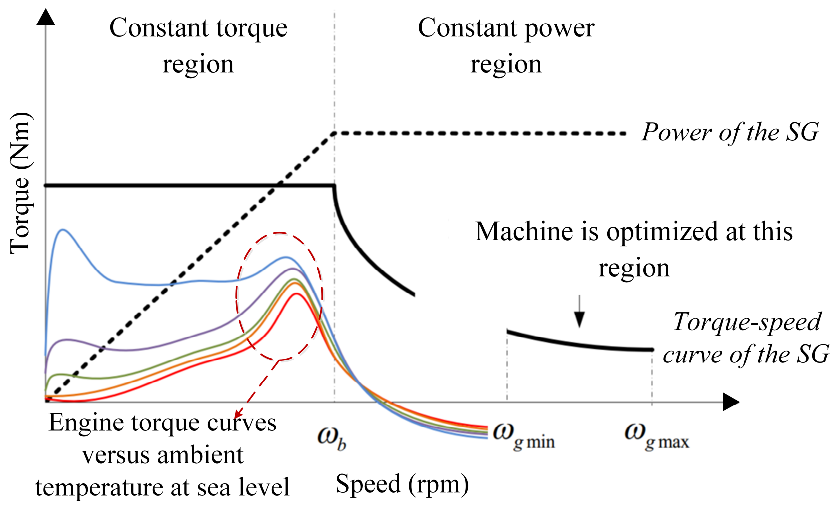

Figure 2.9. Torque-speed characteristic of the AEGART SG.

2.3 Overview of Power Distribution Architectures

2.3.1 Conventional Power Distribution Architecture

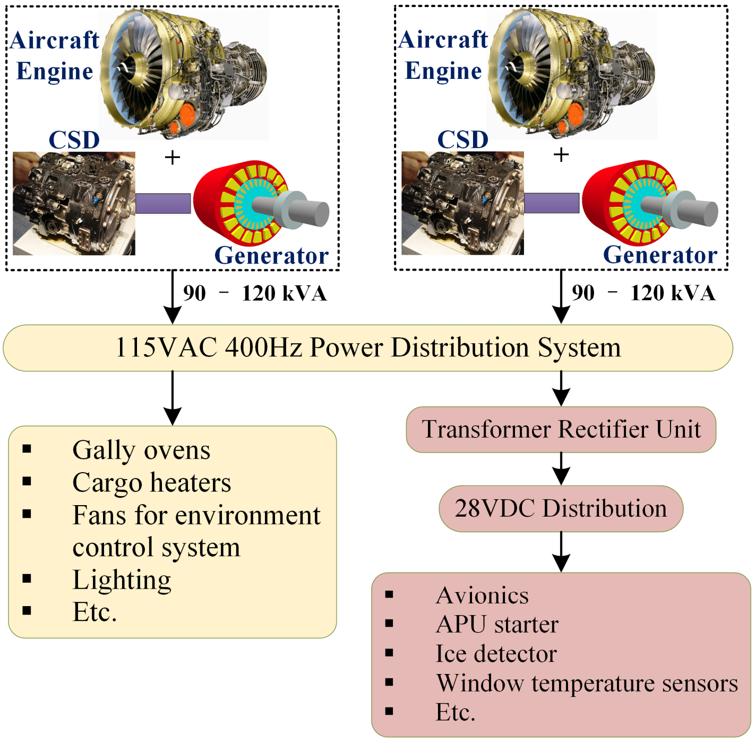

Figure 2.10. Diagrams of power distribution systems for conventional aircrafts such as B767 with 115VAC, 400Hz distribution network.

The power distribution architecture for most civil aircraft in service consists of a hybrid AC/DC topology. Those conventional commercial aircrafts, such as B767, usually use 115VAC voltage with a line frequency of 400 Hz for large loads such as galleys, as shown in Figure 2.10. In this structure, the generator is connected to the main engine through a constant speed drive that keeps the mechanical speed (and therefore the electrical frequency) constant on the AC bus of the aircraft.

Most fans driven by induction motors can directly run at 400 Hz without the use of power electronic converters [75]. The conventional electrical power distribution system also has a 28 VDC bus. By using a transformer rectifier unit [76], the 115 VAC can be converted to 28 VDC, supplying power to the loads such as avionics. The DC voltage is further reduced to obtain lower voltages (such as 5 V and 3.3 V), which are used to power integrated circuits, microprocessors, and signal electronics within equipment [77].

2.3.2 MEA Power Distribution Architectures

An example of a hybrid power distribution system for a MEA was considered in the European Union FP6 project MOET, as shown in [17], [78], [79]. The architecture studied is shown in Figure 2.11.

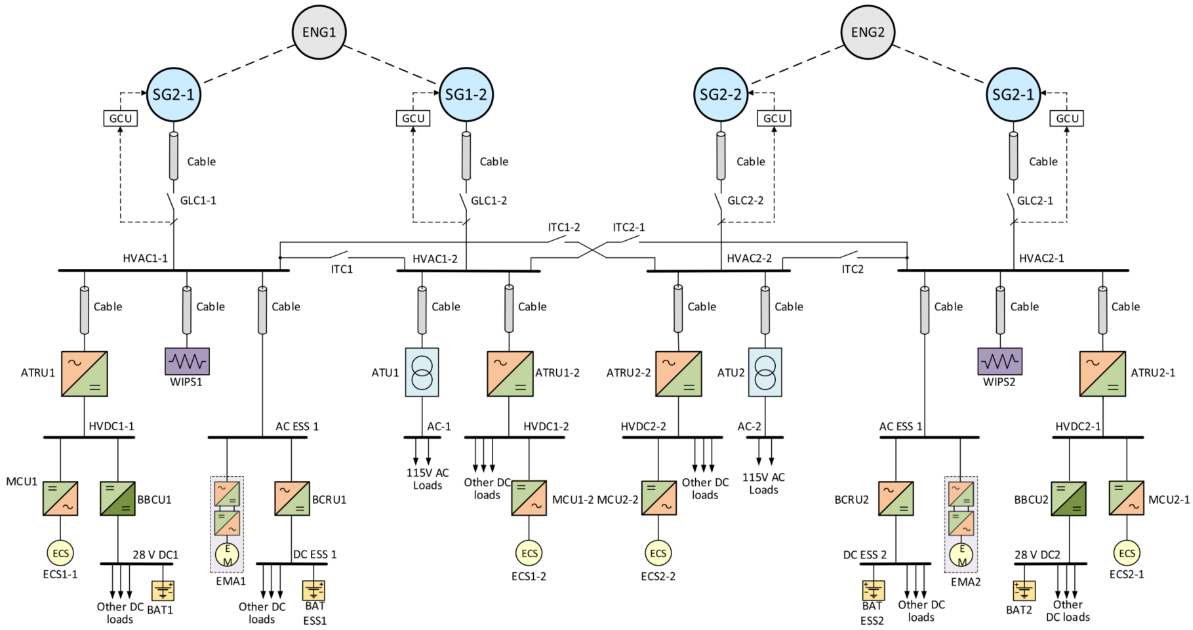

Figure 2.11. MOET electrical power distribution architecture for MEA [89].

This type of power distribution architecture has an island structure under normal conditions: each generator has its own load and distribution layer. In the event of a failure, certain interconnecting contactors can transfer the load to healthy power sources. Another feature of this power distribution architecture is that it relies heavily on power electronic converters (PEC). However, since many loads on the aircraft are required for a relatively short period of time during a flight mission, the utilization rate of PECs can be low. Improving the utilization rate will significantly reduce the total weight and cost of this power distribution system.

To improve the utilization rate of power converters, electrical power distribution system using modular and identical converters have led to a flexible architecture, as shown in Figure 2.12 [79], [80]. Here, each PEC is called a "cell" and can connect any primary bus with any secondary bus. If a cell failure occurs, the other parallel cells still operate to provide continuous power. This architecture uses reduced number of PECs, achieving weight and size benefits. This topology turns the overall power distribution system into a smart microgrid. Its optimal configuration is determined online by the supervisory logic for energy management. This logic can be designed in an analytical way to meet a set of optimization criteria. The latest research shows potential improvement in the power distribution system performance, including a high system reliability, high power supply availability, and minimization of weight [81], [82].

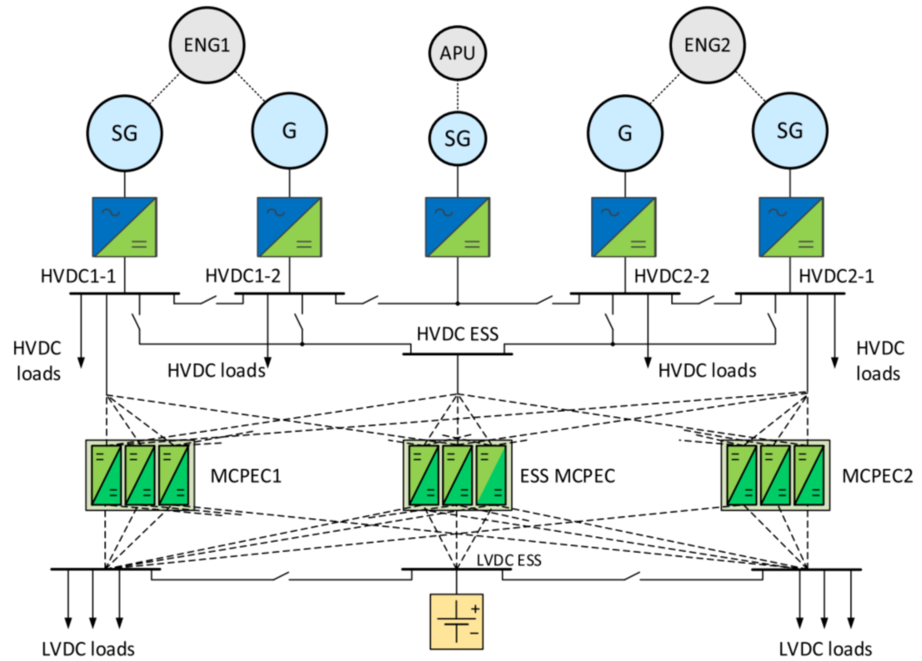

Figure 2.12. Flexible power distribution architecture using modular and identical PECs. ESS: energy storage system. MCPEC: modular cell power electronics converter [89].

Another trend in the development of the MEA power distribution system is the "single bus" concept. According to this concept, a single bus is used to connect all loads and all power sources [21] as shown in Figure 2.13. This topology becomes possible due to the introduction of active rectifiers to control the generators. Various power management equipment can be connected to the HVDC bus. The single DC bus configuration has advantage over AC network in terms of system efficiency, cost, and system size. Because lesser number of power electronic converters is required, the overall efficiency improves. Additionally, AC/DC converters do not require a transformer, which reduces the size of the DC network significantly [83]. However, the DC network suffers a high initial cost due to reasons such as the lack of a standardized plug.

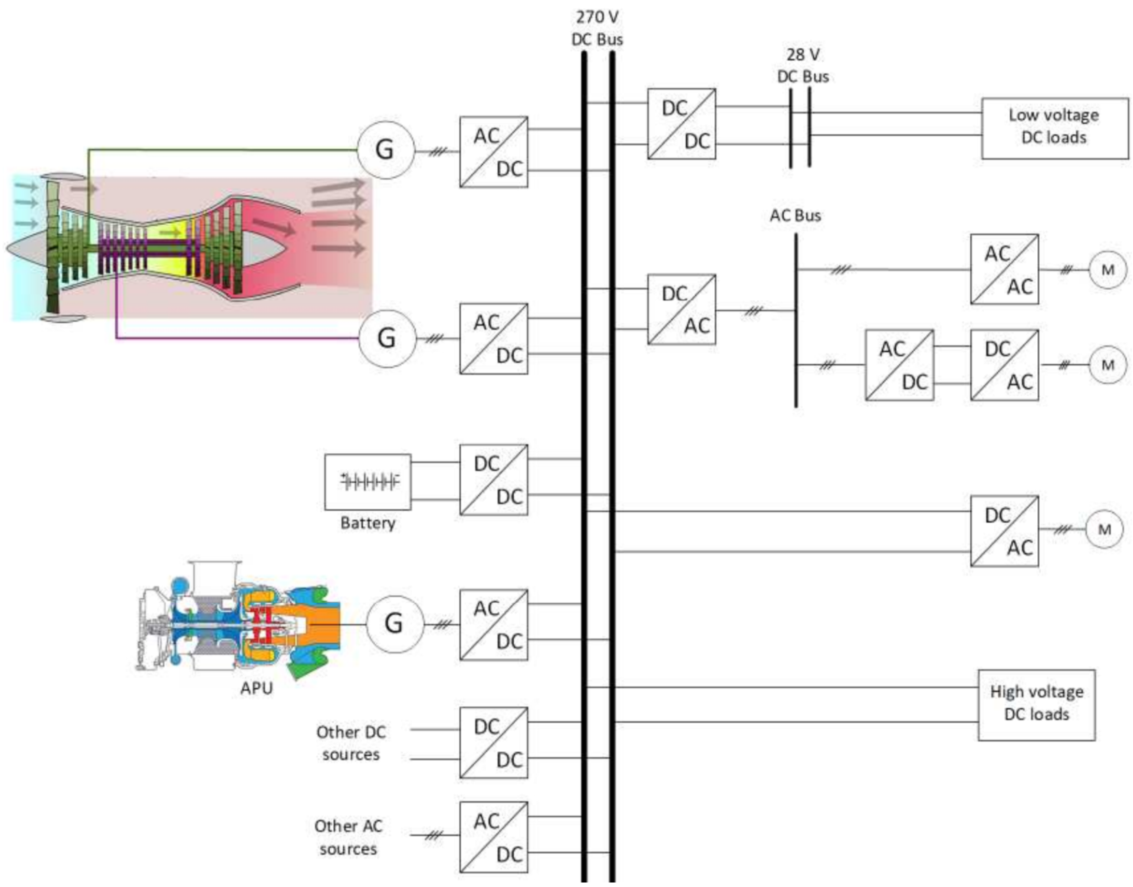

Figure 2.13. Single bus electrical power distribution system.

2.4 Power Consumption (Electric Loads on Aircraft)

In MEA's electrical power systems, there are many different types of physical loads that can be analytically represented by the constant impedance loads (CIL), constant current loads (CCL) and constant power loads (CPL). Typical CILs include resistive loads and other loads whose impedance do not change with operating conditions, such as wing ice protection system, galley ovens, and cargo heaters [2]. CCLs draw constant current from the power supply, for example transducers [84]. Most loads on the HVDC bus fed by power electronic converters/inverters behave as CPLs, such as DC/DC converter for resistive loads and DC/AC inverters for motor drives [84].

The *V-I* characteristics of CIL, CCL and CPL are shown in Figure 2.14. A CIL sinks increasing current as the increase of supplying voltage. A CCL draws a fixed current under wide variations of voltage source. For the CPL, the output voltage of a power converter drops when the current value increases. A CPL presents an incremental negative resistance (INR) characteristic, which degrades the stability of electrical power system [87]. Given the impact of the INR characteristic of a CPL and huge energy consumption of many CILs (e.g., thermal mats for wing ice protection), in the simulations and experiments in the following chapters, the studied electrical power system and power generation centre are loaded with CILs and CPLs.

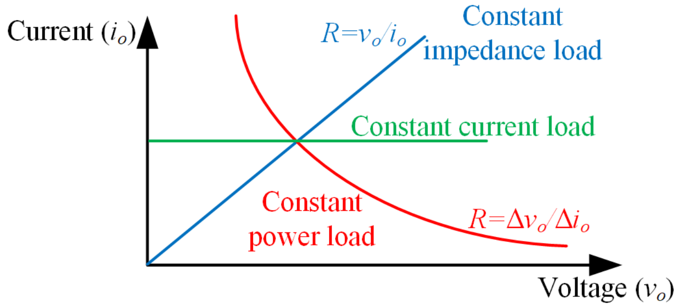

Figure 2.14. *V-I* characteristics of constant impedance load, constant current load, and constant power load.

2.5 The Single-Bus Dual-channel Power Generation Centre

It has been mentioned in Chapter 1 that as designs move towards the MEA concept, more power needs to be extracted from the primary source, the engine, and converted into electrical power to feed onboard loads. Electrical generators can be coupled to both the LPS and the HPS of the engine to exploit the power supply capability of the engine. Generally, the LPS and the HPS have different speeds. This means different AC frequencies from the LP generator (LPG) and the HP generator (HPG). This makes these generators cannot not be connected in parallel due to conflict in frequencies. Various PGCs have been proposed for this application [18], [40], [88]. Among them, a single-bus dual-channel PGC, shown in Figure 2.15, can handle the parallel operation of multiple generators, and has potential benefits in terms of weight, efficiency, availability and cost [89]. Moreover, the twin-generator architecture meets the redundancy and Requirements for Extended Range Twin-engine Operations [6].

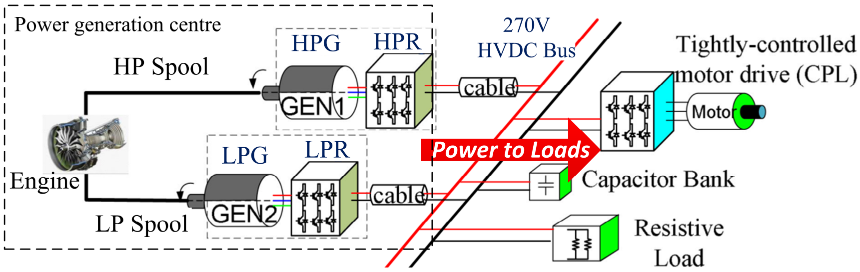

Figure 2.15. A single-bus dual-channel power generation centre.

In this architecture, the rectifiers convert the output of the generators into a single HVDC bus through the supervisory controller to share the load between the power sources. Then, the DC power can be routed by the distribution system around the airframe.

Despite the above-mentioned advantages, there are some key challenges for the PGC that need to be resolved:

- The first issue is related to the power losses caused by the high field-weakening (FW) current of the HPG. At full thrust settings of engine, rotary speed of the HPS of engine can reach 20,000 rpm [37]. Therefore, FW control is considered for the HPG to decrease the magnetic field density in the stator core and hence back electromotive force (back EMF). Significant current for FW is constantly injected into the HPG without outputting active power, leading to considerable power losses.
- Second issue is the poor fault tolerance capability. If failures such as open-circuit fault occurs to the low-pressure channel or high-pressure channel rectifiers (LPR and HPR shown in Figure 2.15), the faulty rectifier needs to be stopped and disconnected from the HVDC grid [28]. However, the associated generators cannot be stopped suddenly as they are connected to the aircraft engine with significant inertia. Even if the generators are stopped smoothly, these generators are no longer available for the loads. This will undermine the power supply capability of this PGC. Furthermore, losing one generator may lead to severe system instability at high load power scenarios.
- According to the relevant research [12], [73], in the high-power settings of engine, such as maximum take-off and top of climb, more power is expected to be extracted from the HPS than LPS to avoid the overspeed and instability of the HPS [74]. However, as revealed in Chapter 6, the LPR delivers more power to the HVDC bus than the HPR benefits the stability of EPS network. With the PGC in Figure 2.15, it is

not possible to extract more power from the HPS meanwhile delivering more power through the LPR to the HVDC bus.

2.6 Proposed Advanced Power Generation Centre with a Bridging Converter

In the PGC shown in Figure 2.15, the reason for FW operation of the HPG is that the back EMF is restricted by the 270V HVDC bus voltage [35]. Hence, to remove the FW operation of HPG and reduce the magnitude of phase current, designers should either reduce the back-EMF through electrical machine design or increase the DC bus voltage. Secondly, to improve the fault tolerance capability of the PGC, an effective way is to deploy more power converters to achieve a high redundancy. Thirdly, to extract more power from the HPS whilst deliver more power to the HVDC bus through the LPR, a bypass electrical path should be established between the HP and LP channel.

Based on the above analysis, an advanced power generation centre (APGC) with a bridging converter is proposed as shown in Figure 2.16. The bridging converter connects the original HP and LP power generation channels. Possible candidates for this bridging converter can be back-to-back converter, cyclo-converters, and matrix converter. With this configuration, the following benefits can be achieved:

- The HPG can operate at a high speed without FW control. This is achieved by setting a high-voltage DC link within the bridging converter, thus the back-EMF of the HPG does not need to be decreased using the FW control. All the current of the HPG can be active current. This helps reduce power losses of the HPG and HPR.
- An improved fault tolerance capability. In the case of either the HPR or LPR failure, the bridging converter can provide an additional power flow path, allowing the two generators to continue operating and supplying uninterruptible power to the downstream loads.
- More power can be extracted from the HPS than the LPS for avoiding the overspeed of the HPS. While on the other hand, the LPR can share more power than the HPR to enhance the HVDC grid stability. This favourable feature makes this APGC more flexible in terms of power flow.

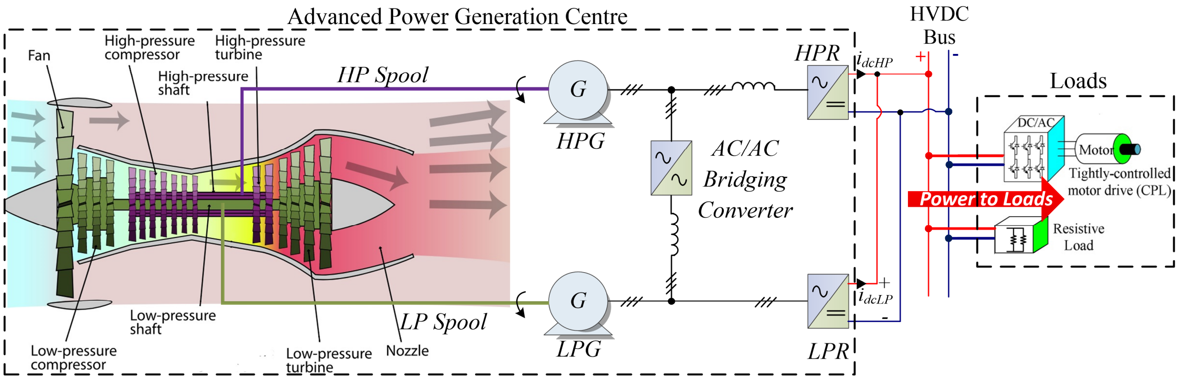

Figure 2.16. Proposed APGC with a bridging converter.

For the proposed APGC, challenges exist in coordinated control of the multiple sources and power converters in both healthy state and in post-fault operation. The design requires proper power management and stability analysis. These topics will be investigated in the following chapters.

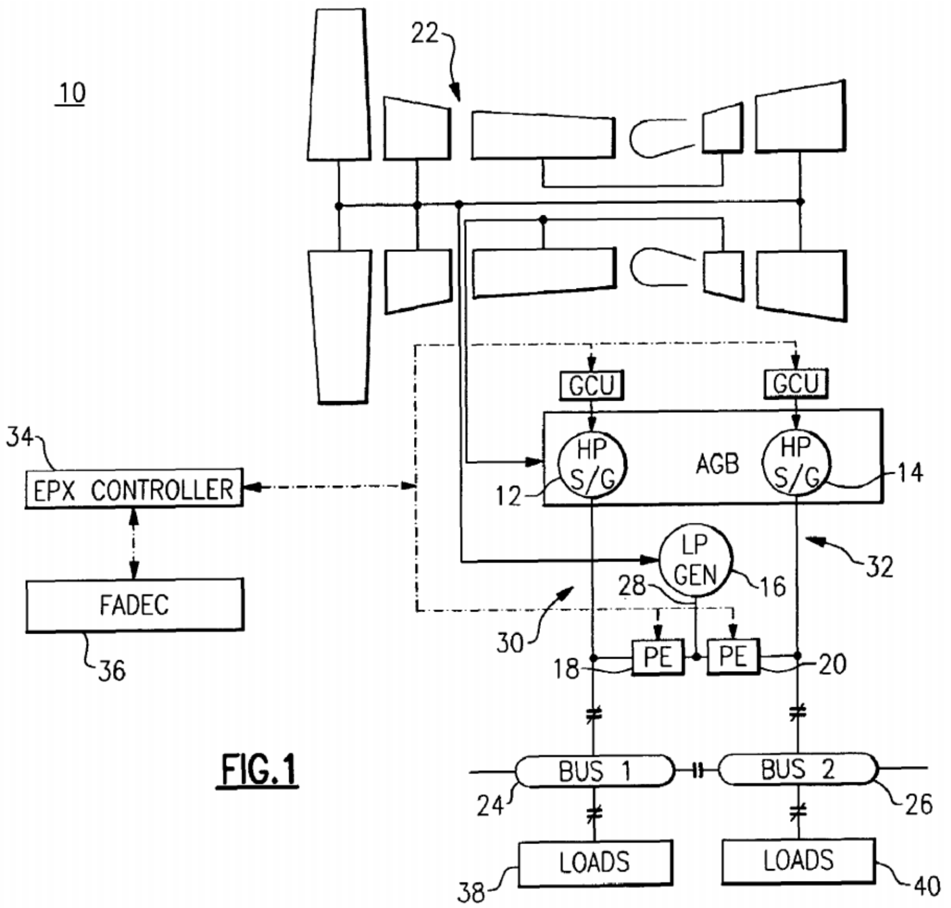

Figure 2.17. An electrical power system architecture in patent [131].

An electrical power system architecture was proposed in [131], as shown in Figure 2.17. It illustrates a wild frequency electrical power extraction system architecture with an externally located LPG.

With continued reference to Figure 2.17, all of the HP starter/generators (12, 14), the LPG (16), and power electronics (PE) (18, 20) associated with electrical power extraction (EPX) system architecture (10) can be seen to be located externally to the engine (22). The electrical power supplied by the LPG is then processed using power electronics and synchronized to each of the independently-supplied wild-frequency or constant-frequency buses (24, 26). The LPG output (28) is divided between two identical channels (30, 32). An EPX controller (34) in communication with a full authority digital engine control (FADEC) unit (36) commands the LP power electronics to pick up or shed AC bus loads (38, 40) for the LPG. This combined approach enables the engine controller (FADEC) to selectively load either LP or HP engine spools, as desired, to yield improvements in fuel efficiency, transient performance, compressor surge margins, or other parameters.

Although the terminals of the LPG and HPG are connected through a PE in Figure 2.17, there are some essential differences between this one and the proposed APGC architecture in Figure 2.16, to be specific:

- In Figure 2.17, if the PE (18, 20) becomes faulty, the LPG can no longer provide power to the loads. This means this architecture has no fault tolerance to the PE failure. However, in the APGC, the LPG can still provide continuous power even with the LPR becomes faulty.
- In Figure 2.17 the main buses are directly connected with the HPG. Considering the voltages of main bus should tightly follow relevant standard for AC or DC network, field weakening is still required for the HPG. As a contrast, the field-weakening operation of the HPG can be removed in the APGC.
- In Figure 2.17, the delivered electrical power to the bus equals to the extracted mechanical power from the engine spools for each HP and LP channel. Hence the stability of engine and HVDC grid cannot be improved at the same time at high power settings of engine. But the APGC can extract more mechanical power from the HPS while delivering more power to the HVDC grid through LPR, which is beneficial for both engine and grid stability.

These differences make the architecture in Figure 2.17 less favourable than the APGC. Detailed study regarding the APGC is illustrated in the following chapters.

2.7 Concept of Electric Power Transfer

Although the low-pressure compressors (LPC) and high-pressure compressors (HPC) are not directly connected, their speeds are thermodynamically coupled through the airflow. The thermodynamic coupling will lead to inflexibility in shaft speeds and a mismatch in performance of the compressors. These mismatches will enforce bleed control between the LPC and the HPC to adjust the airflow rate and avoid compressor surge [12]. However, the bleed action transfers part of the core airflow to the engine bypass duct, resulting in low engine fuel efficiency and inconsistent thrust. This makes the engine operate in a suboptimal condition. In this case, solutions to decouple the engine shaft speeds is desirable.

In order to optimize the engine performance and decouple the shaft speeds, an electrical path is established to achieve electric power transfer (EPT), as shown in Figure 2.15 and Figure 2.16. EPT can be realized by the electrical machines HPG and LPG mounted on the HPS and LPS. HPG and LPG can provide bidirectional power flow, extracting power from the engine spool as a generator or feeding power to the engine spool as a motor. The EPT system is part of the power generation centre, hence no extra hardware components are required.

EPT can be seen as a steppingstone between the current engine architecture and disruptive innovations (such as hybrid propulsion or all-electric aircraft). This is also the concept of supplementing the hybrid concept by improving the performance of the gas turbine. Possible advantages of EPT for the existing turbofan CFM56-3 are described in [73], [74], showing that EPT from the LPS to the HPS can bring significant benefits to the specific fuel consumption and the compressor surge margin under low power conditions. At high-power settings, such as maximum take-off, EPT from the HPS to LPS can prevent the HPS overspeed and maintain the HPC speed within the maximum allowable value. This work will present the effect of EPT on turbofan engine performance.

2.8 Chapter Summary

This chapter outlined the state-of-the-art technologies in the field of aircraft electrical power systems including power generation, distribution, and utilization. Different power generation options are highlighted and reviewed. Candidates for power generation systems, starter/generator motors have been compared. For each of these categories, conventional solutions have been described, and potential future alternatives and their advantages are outlined.

From the literature review it can be seen that the dual-channel single HVDC bus PGC is advantageous in terms of low power losses in the transmission cable and no need for any reactive power compensation equipment. However, the demand for FW operation of the HPG, no fault tolerance to the rectifier failure, and the incapability to achieve stability improvement of HVDC grid and engine, makes this PGC in need of modification. An APGC integrated with a bridging converter is proposed in this chapter to cope with these issues. Since multiple generators and power converters are involved in this system, coordinated control in healthy and post-fault operation state and power management are of great importance. This is the key targets of the research in this Thesis. One of the key advantages of the single HVDC bus architecture is the ease for EPT between the HP and LP power generation channels and the engine spools. The concept and benefits of EPT have been presented in this chapter as a basis for further research.

Chapter 3. The Dual-channel Power Generation Centre

As discussed in Chapter 2, the PGC is advantageous in terms of power system redundancy and integration of various power sources. This chapter starts with the introduction to the PGC concept. Then, the PGC is investigated in two modes, namely in coordinated power offtake (CPO) mode and in electric power transfer (EPT) mode. In the CPO mode, the two electrical machines coupled to the LP and HP spool operate as generators, extracting mechanical power from the engine shafts and supplying electrical power to the loads. While at certain engine operation modes, for fuel efficiency and enlarging compressor' surge margin, some amount of power can be transferred between the LP and HP spools. This is so-called EPT mode. Innovative findings of benefits of EPT on engine performance have been presented in our previous work [11], [12], [48]-[50]. This chapter will focus on the power generation and conversion systems. Analysis, modelling and control design of the system are the key contents of this chapter. System control performance and the benefits for engine in EPT mode are verified in simulation.

3.1 Introduction

The configuration of single bus PGC is presented in Figure 3.1 [54]. A SG is attached to the HP spool and a generator is linked to the LP spool. Both electrical machines are surface-mounted PMSGs controlled by bidirectional converters and supply a common main 270V HVDC bus. The rotary speeds of the two electrical machines are imposed by the coupled engine, and their torques are regulated by controlling their stator currents through controlling the power converter. In this case, mechanical power can be extracted both from the HP and LP spools of the engine, avoiding the drawbacks caused by excessive power extraction from HP spool only. As discussed in Chapter 2, typical loads in MEA can be represented by CIL, such as resistive loads, and CPL, such as motor-driven compressors regulated by power electronics converters.

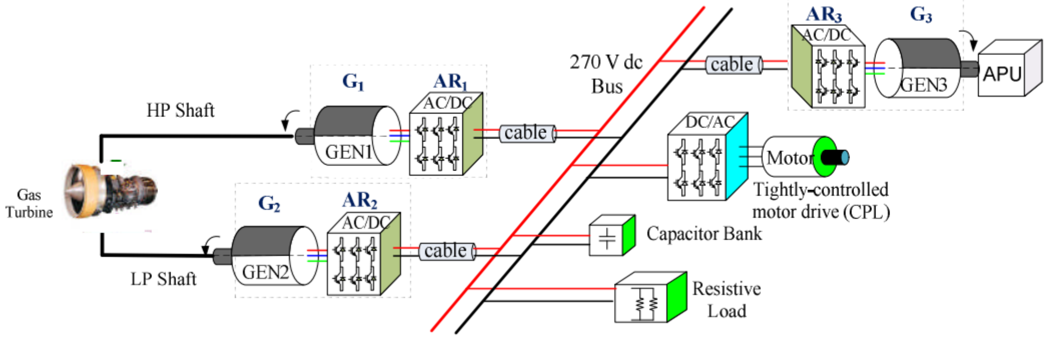

Figure 3.1. A single-bus multi-generator PGC topology [54].

3.2 System Analysis and Control Design

To ensure normal operation of the PGC in Figure 3.1, different objectives should be met:

- Regulating a stable DC bus voltage.
- Appropriate load power sharing between the HP shaft and LP shaft generators.
- Regulating the stator currents and torque of the generators.

To fulfil the above control objective, Figure 3.2 shows the control block diagram for the generator-rectifier system. By controlling the magnetic flux on the *d*-axis and the active power on the *q*-axis, the PMSG can operate in starter or generator mode. The coordinate transformation from *abc* to *dq* and the inverse transformation are given in Appendix A. The conventional proportional-integral (PI) controller is used to control the excitation component (*d*-axis) and the torque component (*q*-axis). When the rotary speed is lower than the base speed (constant torque region), the *d*-axis current component is equal to zero, ensuring the maximum torque to current ratio. In the high-speed operation area, the back electromotive force (EMF) of the PMSG, which is proportional to the speed, may be higher than the AC voltage of rectifier. The maximum value V_{cmax} of the reference voltage of the rectifier defines the constant power area where the FW is implemented. The stator current references on the *d* and *q* axes are obtained from the output of the FW controller and the I_{dc} controller, respectively. The reference of the AC voltage limit V_{cmax} depends on the DC-link voltage. The DC current reference i_{dc}^* is determined by the droop characteristic. This control scheme is applied to the both LP and HP generator-rectifier system.

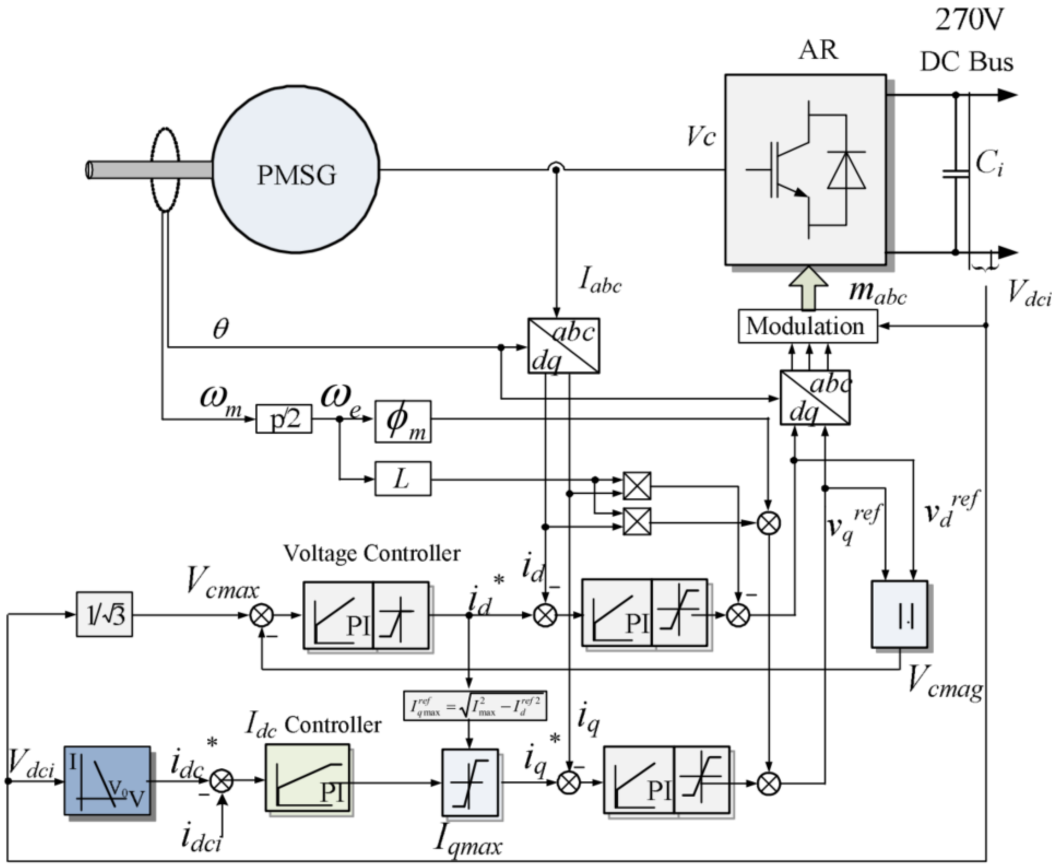

Figure 3.2. Control block diagram for the generator-rectifier system.

In the control block diagram, there are two control objectives: the main HVDC bus voltage and the stator currents of the generator. Instead of directly adjusting the DC bus voltage, the DC current I_{dc} is a control target for adjusting the appropriate active power injected into the DC bus. The output of I_{dc} controller determines i_q^*. The FW loop regulates the stator voltage magnitude V_{cmag}, whose output is d-axis current reference i_d^*. The control design for each controller, i.e., current control, FW control and DC voltage control, is discussed in the following sections.

3.2.1 Current Control Design

The PMM-based generators are considered for both HP and LP power generation channels. The electrical dynamics of PMM in the dq rotary frame in Appendix I are given as follows

$$\begin{cases} \dfrac{di_d}{dt} = \dfrac{1}{L_d}\left(v_d - R_s i_d + \omega_e L_q i_q\right) \\ \dfrac{di_q}{dt} = \dfrac{1}{L_q}\left(v_q - R_s i_q - \omega_e L_d i_d - \omega_e \psi_m\right) \end{cases} \tag{3-1}$$

where v_d and v_q are stator voltages in d and q axes, respectively; i_d and i_q are stator currents in d and q axes, respectively; L_d and L_q are stator inductance; R_s is the stator resistance; ψ_m is the flux linkage of permanent magnet; ω_e is the electrical angular speed in rad/s. For a surface-mounted PMM, $L_d = L_q = L_s$. The derivation process of (3-1) is presented in Appendix B.

The electrical dynamics can be rewritten using Laplace transform as follows

$$\begin{bmatrix} v_d \\ v_q \end{bmatrix} = \begin{bmatrix} L_s s + R_s & -\omega_e L_s \\ \omega_e L_s & L_s s + R_s \end{bmatrix} \begin{bmatrix} i_d \\ i_q \end{bmatrix} + \begin{bmatrix} 0 \\ \omega_e \psi_m \end{bmatrix} \tag{3-2}$$

Based on (3-2), the control plant and respective current loops can be derived as shown in Figure 3.3. It can be seen that for the current control plant, the dq-axes variables are cross coupled. The control performance of i_d will be affected by i_q, and vice versa. To eliminate the cross-coupling effect, a feedforward decoupling strategy is applied [51]. With a classical PI structure [52], the AC voltages of generator are given as follows

$$\begin{cases} v_d = (K_{i\mathrm{P}} + \dfrac{K_{i\mathrm{I}}}{s})(i_d^* - i_d) - \omega_e L_s i_q \\ v_q = (K_{i\mathrm{P}} + \dfrac{K_{i\mathrm{I}}}{s})(i_q^* - i_q) + \omega_e L_s i_d + \omega_e \psi_m \end{cases} \tag{3-3}$$

where $K_{i\mathrm{P}}$, $K_{i\mathrm{I}}$ are the P and I gains of the current controller, respectively. i_d^* and i_q^* are the currents references.

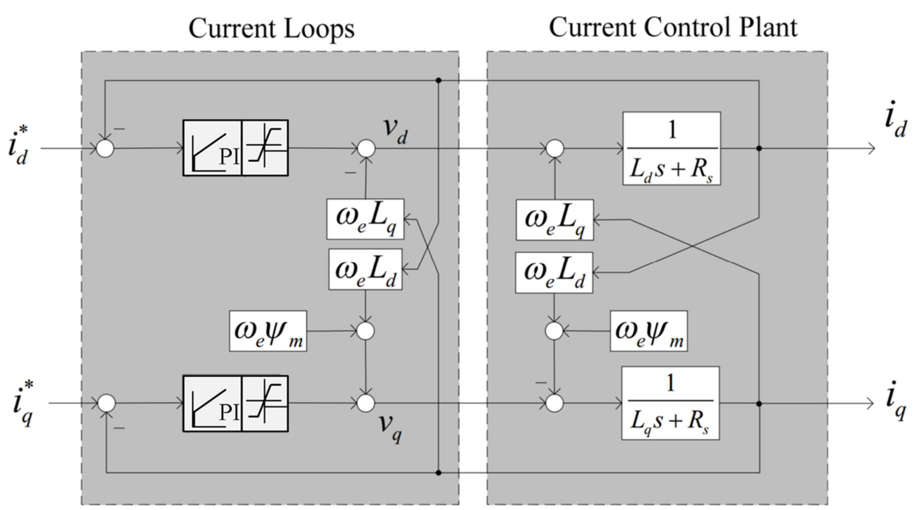

Figure 3.3. Control plant and control loops.

From (3-3) and Figure 3.3, the feedforward decoupling terms in current loops are chosen as below:

$$v_{d\_decouple} = -\omega_e L_s i_q \qquad v_{q\_decouple} = \omega_e L_s i_d + \omega_e \psi_m \tag{3-4}$$

Apply (3-3) into (3-2), the relationships between current references and feedback can be derived:

$$\begin{bmatrix} \dot{i}_d \\ \dot{i}_q \end{bmatrix} = \begin{bmatrix} g & 0 \\ 0 & g \end{bmatrix} \begin{bmatrix} i_d \\ i_q \end{bmatrix} + \begin{bmatrix} n & 0 \\ 0 & n \end{bmatrix} \begin{bmatrix} i_d^* \\ i_q^* \end{bmatrix} \tag{3-5}$$

where $g = -\left[(K_{i\mathrm{P}} + \frac{K_{i\mathrm{I}}}{s}) + R_s \right] \Big/ L_s$, $n = (K_{i\mathrm{P}} + \frac{K_{i\mathrm{I}}}{s}) \Big/ L_s$.

Equation (3-5) indicates that the variation of *dq* currents is only affected by themselves and their references. Therefore, a decoupled control is achieved. The *dq* axes closed-loop transfer function can be derived as follows

$$G_{c.l}(s) = \frac{i_d(s)}{i_d^*(s)} = \frac{i_q(s)}{i_q^*(s)} = \frac{K_{i\mathrm{P}} s + K_{i\mathrm{I}}}{L_s s^2 + \left(K_{i\mathrm{P}} + R_s\right) s + K_{i\mathrm{I}}} \tag{3-6}$$

The denominator of closed-loop transfer function mainly decides the characteristic of the current-loop. Hence, the controller parameters can be tuned by comparing (3-6) to a desired second order system with the characteristic equation given by:

$$c(s) = s^2 + 2\zeta\omega_n s + \omega_n^2 \tag{3-7}$$

Then the controller parameters can be derived:

$$K_{i\mathrm{P}} = 2\zeta\omega_n L_s - R_s \qquad K_{i\mathrm{I}} = \omega_n^2 L_s \tag{3-8}$$

where ω_n is the natural frequency, ζ is the damping ratio. Generally, the damping ratio is set as 0.707, and the natural frequency can be determined by the targeted control bandwidth (ω_b) [67]:

$$\omega_n = \frac{\omega_b}{\sqrt{1 - 2\zeta^2 + \sqrt{4\zeta^4 - 4\zeta^2 + 2}}} \tag{3-9}$$

Although the tuning method is easy to implement, it has disadvantages because of the zero in the closed-loop transfer function (3-6). To analyse the impact of this additional zero, (3-6) can be rearranged as follows:

$$G_{c.I}(s) = \underbrace{\frac{K_{iP}s}{L_s s^2 + (K_{iP} + R_s)s + K_{iI}}}_{G_1(s)} + \underbrace{\frac{K_{iI}}{L_s s^2 + (K_{iP} + R_s)s + K_{iI}}}_{G_2(s)} \tag{3-10}$$

It can be seen in (3-10) that the system response has two components, $G_2(s)$ represents the desired response, and $G_1(s)$ refers to the responses due to zero. To study the effect of the zero on control performance, step response tests are carried out for $G_1(s)$, $G_2(s)$ and $G_{c.I}(s)$, as shown in Figure 3.4. The PI gains are calculated from (3-8) and (3-9) using ζ=0.707, ω_b = 2π×1,000 Hz. L_s =100 uH, R_s =53 mΩ as shown in Table 3-1. It can be seen that the overshoot (Mp) of $G_2(s)$ is 4.5%, while with the effect of zero the Mp significantly rises to 19.8%. The rise time decreases from 0.34ms to 0.15ms due to the zero. Therefore, it can be concluded that the zero can improve dynamic performance but indicate to a lower stability margin.

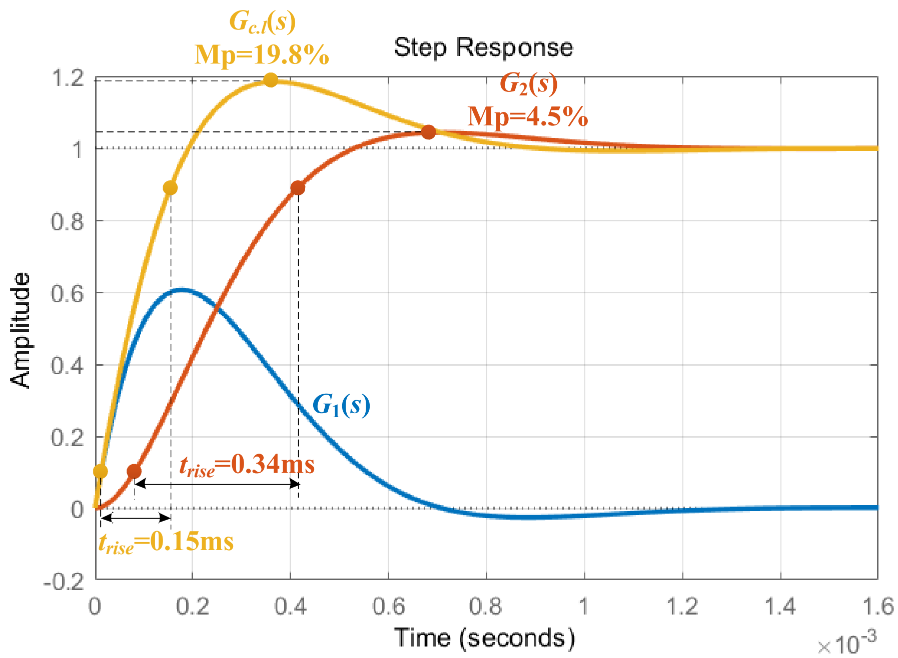

Figure 3.4. Step response of $G_1(s)$, $G_2(s)$ and $G_{c.I}(s)$.

In general, the selection of ω_b for the current loop is preferred to be fast. However, this will introduce large overshoot and may lead to steady-state oscillation [66]. Thus, the selection control bandwidth should be trade-off. According to the machine parameters in Table 3-1, where L_s =100 uH, R_s =53 mΩ, the time constant is L_s/R_s =1.88ms, equivalent to 530Hz. The switching frequency is f_{sw}=16kHz, according to [68], ω_b should be within 0.18f_{sw}, namely 2.8kHz. Hence the control bandwidth f_b should be within the following range:

$$530\text{Hz} < \omega_b < 2.8\,\text{kHz} \tag{3-11}$$

Table 3-1. Parameters of the AEGART project PMM.

Parameter	Rated value
Motor Power	45 kW @ 270VDC
Rated Speed	8000 rpm
Rated Current	170 A
Poles	6
Phases	3
Stator Resistance	53 mΩ
Stator Inductance (in *dq* axes)	100 µH
Flux Linkage of Magnet	0.0365 Wb

For meeting the condition in (3-11), the current controller is designed with 1kHz bandwidth as a trade-off between dynamic and steady-state performance. Then the P and I parameters can be obtained from (3-8).

The overall structure of current controller for both HP and LP power generation channels is demonstrated as shown in Figure 3.5. The *dq*-axes voltage commands, i.e., the outputs of current controllers are limited. When the output of the PI controller goes into a limitation, the current controller will disengage, but its integrator will continue to accumulate without affecting any control actions. This may lead to a high current overshoot, slow down the settling time and eventually lead to instability.

To minimize the impact of oversaturation on control performance, an anti-windup technique is adopted [52]. Figure 3.5 shows that in the used anti-windup scheme, the deviation between the limited voltage commands and the unbounded voltage commands is passed through a proportional gain (K_c), feeding to limit the error to the integrator, thus avoiding windup. The anti-windup parameters can be tuned as follows [52]

$$K_c = \frac{K_{i\mathrm{I}}}{K_{i\mathrm{P}}} \tag{3-12}$$

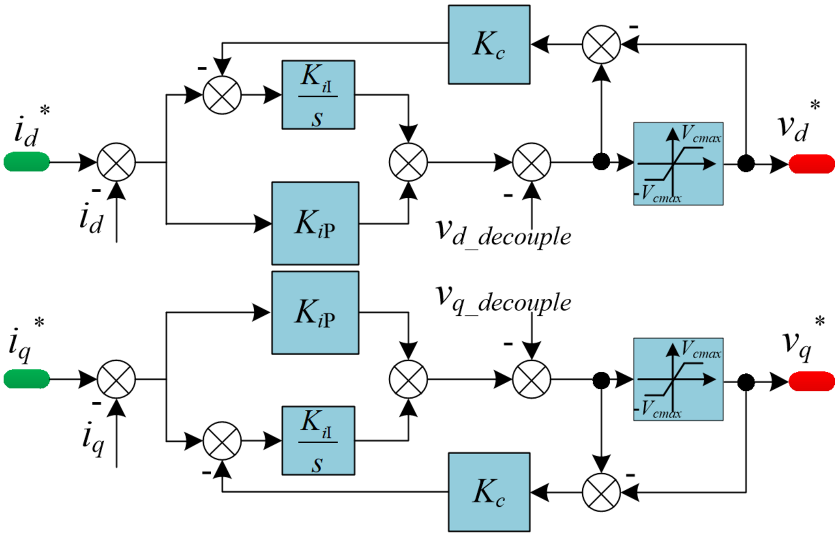

Figure 3.5. Current controller with anti-windup and decoupling terms in (3-4).

3.2.2 Field-Weakening Control Design

In the starter mode of the SG, it performs as a motor to crank the HPS until reaching the self-sustaining speed. While in the majority of flight time the SG operates as a generator, supplying electric power to the downstream loads. The targets of engine start (motoring mode of the SG) and power generation (generator mode of the SG) makes the design of the SG system should include coordinated consideration of machine–converter interactions. Since it operates as a generator in most flight time, the converter must therefore be able to deal with high speeds and associated large induced back EMF. This requires a high voltage rating for the converter. However, the same converter must also be able to handle the starting mode, which requires high torque hence high current rating. Overall, it means that the kVA rating of the converter should be selected at the maximum value based on the point C in Figure 3.6.

However, unfortunately, at point C it means that the converter will be significantly underutilized under normal operating scenarios. Furthermore, the converter kVA rating is related to the weight and volume of the converter, which is critical for the aircraft applications. Although these can be reduced by moving the machine electromagnetic design point down the saturation curve, this will increase the size and weight of the SG [85]. A solution to reduce size and weight of the SG is to implement a set of reconfigurable winding, such as switching from series to parallel connection, in different operation modes (for example, selecting point B or D in Figure 3.6 for design). However, this will lead to an increased number of switches and less efficiency due to additional losses in switching devices [85].

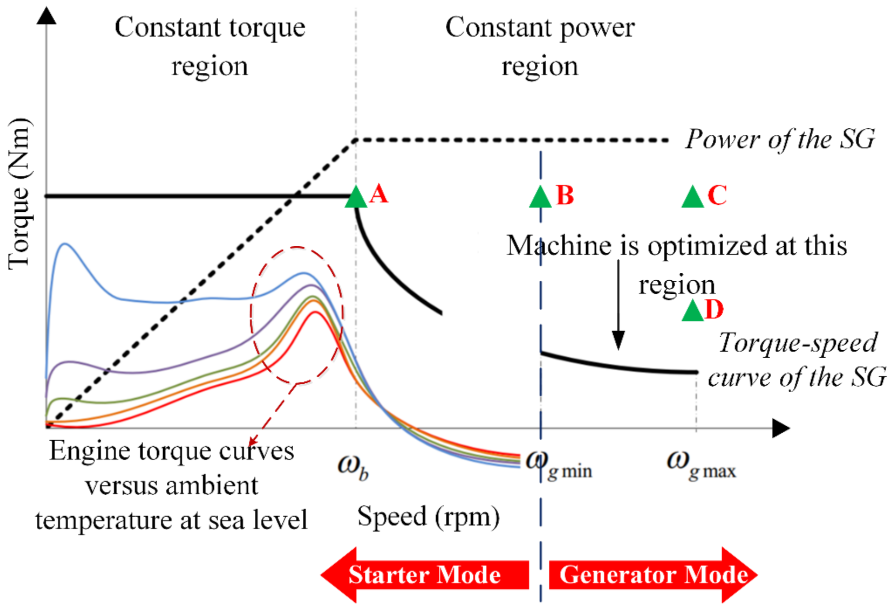

Figure 3.6. Torque and speed characteristics of the SG-converter system. Point A: base speed, maximum torque. Point B: minimum generator speed, maximum torque. Point C: maximum speed, maximum torque. Point D: maximum speed, minimum requirements imposed by the engine torque.

To reduce the kVA rating of the converter, another option is to operate the SG in the FW mode [86]. In this case, when above the base speed shown by the point A in Figure 3.6, a negative *d*-axis current is injected into the machine and the flux linkage is gradually reduced, limiting the back EMF. This means that the voltage rating of converter can be substantially reduced at point A compared with B, C, and D. Therefore, FW control becomes a must which bring benefits for the aircraft SG system, since the 270V DC link voltage is typically low compared to the induced back EMF in practical high-speed generation applications

According to (3-1), the steady state voltage limit equation of SG can be derived as follows

$$v_d^2 + v_q^2 \le V_{c\max}{}^2 \Rightarrow \left(R_s i_d - \omega_e L_s i_q\right)^2 + \left(R_s i_q + \omega_e L_s i_d + \omega_e \psi_m\right)^2 \le V_{c\max}{}^2 \quad (3\text{-}13)$$

Based on the AEGART machine parameters in Table 3-1, the operational limits and trajectory of the SG drive system are presented in Figure 3.7, where the voltage limit circles in green are plotted based on (3-13). In the starter mode, the machine goes into point #1, cranking the engine shaft at its maximum torque. When the speed increases beyond the base speed (8 krpm), the FW operation is automatically activated since the voltage reference magnitude is larger than the actual available voltage as shown in Figure 3.2. A negative *d*-axis current is injected into the machine according to the error between the reference voltage and the voltage limit V_{cmax} set by the inverter (see Figure 3.2). The magnetic field generated by the *d*-axis current is opposite to the magnetic field of the permanent magnet on rotor, diminishing the induced back EMF. At 10 krpm, the engine ignites, and the SG moves to standby mode, where the *q*-axis current falls to zero. The generation mode starts at 20 krpm and outputs up to 45kW power indicting by point #4 with significantly negative *d*-axis current flowing into the machine.

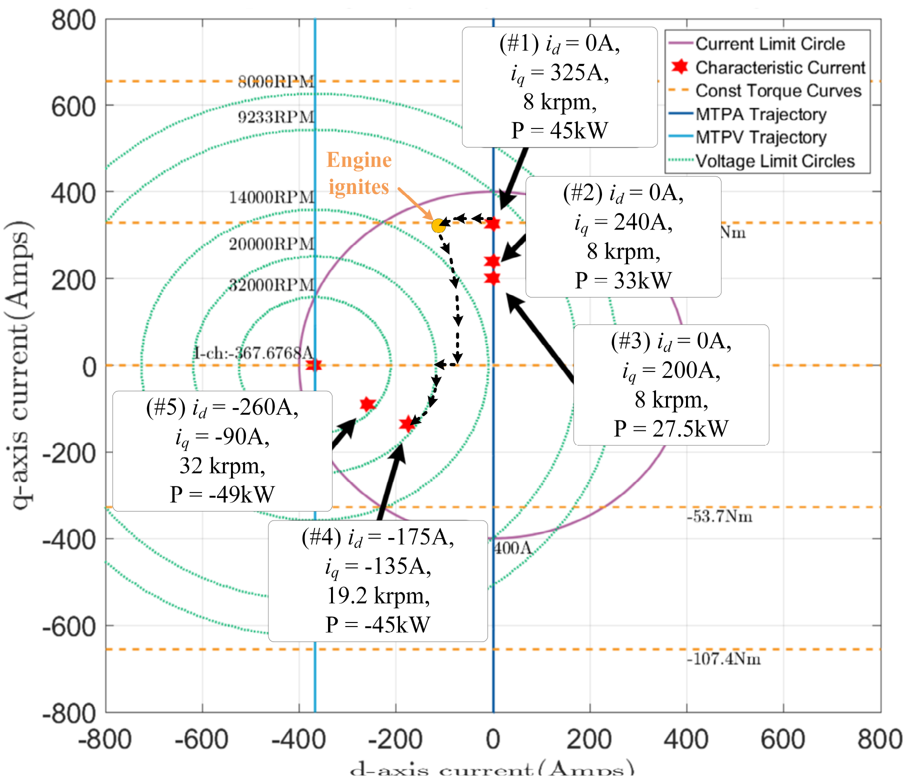

Figure 3.7. Operating trajectory of the SG drive system.

From above analysis the control logic of FW controller can be derived as follows: when the stator voltage is less than the maximum value V_{cmax}, the output of the FW controller, i.e., *d*-axis current reference should be zero. When the stator voltage exceeds the maximum voltage limit, the controller starts to operate, generating a negative *d*-axis current reference. The magnitude of current reference needs to increase as the increase of speed to maintain constant stator voltage. A classical PI control structure is applied for FW purpose [69]:

$$\begin{cases} i_d{}^* = \dfrac{K_{FWp}s + K_{FWi}}{s}(V_{c\max} - v^*) \\ v^* = \sqrt{v_d{}^{*2} + v_q{}^{*2}},\ i_d{}^* \in \left[-I_{\max}, 0\right] \end{cases} \tag{3-14}$$

where K_{FWp} and K_{FWi} is the P and I gain of the FW controller, respectively. $V_{c\max}=v_{dc}/\sqrt{3}$ when using the space-vector pulse width modulation (SVPWM). $I_{\max}$ is the machine current limitation.

The d-axis current set-point given in (3-14) is automatically adjusted by voltage feedback through tracking the voltage constraints as the speed varies [53]. Unlike model-based FW controls, such as model predictive control [70], the tuning of control gains in (3-14) does not require accurate machine parameters. It can maintain consistent control performance when the motor parameters change due to temperature rise or magnetic saturation. Hence, it is considered robust against machine parameters variation [69].

3.2.3 Analysis and Control Design of the DC Voltage Loop

As shown in the system schematic diagram in Figure 3.1, the DC bus can be regarded as the “energy interface” between the PGC and the various onboard loads. The onboard loads acquire power from the DC bus, whilst the PGC supplies power to the DC bus. To ensure the normal operation of the generators and loads, the DC bus voltage should be actively regulated. In this subsection, a DC voltage control loop is established to fulfil the regulation of the DC bus voltage, where the control plant and control design are specifically analysed.

3.2.3.1 DC Bus Voltage Control: The Control Plant

Since multiple power sources are involved in the PGC, appropriate power sharing between power sources is required. A current-mode droop control method presented in [54] is adopted due to advantages including the absence of communication link, high modularity, and immunity from the impact of cable impedance. The power sharing is achieved by splitting the total load current i_{dc} into currents i_{dcLP} and i_{dcHP}. Using droop control characteristic, the DC current reference can be derived as follows:

$$i_{dc}{}^* = \frac{v_{dc}{}^* - v_{dc}}{g_D} \tag{3-15}$$

where g_D is the droop gain.

With the current-mode droop control, the output of control plant should be the DC current i_{dc} to regulate DC voltage changes caused by the load currents.

The DC link equation can be formulated as:

$$C\frac{dv_{dc}}{dt} = i_{dc} - i_L \tag{3-16}$$

The control plant for i_{dc} control can be derived from the electrical dynamics of PMM shown in (3-1) and the DC link dynamics shown in (3-16) using small signal analysis, given as follows:

$$\begin{aligned}&\left[\bar{v}_{dc} - \frac{3\left(\bar{v}_d\bar{i}_d + \bar{v}_q\bar{i}_q\right)}{2\bar{v}_{dc}Cs}\right]\Delta i_{dc} = -\frac{3}{2}\left(\bar{v}_d\Delta i_d + \bar{v}_q\Delta i_q\right) - \\ &\frac{3}{2}\left\{\bar{i}_d\left[\left(R_s + L_s s\right)\Delta i_d - \omega_e L_s\Delta i_q\right] + \bar{i}_q\left[\left(R_s + L_s s\right)\Delta i_q + \omega_e L_s\Delta i_d\right]\right\}\end{aligned} \tag{3-17}$$

where the superscript "‾" indicates the selected operating points. i_d and i_q are the stator currents of the PMM generator in dq frame. v_d and v_q are the terminal voltages of PMM generator in dq frame.

The relation shown in (3-17) can be rearranged as follows:

$$\begin{aligned}\Delta i_{dc} = &-\frac{3\bar{v}_{dc}Cs\left[\bar{v}_d + \omega_e L_s\bar{i}_q + \left(R_s + L_s s\right)\bar{i}_d\right]\Delta i_d}{2\bar{v}_{dc}^2Cs - 3\left(\bar{v}_d\bar{i}_d + \bar{v}_q\bar{i}_q\right)} \\ &-\frac{3\bar{v}_{dc}Cs\left[\bar{v}_q - \omega_e L_s\bar{i}_d + \left(R_s + L_s s\right)\bar{i}_q\right]\Delta i_q}{2\bar{v}_{dc}^2Cs - 3\left(\bar{v}_d\bar{i}_d + \bar{v}_q\bar{i}_q\right)}\end{aligned} \tag{3-18}$$

Based on (3-18) and the current loop transfer function shown in (3-6), the control plant can be derived as shown in Figure 3.8, where the expression of f_d and f_q are given as follows:

$$\begin{cases} f_d = -\dfrac{K_{i\mathrm{P}}s + K_{i\mathrm{I}}}{L_s s^2 + \left(K_{i\mathrm{P}} + R_s\right)s + K_{i\mathrm{I}}}\dfrac{3\bar{v}_{dc}Cs\left[\bar{v}_d + \omega_e L_s\bar{i}_q + \left(R_s + L_s s\right)\bar{i}_d\right]}{2\bar{v}_{dc}^2Cs - 3\left(\bar{v}_d\bar{i}_d + \bar{v}_q\bar{i}_q\right)} \\ f_q = -\dfrac{K_{i\mathrm{P}}s + K_{i\mathrm{I}}}{L_s s^2 + \left(K_{i\mathrm{P}} + R_s\right)s + K_{i\mathrm{I}}}\dfrac{3\bar{v}_{dc}Cs\left[\bar{v}_q - \omega_e L_s\bar{i}_d + \left(R_s + L_s s\right)\bar{i}_q\right]}{2\bar{v}_{dc}^2Cs - 3\left(\bar{v}_d\bar{i}_d + \bar{v}_q\bar{i}_q\right)} \end{cases} \tag{3-19}$$

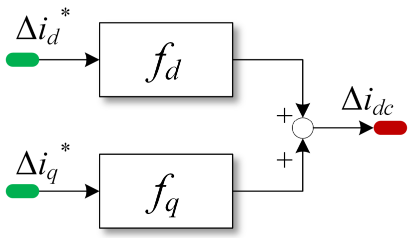

Figure 3.8. Control plant for the i_{dc} control.

Before moving to the control design, the control plant is verified with a nonlinear equivalent model in the Matlab/Simulink environment as presented in Appendix C. The derived control plant is verified by comparison with the non-linear model in Simulink. The characteristics of the derived control plant depend on operating point. The operating point used for control plant verification are obtained in the steady state, as shown in Table 3-2.

Table 3-2. Operating point used for control plant verification.

Parameter	Value	Parameter	Value
$\overline{v}_d$	30 V	$\overline{i}_d$	-128 A
$\overline{v}_q$	143 V	$\overline{i}_q$	-60 A
$\overline{v}_{dc}$	270 V	ω_e	6283 rad/s (20k rpm)
K_{iP}	0.87	K_{iI}	3908

With the operating points shown in Table 3-2, the expressions of f_d and f_q can be derived as follows:

$$\begin{cases} f_d = \dfrac{0.87s+3908}{10^{-4}s^2+0.928s+3908}\,\dfrac{0.0128s^2+14.88s}{174.96s+37621} \\ f_q = \dfrac{0.87s+3908}{10^{-4}s^2+0.928s+3908}\,\dfrac{0.0058s^2-216.14s}{174.96s+37621} \end{cases} \tag{3-20}$$

The step responses of the derived control plant and the nonlinear model are presented in Figure 3.9. It can be seen that the step responses of control plant and nonlinear model are very close in terms of transient and steady state performances. Hence, the derived control plant is verified. Moreover, it can be seen from (3-19) that there is a positive zero in f_q. This positive zero will lead to a non-minimum phase characteristic, delaying the response and causing opposing response to the input [93]. This is the reason why an initial undershoot occurs in Figure 3.9(b).

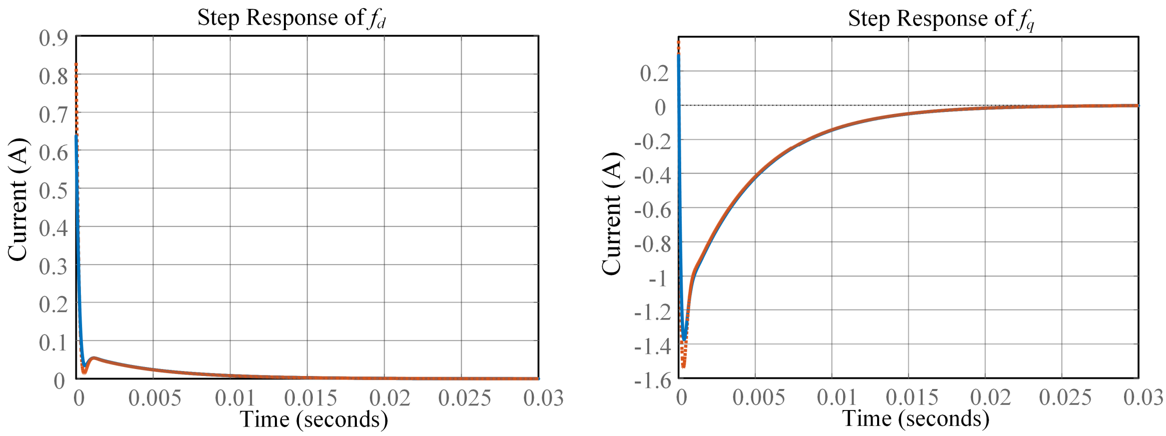

(a) (b)

Figure 3.9. Step response of the derived control plant (blue curves) and the nonlinear equivalent model in Simulink (red curves). (a) step response of f_d with $\Delta i_d = 1$A. (b) step response of f_q with $\Delta i_q = 1$A.

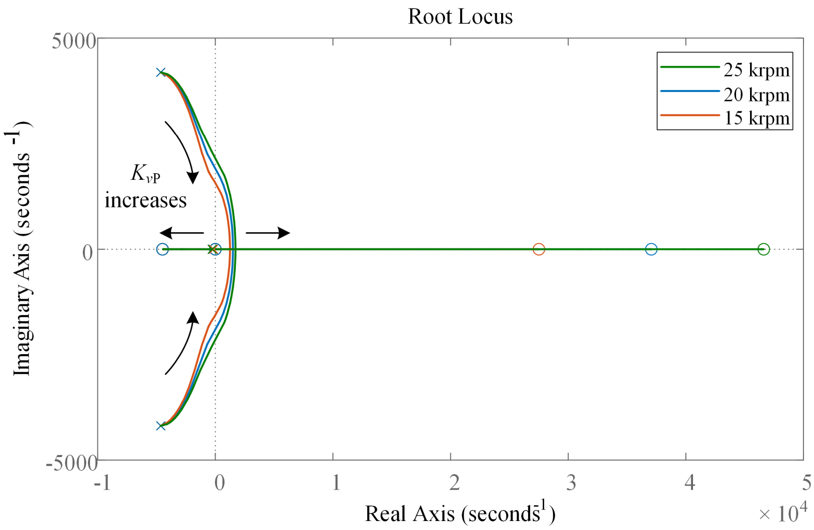

(a)

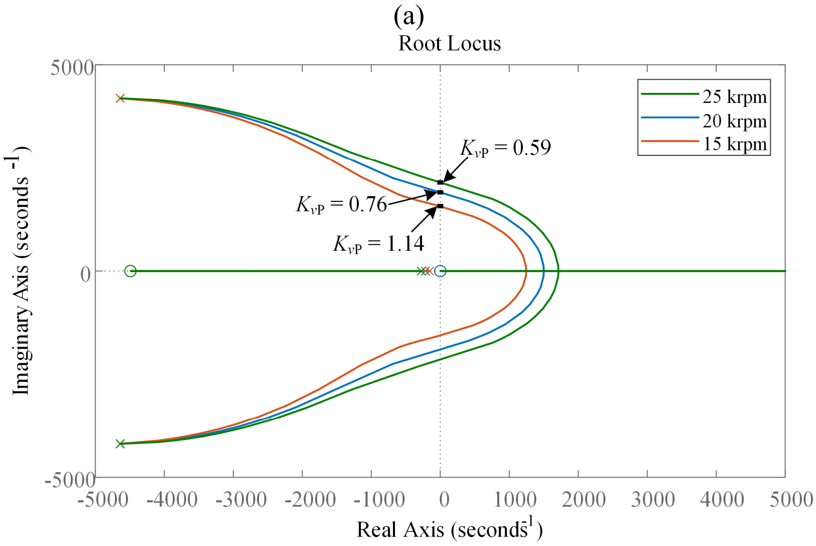

(b)

Figure 3.10. Closed loop root locus of control plant at different speeds. (a) overview. (b) zoomed area. Load power is 15kW.

To study how the poles and zeros of the control plant will move with different operating points, the closed loop response of the plant was investigated, where a proportional (P) controller is used since the P controller will not introduce additional poles or zeros. The proportional gain is denoted as K_{vP}. Figure 3.10 and Figure 3.11 show the closed loop root locus at different speeds of generator and different load powers. It can be seen that the closed loop poles move towards the right half plane (RHP) as the increase of K_{vP}. The value of K_{vP} must be carefully selected to ensure that the poles do not move cross the imaginary axis into the RHP, otherwise the system will become unstable.

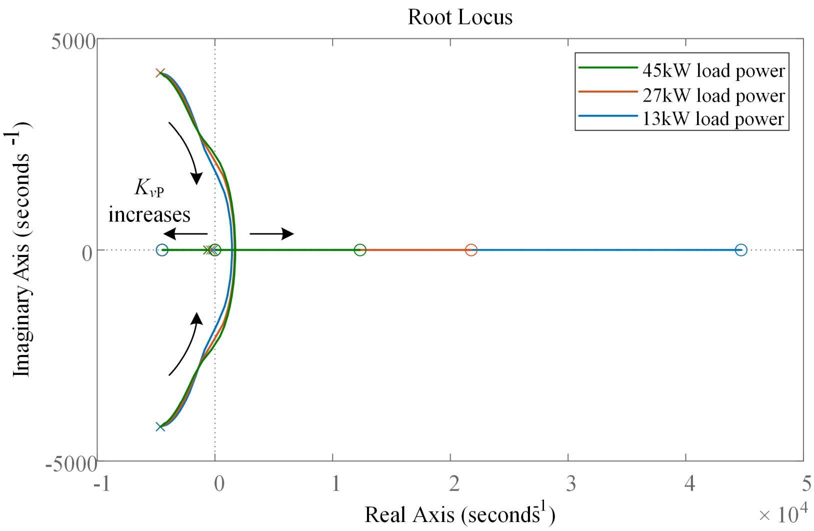

(a)

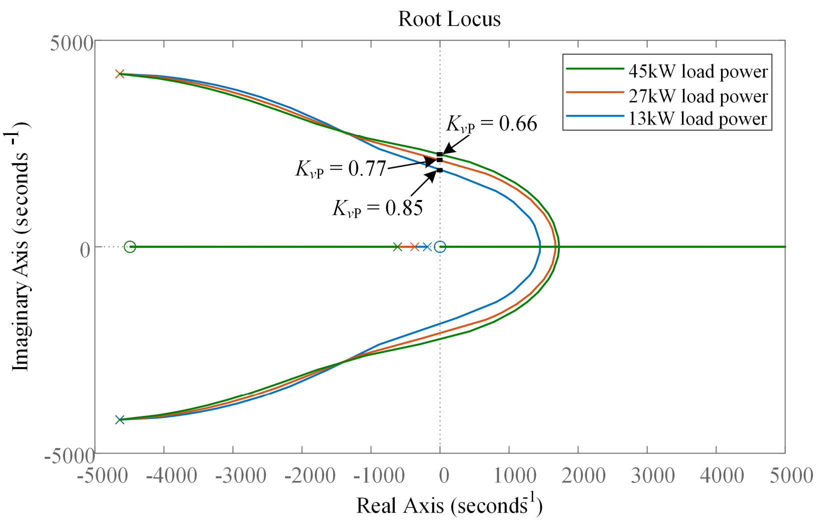

(b)

Figure 3.11. Closed loop root locus of control plant at different load powers. (a) overview. (b) zoomed area. Operating speed is 20 krpm.

It can be seen from Figure 3.10 that as the increase of speed, the allowable value for K_{vP} decreases from 1.14 to 0.59. Also, from Figure 3.11, it can be seen that as the increase of load power, the allowable value for K_{vP} decreases from 0.85 to 0.66. These results show that the worst operating point corresponds to the highest speed and full power. Hence, this operating point is specifically considered when designing the i_{dc} proportional-integral controller.

3.2.3.2 DC Bus Voltage Control Design

In the proposed APGC, the DC-link voltage within the back-to-back converter can be set to a high value, ensuring the HP generator to operate without field weakening. Thus, i_d can be controlled to be zero for the surface-mounted PMM in use. Hence, a reasonable assumption was made for the following control design, which is that the influence of i_d is neglected. The dynamics of Δi_{dc} are dominantly contributed by Δi_q. With this assumption, the block diagram of the DC bus voltage control can be derived as shown in Figure 3.12.

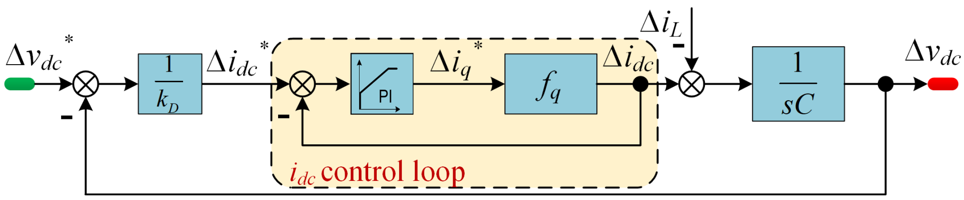

Figure 3.12. Block diagram of the DC bus voltage control.

As shown in Figure 3.12, a PI controller is applied to regulate the inner i_{dc} control loop. The controller can be expressed as:

$$G_{pi}(s) = K_{vP} + \frac{K_{vI}}{s} \tag{3-21}$$

With the f_q in (3-19) and (3-21), the open loop transfer function of the i_{dc} control loop can be written as follows:

$$G_{idc}(s) = -\frac{(K_{iP}s + K_{iI})(K_{vP}s + K_{vI})}{L_s s^2 + (K_{iP} + R_s)s + K_{iI}} \frac{3\overline{v}_{dc}C\left[\overline{v}_q - \omega_e L_s \overline{i}_d + (R_s + L_s s)\overline{i}_q\right]}{2\overline{v}_{dc}^2 Cs - 3(\overline{v}_d \overline{i}_d + \overline{v}_q \overline{i}_q)} \tag{3-22}$$

As can be seen in (3-22), there are three poles in $G_{idc}(s)$, and two out of the three are conjugate poles brought by the current loop transfer function. To study the effect of the three poles, their locations on the complex plane are plotted with respect to different speeds and load power, as shown in Figure 3.13. It can be seen from Figure 3.13 that the location of the two conjugate poles is fixed since it only depends on the current loop control parameters and generator parameters. The dominant pole depends on the operating point. With the increase of speed and load power, it moves towards the right half plane, indicating a degraded stability.

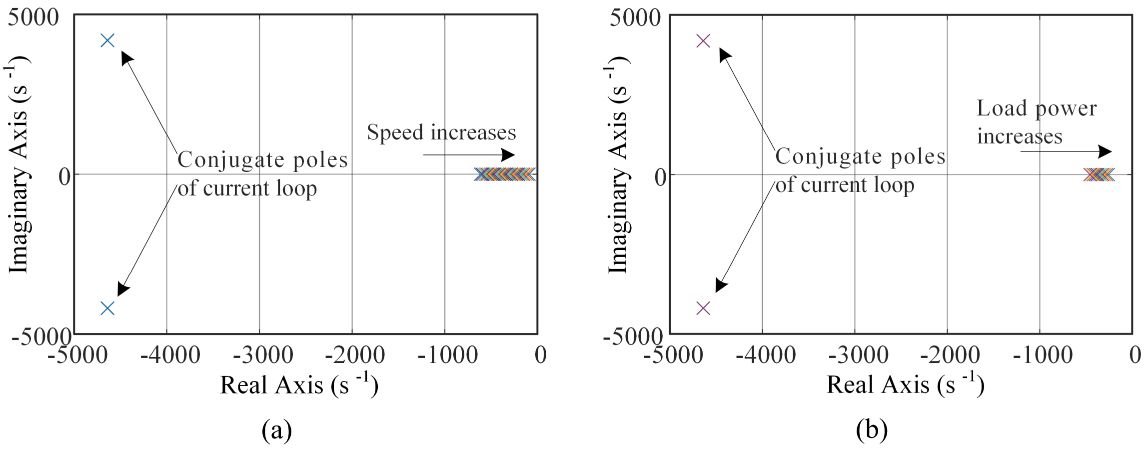

Figure 3.13. Locations of poles of $G_{idc}(s)$ at different speeds and load powers. (a) Poles are obtained at 20kW load power, speed increases from 15 krpm to 25 krpm. (b) Poles are obtained at 20 krpm, load power increases from 5 kW to 35 kW.

The i_{dc} PI controller shown in (3-21) provides a zero. To cancel the dominant pole with this zero, the control parameters can be set as follows:

$$\begin{cases} K_{v\mathrm{P}} = 2\overline{v}_{dc}{}^{2}C \cdot \gamma \\ K_{v\mathrm{I}} = -3\left(\overline{v}_{d}\overline{i}_{d} + \overline{v}_{q}\overline{i}_{q}\right) \cdot \gamma \end{cases} \tag{3-23}$$

where γ is a gain used to tune the control parameters.

From (3-23) it can be seen that the PI parameters depend on operating points and a gain γ. By applying (3-23) into (3-22), the open loop transfer function of the i_{dc} control loop can be derived as:

$$G_{idc}(s) = -\frac{3\gamma\overline{v}_{dc}C\left[\overline{v}_{q} - \omega_{e}L_{s}\overline{i}_{d} + \left(R_{s} + L_{s}s\right)\overline{i}_{q}\right]\left(K_{i\mathrm{P}}s + K_{i\mathrm{I}}\right)}{L_{s}s^{2} + \left(K_{i\mathrm{P}} + R_{s}\right)s + K_{i\mathrm{I}}} \tag{3-24}$$

As concluded in the above section, the highest speed and heaviest load power is identified as the worst operating condition in terms of control stability. The root locus of $G_{idc}(s)$ in (3-24) is analysed at the operating point (32k rpm, 45kW), as shown in Figure 3.14. The trajectory means the locations of closed loop poles with respect to different values of the gain γ. It can be seen when γ is set as 0.4, the damping ratio is 0.707 and the overshoot is 3.9%. This is an acceptable performance considering the worst operating condition. Hence, the gain γ is set as 0.4 in the following analysis. With a known γ, the control parameters can be adaptively tuned based on the relation in (3-23).

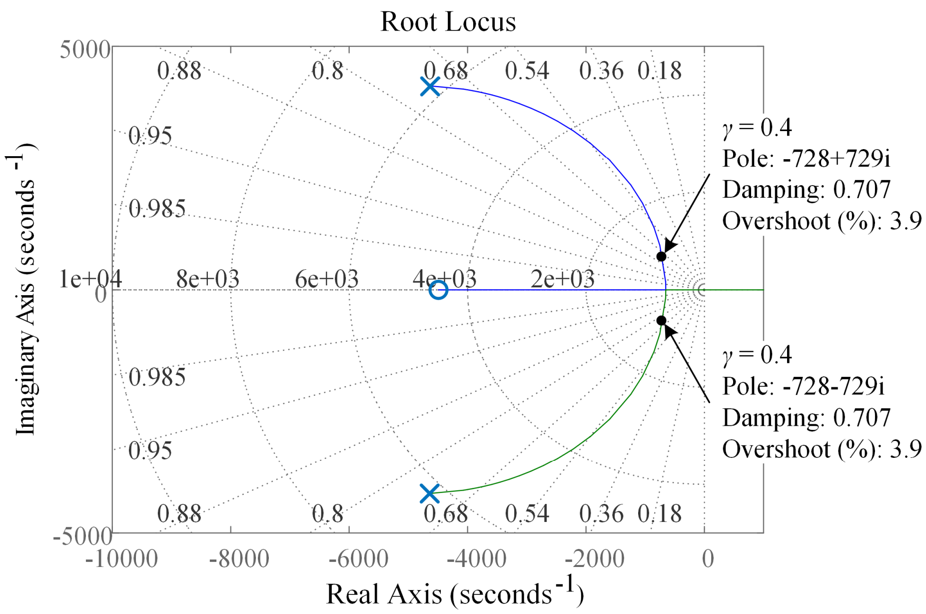

Figure 3.14. Root locus of $G_{idc}(s)$ at 32 krpm, 45kW.

To conclude above, the control block diagram can be built as shown in Figure 3.15, where the design criteria of control parameters are highlighted. DC current reference comes from the predefined *V-I* droop characteristic, then with a closed-loop calculation, optimal q-axis current reference is derived. Subsequently, the inner current loop generates voltage references in the dq frame. With the aid of the SVPWM technique, the voltage references are transformed into certain PWM switching sequences for driving the power electronics modules of the HP or LP rectifier.

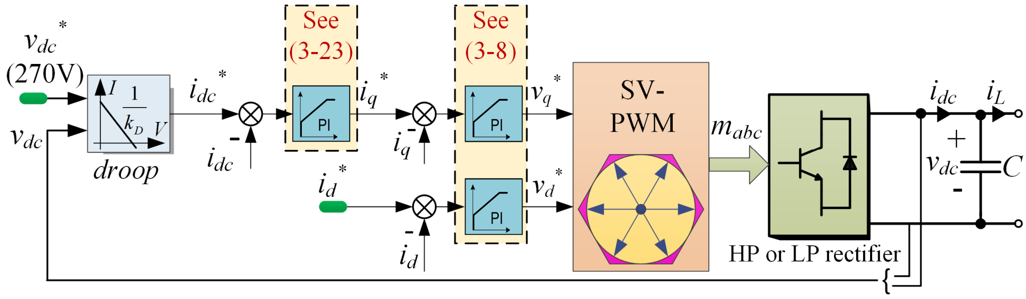

Figure 3.15. Control block diagram of the electrical power generation channels.

3.2.4 Power Transfer Control Design

The LP and HP spools of a turbofan engine independently rotate without mechanical coupling between them. In [11] it has been proved that transferring a certain amount of power between two shafts could improve the engine performance in different engine operating modes (EOM). The idea of power transfer can be studied into two cases: electric power transfer (EPT) mode and coordinated power offtake (CPO) mode.

3.2.4.1 Electric Power Transfer Mode

The PGC can provide power transfer between the two shafts by manipulating one of the rectifiers as inverter and controlling the associated electrical machine in motoring mode. Hence, the speeds of LP and HP shafts can be decoupled to some degree, depending on the amount of transferred power from one shaft to the other. In this regard, the power transfer between engine shafts is expected to realize the following goals:

- Optimize compressor performance to obtain higher efficiency with proper surge margin.

Engine efficiency is related to the core compression ratio. However, the surge margin usually limits the maximum usable pressure ratio of the engine. Since thermodynamic coupling exists for a wide range of EOMs, designers have considered the excessive surge margin to meet the requirements of off-design conditions. But this is fuel inefficient. Power transfer can decouple the shaft speed and control the engine around more optimised operating point [71].

- Remove Variable Bleed Valves (VBVs).

Using variable geometry systems (including VBV) in low-speed settings can control core airflow and avoid compressor instability. The disadvantages of VBVs include not only their complexity and higher cost, but also the adverse effects on the engine efficiency. Therefore, there is a need for alternatives to variable geometry methods. By rearranging the speed of the compressor, power transfer can control the operating point of the compressor during low speed and transient EOMs. This can result in the removal of part or all of the operated VBVs, making the engine lighter and cheaper [72].

In addition to the above benefits, power transfer between engine shafts can also manage the thrust to make it compatible with the flight mission, enable power extraction from windmilling engines, and help the engine to overcome surge incidence [73], [74]. In the following analysis, power transfer from the LP to HP spool is considered as an example of power transfer.

The idea of EPT can be depicted using the following mechanical dynamics

$$T_{turbin} - T_{compressor} - T_{EM} = J\frac{d\omega_m}{dt} \tag{3-25}$$

where T_{turbin} is the torque of turbine. $T_{compressor}$ is the torque of compressor stages. T_{EM} is the torque of coupled electrical machines. When the machine operates in generator mode, T_{EM} is positive. In motoring mode, T_{EM} is negative. J is the moment of inertia. ω_m is the rotary speed of engine's shaft.

Consider EPT from the LP to HP spool. For the LP spool, the LP machine operates in generator mode, generating an increasing positive T_{EM}. Hence, the speed and kinetic energy of the LP spool will decrease. For the HP spool, the HP machine operates in motoring mode, generating a negative T_{EM} to crank the HP spool. Hence, the speed and kinetic energy of the HP spool will increase. Then the power is transferred from the LP spool to HP spool.

Assuming the rotary speed of the HP machine as ω_m, the mechanical power of the HP machine is product of ω_m and T_e, where T_e is the torque of the HP machine. ω_m is imposed by the engine. Therefore only torque, or current can be controlled when off-taking power. For a surface-mounted PMM, the torque can be expressed as

$$T_e = 1.5 p \psi_m i_{qH} \tag{3-26}$$

Subsequently, the i_{qH} reference can be obtained for a given power:

$$i_{qH}^{*} = \frac{P_{HP}}{1.5 p \psi_m \omega_m} \tag{3-27}$$

where P_{HP} is the power transferred from LP spool to HP spool.

From (3-27), the i_{qH}^{*} can be found for a given P_{HP}. i_{dH}^{*} comes from the field-weakening controller discussed in subsection 3.2.2. The current control structure of generators has been presented in Figure 3.5. Therefore, the power transfer from LP to HP shaft can be realized by controlling i_{dH} and i_{qH}.

It should be noted that the calculated i_{qH}^{*} need to be limited. If $\mathrm{d}i_q/\mathrm{d}t$ is too large, the inductance of electrical machine's stator windings will lead to high induced voltage. Besides, the sudden change of electromagnetic torque may also deteriorate the performance of mechanical system.

Moreover, in the power transfer process, the LP machine on the one hand transfers power to the HP machine, on the other hand, it feeds the main DC bus. Therefore, the droop control should be revised since there is no need for power sharing between multiple sources. For this purpose, a compensation term is proposed to compensate the voltage deviation caused by the droop control, and the new voltage reference is given as follows:

$$v_{dc}^{*} = v_{rated} + i_{dcLP} g_{LP} \tag{3-28}$$

where for the MEA application the value of v_{rated} is 270V.

Compared with the fixed voltage reference 270V, the voltage reference is calculated from (3-28) when power is transferred from LP shaft to HP shaft. This will keep the DC voltage strictly to 270V in the power transfer mode. However, the change of the voltage reference will cause transients on the DC bus voltage when switching between different modes. This point will be checked in the following simulation.

3.2.4.2 Coordinated Power Offtake Mode

Compared with the EPT mode, in the CPO mode, the HP and LP machines still operate as generators while the power split ratio between them is dynamically changed. For example, increasing power from the LP generator and decreasing power from the HP generator. This is a gentler method compared with EPT, because the direction of torque and power flow of HP machine is not reversed during the operation of engine. The entire system is still maintained near the original steady-state operating point. The research of CPO mode on engine performance is still under development.

3.3 Simulation Results of The Single-Bus Power Generation Centre

A PGC model is built in the Simulink in the continuous domain, where averaged model for power converters is adopted. The transmission cable impedance is omitted. Subsystems of the model can be found in Appendix C. Control performance for the PGC in both CPO mode and EPT mode are investigated. In the CPO mode, the HP and LP machines both perform as generators, supplying power to the loads. Power sharing ratio depends on droop gains. In the EPT mode, the HP machine is controlled in motoring mode and LP machine operates in generator mode, hence some amount of power of LP spool is transferred to the HP spool. The main parameters of two AEGART PMMs have been presented in Table 3-1. More details about design of the AEGART machine can be found in [58], [59].

As discussed above, in MEA many conventional onboard systems are replaced by electrically powered ones, which are regulated by power electronic converters. For example, for the environmental control system (ECS), conventionally, bleed air from one or two of the compressor stages of the main engine is used to regulate the cabin temperature and pressure. However, in MEA such as Boeing 787, a set of electrical compressors driven by power converters is used to regulate the temperature and pressure [6]. As discussed in Chapter 2, tightly controlled power electronic converters and motor drives often behave as constant power load (CPL) which show the constant power characteristic. Therefore, an inverter controlled PMM that performs as a CPL is used as DC bus load in the simulation. The system parameters are given in the Table 3-3.

Table 3-3. Parameters of the studied power generation centre.

Category	Parameter	Value
Electrcial machines	Speed of LP machine	7,000 rpm
	Speed of HP machine	20,000 rpm
Rectifeirs	Topology	Two level, bidirectional
	Maximum current	400 A
DC Link	Rated voltage	270 V
	Local shunt capacitor	1 mF
	Main bus capacitor	1.2 mF
CPL	Load power	From 10 kW to 30 kW
Control paramters	Current loop PI gains	0.87, 3908
	Voltge loop PI gains	Adaptive tuned by setting the gain γ = 0.4 in (3-23)
	FW control PI gains	1.5, 2000
	Droop gains	g_{LP}=1/8, g_{HP}=1/4

3.3.1 Results in the Coordinated Power Offtake Mode

The simulation results for the CPO mode are demonstrated in Figure 3.16. The cruise mode of engine is considered, where the speed of HP generator is set as 20,000 rpm and that of LP generator is 7,000 rpm. The findings in [73], [74] reveal that extracting more power from the LP spool than HP spool of the engine is beneficial for the compressor surge margin. Hence, in this study, the droop gains for the LP and HP rectifier are set as 1/8 and 1/4, respectively. Then the power sharing ratio between the LP and HP rectifier is 2:1. During simulations, the power demand of CPL is changing at 0.05s, 0.1s, 0.15s, 0.2s and takes values 10kW, 20kW, 30kW, and 20kW, respectively. The main findings are listed as follows:

- Figure 3.16(a) shows that as the CPL power demand increases, the DC bus voltage will slightly drop due to the droop effect.
- Figure 3.16(b) exhibits the output power of the LP and HP rectifiers. It can be seen that the power ratio is kept to 2:1 in the whole process.
- Figure 3.16(c) shows the *d*-axis currents of LP and HP generators. Since the speed of LP generator is relatively low, there is no need for FW and its *d*-axis current remains zero. While a significant negative *d*-axis current is injected into the HP generator for FW purpose. The *dq* currents can also be seen from the operating trajectory in Figure

3.7. Moreover, as the increase of power, the magnitude of i_d will slightly increase. This can be explained by Figure 3.17, from which it can be seen that the magnitude of i_d will increase as the operating points (the green dots) moving on the boundary of voltage limit circle in the 3rd quadrant. This significant i_d current is expected to lead to considerable power losses in both the HP machine and the HP rectifier. In contrast, as it will be discussed in Chapter 4, in the proposed APGC, this significant i_d current is eliminated by a back-to-back converter, achieving a higher efficiency.

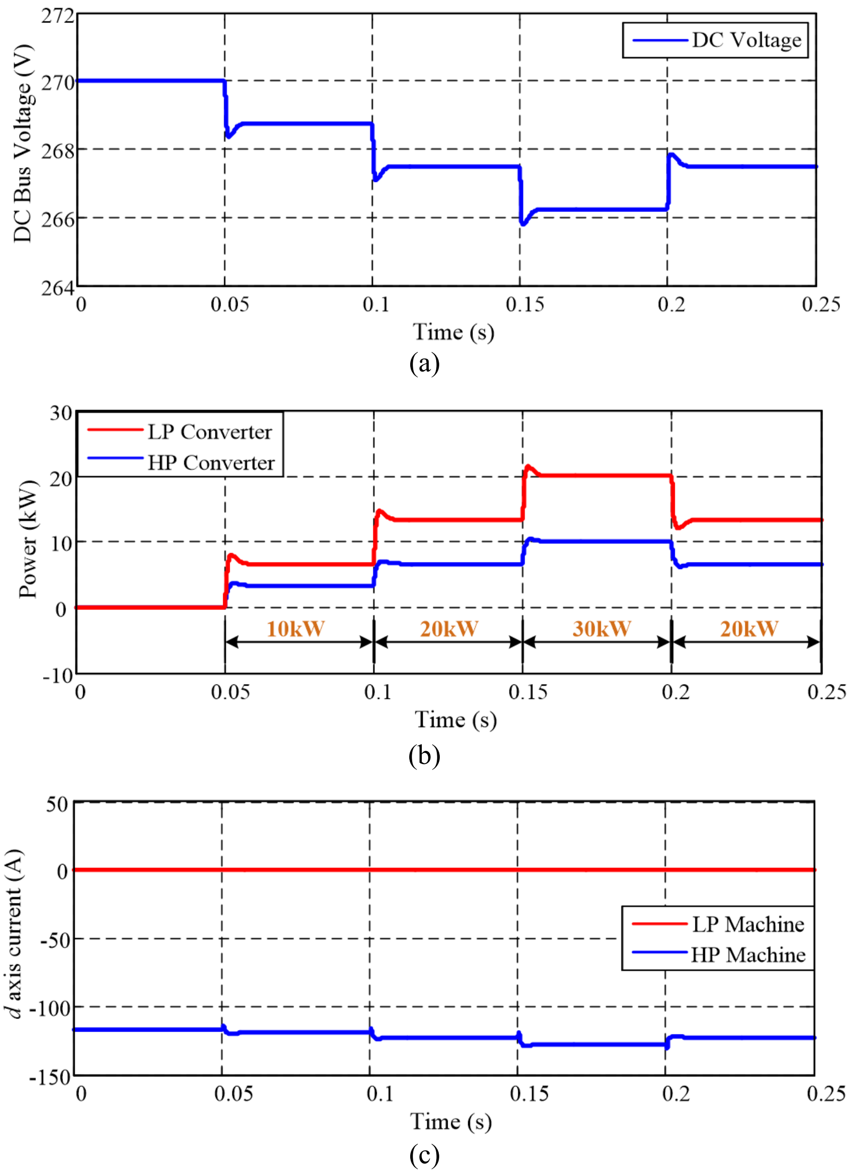

Figure 3.16. Simulation results in the CPO mode. (a) DC bus voltage; (b) output power of LP and HP rectifiers; (c) *d*-axis currents of LP and HP machines.

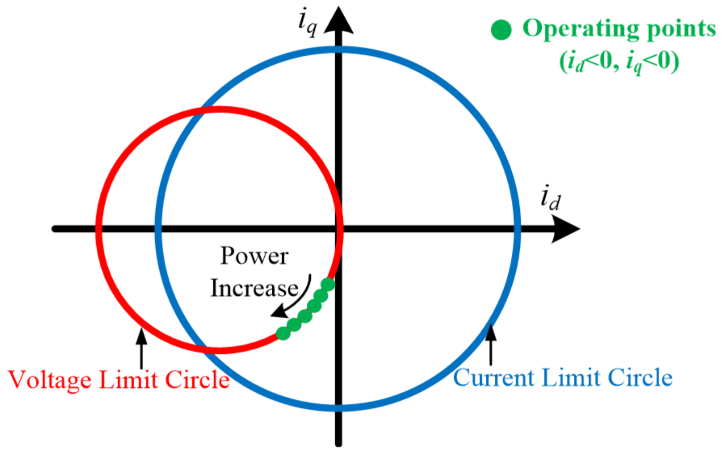

Figure 3.17. Operating points of the HP generator with increased power.

3.3.2 Results in The Electric Power Transfer Mode

Simulation results in the EPT mode are demonstrated in Figure 3.18. Before 0.1s, the system operates in the CPO mode, machine speeds and power ratio configurations are the same as that in Table 3-3. At 0.1s, the HP machine converts into motoring mode, transferring power to the HP shaft. The absorbed power P_{HP} is set as 20kW. At 0.15s, the speed of HP machine steps to 25,000 rpm. At 0.2s, the CPL requires extra 10kW power from the DC bus.

Figure 3.18(a) shows that in the steady state, the DC bus voltage keeps at 270V, which confirms the effectiveness of the voltage compensation term in (3-28). Although voltage oscillation can be observed in the transient process when switching to the EPT mode at 0.1s, or load power steps at 0.2s, it can be stabilized to the rated value afterwards, validating the designed DC voltage control. Figure 3.18(b) exhibits the power of the LP and HP converters. It can be seen at 0.1s the HP converter absorbs 20kW, which means 20kW power is transferred from the LP shaft to HP shaft. At 0.2s, LP channel's power increase to 30kW to balance the CPL load demand. Figure 3.18(c) shows the *d*-axis currents of the LP and HP machines. As that in dual-generator mode, the *d*-axis current of LP machine remains zero. While a negative *d*-axis current injects into HP machine and its magnitude increases when the speed of HP machine steps at 0.15s.

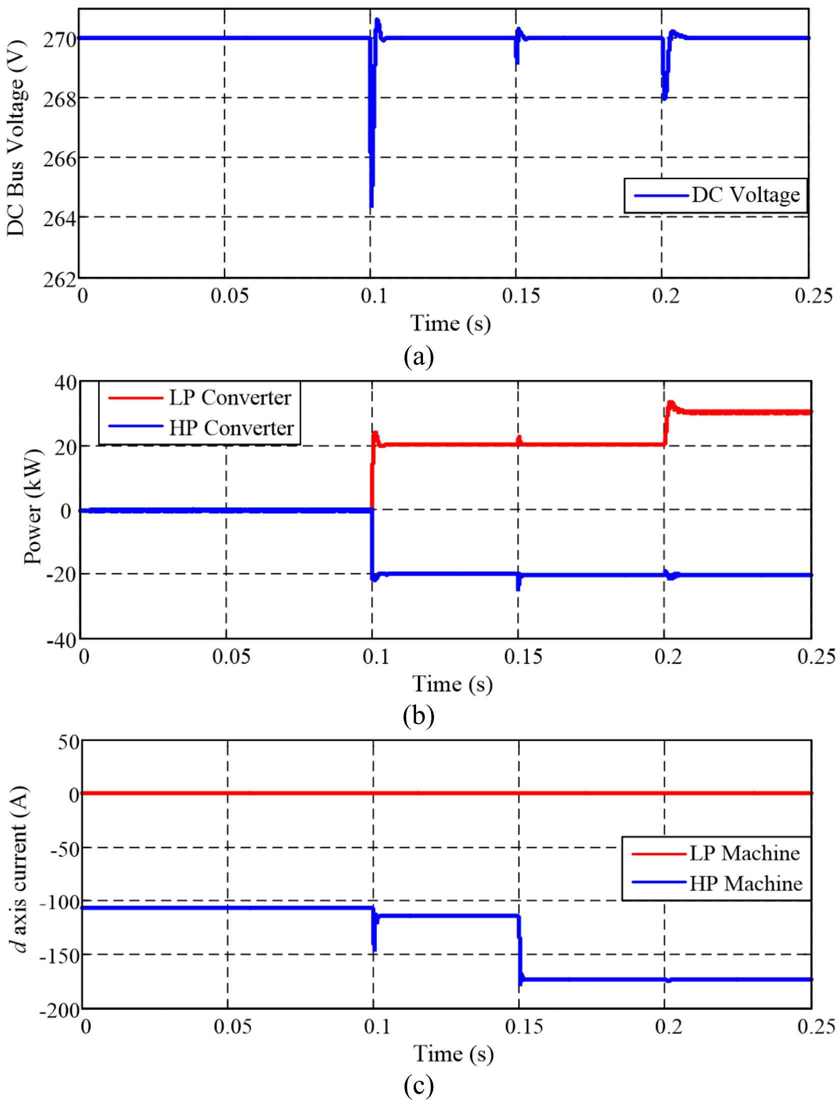

Figure 3.18. Simulation results in the EPT mode. (a) DC bus voltage; (b) output power of the LP and HP converters; (c) *d*-axis currents of the LP and HP machines.

3.3.3 Engine Performance with Electric Power Transfer

Transferring power from the LP spool to HP spool at low-speed settings can benefit both fuel efficiency and compressor surge margin. More detailed analysis is provided in [48]. In order to prove the benefits, CFM56 engine maps [11] have been used to establish a twin-spool high bypass ratio unmixed flow 140 kN turbofan engine.

For the compressor stages of a turbofan engine, HPC swallows and passes air flow delivered by LPC. For the same speed line of LPC, if the speed of HPC is less than matched value, HPC will demands less air flow. As a result, it acts as a blockage for the rear side of LPC, pushing LPC to decrease its mass flow on the same speed line (the green curve). This is depicted by Figure 3.19, where the pressure ratio (PR) of LPC increases, making the operating point closer to the surge line (the red dashed line).

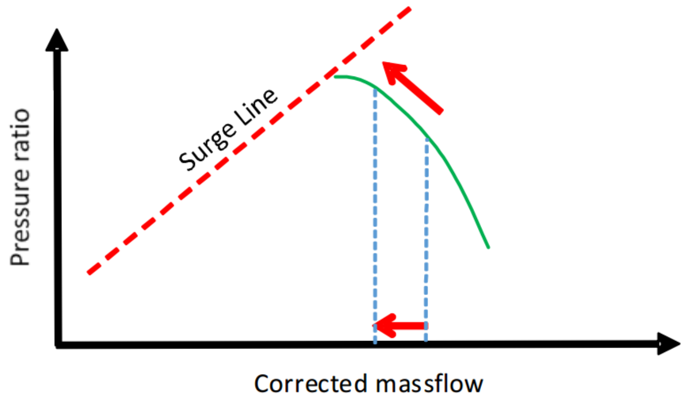

Figure 3.19. Operating line on the low-pressure compressor map (Page 116 in [121]).

To ensure a sufficient surge margin, conventionally, the variable bleed valves are placed between LPC and HPC to regulate the mainstream entering the HPC and bypass excess air from the core to the fan exhaust duct. However, this is not the optimal choice because bleeding the compressed air to the discharge duct is a waste of energy. As mentioned in subsection 3.2.4, a concept of EPT is proposed to address this issue.

Compressor map and operating points with and without power transfer from the LP to HP spools are presented in Figure 3.20. It can be seen that with EPT, the operating point moves to a higher efficiency contour and far away from the surge line.

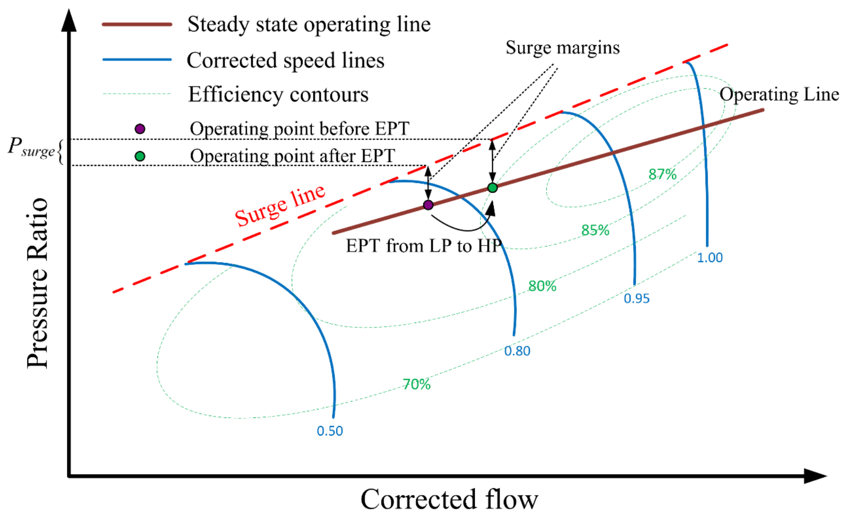

Figure 3.20. LPC compressor map and operating point with and without EPT.

Quantitative results for flight idle mode at 20,000ft are obtained from the designed engine model as shown in Figure 3.21, where a positive EPT means power transfer from the LP to HP spool and negative EPT means HP to LP spool. Figure 3.21(a) reflects that with a positive EPT, the speed of LP spool will decrease and that of HP spool will increase. This is consistent with the analysis in section 3.2.4.1 using (3-25). Since the efficiency of engine is related to the core speed, a higher HP spool speed will lead to higher pressure ratio and efficiency. This will reduce the fuel consumption. It can be noted that the speed of the LP spool cannot be further decreased because it is coupled with fan, hence a minimum speed is required to keep a sustainable thrust. Figure 3.21(b) presents that the available compressors surge margins are significantly increased with positive EPT.

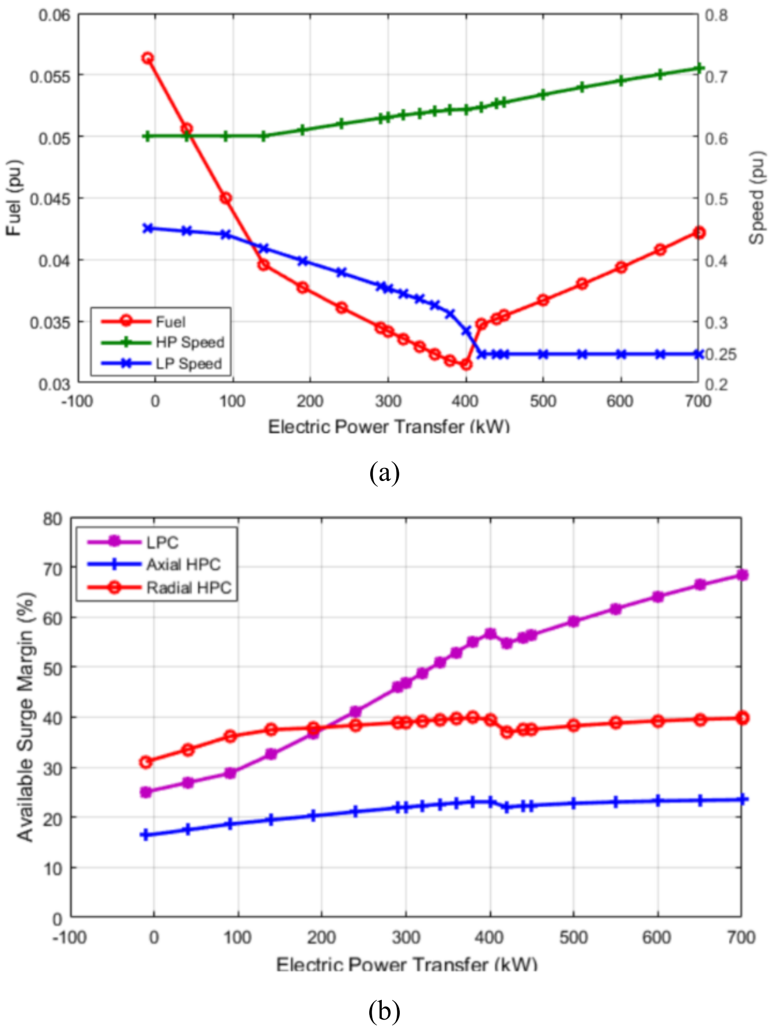

Figure 3.21. Engine performance with EPT in flight idle mode, 20,000ft. (a) Fuel consumption and shaft speeds. (b) Surge margins of compressors. [122]

3.4 Chapter Summary

In this chapter, a single bus PGC is studied for the MEA application. The main points can be summarized as follows:

- The PGC can operate in two modes: coordinated power offtake (CPO) mode and electric power-transfer (EPT) mode. Control schemes for the PGC in CPO mode are developed, including current-loop control, field weakening control, and DC bus voltage control. These findings are used in the Chapter 4 when designing control schemes for the proposed APGC with a back-to-back converter.
- The concept of EPT has been presented. For example, in the flight idle mode, some amount of power can be transferred from the LP to HP spool by controlling the HP machine in motoring mode to speed up the HP spool. Since the speed of HP machine is imposed by the HP spool, by controlling the torque of HP machine, the transferred power can be regulated. An additional compensation terms is added into the DC voltage control to restore the DC voltage to its rated value.
- Simulation results show that in the CPO mode, the two generators can supply power to the DC bus. Power sharing ratio is set by individual droop gains. It also shows that significant i_d flows in the HP machine due to a high speed with limited DC bus voltage. This current is expected to lead to considerable power losses in both HP machine and rectifier. However, as will be discussed in Chapter 4, in the proposed APGC, this significant i_d current is eliminated, which achieves a higher efficiency.
- The results of engine performances in the EPT mode confirm the improvement of fuel efficiency and compressor surge margin in the flight idle mode of engine if power transfer is carried out from the LP to HP spool.

Chapter 4. The Proposed Advanced Power Generation Centre with a Bridging Converter

Although the PGC studied in Chapter 3 can effectively control the DC bus voltage and power flows of both the HP and LP power generation channels, this solution presents some drawbacks which may undermine the feasibility in practical application.

One of the issues is related to the power losses caused by the high current of the HPG for FW purpose. At the high-speed settings of engine, the speed of HPS can reach 20,000 rpm [37]. In typical arrangements it means that FW is needed to decrease the magnetic field density in the stator core and reduce back EMF. This implies that a significant amount of de-fluxing current is constantly injected into the HPG. This de-fluxing current means the machine should develop a significant amount of reactive power in addition to a required active power in most of flight conditions. Hence, the increased total current reduces the power factor of HPG and incurs considerable additional losses, as well as increases the power rating of HPR to accommodate for the required reactive power. To address these issues, an APGC containing a bridging converter is proposed in this chapter.

4.1 Description of The Advanced Power Generation Centre

The diagram of the APGC with a bridging converter to address the abovementioned issues is shown in Figure 4.1. Both electrical generators (HPG and LPG) are supplying a common HVDC bus through their dedicated converters, similar to arrangements considered in previous chapters. A back-to-back (BTB) converter is proposed as a bridge to connect the HPG and LPG. Power transfer between the HP spool and the LP spool of engine can be realized through this BTB converter. With the modern engine designs for MEA moving towards much higher bypass ratio, the electrical power which can be available for extraction from the HP spool will become further limited. Thus, it is considered that LPG generally outputs much more power than HPG. In this case, the BTB converter offers a route to transfer power from the LP channel to HP one. The converter connected to the LPG within the BTB converter are denoted as BTB_L and the other is denoted as BTB_H. It is worth to note that the internal DC-link voltage v_{BTB} in the BTB converter can be set to a value much higher than 270V as it does not supply onboard loads directly.

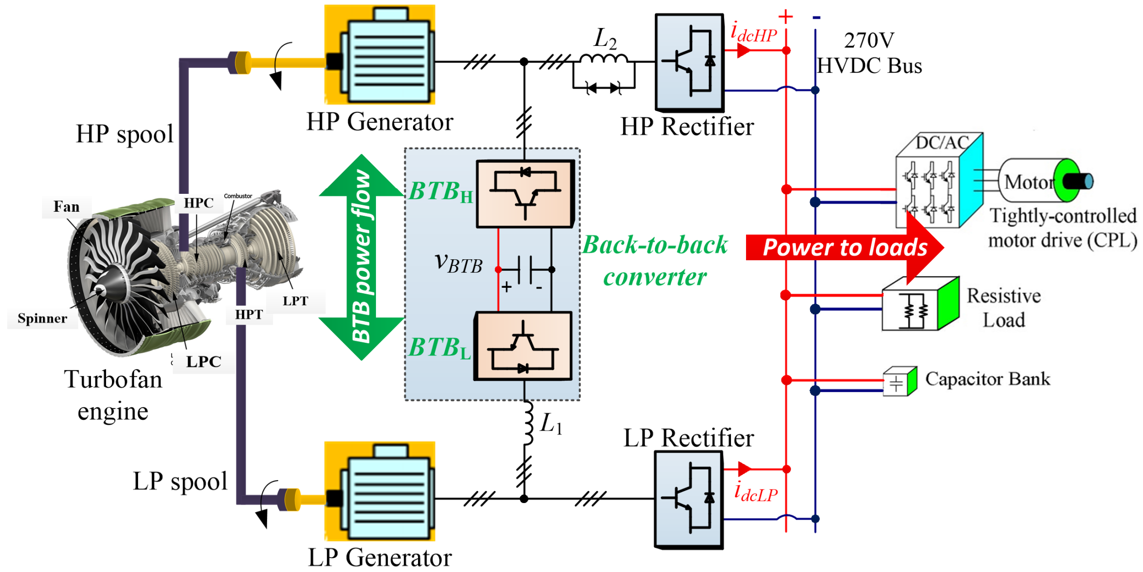

Figure 4.1. Proposed power generation centre with a back-to-back converter.

It can be seen from Figure 4.1 that the four power converters, i.e., HP rectifier (HPR), LP rectifier (LPR), BTB_H converter and BTB_L converter, are all voltage source converters (VSC). To make them operate compatibly, inductors should be deployed to separate these VSCs. Moreover, inductors can filter high frequency pulse-width modulation harmonics generated by the switching actions of power devices. There are four possible topologies in total with different locations of inductors, as shown in Figure 4.2.

In Figure 4.2(a) and (b), an inductor, denoted as L_2, is placed at the front end of the BTB_H converter. In this case, the terminals voltages of HPG are limited to $\frac{v_{dc}}{\sqrt{3}}$ using the typical space vector pulse-width modulation (SVPWM) for the typically used two-level three-phase AFE [37], where v_{dc} is the main HVDC bus voltage. The value of v_{dc} is considered as 270V to follow the aerospace standards [35]. Hence, for the considered AEGART PMM, it means that field-weakening operation is still needed to for the HPG with the configurations shown in Figure 4.2(a) and (b).

In Figure 4.2(c) and (d), L_2 is deployed at the front of the HPR. In this case, the terminals voltages of HPG are limited to $\frac{v_{BTB}}{\sqrt{3}}$ using the SVPWM, where v_{BTB} is the DC-link voltage within the BTB converter. By increasing the voltage of v_{BTB}, the HPG can operate at a high speed without field-weaking control. The difference between Figure 4.2(c) and (d) is the location of inductor L_1. Since in most cases, most of the LP channel' power goes through the LPR to feed the onboard loads, and a relatively small proportion of this power is transferred through the BTB converter, the phase currents of LPR are larger than those of BTB_L converter. Placing L_1 at the front end of BTB_L converter instead of LPR can reduce the power losses in the inductor L_1. To conclude above, the configuration of inductors shown in Figure 4.2(d) are chosen to build the APGC shown in Figure 4.1.

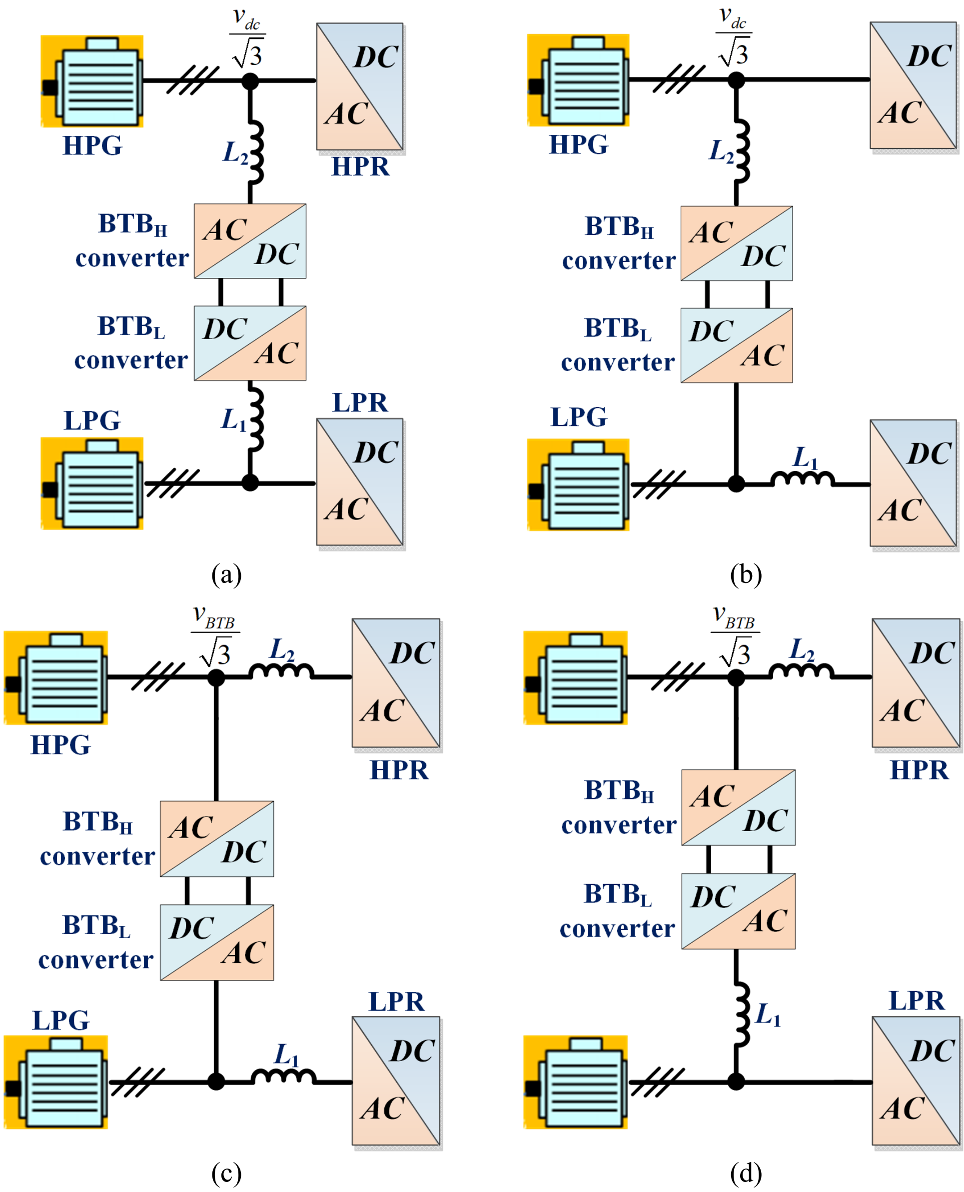

Figure 4.2. The four configurations with different locations of inductors.

Since multiple converters are involved in the APGC, proper control is of great importance. In the following subsections, control design for the power converters to achieve required power and voltage control is reported. Design criteria for the passive components such as filtering inductors and DC capacitors is also considered.

4.2 Control Design for the Back-to-back Converter

The control design for the HP and LP rectifiers has been presented in Chapter 3. This section will focus on the control design for the BTB converter.

4.2.1 Control Design for the BTB_L Converter

As shown in Figure 4.1, the BTB consists of two separate AC/DC converters, i.e., BTB_L converter and BTB_H converter, respectively. For the BTB_L converter, since the AC terminals of LPG and BTB_L converter share the same junctions *a*, *b*, and *c* as shown in Figure 4.3, an effective way to control the transferred power from the LP channel to the BTB converter is to control the phase currents of LPG (i_{xLP}) and BTB_L converter (i_{xBTBL}, $x=a,b,c$) (as shown in Figure 4.3) in phase. If i_{xLP} and i_{xBTBL} can be synchronized, i.e., controlled in phase, by manipulating the ratio of magnitude of AC currents i_{xLP} and i_{xBTBL}, the power transferred to/from the BTB converter can be controlled.

Apart from regulating currents in phase, control scheme for the BTB_L converter is also responsible for the BTB converter DC-link voltage (v_{BTB}) control. However, as shown in Figure 4.4, in the conventional control schemes for applications such as active front end (AFE) [61] or flywheel energy storage system [62], the output of outer voltage controller is the reference of active power or active current. This structure will not be able to control i_{xBTBL} and i_{xLP} in phase. To address this issue, a new method is proposed to realize the following two functions:

1) BTB converter DC-link voltage (v_{BTB}) regulation.
2) In-phase control of phase currents i_{xBTBL} and i_{xLP} ($x=a,b,c$).

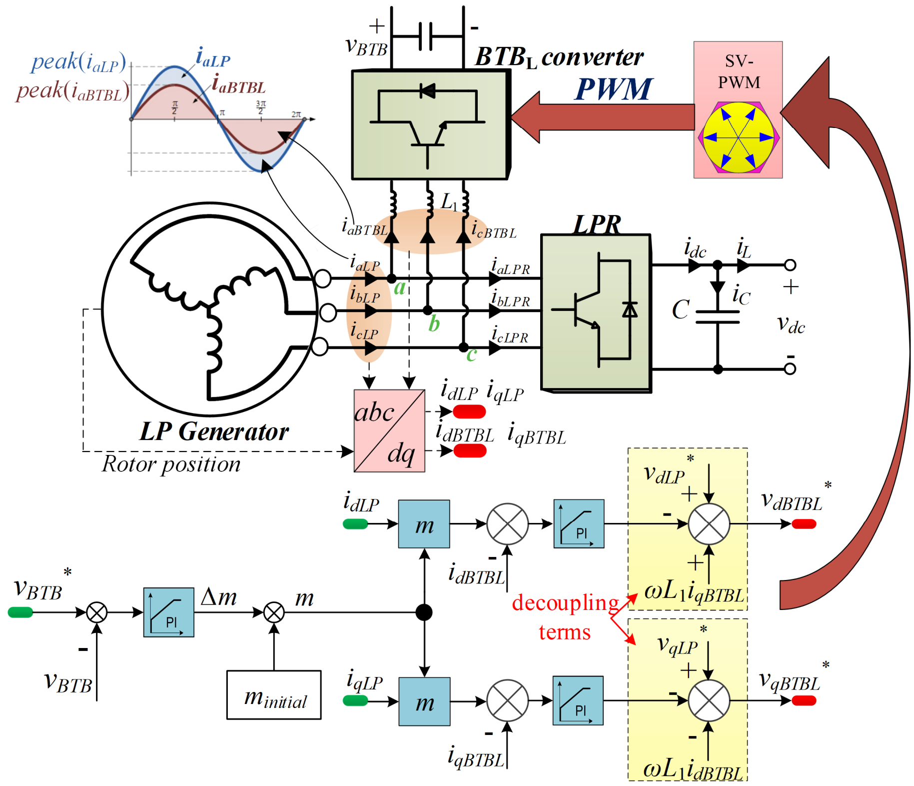

Figure 4.3. The control schematic for the BTB_L converter.

As can be seen from Figure 4.3, in contrast to the control schemes [61], [62], where the output of voltage controller is active current or power reference, in the proposed structure, both *dq* axes current references are the sensed LPG's *dq* axes currents multiplied by a gain *m*. If the phase currents i_{xBTBL} and i_{xLP} are processed by the same *abc/dq* transformation related to the LPG rotor position in the studies case, it is expected that i_{xBTBL} and i_{xLP} will be synchronized in phase, and the gain *m* defines their magnitude ratio (i_{xBTBL} over i_{xLP}).

Based on the synchronized phase currents i_{xBTBL} and i_{xLP}, the gain *m* is used to regulate the DC voltage v_{BTB} as shown in Figure 4.3. If v_{BTB} drops below its reference, *m* will be increased by the control action so that more power will be transferred to the BTB converter to charge the internal DC-link capacitor, increasing v_{BTB}, and vice versa. Therefore, with the proposed control strategy, v_{BTB} can be stabilized and i_{xBTBL} and i_{xLP} can be synchronized. In the steady state, the power generated by LPG P_{LPG} and the power transferred to the BTB converter P_{BTB} have the following relation:

$$\frac{peak(i_{aLP})}{peak(i_{aBTBL})} = \frac{i_{qLP}}{i_{qBTBL}} = \frac{i_{dLP}}{i_{dBTBL}} = \frac{P_{LPG}}{P_{BTB}} = \frac{1}{m} \tag{4-1}$$

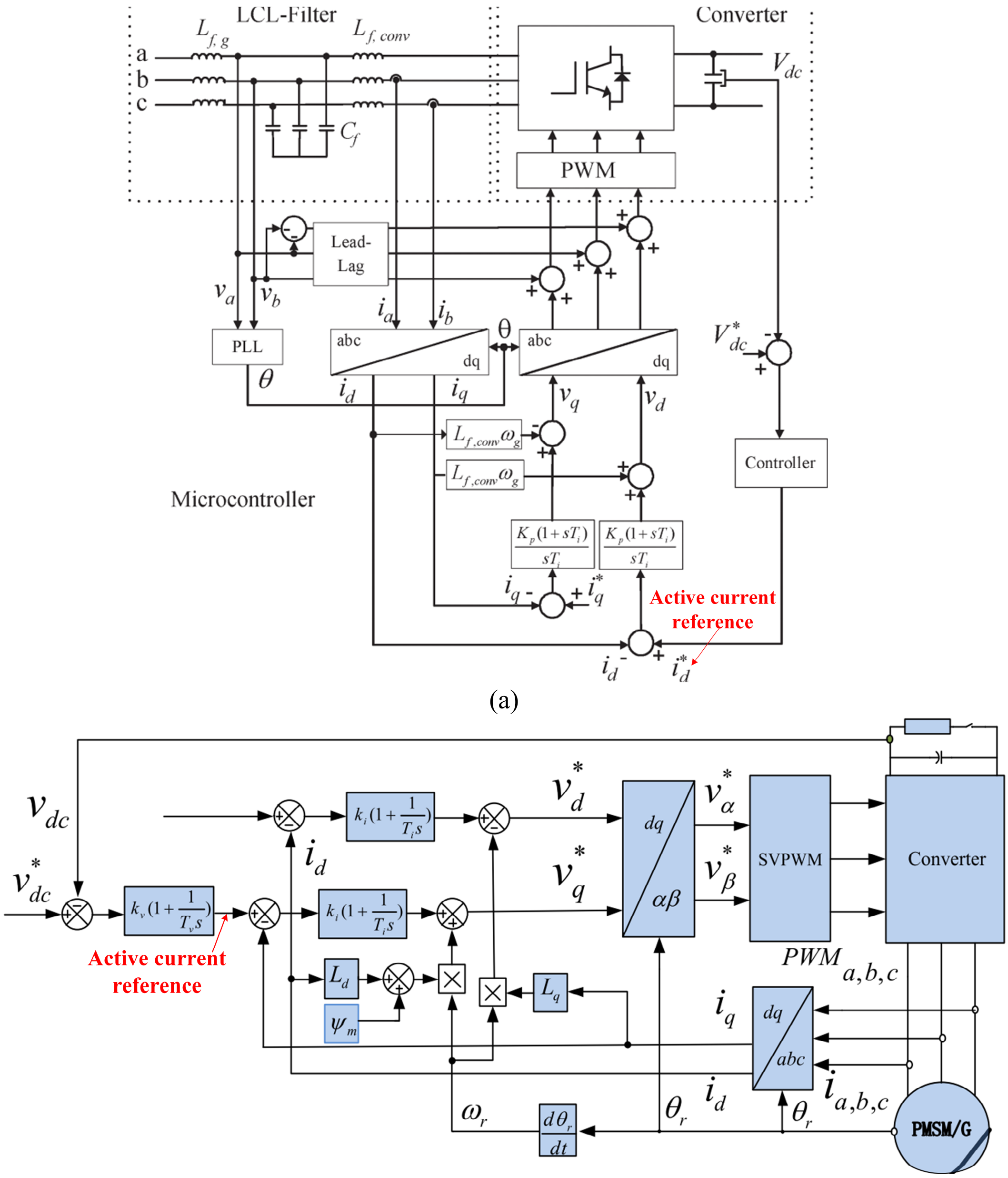

(a)

(b)

Figure 4.4. Conventional DC voltage control schemes for (a) active front end (see Fig.11 in [61]). (b) flywheel energy storage system (see Fig.3 in [62]).

To conclude, the main difference of the proposed control scheme in Figure 4.3 and the conventional control schemes in Figure 4.4 is how to acquire current reference, in specific:

- In the conventional control schemes, active current reference directly comes from the output of voltage controller.
- In the proposed control scheme, current references are measured *dq* axes currents of LPG multiplied by the factor *m* defined by (4-1). The value of *m* is defined by the outer voltage loop to stabilize the DC-link voltage of the BTB converter.

The proposed phase current synchronization method and BTB converter DC voltage control method is further analysed in the following subsections to ensure stability and control performance.

4.2.1.1 Current-Loop Bandwidth for the BTB$_L$ Converter

As shown in Figure 4.3, the current references are measured *dq* axes currents of LPG multiplied by the factor *m*. Hence, when selecting the current-loop bandwidth for the BTB$_L$ converter, the bandwidth of LPG's stator current control loop should be considered. A *q*-axis current step response test is carried out as shown in Figure 4.5, where the LPG's stator current loop bandwidth is selected as 1kHz in subsection 3.2.1, and the current-loop bandwidth for the BTB$_L$ converter is 700Hz, 1kHz and 1.5kHz, respectively.

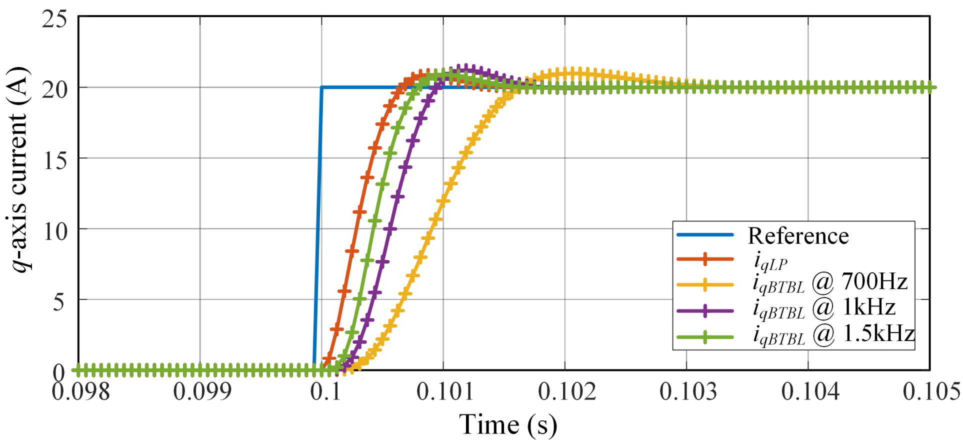

Figure 4.5. Step response test of i_q with different current-loop bandwidth for the BTB$_L$ converter.

In Figure 4.5, the reference for *q*-axis current of LPG (i_{qLP}) steps to 20A at 0.1s. The response can be observed in the red curve. i_{qLP} response serves as *q*-axis current reference for the BTB$_L$ converter. It can be seen that as the increase of bandwidth for the BTB$_L$ converter, the *q*-axis current of the BTB$_L$ converter (i_{qBTBL}) processes the i_{qLP} reference faster. However, as revealed in section 3.2.1, the current-loop bandwidth is physically restricted by the switching frequency f_{sw}. In our case, f_{sw}=16kHz, so the bandwidth should be smaller than 0.18×16kHz =2.8 kHz [68]. As a trade-off, the current-loop bandwidth for the BTB$_L$ converter is set as 1.5kHz.

4.2.1.2 Issue with High Fundamental Frequency and Sample Delay

With the studied AEGART machine which can operate up to 32krpm, the equivalent fundamental frequency needs to be processed by the digital controller is up to 1.6kHz. In relation to the PWM frequency of 16kHz in the studied system, the lowest pulse ratio is 10:1. Such a low pulse ratio yields fewer sample points, yielding a degraded control performance.

Moreover, as pointed out in [37], 1.5 sample period delay exists in the digital control system due to the PWM and control computation. Generally, this delay effect can be ignored in an electrical machine drive system with high enough pulse ratio (pulse ratio > 40). However, for the high-speed drive applications with low pulse ratio, the sample delay needs to be considered. As shown in Figure 4.6 where the pulse is 10:1, if the sampling of i_{aBTBL} takes place at t_{k+4} instant, the control actions calculated based on $i_{aBTBL}(k+4)$ will be applied at $t_{k+5.5}$ instant. While the polarity of i_{aBTBL} has changed from positive at t_{k+4} instant to negative at $t_{k+5.5}$ instant. Thus, it can be expected that the control performance will be deteriorated due to the significant difference between the sampled phase current and the phase current when control actions are applied.

Given the operating speed of generator as 32krpm and PWM frequency is 16kHz, the equivalent phase lag in electrical angle can be calculated as:

$$\Delta\theta = 1.5T_{PWM}\omega_e = 1.5\times\frac{32000}{60\times 16000}\times 360^\circ = 18^\circ \tag{4-2}$$

This phase lag has a negative influence on control. To address the sample delay, the rotor flux position variation during sampling period can be compensated as follows:

$$\theta_r^{k+1.5} = 1.5T_{PWM}\omega_e + \theta_r^k \tag{4-3}$$

where θ_r^k is the measured rotor position angle. $\theta_r^{k+1.5}$ is the compensated rotor position angle. By applying the compensated rotor angle in the inverse Park transformation presented in Appendix A, the delay effect can be reduced.

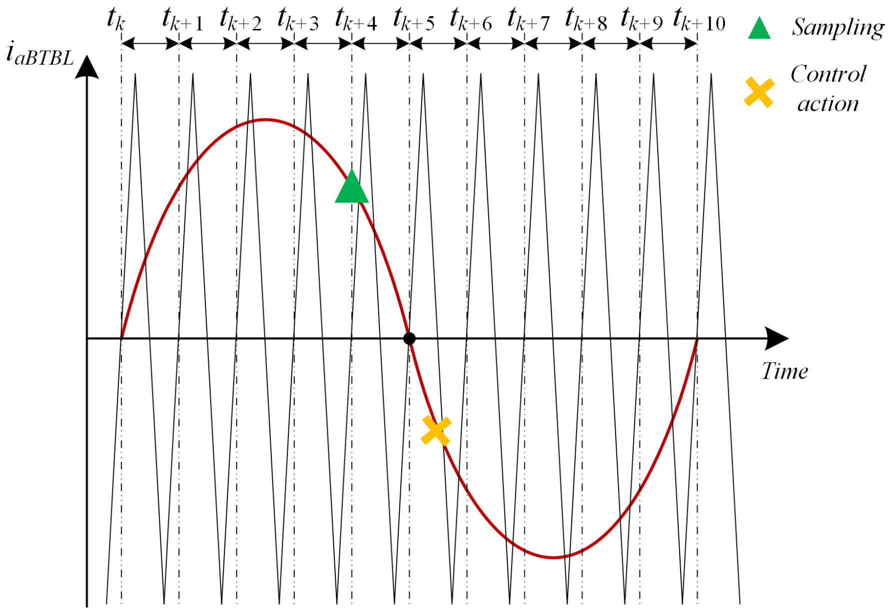

Figure 4.6. Difference between sampled phase current and the phase currents when control actions are applied in the low pulse ratio system.

4.2.1.3 Adaptive DC-link Voltage Control for the BTB Converter

As shown in Figure 4.3, there is a PI controller to regulate the gain *m*. The PI parameters need to be carefully selected to ensure stability and control performance. The modelling, control plant analysis, and control design are presented in the following.

Based on the assumption that power losses in the BTB_L converter are negligible compared with the transferred power, the power balance between the AC input and the DC output of the BTB_L converter can be expressed as:

$$\frac{3}{2}\left(v_{dBTBL}i_{dBTBL}+v_{qBTBL}i_{qBTBL}\right)=v_{BTB}i_{BTB} \tag{4-4}$$

where v_{BTB} and i_{BTB} are the DC voltage and DC current of the BTB_L converter, respectively. v_{dBTBL}, v_{qBTBL}, i_{dBTBL} and i_{qBTBL} are the *dq* axes voltages and currents of the BTB_L converter, respectively.

The power relation in (4-4) can be linearized as follows:

$$\begin{aligned}&\frac{3}{2}\left[\left(\bar{v}_{dBTBL}+\Delta v_{dBTBL}\right)\left(\bar{i}_{dBTBL}+\Delta i_{dBTBL}\right)+\left(\bar{v}_{qBTBL}+\Delta v_{qBTBL}\right)\left(\bar{i}_{qBTBL}+\Delta i_{qBTBL}\right)\right]\\&=\left(\bar{v}_{BTB}+\Delta v_{BTB}\right)\left(\bar{i}_{BTB}+\Delta i_{BTB}\right)\end{aligned} \tag{4-5}$$

where the "¯" and "Δ" are used to denote a steady state operating point and a small deviation, correspondingly.

In steady state, the following relations can be derived considering that LPG operates without field-weakening:

$$\begin{cases} 1.5\left(\overline{v}_{dBTBL}\overline{i}_{dBTBL}+\overline{v}_{qBTBL}\overline{i}_{qBTBL}\right)=\overline{v}_{BTB}\overline{i}_{BTB} \\ \Delta v_{dBTBL}\Delta i_{dBTBL}\approx 0 \quad \Delta v_{qBTBL}\Delta i_{qBTBL}\approx 0 \quad \Delta v_{BTB}\Delta i_{BTB}\approx 0 \\ \overline{i}_{dBTBL}=m\cdot\overline{i}_{dLP}=0 \end{cases} \tag{4-6}$$

Substituting (4-6) into (4-5), yielding:

$$\frac{3}{2}\left[\overline{v}_{dBTBL}\Delta i_{dBTBL}+\overline{v}_{qBTBL}\Delta i_{qBTBL}+\overline{i}_{qBTBL}\Delta v_{qBTBL}\right]=\overline{v}_{BTB}\Delta i_{BTB}+\overline{i}_{BTB}\Delta v_{BTB} \tag{4-7}$$

The DC-link relation of the BTB_L converter can be expressed as follows:

$$C_{BTB}s\cdot\Delta v_{BTB}=\Delta i_{BTB}-\Delta i_L \tag{4-8}$$

According to the control diagram shown in Figure 4.3, the following relation can be derived:

$$\begin{cases} \Delta m=(K_{pBTB}+\dfrac{K_{iBTB}}{s})\left(\Delta v_{BTB}{}^{*}-\Delta v_{BTB}\right) \\ \Delta i_{dBTBL}=i_{dLP}\Delta m \qquad \Delta i_{qBTBL}=i_{qLP}\Delta m \end{cases} \tag{4-9}$$

where K_{pBTB} and K_{iBTB} are the v_{BTB} controller parameters.

The AC side electrical dynamics of the BTB_L converter can be described as follows in the *dq* frame

$$\begin{cases} v_{dLP}=L_1\dfrac{di_{dBTBL}}{dt}+v_{dBTBL}-\omega_{eLP}L_1 i_{qBTBL} \\ v_{qLP}=L_1\dfrac{di_{qBTBL}}{dt}+v_{qBTBL}+\omega_{eLP}L_1 i_{dBTBL} \end{cases} \tag{4-10}$$

where L_1 is the equivalent inductance of the inductor L_1 shown in Figure 4.3, v_{dLP} and v_{qLP} are the *dq* voltages of the LPG, respectively, and ω_{eLP} is the electrical speed of the LPG.

Applying the (4-8)-(4-10) into (4-7), (4-7) can be rewritten as follows:

$$\frac{3}{2}\left[\overline{i}_{qLP}\left(\overline{v}_{qBTBL}-\overline{i}_{qBTBL}L_1\cdot s\right)\Delta m+\overline{i}_{qBTBL}\Delta v_{qLP}\right]=\left(\overline{v}_{BTB}C_{BTB}\cdot s+\overline{i}_{BTB}\right)\Delta v_{BTB}+\overline{v}_{BTB}\Delta i_L \tag{4-11}$$

Based on (4-11) the block diagram of the BTB converter DC-link voltage control can be built as shown in Figure 4.7, where the derived control plant is outlined. T_d is the time constant of a first-order module which represents the time delay [20] from sensing LPG's phase currents to taking the control actions for the BTB_L converter. T_d is regarded as 1.5(PWM period) [37].

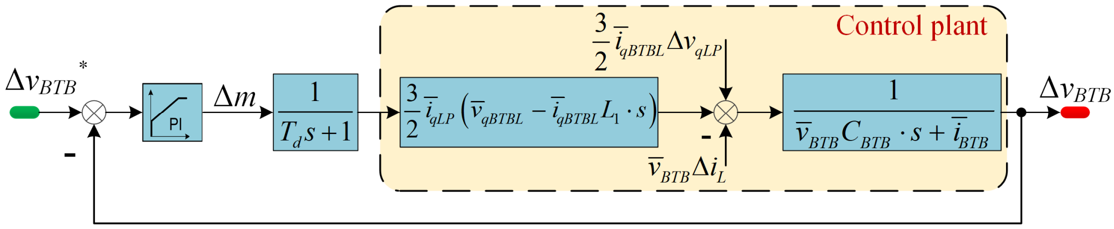

Figure 4.7. Block diagram of the BTB converter DC-link voltage control.

The zero provided by the v_{BTB} controller is used to cancel the dominant pole of forward path. Hence, the tuning criteria for control parameters can be derived as follows:

$$\begin{cases} K_{pBTB} = \alpha \cdot \bar{v}_{BTB} C_{BTB} \\ K_{iBTB} = \alpha \cdot \bar{i}_{BTB} \end{cases} \tag{4-12}$$

where α is a gain used to tune the control parameters.

As revealed in Chapter 3, operation at the highest speed and the heaviest loading is the worst operating condition. Based on the system parameters shown in Table 4-1 and the worst operating point, the root locus of the BTB converter DC-link voltage control system with respect to the gain α is presented in Figure 4.8. It can be seen that when α = 0.05, the damping ratio is 0.707 and the overshoot is 4.25%. The closed-loop poles (-3150±3130i) are located in the left half plane, which ensures the stability. Hence, α = 0.05 is used for the following simulation verifications.

Table 4-1. Parameters of the proposed APGC and Engine

Parameters	Value
Rated main DC bus voltage	270 V
Rated DC voltage of the BTB converter	400 V
DC capacitpor of the BTB converter	1600 μF
The inductance of L_1	1.0 mH
The inductance of L_2	0.85 mH
Switching frequency	16 kHz
Full thrust speed of HP shaft	20,000 rpm
Full thrust speed of LP shaft	7,000 rpm

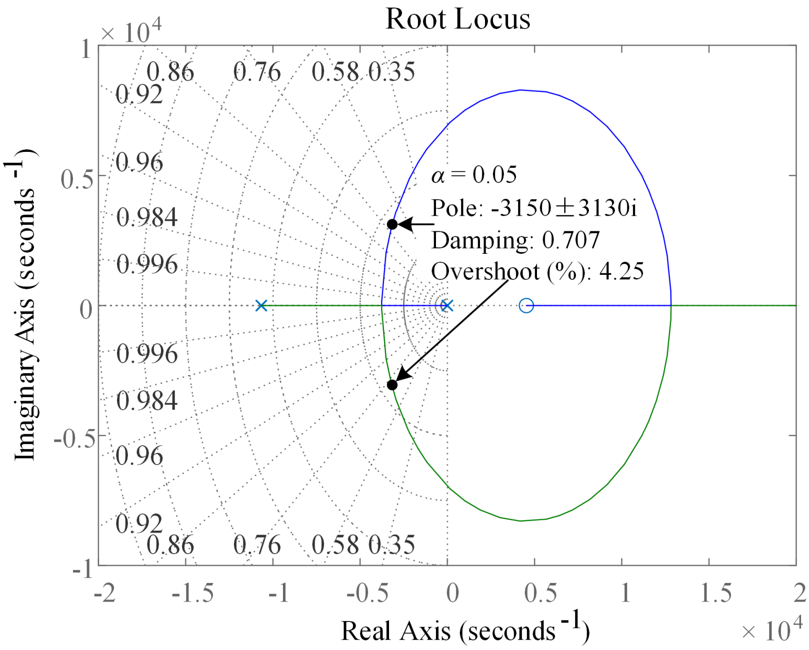

Figure 4.8. Root locus of the BTB converter DC-link voltage control system.

4.2.2 Comparison of the Alternative Instantaneous Power Control based Method with the Proposed Method for the BTB$_L$ Converter

To achieve a fast and stable power control, in recent years the instantaneous power control (IPC) emerges as a preferrable solution. The concept of IPC was firstly proposed by Akagi *et. al.* based on the *pq* theory to compensate the reactive power in a balanced three phase system with an ideal voltage source [132]. Then it was further successfully developed for power control in more complex applications such as unbalanced grid and load [133], [134], advanced electrical machine drives [135], [136], and pulse-width modulated (PWM) rectifier [137].

A typical structure of a static synchronous compensator (STATCOM) using IPC is shown in shown in Figure 4.9(a). The key parts have been highlighted as source, load, and additional compensator. The architecture of the LP channel is presented in Figure 4.9(b). It can be seen that the LP channel is with an identical structure as the STATCOM, where the LPG can be regarded as source, the LPR as the load, and the BTB_L converter as the compensator.

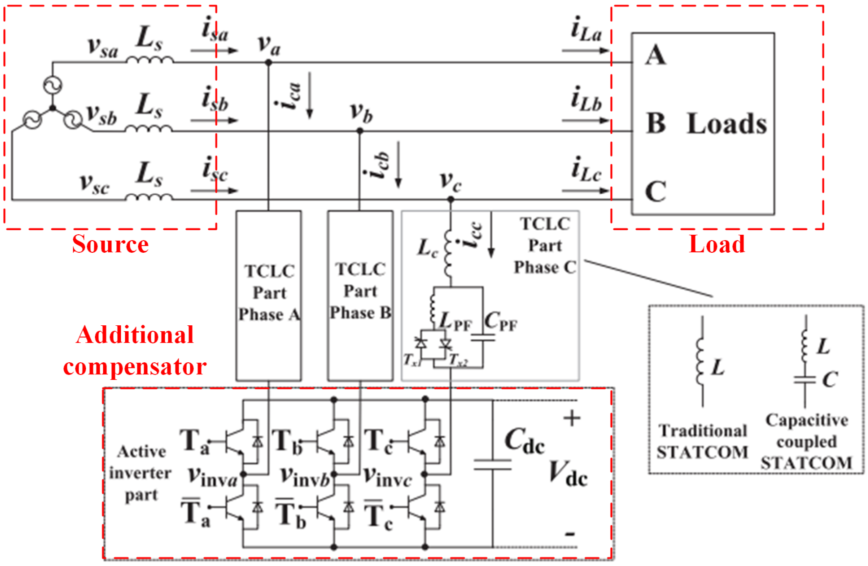

(a)

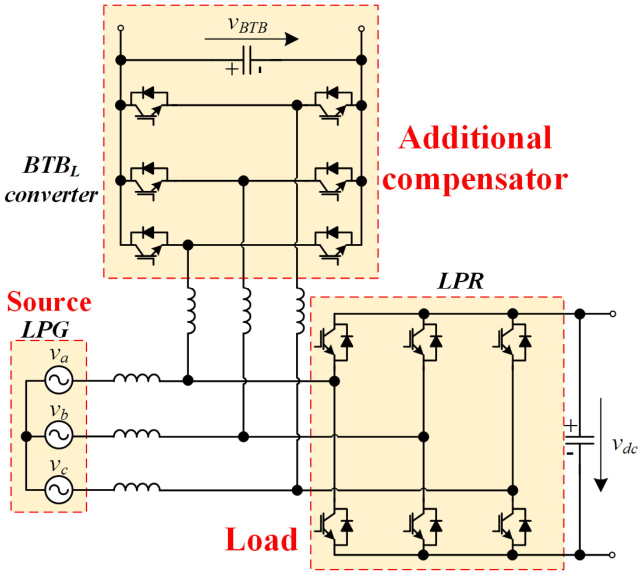

(b)

Figure 4.9. Structure of a typical STATCOM and the APGC. (a) STATCOM [138]. (b) LP channel of the APGC.

Due to the similarity of structure, the IPC concept can be considered to be applied to the APGC system as an alternative to the phase current synchronization method discussed in subsection 4.2.1. The basic procedure of the IPC method can be explained as follows.

Considering a three-phase source whose fundamental voltages are v_{a1}, v_{b1}, and v_{c1}, and fundamental currents are i_{a1}, i_{b1}, and i_{c1}, the following relations in $\alpha\beta$ frame can be obtained:

$$\begin{cases} \boldsymbol{v}_{\alpha\beta}{}^{T} = T_{3/2}\boldsymbol{v}_{abc}{}^{T} \\ \boldsymbol{i}_{\alpha\beta}{}^{T} = T_{3/2}\boldsymbol{i}_{abc}{}^{T} \end{cases} \tag{4-13}$$

where $\boldsymbol{v}_{abc} = \left[v_{a1}\ v_{b1}\ v_{c1}\right]$, $\boldsymbol{i}_{abc} = \left[i_{a1}\ i_{b1}\ i_{c1}\right]$, $\boldsymbol{v}_{\alpha\beta} = \left[v_{\alpha}\ v_{\beta}\right]$, $\boldsymbol{i}_{\alpha\beta} = \left[i_{\alpha}\ i_{\beta}\right]$, $T_{3/2} = \sqrt{\dfrac{2}{3}}\begin{bmatrix} 1 & -1/2 & -1/2 \\ 0 & \sqrt{3}/2 & -\sqrt{3}/2 \end{bmatrix}$.

For a three-phase system, the instantaneous active power p and reactive power q can be given in a matrix form as follows:

$$\begin{bmatrix} p \\ q \end{bmatrix} = \begin{bmatrix} v_{\alpha} & v_{\beta} \\ -v_{\beta} & v_{\alpha} \end{bmatrix}\begin{bmatrix} i_{\alpha} \\ i_{\beta} \end{bmatrix} = A\begin{bmatrix} i_{\alpha} \\ i_{\beta} \end{bmatrix} \tag{4-14}$$

Therefore, the targeted currents can be expressed with targeted instantaneous power $[p^*, q^*]^T$ in the $\alpha\beta$ frame as follows:

$$\begin{bmatrix} i_{\alpha}^{*} \\ i_{\beta}^{*} \end{bmatrix} = \frac{1}{\det(A)}\begin{bmatrix} v_{\alpha} & -v_{\beta} \\ v_{\beta} & v_{\alpha} \end{bmatrix}\begin{bmatrix} p^{*} \\ q^{*} \end{bmatrix} \tag{4-15}$$

where the determinant $\det(A) = v_{\alpha}^2 + v_{\beta}^2$

With targeted active power p^* and reactive power q^* that the BTB converter should supply, the current references can be obtained. Then the current references are used in subsequent closed-loop current control.

From above it can be seen that the basic principles of the IPC concept are straightforward. However, for the specific application of BTB converter control in the APGC, two problems can be identified:

- From (4-15), it can be seen that v_{α} and v_{β} are required to derive the optimal current references for the BTB converter. However, in practice due to the switching behavior of the pulse-width modulation of the LPR, these phase voltages are in pulsating manners. This will lead to pulsating voltages of v_{α} and v_{β}. Using such pulsating voltages will result in a pulsating current references i_{α}^* and i_{β}^* in (4-15). These pulsating current references i_{α}^* and i_{β}^* are not ideal for control. One way to address this issue is to use the voltage references from the LPR controller. Although the AC terminals of the LPG and LPR are essentially the same, the voltage references of the

LPR will inevitably deviate from the actual ones due to the dead-time effect and nonlinearities of the converter, and resulted in a compromised control performance.

- Generally the targeted instantaneous reactive power q^* is used to compensate the required reactive power of the load, thus the three-phase source only needs to provide active power, which can reduce the power rating of source and minimize the copper losses on the cable. While in the APGC application, this reactive power component is difficult to obtain in real time.

Despite these challenges, the IPC concept features fast power control and active and reactive power component decoupling, it is still a promising candidate to control the BTB converter in the APGC. Relevant research can be focused on this application in future study.

4.2.3 Control Design for the BTB$_H$ Converter

As can be seen in Figure 4.1, terminals of the HPG are directly connected to the BTB$_H$ converter. Therefore, operation of the HPG is controlled by the BTB$_H$ converter. The rotary speed of HPG is set by the HP shaft of engine, denoted as ω_{mHP}. Then, the mechanical power extracted from the HP shaft is $P_m = \omega_m T_e$, where T_e is the electromagnetic torque of HPG. The adopted HPG is a surface-mounted PMM, whose torque can be expressed as follows:

$$T_e = 1.5 p \psi_m i_{qHP} \tag{4-16}$$

where p is the pole pairs, ψ_m is the flux linkage of magnet, i_{qHP} is the q-axis currents of HPG.

Based on (4-16), the i_{qHP} reference can be obtained:

$$i_{qHP}^* = \frac{P_{HP}}{1.5 p \psi_m \omega_{mHP}} \tag{4-17}$$

where P_{HP} is the desired output power of HPG.

In (4-17), p and ψ_m are machines parameters. ω_{mHP} can be measured using position sensor or estimated using sensorless scheme. P_{HP} can be calculated by total power P_t and designed power sharing ratio. Then, i_{qHP}^* can be obtained using (4-17). Since the DC-link voltage in the BTB converter v_{BTB} is set at a high value as can be seen in Table 4-1, HPG can operate without field weakening. This means i_{dHP}^* can be set as 0 to realize maximum torque per ampere control. Control scheme for the BTB$_H$ converter is shown in Figure 4.10.

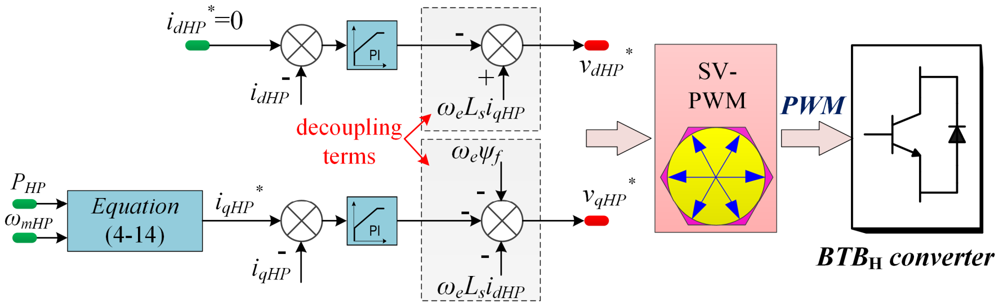

Figure 4.10. Control scheme for the BTB_H converter.

4.3 Passive Filters in The System

4.3.1 Filtering Inductors

As shown in Figure 4.1, inductor L_1 is deployed between the AC terminals of LPG and BTB converter. This inductor is important due to two main reasons:

- LP rectifier (LPR) and BTB_L converter are both voltage source converters. L_1 separates the AC voltages of LPR and BTB_L converter.
- L_1 filters high frequency PWM harmonics generated by the switching actions of power converters.

Therefore, the optimal value of L_1 should be carefully selected. If the value is too large, weight and size of the core of L_1 will increase. If the value is too small, it cannot fulfil the function to filter the high frequency PWM harmonics and the system may lose stability [106].

From Figure 4.1, the equivalent circuit of LP channel can be derived as shown in Figure 4.11(a), where v_{aLPR} is the a phase voltage generated by LPR, v_{aBTBL} is the a phase voltage generated by BTB_L converter. N is reference point of the BTB_L converter, N' is the reference point of the LPR. L_1 and R_1 are the equivalent inductance and resistance of the filter.

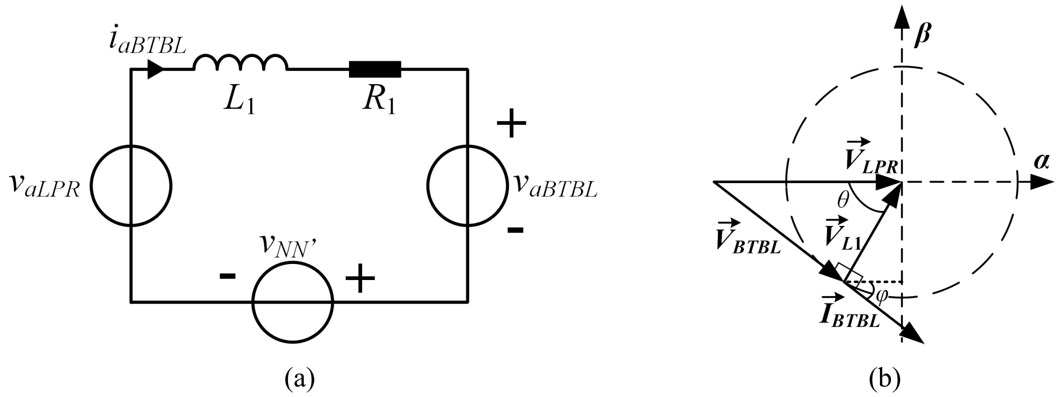

Figure 4.11. Equivalent circuit and phase diagram of LP channel circuit. (a) The equivalent circuit of *a* phase. (b) Phase diagram of LP side voltage phasors.

The following voltage equation can be obtained from the Figure 4.11(a) using Kirchhoff voltage law, give as follows:

$$v_{aLPR} = R_1 i_{aBTBL} + L_1 \frac{di_{aBTBL}}{dt} + v_{aBTBL} + v_{NN'} \tag{4-18}$$

The relation shown in (4-18) is also valid for *b* and *c* phases. Multiplying *a, b,* and *c* phase voltage equations by a coordinate transformation vector **T**=[1, $e^{j(2\pi/3)}$, $e^{j(4\pi/3)}$], the synthesized voltage phasors can be obtained, as illustrated by Figure 4.11(b), where $\vec{V}_{LPR}$ is the AC side voltage phasor of the LPR, $\vec{V}_{BTBL}$ is the AC side voltage phasor of the BTB_L converter, $\vec{V}_{L1}$ is the voltage phasor across the inductor L_1, $\vec{I}_{BTBL}$ is the current phasor of the BTB_L converter. It needs to be noted that the neutral-to-neutral voltage $v_{NN'}$ is removed by multiplying the vector **T**.

According to cosine theorem, the following equation can be obtained from the relationship in Figure 4.11(b)

$$\left|\vec{\boldsymbol{V}}_{\boldsymbol{BTBL}}\right|^2 = \left|\vec{\boldsymbol{V}}_{LPR}\right|^2 + \left|\vec{\boldsymbol{V}}_{\boldsymbol{L1}}\right|^2 - 2\left|\vec{\boldsymbol{V}}_{LPR}\right|\left|\vec{\boldsymbol{V}}_{\boldsymbol{L1}}\right|\cos\theta \tag{4-19}$$

Since $\left|\vec{\boldsymbol{V}}_{\boldsymbol{L1}}\right| = j\omega L_1 \left|\vec{\boldsymbol{I}}_{BTBL}\right|$, (4-19) can be rewritten as:

$$\left|\vec{\boldsymbol{V}}_{BTBL}\right|^2 = \left|\vec{\boldsymbol{V}}_{LPR}\right|^2 + \omega^2 L_1^{\,2} \left|\vec{\boldsymbol{I}}_{BTBL}\right|^2 - 2\omega L_1 \left|\vec{\boldsymbol{V}}_{LPR}\right|\left|\vec{\boldsymbol{I}}_{BTBL}\right|\cos\theta \tag{4-20}$$

Selecting L_1 as the variable, L_1 can be formulated as:

$$L_1 = \frac{\left|\vec{V}_{LPR}\right|\cos\theta + \sqrt{\left|\vec{V}_{LPR}\right|^2\cos^2\theta + \left|\vec{V}_{BTBL}\right|^2 - \left|\vec{V}_{LPR}\right|^2}}{\omega\left|\vec{I}_{BTBL}\right|} \tag{4-21}$$

The phase diagram of LPG in Figure 4.12 considers that LPG operates in i_d=0 mode. The expressions of LP channel variables can be given as follows:

$$\begin{cases} \left|\vec{V}_{LPR}\right| = \sqrt{\left(\omega_e\psi_m - R_s i_{qLP}\right)^2 + \left(\omega_e L_q i_{qLP}\right)^2} \\ i_{qLP} = \dfrac{P_{LP}}{1.5\psi_m\omega_e} \qquad \left|\vec{I}_{BTBL}\right| = \dfrac{\left|\vec{I}\right|}{n} = \dfrac{\left|\vec{I}_{qLP}\right|}{n} = \dfrac{i_{qLP}}{n} \end{cases} \tag{4-22}$$

where ω_e, i_{qLP} and P_{LP} are speed, q-axis current and output power of the LPG, respectively. n is the ratio between the power generated by LPG and the power transferred to the BTB converter.

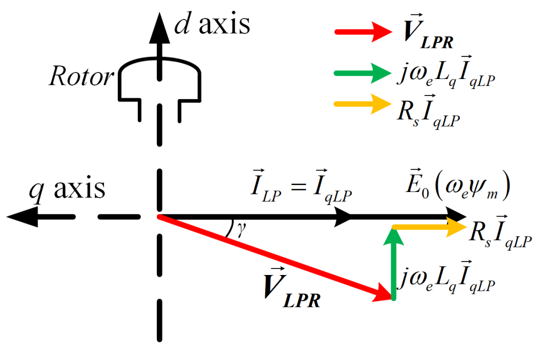

Figure 4.12. Phase diagram of the LPG.

As shown in Figure 4.12, γ is the phase shift angle between the voltage phasor $\vec{V}_{LPR}$ and current phasor $\vec{I}_{LP}$. As pointed out in 4.2.1, i_{xLP} and i_{xBTBL} (x=a,b,c) are controlled in phase. Hence, γ is the also the phase shift angle between the voltage phasor $\vec{V}_{LPR}$ and current phasor $\vec{I}_{BTBL}$. From Figure 4.11 and Figure 4.12, the relationship of θ and γ is derived as follows

$$90^\circ - \theta = -\gamma = -\tan^{-1}\left(\frac{\omega_e L_q i_{qLP}}{\omega_e\psi_m - R_s i_{qLP}}\right) \tag{4-23}$$

The modulation technique applied to the BTB$_L$ converter is the space vector PWM [94], the maximum modulation index (MI) is $\sqrt{3}/3$. Hence the following expression for $\vec{V}_{BTBL}$ can be derived considering both largest MI and phase diagram in Figure 4.11(b):

$$\left|\vec{V}_{LPR}\right|\sin\theta \le \left|\vec{V}_{BTBL}\right| \le \frac{\sqrt{3}}{3}v_{BTB} \tag{4-24}$$

Substituting (4-22)-(4-24) into (4-21), the value of L_1 can be found as the function of ω_e, P_{LP} and n, which is shown below:

$$J(\Theta)_{\min} \le L_1 = J(\Theta) \le J(\Theta)_{\max} \tag{4-25}$$

where $\begin{cases} J(\Theta)_{\min} = nL_q \\ J(\Theta)_{\max} = nL_q + \dfrac{1.5n\psi_m\sqrt{{v_{BTB}}^2/3-\left(\omega_e\psi_m - \dfrac{R_sP_{LP}}{1.5\psi_m\omega_e}\right)^2}}{P_{LP}} \end{cases}$. $\boldsymbol{\Theta} = \{\omega_e,\ P_{LP},\ n\}$. $J(\cdot)$ is a function where $\boldsymbol{\Theta}$ is the independent variable, $L_1 = J(\boldsymbol{\Theta})$ is the dependent variable.

To define the range of L_1, the maximum value of $J(\boldsymbol{\Theta})_{\min}$ and the minimum value of $J(\boldsymbol{\Theta})_{\max}$ should be derived. Here the gradient descent method formulated in (4-26) is utilized for solving this multivariable optimization problem [95]:

$$\Theta^{(i+1)} = \Theta^{(i)} - \eta\nabla J\left(\Theta^{(i)}\right)_{\max} \qquad i = 1,2,3\ldots i_{\max} \tag{4-26}$$

For the studied AEGART machine, the power range is P_{LP} 10kW – 60kW and n is considered in the range $n \in (5,7)$. Hence, the maximum value of $J(\boldsymbol{\Theta})_{\min}$ is $n_{\max} * L_q = 0.7$mH. The minimum value of $J(\boldsymbol{\Theta})_{\max}$ can be obtained by solving the iterative equation in (4-26). The relation of $J(\boldsymbol{\Theta})_{\max}$ with respect to ω_e, P_{LP}, and n are illustrated in Figure 4.13. Here two main findings can be summarized:

1) From Figure 4.13(a) it can be seen that the minimum value of $J(\boldsymbol{\Theta})_{\max}$ is almost independent on the LPG speed ω_e. This means the selection of L_1 is not affected by ω_e.
2) From Figure 4.13(b) it follows that the minimum value of $J(\boldsymbol{\Theta})_{\max}$ locates on the point of maximum power of P_{LP} and minimum power ratio n. This indicates that the value of L_1 is very sensitive to P_{LP} and n.

The result in Figure 4.13 shows that the minimum value of $J(\boldsymbol{\Theta})_{\max}$ within the studied operating region is 1.5mH. Hence, based on above analysis, the inductance value of L_1 should be chosen between 0.7mH and 1.5mH.

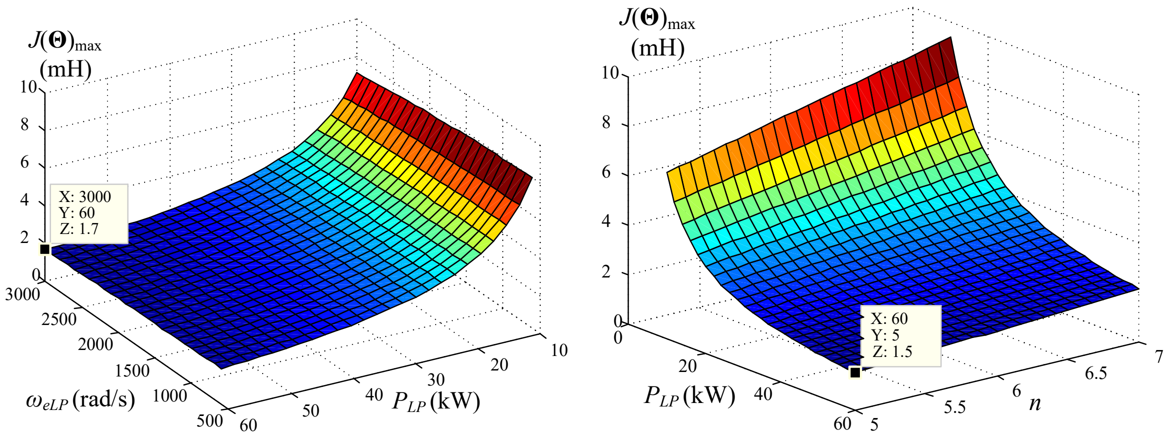

(a) (b)

Figure 4.13. The value of $J(\mathbf{\Theta})_{max}$ with respect to ω_e, P_{LP}, and n.

4.3.2 DC-Link Capacitors

Apart from inductor, another passive component that affects the overall system weight and volume is the DC-link capacitor. Film capacitor is preferred in our application for its high current carrying capabilities in high switching frequency applications and capacitance stability with respect to temperature rise. A variety of methods have been presented for the calculation of DC-link capacitance, for example [63]-[65].

In [63] authors consider that the DC-link capacitor can absorb the maximum surplus current generated within a switching period by the switching actions and maintain the DC-link voltage ripple under specified value. Here this method is denoted as *Per Ts ripple* method. The equation for DC-link capacitance C is presented as follows:

$$C = \frac{v_{BTB}}{32 \cdot \Delta V_{pp} \cdot L_{ph} \cdot f_{sw}^{\ 2}} \tag{4-27}$$

where ΔV_{pp} is the acceptable voltage ripple of the DC-link voltage, f_{sw} is the switching frequency, and L_{ph} is the equivalent inductance per phase.

In [64], a DC-link capacitance calculation approach is tailored for a back-to-back system where one side of the DC-link capacitor is an active rectifier, and the other side of the capacitor is an inverter. The DC-link voltage should be maintained under instantaneous power imbalance. Here this method is denoted as *BTB Energy storage* and the DC-link capacitance is derived as:

$$C = \frac{P_{\max}}{\left(v_{BTB}\Delta V_{pp} + \frac{1}{2}\Delta V_{pp}{}^{2}\right) f_{sw}} \tag{4-28}$$

where $P_{\max}$ is the maximum power delivered by the DC bus.

According to [65], the relation of the DC-link capacitor's root mean square (RMS) current with respect to the RMS value of phase current is derived as:

$$\frac{I_{cap,RMS}}{I_{ph,RMS}} = \sqrt{2 \cdot MI \cdot \left(\frac{\sqrt{3}}{4\pi} + \left(\frac{\sqrt{3}}{\pi} - \frac{9 \cdot MI}{16}\right)\cos^2\varphi\right)} \tag{4-29}$$

where $I_{cap,RMS}$ and $I_{ph,RMS}$ are the RMS values of DC-link capacitor's current and phase current, respectively. MI is the abbreviation for modulation index. φ is the power factor angle.

Under unity power factor and a modulation index of 0.612, the maximum ratio can be obtained as 1.55 [65]. Therefore, the following equation can be used to decide the capacitance. This method is referred as *Cap RMS*.

$$C = \frac{I_{cap,RMS}}{\Delta V_{pp} \cdot f_{sw}} \tag{4-30}$$

The minimum DC-link capacitance value on switching frequency according to different methods is illustrated by Figure 4.14. Since the *Per Ts ripple* method only considers the absorption of the increased current ripple within a switching period, the calculated capacitance is significantly lower than other methods. the *Per Ts ripple* method is only valid when there is a stable bidirectional DC source connected to the DC-link capacitor. The *Cap RMS* method calculates capacitance based on RMS of capacitor current stress. While the *BTB Energy storage* method calculates capacitance based on energy storage capacity during instantaneous power imbalance. Since in the application of the proposed APGC, the BTB converter transfers power between the LP channel and the HP channel. It is desired to minimize the impact of instantaneous power imbalance within the BTB converter on the operation of generators and rectifiers. Hence, the *BTB Energy storage* method is adopted to theoretically determine the minimum DC-link capacitance. According to the calculated values shown in Figure 4.14, the minimum DC-link capacitance at 16kHz switching frequency using the *BTB Energy storage* method is 1163μF. For the lab prototype, 4×400μF film capacitors are parallel connected to construct a 1600μF DC-link capacitor bank.

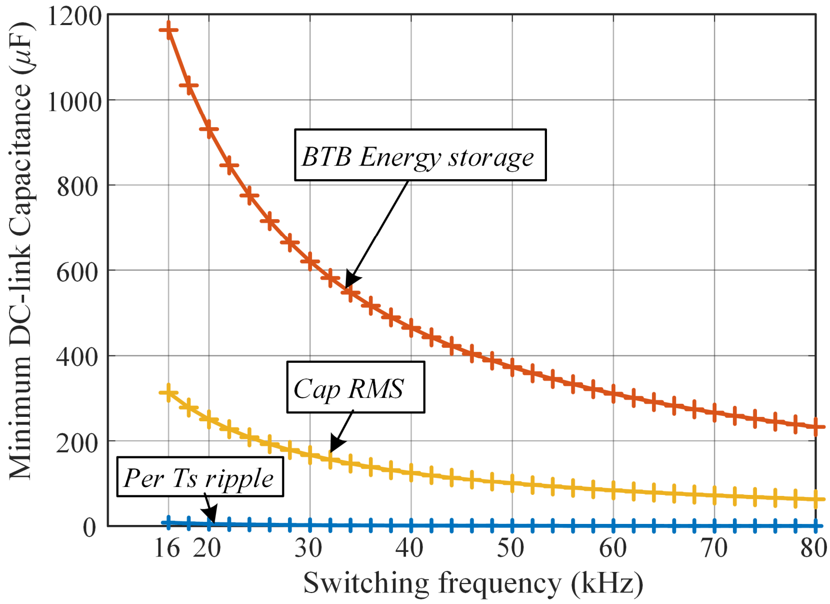

Figure 4.14. DC link capacitance comparison with different methods at various switching frequency. v_{BTB} = 400V, L_{ph} = 1mH, $P_{\max}$ = 45kW, DC-link voltage ripple is 1.5% v_{BTB}.

4.4 Simulation Results

To investigate the control performance of the APGC, an APGC model is built in the Simulink environment. The power converters are configured with PWM averaging model, which means that these converters are modelled using a switching-function model controlled by averaging the firing pulses produced by the PWM generators over a specified period. Solver of the powergui block is set in continuous mode. Hence, controllers in the system, such as DC voltage and current controllers, are implemented in the *s* domain. The transmission cable impedance is omitted. Subsystems of the model can be found in Appendix D. A resistor bank and a motor drive subsystem are connected to the main DC bus as the CIL and CPL, respectively. The control performance and power losses reduction are presented in this section.

4.4.1 Control Performance of the Proposed Power Generation Centre

In this subsection, control performance of the APGC using the proposed control and power management schemes in this chapter is investigated. The purpose of this simulation and core characteristics that will be checked include:

- The main DC bus voltage v_{dc} and DC currents of the LP and HP rectifiers i_{dcLP} and i_{dcHP}. This is used to check the effectiveness of main DC bus voltage control and droop control.
- The DC-link voltage within the BTB converter v_{BTB}, and the gain m. This is used to check the effectiveness of the proposed control scheme for the BTB_L converter as shown in Figure 4.3.
- The phase current of the LPG, LPR and BTB converter. This is used to check that the three phase currents are synchronized in phase.
- The dq axes currents of the LPG and HPG, i.e., i_{dL}, i_{dH}, i_{qL}, and i_{qH}. This is used to prove that the field-weakening operation of the HPG is removed in the APGC, and also to check torque of the LPG and HPG at different output powers.
- Output power of the HPG, LPG HPR and LPR. This is used to check the effectiveness of power flow control in the APGC.

The simulation results are shown in Figure 4.15(a) to (e). The operating conditions are detailed in Table 4-2. It can be seen that two equivalent droop gains are set for the LPR and HPR, thus they share the same amount of power (P_{LPR}=P_{HPR}). Before t=0.09s, the output power between the LPG (P_{LPG}) and HPG (P_{HPG}) is 2:1, which means the amount of power transferred from the LP channel to HP channel through the BTB converter (P_{BTB}) is P_{LPG} - P_{LPR} $=(2/3 - 1/2) = 1/6$ of total load power (P_t). To investigate the dynamic performance when changing the amount of transferred power, at t=0.09s, the power ratio between P_{LPG} and P_{HPG} increases to 3:1, which means P_{BTB} increases to $(3/4 - 1/2) = 1/4$ of total load power P_t.

The main DC bus voltage and currents are presented in Figure 4.15(a). v_{dc} decreases from the rated 270V to 265.3V due to the droop control effect. In the steady state, i_{dcHP} and i_{dcLP} are equal due to the identical droop gains, showing an equivalent power sharing performance. When increasing the proportion of LPG's power at 0.09s, during the transient, more power will be transferred to the HP channel from the LP channel through the BTB converter. Hence, the power of LPR is affected, leading to a dip in i_{dcLP} and also v_{dc}. In contrast, a short-term current surge occurs in i_{dcHP}.

Table 4-2. Simulation parameters of the proposed APGC.

Category	Parameter	Value
Electrcial machines	Speed of LP generator	7,000 rpm
	Speed of HP generator	20,000 rpm
Rectifeirs	Topology	Two level, bidirectional
	Maximum current	400 A
Main DC Bus	Rated voltage	270 V
	Local shunt capacitor	1 mF
	Main bus capacitor	1.2 mF
Back-to-back Converter	DC-link voltage	400 V
	DC-link capacitor	1.6 mF
CPL + CIL	Total load power	20 kW
Control paramters	Current loop PI gains	0.87, 3908
	Voltge loop PI gains for the rectifiers	Adaptively tuned by setting the gain $\gamma = 0.4$ in (3-23)
	Voltge loop PI gains for the BTB_L converter	Adaptively tuned by setting the gain $\alpha = 0.05$ in (4-12)
	Droop gains for rectifiers	0.25 and 0.25
Power flow	Ouput power of the LPG	t<0.09s, $P_{LPG} = 2P_t/3$; t>0.09s, $P_{LPG} = 3P_t/4$
	Ouput power of the HPG	t<0.09s, $P_{HPG} = P_t/3$; t>0.09s, $P_{HPG} = P_t/4$
	Power of the BTB converter	t<0.09s, $P_{BTB} = P_t/6$; t>0.09s, $P_{HPG} = P_t/4$

The DC-link voltage of the BTB converter v_{BTB} and the gain m are presented in Figure 4.15(b). According to the relation in (4-1), $P_{BTB}/ P_{LPG} = m$. From the relation of power flow in Table 4-2, m should be 0.25 before 0.09s and 1/3 after 0.09s, respectively. This is consistent with the results of the gain m (0.246) before 0.09s in Figure 4.15(b). With an increased m, more power is routed to the BTB converter to charge the DC-link capacitor. Hence, v_{BTB} recovers to the setpoint at 400V as the gain m reaches to the new steady value 0.331 at 0.12s.

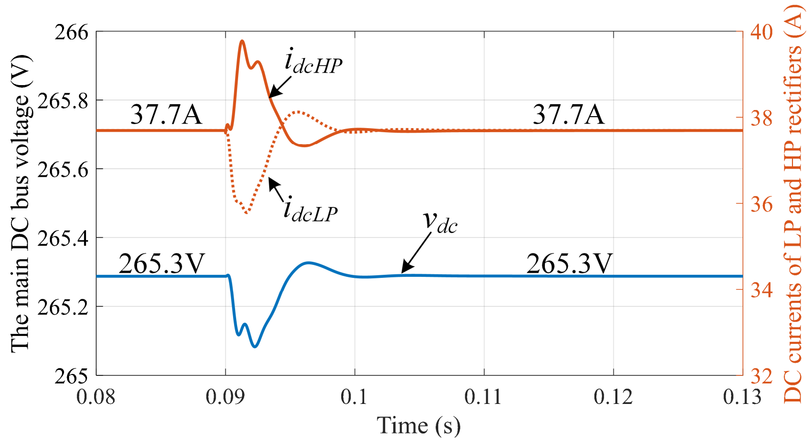

The main DC bus voltage (V)
DC currents of LP and HP rectifiers (A)
i_{dcHP}
i_{dcLP}
v_{dc}
37.7A
37.7A
265.3V
265.3V
Time (s)

(a)

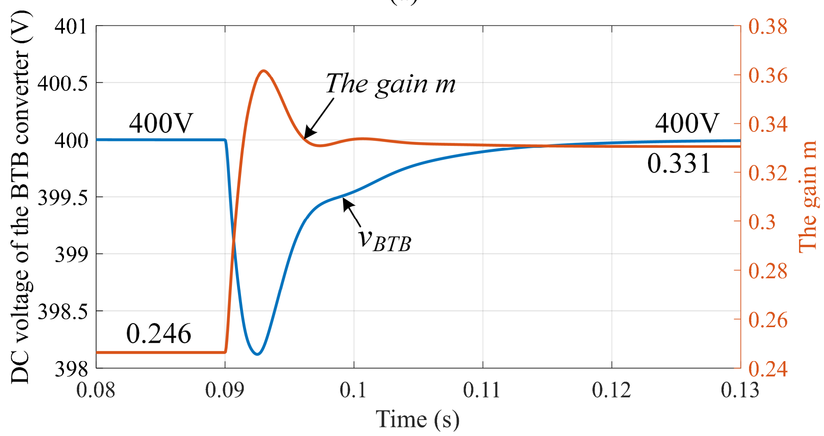

DC voltage of the BTB converter (V)
The gain m
The gain m
v_{BTB}
400V
400V
0.331
0.246
Time (s)

(b)

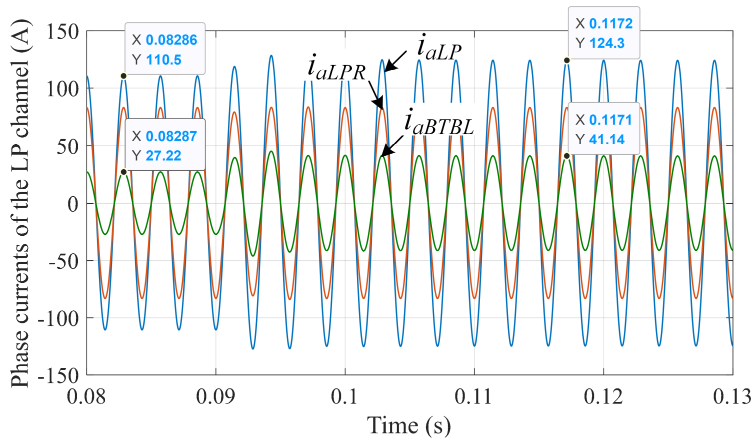

Phase currents of the LP channel (A)
i_{aLPR}
i_{aLP}
i_{aBTBL}
X 0.08286
Y 110.5
X 0.08287
Y 27.22
X 0.1172
Y 124.3
X 0.1171
Y 41.14
Time (s)

(c)

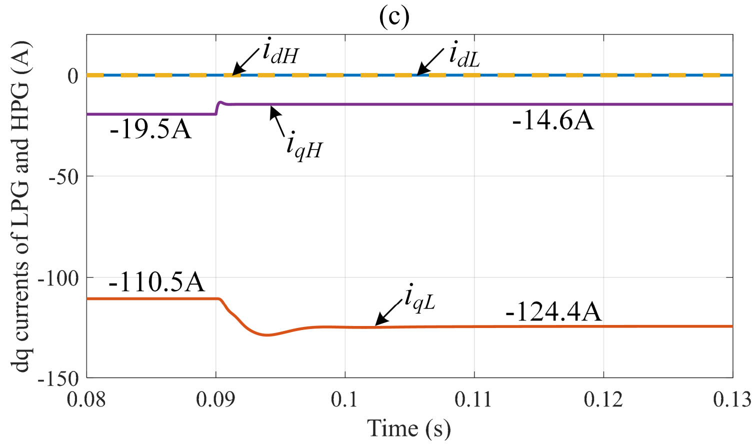

dq currents of LPG and HPG (A)
i_{dH}
i_{dL}
i_{qH}
i_{qL}
-19.5A
-14.6A
-110.5A
-124.4A
Time (s)

(d)

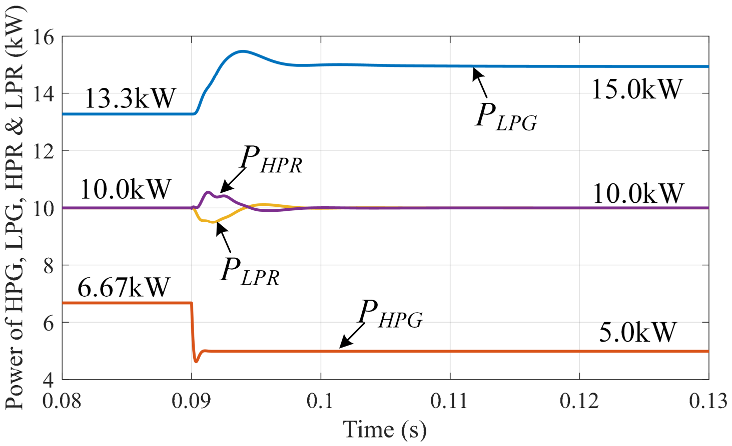

(e)

Figure 4.15. Simulation results of the APGC. (a) The main DC bus voltage and currents; (b) The DC-link voltage within the BTB converter, and the gain m; (c) LPG phase current i_{aLP}, BTB_L converter phase current i_{aBTBL} and LPR phase current i_{aLPR}. Red curve: i_{aLPR}; Blue: i_{aLP}; Green: i_{aBTBL}. (d) dq axes currents of the LPG and HPG. (e) Output power of the HPG, LPG, HPR, and LPR.

The phase current of LPG (i_{aLP}), LPR (i_{aLPR}) and BTB converter (i_{aBTBL}) are presented in Figure 4.15(c). It can be seen that the three phase currents are synchronized in phase. Moreover, according to the relation in (4-1), $peak(i_{aBTBL})/peak(i_{aLP})=m$ in the steady state. As shown in Figure 4.15(c), $peak(i_{aBTBL})/peak(i_{aLP})$=27.2A/110.5A= 0.247 before 0.09s, and 41.2A/124.3A =0.331 after 0.09s, respectively. This is consistent with the gain m in Figure 4.15(b). The results in Figure 4.15(b) and (c) both verify the effectiveness of the designed control scheme for the BTB_L converter in subsection 4.2.1.

The currents of LPG and HPG are shown in Figure 4.15(d). i_{dH} is controlled to be 0A due to a high DC-link voltage v_{BTB}. This confirms that the APGC allows HPG to operate without field weakening even at a high speed 20,000 rpm. However, with the PGC studied in Chapter 3, i_{dH} exceeds 100A as shown in Figure 3.16(c). As will be shown in the next subsection, the reduced current significantly improves efficiency of HPG and HP rectifier.

The output power of HPG, LPG, and delivered power of the HPR and LPR to the main DC bus are shown in Figure 4.15(e). The total load power P_t is 20kW, due to the identical droop gains, HPR and LPR share equivalent power 10kW in the steady state. LPG outputs 13.3kW ($2P_t/3$) before 0.09s and 15kW ($3P_t/4$) after 0.09s, respectively. That of HPG is 6.67kW ($P_t/3$) and 5.0kW ($P_t/4$), respectively. The simulation results are perfectly matched with the expected power flow shown in Table 4-2, category power flow.

To conclude, all the purposes and points presented in the beginning of this section have been checked. The simulation results in Figure 4.15 have demonstrated that the control and power management schemes designed in this chapter can effectively regulate the APGC.

4.4.2 Power Losses Comparison between the PGC and APGC

In this section, power losses within the PGC and the APGC are compared, including the power converter losses and electrical machine losses. Co-simulation of Simulink and PLECS are adopted for converter power losses analysis. The finite element analysis (FEA) tool MagNet is utilized for the calculation of electrical machine power losses. The results show that by using the APGC with a back-to-back converter, the efficiency can be improved from 94.0% to 95.0% at the studied operating point in simulation.

4.4.2.1. Electrical Machine Power Losses

To compare both solutions, the simulations have been conducted for the same settings as shown in Table 4-2. The phase currents of the HPG in the PGC are shown in Figure 4.16(a). Magnetic field of the HPG is given in Figure 4.16(b). It can be seen that the magnitude of phase current is 130A. This is because of the large field-weakening current component (in the *d*-axis), which can be seen in Figure 3.16(c). Hence, high copper losses in the HPG can be expected. These currents are fed into the FEA model of the HPG and power losses of the HPG were obtained. The averaged copper and iron losses are 201W and 232W, respectively. As it can be seen, the losses in iron are higher than in the copper. This is because iron losses are proportional to the electrical speed and fundamental frequency of an electrical machine. Hence, generally copper losses are more significant than iron ones in the low-speed region. While in the high-speed region, iron losses which occurs in the stator yoke accounts for the main part of total power losses [96].

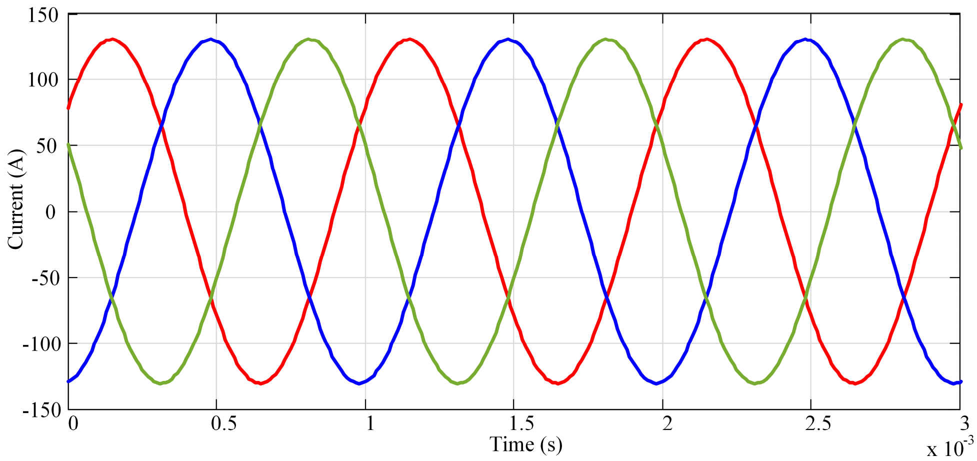

(a)

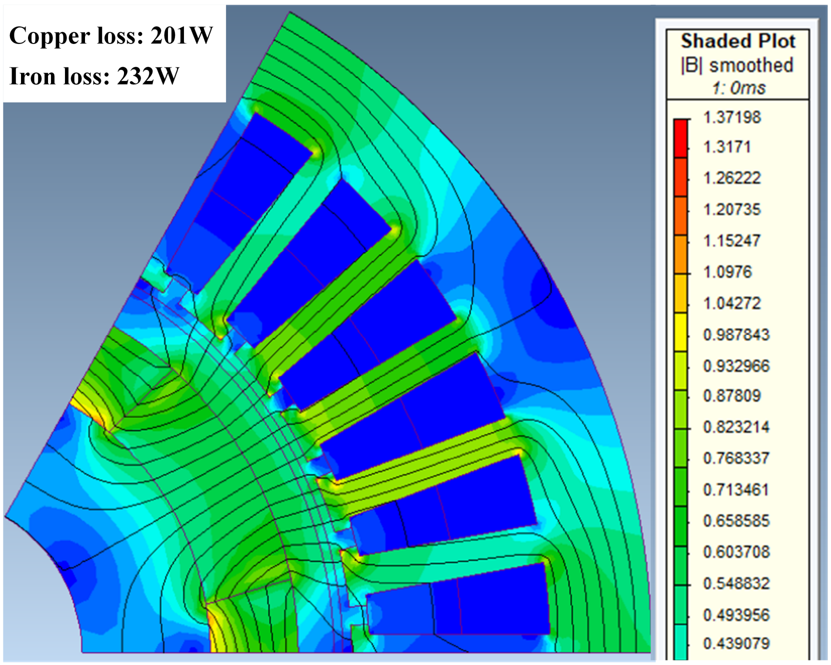

(b)

Figure 4.16. Characteristics of the HPG at 20,000 rpm, 6.7kW power output in the PGC. (a) phase currents of the HPG. (b) magnetic field of the HPG.

As a comparison, phase currents of the HPG in the proposed APGC are shown in Figure 4.17(a). Magnetic field of HPG is given in Figure 4.17(b). As can be seen in Figure 4.17(a), the magnitude of phase current is significantly reduced from 130A to 12.5A compared to that in Figure 4.16(a), this is due to the removal of the field-weakening operation of the HPG. All the current is in q-axis to generate active power only. Thus, reduction of power losses in the HPG can be expected. These currents are fed into the FEA model of the HPG and power losses of the HPG can be obtained. The averaged copper and iron losses of the HPG are 52W and 335W, respectively. Compared with the 201W in PGC, copper losses in the APGC are substantially reduced. The reduction of copper losses is attributed to the use of the BTB converter to eliminate the field weakening current in *d* axis of the HPG.

However, without field-weakening the magnetic field density in the HPG's stator is increased from 0.8T in the PGC to 1.2T in the APGC. Iron losses of an electrical machine are proportional to the magnetic field density [96]. Hence, iron losses of the HPG in the APGC (335W) is higher than that in the PGC (232W).

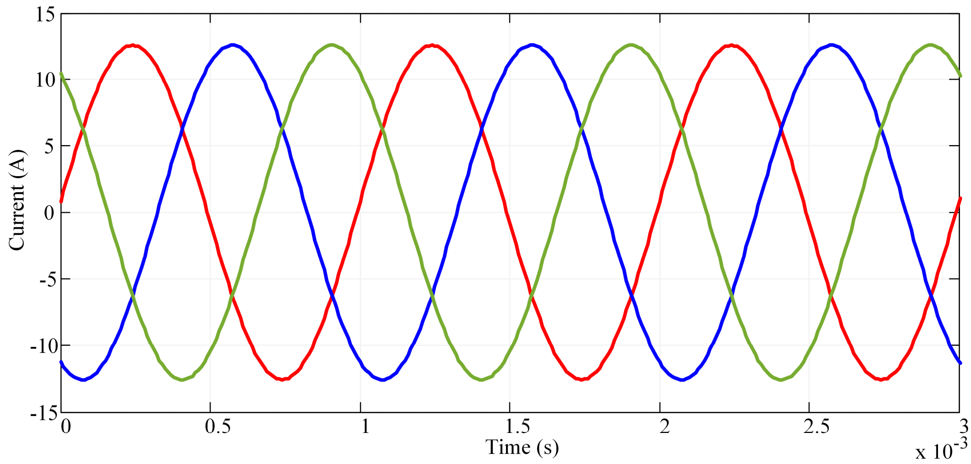

(a)

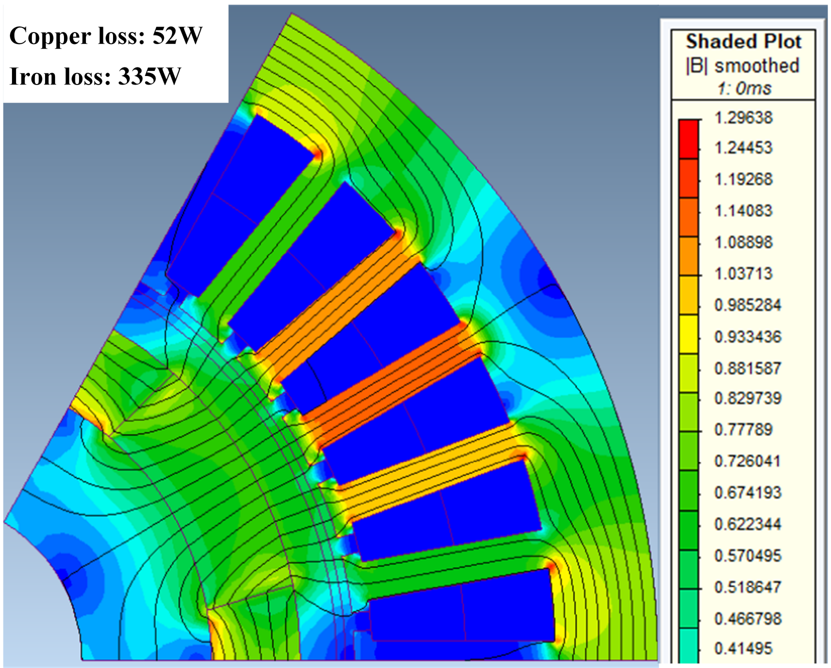

(b)

Figure 4.17. Characteristics of the HPG at 20,000 rpm, 6.7kW power output in the APGC. (a) phase currents of the HPG. (b) magnetic field of the HPG.

4.4.2.2. Overall Power Losses Comparison between the PGC and APGC

To compare the power losses of PGC and APGC, Figure 4.18 illustrates the power losses of the HP rectifier, LP rectifier, BTB_L converter, BTB_H converter, HPG iron losses, HPG copper losses, LPG iron losses and LPG copper loss. The total power losses of the PGC and APGC are also demonstrated.

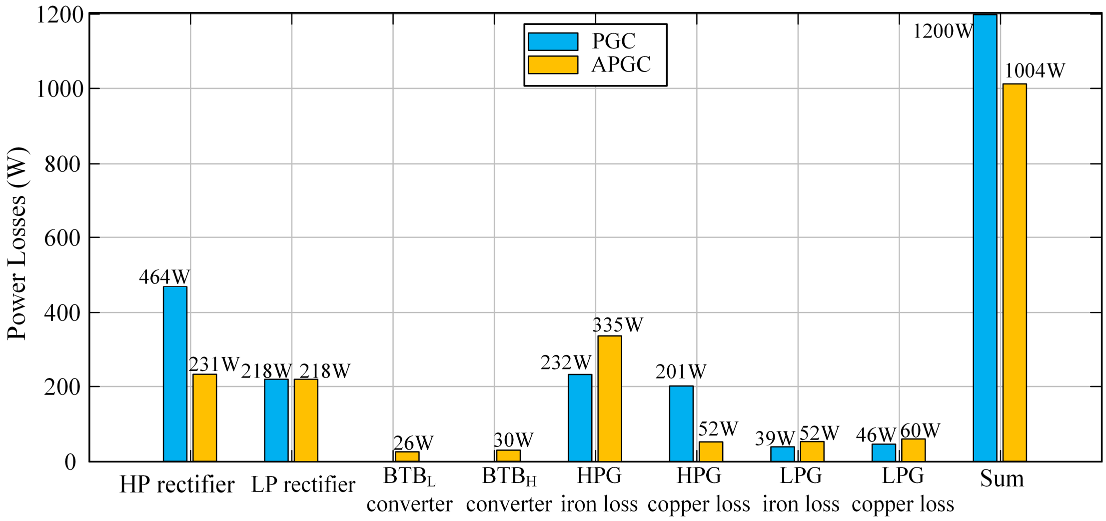

Figure 4.18. Power losses comparison of the PGC and APGC when HPG operates at 20,000 rpm, LPG operates at 7,000 rpm. Power sharing ratio of the two rectifiers is 1:1. BTB converter transfers one sixth of total power from the LP channel to HP channel. Load power is 20kW.

The following findings can be drawn from Figure 4.18:

1) Overall power losses of the proposed APGC are smaller than that of the PGC even though a back-to-back converter is involved in the APGC.
2) Power losses of the HP rectifier is greatly reduced since the HPG does not need field-weakening operation and i_d=0, leading to less current to conduct by the HP rectifier. This is the reason for power losses of the HP rectifier in the APGC smaller than that of the PGC.
3) The copper losses of HPG in the APGC is significantly reduced compared with that in the PGC due to decreased phase current of the HPG.
4) Iron losses of an electrical machine is proportional to the flux density B in the stator core. In the field weakening mode in PGC as shown in Figure 4.16(b), B≈0.8T. While in the APGC, filed weakening operation of the HPG is removed, and B increases to 1.2T, as shown in Figure 4.17(b). Hence, iron losses of the HPG in the PGC is smaller than that in the APGC.

To conclude, reduction of power losses in the APGC is due to the elimination of the HPG's field-weakening operation and field-weakening current in the *d* axis. For the studied operating point in Figure 4.18, the overall efficiency is improved from 94% in the PGC to 95% in the proposed APGC.

Although a higher efficiency can be achieved in the sector of electrical power generation, the extra components in the APGC brings additional weight and may change the fuel burn. To investigate to what extent the positive effect of efficiency improvement can counter the negative effect of extra weight, a preliminary weight and fuel burn analysis has been conducted to evaluate the impact of the extra components of the APGC. Details can be found in Appendix G.

4.5 Chapter Summary

In this chapter, an advanced power generation centre (APGC) for the MEA application is proposed that utilises a back-to-back (BTB) converter to transfer power between the LP and HP power generation channels and engine shafts. System modelling and control design is reported. Passive components are designed as well. The main contributions of this Chapter can be highlighted below:

- The APGC can allow the HPG operate at a high speed without field weakening control. All phase currents can be distributed on the *q* axis without the need for de-fluxing current on the *d* axis, reducing the stator current in the HPG. At the selected operating point, the overall efficiency is improved from 94.0% in the case of the PGC to 95.0% for the APGC in simulation. Efficiency will be further improved as operation speed increases.
- A phase currents synchronization strategy is proposed to regulate the BTB converter. By controlling the phase currents of the LPG, LPR and BTB_L converters in phase, the transferred power through the BTB converter depends on their magnitude ratio *m*. The ratio *m* is actively controlled for stabilizing the DC-link voltage in the BTB converter.
- Detailed selection criteria for the passive components are presented.

As described in Chapter 2, the proposed APGC has advantages over the PGC in terms of 1) electric power transfer; 2) elimination of FW operation of the HPG; 3) fault tolerance to the rectifier's failure; and 4) stability improvement of both engine and HVDC grid. The first two points have been investigated and verified. Point 3) and 4) will be studied in the following Chapters.

Chapter 5. System Reconfiguration and Fault Tolerant Control for the Proposed Advanced Power Generation Centre

5.1 Introduction

Field-weakening operation of the HPG and associated power losses due to the considerable FW current is a drawback of the PGC as discussed in previous Chapters. Another critical constraint of the considered PGC is the poor fault tolerance capability in terms of power conversion. In traction and power generation related systems, power converters are identified as the most vulnerable parts in terms of reliabilities [107], [108]. If contingency such as open-circuit fault occurs to the low-pressure channel or high-pressure channel rectifiers due to gate-driver fault or cycling high currents, the faulty rectifier needs to be stopped and disconnected from the DC grid [28]. However, the associated generators cannot be shut down suddenly as they are connected to the aircraft engine, which has a significant inertia. Moreover, even if the generators are stopped smoothly, these generators are no longer available for the electrical loads. This will undermine the power generation capability and thus limit large-scale applications of onboard electrical equipment. Furthermore, losing one generator may lead to severe system instability at high load power scenarios [54].

To enhance the reliability of a PMSG based power generation system, additional research is required to focus on the fault tolerance control for the main rectifiers. For example, in the case of a single-phase open circuit fault of a three-level rectifier, fault tolerance is achieved using redundant voltage vectors to synthesize the targeted voltage vector [109], [110]. In [111], a carrier-based pulse-width modulation with zero-sequence voltage injection is proposed to reduce current distortion in the case of open-circuit failure. Although these methods do not require additional hardware setup, the rectification performance in the healthy state cannot be fully restored. In order to achieve the same control performance as in a healthy state, a redundant phase leg is deployed to replace the faulty phase leg hence a healthy three-phase rectifier can be reconstructed [112], [113]. However, this method requires additional power modules and switches.

Although the above-mentioned strategies can provide fault tolerance control, they are only effective in addressing the single-phase fault. In practice, due to the power modules of the three-phase legs being spatially close, when one leg fails due to high ambient temperature or high current, other legs are also prone to failure. The above-mentioned fault tolerance methods are not suitable to deal with this multi-phase failure situation, but an effective solution is to deploy multiple redundant phase legs or multiple converters in parallel. However, this will undoubtably increase the overall cost [114], [115].

The APGC can handle the requirement of fault tolerance for rectifiers. As studied in Chapter 4, under normal conditions, the two APGC generators extract mechanical power from the two separate jet engine shafts and supply electrical power to a common HVDC bus through their dedicated AC/DC rectifiers. A BTB converter, which is used to connect the generators, provides an extra power flow path from generators to the HVDC bus. This architecture provides merits of fault tolerance of the APGC in case of the main AC/DC rectifiers failure through system reconfiguration. It should be noted that despite the incorporation of an extra BTB converter in the APGC, the two objectives of FW elimination and improved fault tolerance are achieved at the same time. Therefore, deploying a BTB converter is considered better than simply adding parallel converters [114], [115].

During the transition from normal operation state to fault and then post-fault operation, the torque of generators may change abruptly. This needs to be avoided as an abrupt change of generator torque may have significant negative impacts on the aircraft engines. To guarantee post-fault operation of the APGC in case of the main rectifiers failure, system reconfiguration and fault tolerant control with smooth transition from normal to post-fault conditions is essential. This study is reported in this Chapter, including both the LPR and HPR open-circuit failure.

5.2 Emulation of the Rectifier Failure and Fault Detection

In this investigation, to emulate the rectifier faulty scenario, PWM firing pulses for the rectifiers are disabled to simulate the open-circuit fault condition (three-phase open circuit fault). As can be seen in Figure 5.1(a), by setting all the gate drive signals as “low”, the IGBTs can be considered open circuited, and the rectifier can be regarded as a three-phase, full-wave diode bridge rectifier. In Figure 5.1(b), since the 270V DC voltage is higher than the voltage in solid black line, all the diodes are reversely biased. There is no current flow in the rectifier. Hence, the whole rectifier is in an equivalent open-circuit state.

Since the main objective of this paper is to investigate the post-fault reconfiguration and the associated control for the APGC, regarding the fault detection, this paper did not propose a new method. The open circuit fault detection method proposed in [116] is adopted because it is simple for implementation, fast and accurate for detection, and needless for extra sensors.

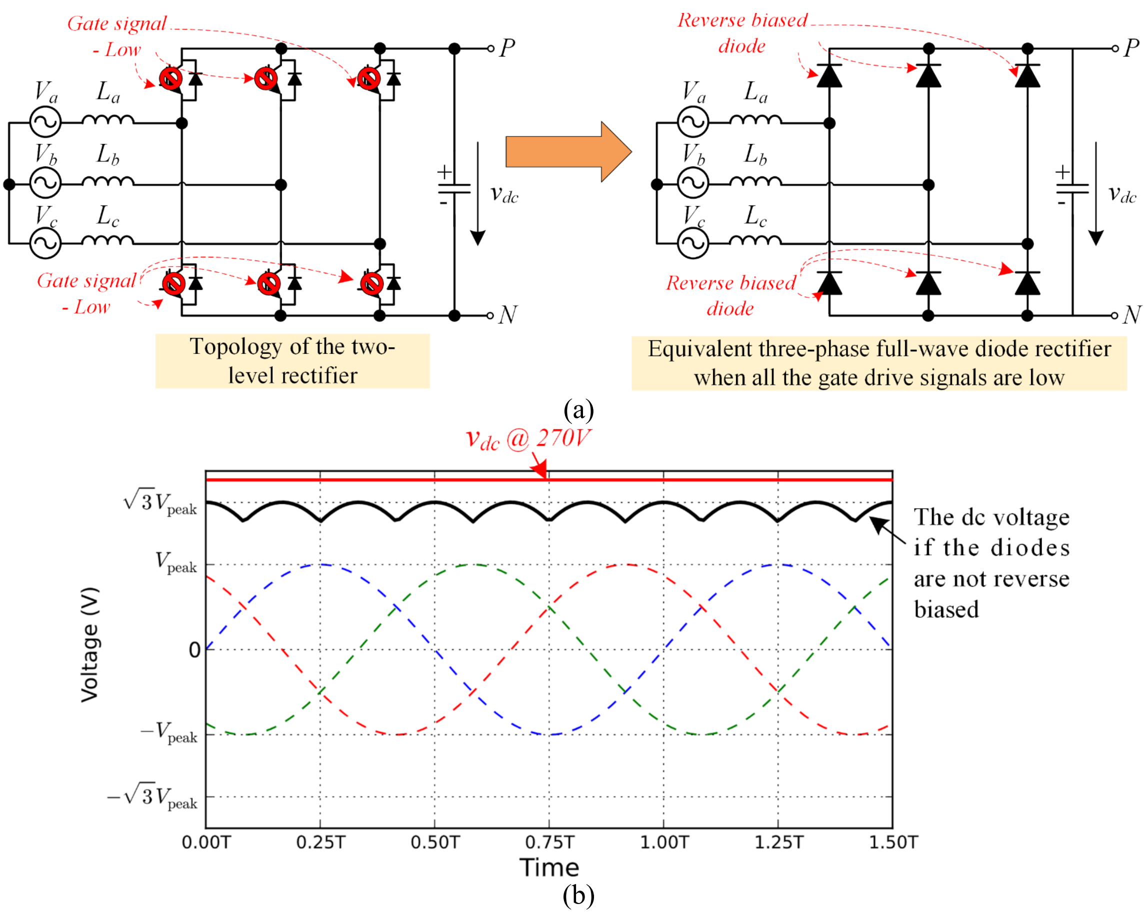

Figure 5.1. Emulation of the recitfeir failure. (a) Electrical diagram of the rectifier. (b) DC bus voltage and the rectifiered voltage.

The detection logic is straightforward: once a three-phase open circuit fault occurs, the phase currents drop to zero. This means that after coordinate transformations, the q-axis current i_q^{fdb} is also zero. However, in the digital controller, the output of the dc current controller, which is the reference of q-axis current i_q^{ref} is not zero. If the actual q-axis current i_q^{fdb} is zero whilst the gap between i_q^{ref} and i_q^{fdb} is larger than a defined threshold, the associated rectifier can be considered open circuited. The fault detection process is summarized in the flowchart as shown in Figure 5.2.

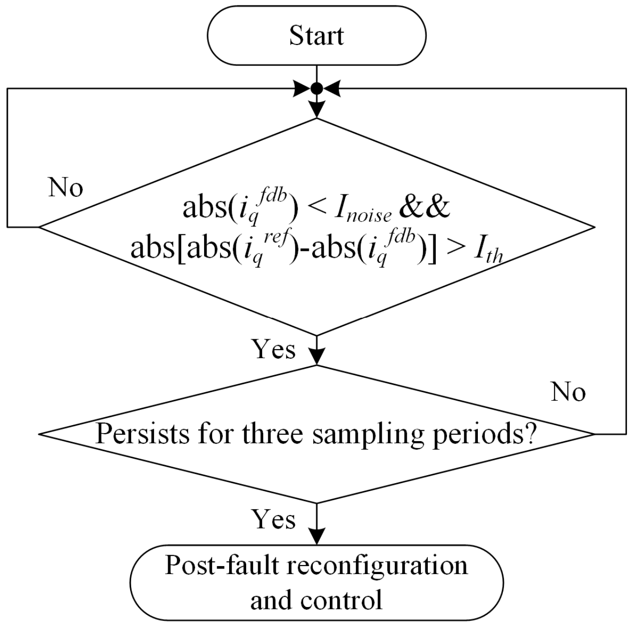

Figure 5.2. Flowchart of the open circuit fault detection method.

In Figure 5.2, I_{noise} is the noise tolerance for current measurement because even if in the open circuit condition where the actual i_q^{fdb} is zero, the measured i_q^{fdb} can still have some value due to noises. In this paper I_{noise} is designed as 0.2A. I_{th} is the threshold gap between abs(i_q^{ref}) and abs(i_q^{fdb}). In this paper I_{th} is set as 50%× abs(i_q^{fdb}). If the two conditions are met for more than three consecutive sampling periods, the fault detector will report an open circuit fault and the system is reconfigured for post-fault operation. The maximum detection delay is only three sampling periods. The detection sensitivity can be easily adjusted by tuning I_{noise} and I_{th}.

5.3 System Reconfiguration and Transition Scheme Considering the LP Rectifier Failure

The method of simulating the fault of the rectifiers and the fault detection method were introduced in the subsection 5.2. This section will focus on the detailed post-fault system reconfiguration and fault tolerant control in the case of the LPR failure. Investigation in the case of the HPR failure will be articulated in the next subsection.

Once a fault within the LPR is detected, the circuit breaker at the LPR's DC side will disconnect the LPR from the HVDC grid. The rest of the system will be reconfigured as shown in Figure 5.3. In the post-fault operation conditions, all the power of LPG is transferred to the HP channel and then fed to the main DC bus by the HPR. LPG will continuously supply power to the HVDC grid. The impacts of failure on electrical loads will need to be minimised with smooth reconfiguration transition.

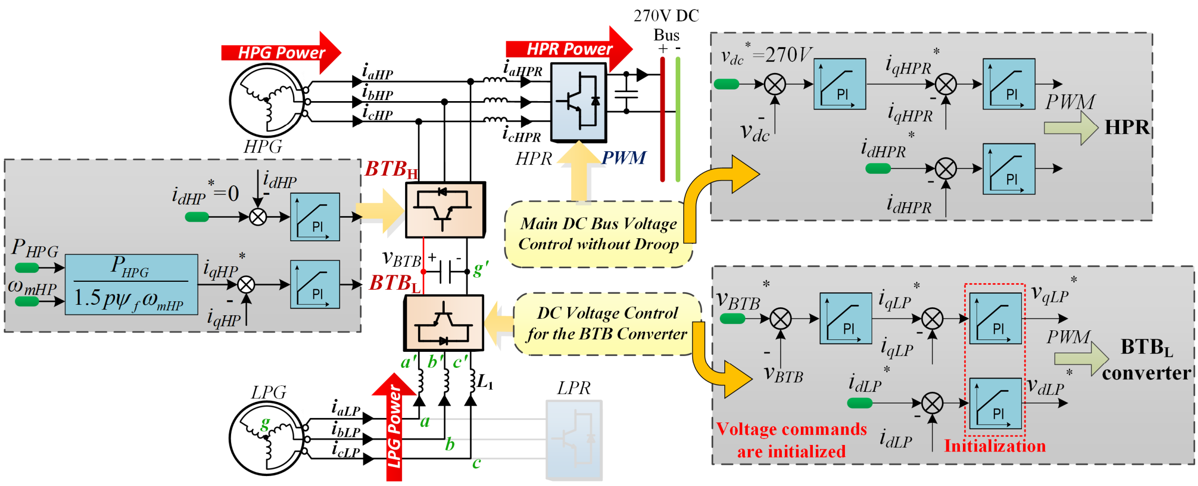

Figure 5.3. The power flow diagram and control schemes at LP rectifier fault.

After reconfiguration, the HPR control will be changed to stabilize the main DC bus voltage. As can be seen in Figure 5.3, the inner loop of HPR control is i_{dHPR} and i_{qHPR} control, where i_{dHPR} and i_{qHPR} are the currents (in dq frame) flowing into the HPR. The outer loop is to maintain the main DC bus at the reference level (270V in this case). The HPR's droop control used for power sharing is deactivated as the paralleled LPR is no longer available.

Since the LPR is disconnected, the phase current synchronization strategy for the BTB_L converter needs to be changed. The BTB_L converter will be running as an active front-end (AFE) to regulate the internal DC-link voltage v_{BTB} of the BTB converter. All the LPG's power will be routed through the BTB converter. Inner loop of the BTB_L converter includes i_{dLP} and i_{qLP} current controls. The outer loop is the DC-link voltage (v_{BTB}) control. For the BTB_H converter, the control scheme presented in section 4.2.2 is remained the same to regulate the active power of the HPG. To summarize, the BTB_L converter is used for stabilizing the DC-link voltage within the BTB converter, and the control for BTB_H converter is to regulate HPG's power.

Considering power flows, there are two essential electrical power sources in the reconfigured system, i.e., the HPG and the LPG. The HPG's power can be actively managed by controlling its torque as its speed is dependent on aircraft engines. The LPG's power is transferred from the LP to HP channel through the BTB converter. The LPG will need to automatically compensate the difference between total load power and HPG's power. The functions and control objectives before and after fault of each converter are summarized in Table 5-1.

Table 5-1. Functions and control objectives for each remaining converter when the LPR is disconnected due to fault.

Remaining power converter	Functions	Control objectives	
		Before fault	After fault
HPR	Delivering power to the main DC bus, feeding onboard loads.	Sharing load power under droop control	Stabilizing the main DC bus voltage to 270V
BTB_L converter	Providing an additional power flow path to the LPG when the LPR is disconnected.	Synchronize the phase currents and stabilizing the DC voltage of the BTB converter	Performing as an AFE to stabilize the DC-link voltage of the BTB converter
BTB_H converter	Controlling the operating state and power of the HPG.	Controlling the *dq*-axes currents of the HPG to generate active power P_{HPG}	Controlling the *dq*-axes currents of HPG to output power P_{HPG}

As can be seen in Figure 5.3, the terminals of the LPG are connected with the AC side of the LPR. Therefore, directly disconnecting the LPR from the HVDC grid when the LPR is detected faulty will result in an abrupt change of the LPG's terminal voltages and thus draw excessive currents from the LPG. The abrupt change of the stator currents, in return, will lead to an undesired or even oscillated torque. In the worst case, it might damage the LPG's mechanical transmission. To avoid this and to achieve a smooth transition from normal to post-fault operations, the terminal voltages of the LPG should remain unchanged during this transition. Since the LPG's AC terminals and the BTB_L converter's AC terminals are connected through L_1, in this case the LPG's terminal voltage will depend on current through L_1. Also, this current is controlled by the current loops of the BTB_L converter by manipulating its terminal voltage, in other words, maintaining the LPG's terminal voltages thus can be achieved by actively controlling the AC terminal voltages of the BTB_L converter through closed loop control and PWM techniques.

The equivalent circuit of LPG-BTB_L converter subsystem after fault is built as shown in Figure 5.4. The definitions of variables and nodes are shown in Figure 5.3, where v_{ag} is the phase-to-neutral voltage of LPG, $v_{a'g'}$ is the leg voltage of the BTB_L converter, L_1 and R_1 are the inductance and equivalent resistance of the filter whose voltage drop is $v_{aa'}$.

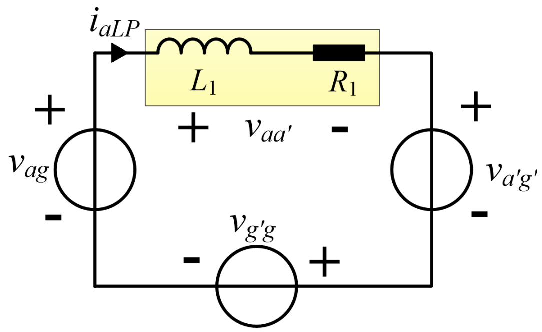

Figure 5.4. The equivalent circuit of a-phase of LPG-BTB_L converter subsystem.

Based on Figure 5.4, the following relationships can be derived:

$$\begin{cases} v_{xg} = R_1 i_{xLP} + L_1 \dfrac{di_{xLP}}{dt} + v_{x'g'} + v_{g'g},\ x = a,b,c & \text{(i)} \\ \sum\limits_{x=a,b,c} i_{xLP} = 0 & \text{(ii)} \\ \sum\limits_{x=a,b,c} v_{xg} = 0 & \text{(iii)} \end{cases} \quad (5\text{-}1)$$

Adding the three equations in (i) and considering (ii) and (iii), the voltage difference between the reference points *g'* at the BTB DC-link and the LP generator neutral point *g* can be obtained as

$$v_{g'g} = -\frac{1}{3}\sum_{x=a,b,c} v_{x'g'} \tag{5-2}$$

Applying *abc/dq* transformation to (5-1) and considering (5-2), the electrical relationship of the LPG-BTB_L converter subsystem can be derived as follows:

$$\begin{cases} v_{dLP} = R_1 i_{dLP} + L_1 \dfrac{di_{dLP}}{dt} + v_{dBTBL} - \omega_{eLP} L_1 i_{qLP} \\ v_{qLP} = R_1 i_{qLP} + L_1 \dfrac{di_{qLP}}{dt} + v_{qBTBL} + \omega_{eLP} L_1 i_{dLP} \end{cases} \tag{5-3}$$

where v_{dLP} and v_{qLP} are the LPG's *dq*-axes terminal voltages. v_{dBTBL} and v_{qBTBL} are the AC voltages of the BTB_L converter in the *dq* frame.

Using the first-order Taylor expansion, (5-3) can be discretised as follows:

$$\begin{aligned} \begin{bmatrix} v_{dBTBL}(k) \\ v_{qBTBL}(k) \end{bmatrix} = \begin{bmatrix} v_{dLP}(k) \\ v_{qLP}(k) \end{bmatrix} + \begin{bmatrix} -(R_1 + L_1/T_s) & \omega_{eLP}(k) L_1 \\ -\omega_{eLP}(k) L_1 & -(R_1 + L_1/T_s) \end{bmatrix} \begin{bmatrix} i_{dLP}(k) \\ i_{qLP}(k) \end{bmatrix} + \\ \begin{bmatrix} L_1/T_s & 0 \\ 0 & L_1/T_s \end{bmatrix} \begin{bmatrix} i_{dLP}(k-1) \\ i_{qLP}(k-1) \end{bmatrix} \end{aligned} \tag{5-4}$$

where T_s is the sampling period. *k* is the index of sample.

As mentioned before, the core of smooth transition control is to ensure that the terminal voltages of LPG remain unchanged before and after change of control scheme for the BTB_L converter. Thus, assuming a fault occurs to the LPR in the $(k)_{th}$ sampling interval, a seamless transition requires

$$v_{dLP}(k) = v_{dLP}^{*}(k-1) \quad v_{qLP}(k) = v_{qLP}^{*}(k-1) \tag{5-5}$$

As long as the appropriate initialized voltages are applied to the BTB converter, a smooth transition from the healthy to post-fault operation state can be achieved. This can be seen from the simulation results in later sections and the experimental results in Chapter 7.

Using (5-4) and (5-5), the BTB$_L$ converter voltage commands at time $(k)_{th}$, i.e., $v_{dBTBL}(k)$ and $v_{qBTBL}(k)$, can be derived. The implementation of such a transient control is shown in Figure 5.5. Within the digital controller, in each sampling interval, a few events will be implemented in sequence, i.e., fault detection and protection, control scheme application and update the PWM registers based on dq-axes voltage commands. At each sampling interval, $v_{dLP}^*(k\text{-}1)$, $v_{qLP}^*(k\text{-}1)$, $i_{dLP}(k\text{-}1)$, $i_{qLP}(k\text{-}1)$, $i_{dLP}(k)$, and $i_{qLP}(k)$ are stored and updated. With these stored values and the relation in (5-5), voltage commands for the BTB$_L$ converter, i.e., $v_{dBTBL}(k)$ and $v_{qBTBL}(k)$, can thus be calculated using (5-4). This process is indicated by the star #1 in Figure 5.5.

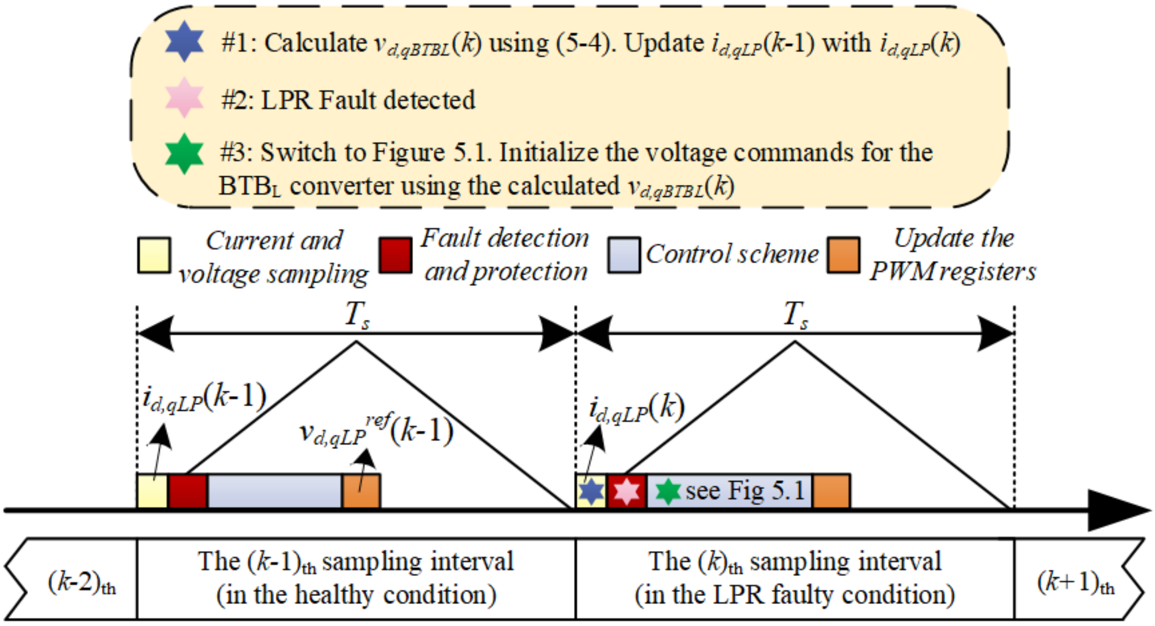

Figure 5.5. Schematic diagram of program execution.

Once the fault has been detected and captured by the controller in the $(k)_{th}$ sampling interval, denoted as #2, the system will be reconfigured and the BTB$_L$ converter control scheme is changed from Figure 4.3 to that in Figure 5.3 within the control scheme application cycle in #3. The voltage commands for the BTB$_L$ converter are set to the calculated $v_{dBTBL}(k)$ and $v_{qBTBL}(k)$ using (5-4) and (5-5). Using these revised $v_{dBTBL}(k)$ and $v_{qBTBL}(k)$ to initialize the voltage commands for the BTB$_L$ converter will help avoid an abrupt change of the LPG's currents.

5.4 System Reconfiguration and Transition Scheme Considering the HP Rectifier Failure

The system reconfiguration and fault tolerant control in the case of the LPR failure has been thoroughly analysed in 5.3. However, due to the different locations of the inductors L_1 and L_2, the system reconfiguration and fault tolerant control tailored for the LPR failure cannot be applied to the case of the HPR failure. This section is dedicated to address this issue.

In the case of HPR failure, it can be disconnected from the system and the rest of system is reconfigured to a structure shown in Figure 5.6, where the control schemes for each converter are exhibited. In normal operation conditions, the HPG's power is delivered to the main DC bus through the HPR. In this post-fault operation conditions, all the HPG's power is transferred to the HVDC bus through the BTB converter and then the LPR.

Within this post-fault architecture, the LPR is controlled to stabilize the main DC bus voltage. The LPR inner control loop is a current loop of i_{dLPR} and i_{qLPR}, the outer loop is to maintain the HVDC bus voltage. The droop control used for power sharing for the LPR is deactivated as the paralleled HPR is unavailable in this scenario.

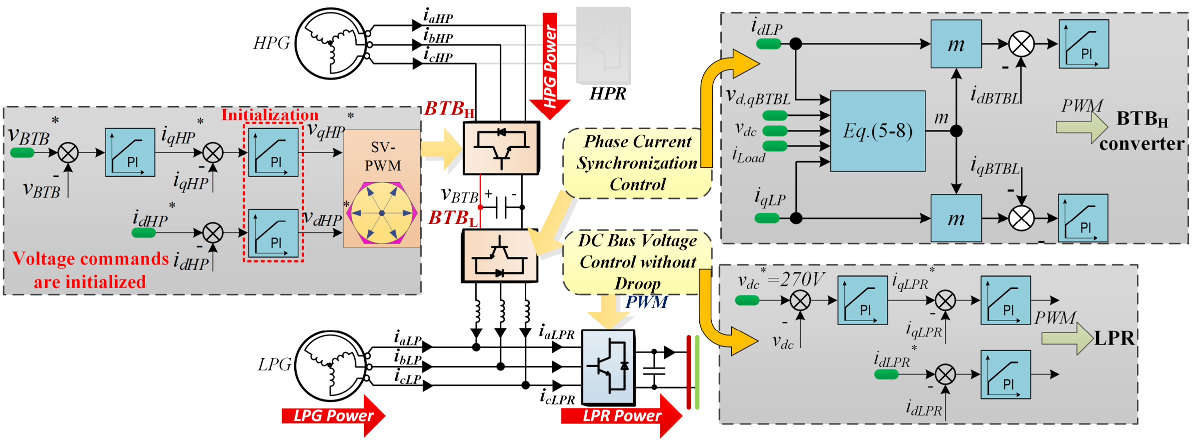

Figure 5.6. The power flow diagram and control schemes at the HP rectifier fault.

Since the power flow direction is from the HP to the LP channel through the BTB converter, control of the BTB_H converter is changed to regulate the internal DC-link voltage (which used to be the BTB_L converter for this function when the LPR fails). As can be seen in Figure 5.6, while the inner loop of the BTB_H converter is still the i_{dHP} and i_{qHP} current control, the outer loop is changed to the DC-link voltage v_{BTB} control. For the BTB_L converter, the proposed phase current synchronization strategy shown in Figure 4.3 will be used. However, the method to derive the control gain 'm' is different from that in Figure 4.3.

In the control schemes shown in Figure 5.6, the relations of power flow are used to derive the control gain m for the BTB_L converter. Details are presented as follows. From the viewpoint of power, the power delivered by the BTB converter from the HP to LP channel essentially comes from the HPG. Assuming the targeted power ratio between the LPG and HPG is ρ_{LP} : ρ_{HP}, then following relation can be derived

$$\frac{3}{2}\left(v_{dBTBL}i_{dBTBL} + v_{qBTBL}i_{qBTBL}\right) = \frac{\rho_{HP}}{\rho_{LP}+\rho_{HP}}P_t \tag{5-6}$$

where P_t is the total load power. It can be obtained by the measured DC voltage v_{dc} and load current i_{Load}, where $P_t = v_{dc} \cdot i_{Load}$. The left side of (5-6) is the power transferred through the BTB converter, and the right side of (5-6) is the power of the HPG.

Applying the power relation equation (4-1) into (5-6), it can be rewritten as:

$$\frac{3}{2}m\left(v_{dBTBL}i_{dLP} + v_{qBTBL}i_{qLP}\right) = \frac{\rho_{HP}}{\rho_{LP}+\rho_{HP}}v_{dc}i_{Load} \tag{5-7}$$

With the defined power ratio ρ_{LP} and ρ_{HP}, the gain m can be calculated as follows:

$$m = \frac{2\rho_{HP}v_{dc}i_{Load}}{3\left(v_{dBTBL}i_{dLP} + v_{qBTBL}i_{qLP}\right)\left(\rho_{LP}+\rho_{HP}\right)} \tag{5-8}$$

The control scheme for the BTB_L converter under the HPR faulty scenario can thus be given as the structure shown in Figure 5.7. The functions and control objectives before and after HPR fault for each converter are presented in Table 5-2.

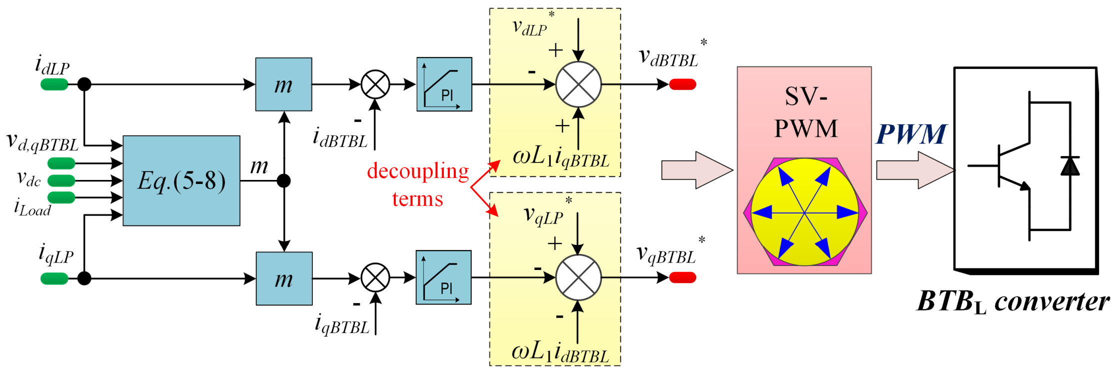

Figure 5.7. Control scheme for the BTB_L converter under HPR faulty scenario.

Table 5-2. Functions and control objectives for each remaining converter when the HPR is disconnected due to fault.

Remaining power converter	Functions	Control objectives	
		Before fault	After fault
LPR	Delivering power to the main DC bus, feeding onboard loads.	Sharing load power under droop control	Stabilizing the main DC bus voltage to 270V (see Figure 5.6)
BTB_L converter	Controlling the amount of power drawn from HPG.	Synchronize the phase currents and stabilizing the DC voltage of the BTB converter	Managing how much power is extracted from the HPG the by controlling the gain m (see Figure 5.6)
BTB_H converter	Providing an additional power flow path to the HPG when the HPR is disconnected.	Controlling the dq-axes currents of the HPG to output power P_{HPG}	Performing as an AFE to stabilize the internal DC-link voltage within the BTB converter (see Figure 5.6)

As can be seen, the control scheme will be changed for the BTB_H converter before and after the HPR fault. Since the terminals of the HPG are directly connected with the BTB_H converter, to avoid the abrupt change of the HPG's currents when switching control schemes for the BTB_H converter, the voltage commands in the new control scheme in Figure 5.6 needs to be initialized. Similar to that process after the LPR fault, to achieve a seamless transition before and after the HPR fault, terminal voltages of the HPG during transition should remain the same. Assuming at $(k\text{-}1)_{th}$ interval, the voltage commands of healthy state control scheme are $v_{dHP}^*(k\text{-}1)$ and $v_{qHP}^*(k\text{-}1)$. At the $(k)_{th}$ sampling interval, a fault occurs to the HPR and it is disconnected from the system. The system is reconfigured to Figure 5.6**.** The voltage commands of the new control scheme for the BTB_H converter are initialized as $v_{dHP}^*(k\text{-}1)$ and $v_{qHP}^*(k\text{-}1)$, respectively.

5.5 Simulation Results

In this section, the proposed fault tolerant control for the APGC in both cases of the LPR failure and HPR failure are investigated. As will be introduced in Chapter 7, a downscaled lab prototype of the APGC is built for experimental verification. The power rating and settings for simulations in this chapter are consistent with the lab prototype and experimental results in Chapter 7.

The characteristics that will be checked in this subsection are included in Table 5-3.

Table 5-3. The core characteristics and variables that will be checked in simulation.

Point 1	• The main DC bus voltage v_{dc}, and the DC currents of the LPR and HPR, i_{dcLP} and i_{dcHP}. This is used to check the effectiveness of the essential main DC bus voltage control and the droop control.
Point 2	• In the case of triggering the open-circuit fault for the LPR, investigating whether system reconfiguration and fault tolerant control in Section 5.3 can ensure that the two generators continue operating, and all the power is delivered to the DC bus through the remaining HPR. Moreover, during the transition from the healthy state to the post-fault operation state, checking whether the LPG's phase current using the voltage command initialization strategy in Section 5.3 can be smoother than not using the initialization strategy.
Point 3	• In the case of triggering the open-circuit fault for the HPR, investigating whether system reconfiguration and fault tolerant control in Section 5.4 can ensure that the two generators continue operating, and all the power is delivered to the DC bus through the remaining LPR. Moreover, during the transition from the healthy state to the post-fault operation state, checking whether the HPG's phase current using the voltage command initialization strategy in Section 5,4 can be smoother than not using the initialization strategy.
Point 4	• Checking whether the power flow of the generators, rectifiers and the BTB converter follows the designed relation.

5.5.1 LPR Channel Failure

In this simulation study, the APGC starts running under a normal operation condition. A load change is then applied from the start of scenario to test the power control in a healthy condition before the LPR failure. The APGC supplies a 40Ω CIL through the HVDC bus. At t=1.5s, a CPL is applied increasing the total load power to 3.3kW. At t=2s, PWM signals for the LPR are disabled to simulate the LPR faulty scenario. Meanwhile, the fault tolerant control is activated. By disabling the PWM signals, the LPR is unable to deliver power to the HVDC bus. Hence, the LPR can be regarded as disconnected from the HVDC bus. For the results in Figure 5.8, the voltage command initialization method is not applied. Currents are normalized into per-unit (pu) where the benchmark current for the lab prototype is 35A.

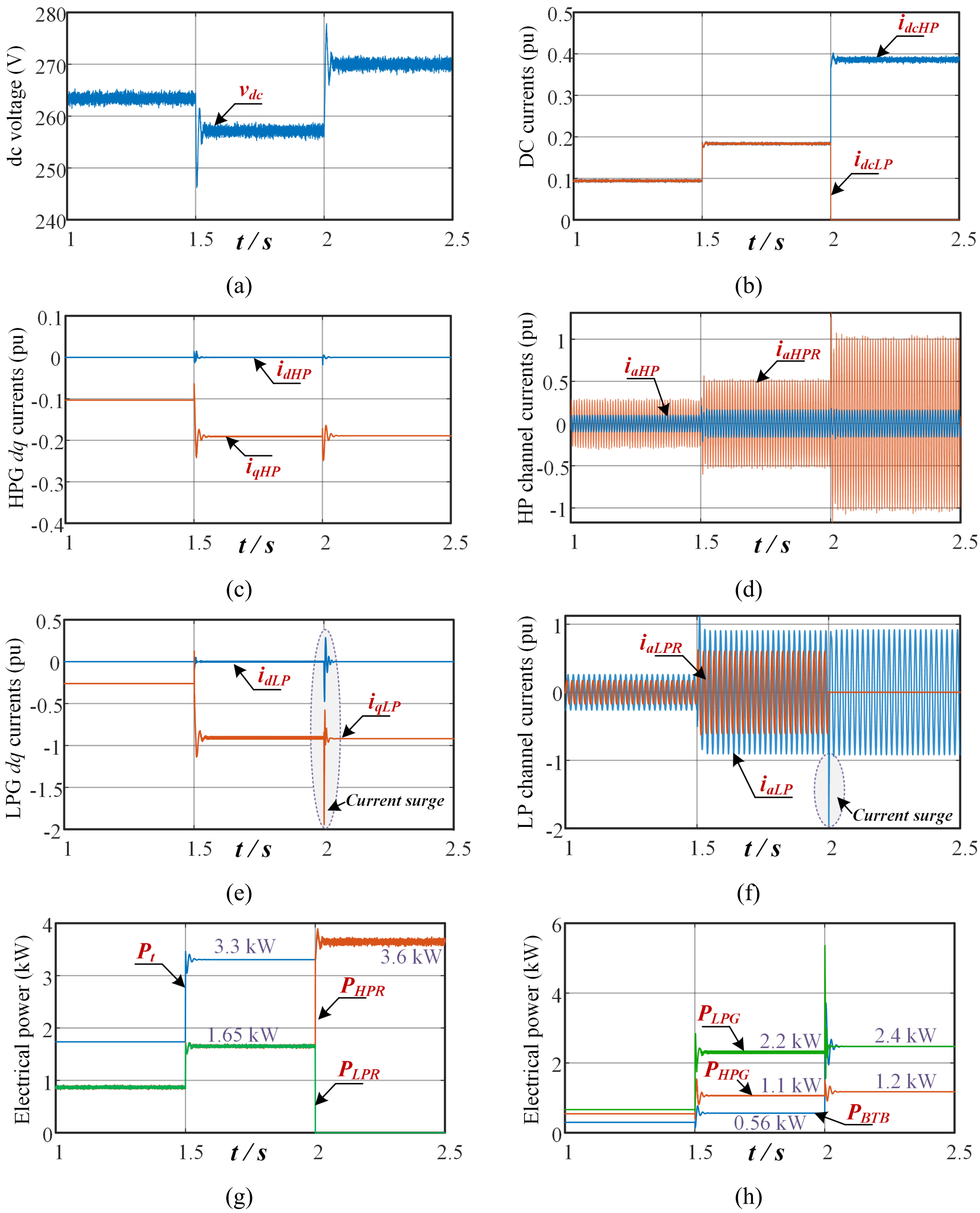

Figure 5.8. Simulation results in the scenario of disabling the LPR without voltage command initialization. (a) DC bus voltage v_{dc}. (b) DC currents of rectifiers i_{dcLP} and i_{dcHP}. (c) dq currents of the HPG. (d) phase currents of the HPG and HPR. (e) dq currents of the LPG. (f) phase currents of the LPG and LPR. (g) Total load power; output powers of the HPR and LPR. (h) Powers of the LPG, HPG, and BTB converter.

The main DC bus voltage v_{dc} is presented in Figure 5.8(a). It can be seen that v_{dc} deviates from the reference (270V) due to the application of droop control. With the increase of load power at t=1.5s, the deviation becomes larger and more DC current will be supplied to the HVDC bus from the HPR and LPR. Following disabling of the LPR's PWM signals at t=2s, only the HPR is left in the system and there is no need for droop control. Therefore, v_{dc} is restored to the rated value 270V.

DC currents of the HPR and LPR are shown in Figure 5.8(b). During this test case, the droop gains of these two converters are initially set to be identical. As a result, before the fault happens at t=2s, the DC current of the HPR i_{dcHP} equals to that of the LPR i_{dcLP}. When disabling the PWM for the LPR at t=2s, the LPR can be regarded as disconnected hence i_{dcLP} is zero. All the power is delivered by the remaining HPR, thus i_{dcHP} doubles in this case from 0.19 pu to around 0.38 pu. Hence, the first point in the checklist in Table 5-3 is validated, confirming the effectiveness of the DC bus voltage control and the droop control.

The *dq* currents of the HPG and phase currents of the HP channel are exhibited in Figure 5.8(c) and (d). It can be seen that the *d*-axis current of the HPG is kept to zero. As the increase of load power at t=1.5s, the magnitude of *q*-axis current of HPG also increases. The steady state values of i_{qHP} during t=1.5s to 2s and after t=2s are the same, which means that removal of the LPR does not affect the steady-state operation of the HPG. This can also be observed from the unchanged HPG's phase current i_{aHP}. Since both the HPG and LPG powers are directed to the HPR, the magnitude of the HPR's phase current i_{aHPR} increases significantly after fault happens t=2s.

The *dq* currents of the LPG and phase currents of the LP channel are given in Figure 5.8(e) and (f). It can be seen that the phase current of the LPR is zero after t=2s because of the disconnection of the LPR. The steady-state *q*-axis current and phase current of the LPG are kept unchanged after t=2s. However, since the voltage command initialization for the BTB_L converter is not considered, current surge occurs in the transient process, which will lead to undesirable torque on the LPG and trigger overcurrent protection of the system. From Figure 5.8(c)-(f), the second point in Table 5-3 is validated, confirming that in the case of the LPR failure, the system reconfiguration and fault tolerant control can ensure the generators continue operating as normal.

Electrical powers of the HPR (P_{HPR}), LPR (P_{LPR}), HPG (P_{HPG}), LPG (P_{LPG}) and total load power (P_t) during the simulation scenario are shown in Figure 5.8(g) and (h). Before t=2s, P_{HPR} and P_{LPR} are both 1.65kW due to identical droop gains. At t=2s, PWM signals for the LPR are disabled, hence P_{LPR} =0 and $P_{HPR} = P_t$. The power ratio between the LPG and HPG is set as 2:1. Hence, power of the HPG is one-third of total power P_t. Before the fault happens at t=2s, P_{BTB} = HPR Power - HPG Power = $({}^1\!/_2 - {}^1\!/_3)P_t$ = 0.56kW. After t=2s, the total power increases to 3.6kW as v_{dc} increases to 270V. All the power of LPG is transferred by the BTB converter, hence, $P_{LPG} = P_{BTB}$ = 2.4kW.

To diminish the current surge during the transition of disabling the LPR, the voltage command initialization strategy proposed in Section 5.3 is applied and results are shown in Figure 5.9.

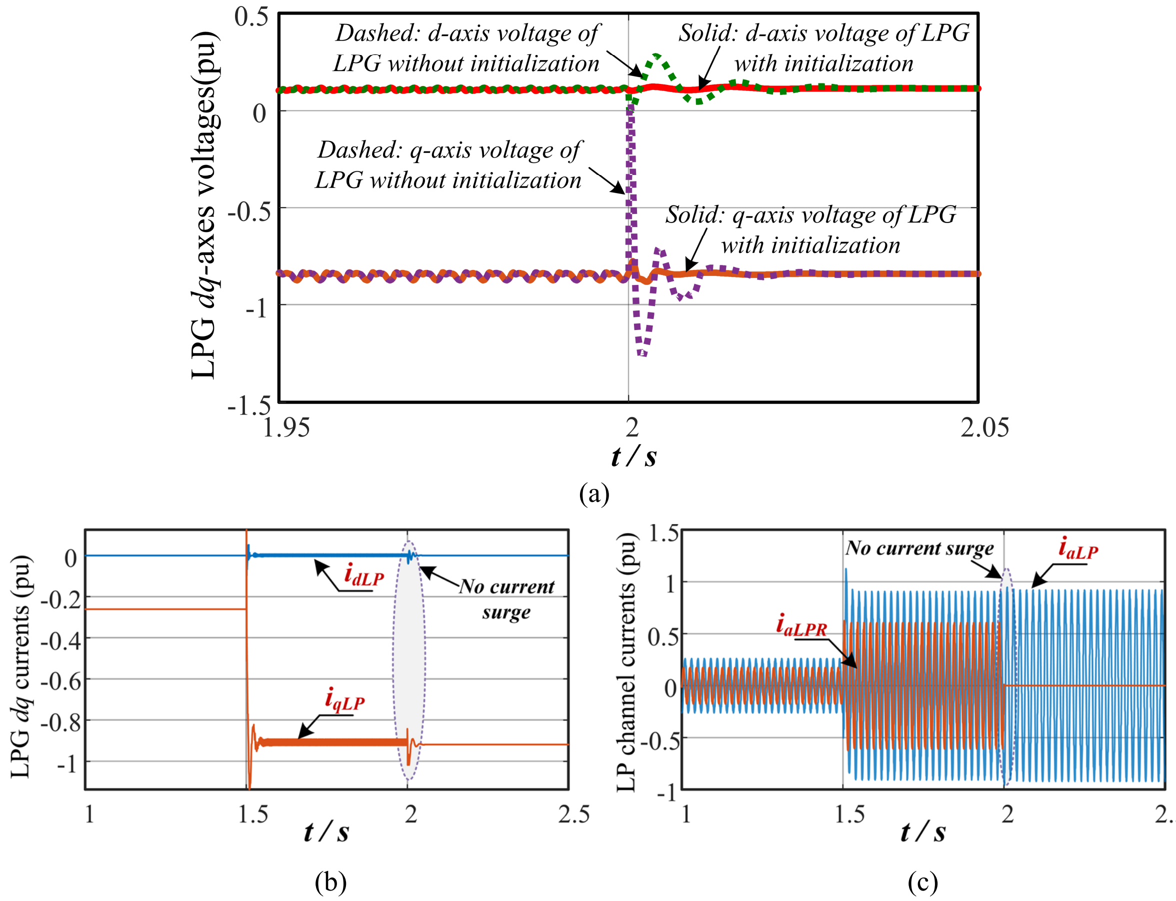

Figure 5.9. Simulation results with voltage command initialization. (a) comparison of *dq* voltages of the LPG with and without voltage command initialization. (b) *dq* currents of the LPG with initialization. (c) phase currents of the LPG and LPR with initialization.

It can be seen from the dashed lines in Figure 5.9(a) that without initialization, the *dq* voltages of the LPG restore to zero volts at t=2s because of switching to a new control scheme for the BTB_L converter. The oscillated *dq* voltages will lead to oscillated currents. This is the reason for the current surge seen in Figure 5.8(e) and (f). As a comparison, the solid lines show the *dq* voltages when the smooth transition scheme is applied after fault happens. Consequently, comparing with Figure 5.8(e) and (f), the currents in Figure 5.9(b) and (c) transit smoothly with negligible current surge at t=2s. The results confirm the effectiveness of the proposed seamless transition control and thus the second point in the Table 5-3 is validated.

5.5.2 HPR Channel Failure

Simulation results for the HPR fault scenario are demonstrated in Figure 5.10. The operation timeline is presented as follows: t=1s-1.5s, the DC bus is loaded with a 40Ω CIL. From t=1.5s to 2s, the load power increases to 3.3kW using a CPL. At t=2s, the PWM signals for the HPR are disabled to emulate the HPR faulty scenario.

Performance of the main DC bus voltage control is presented in Figure 5.10(a). Here, v_{dc} deviates from the reference 270V due to the application of droop control. As disabling the PWM signals for the HPR at t=2s, only the LPR is left in the system and the droop control is removed. Therefore, v_{dc} is restored to the rated value 270V.

For the DC currents demonstrated in Figure 5.10(b), since the two droop gains are identical, hence before t=2s, $i_{dcHP} = i_{dcLP}$. At t=2s, i_{dcHP} changes to zero because the PWM drive signals for the HPR are disabled. Hence, HPR can be regarded as disconnected from the DC bus. Hence, the first point in the Table 5-3 is validated, proving the effectiveness of the DC bus voltage control and the droop control.

The *dq* currents of the HPG and phase currents of the HP channel are presented in Figure 5.10(c) and (d). It can be seen that the phase current of HPR, i_{aHPR}, is zero after t=2s due to disabling the HPR. The values of other currents are kept unchanged after the HPR fails, which means the operation of the HPG are not affected. However, since the voltage command initialization for the BTB$_H$ converter is not considered, current surge of the HPG can be observed in the transient process.

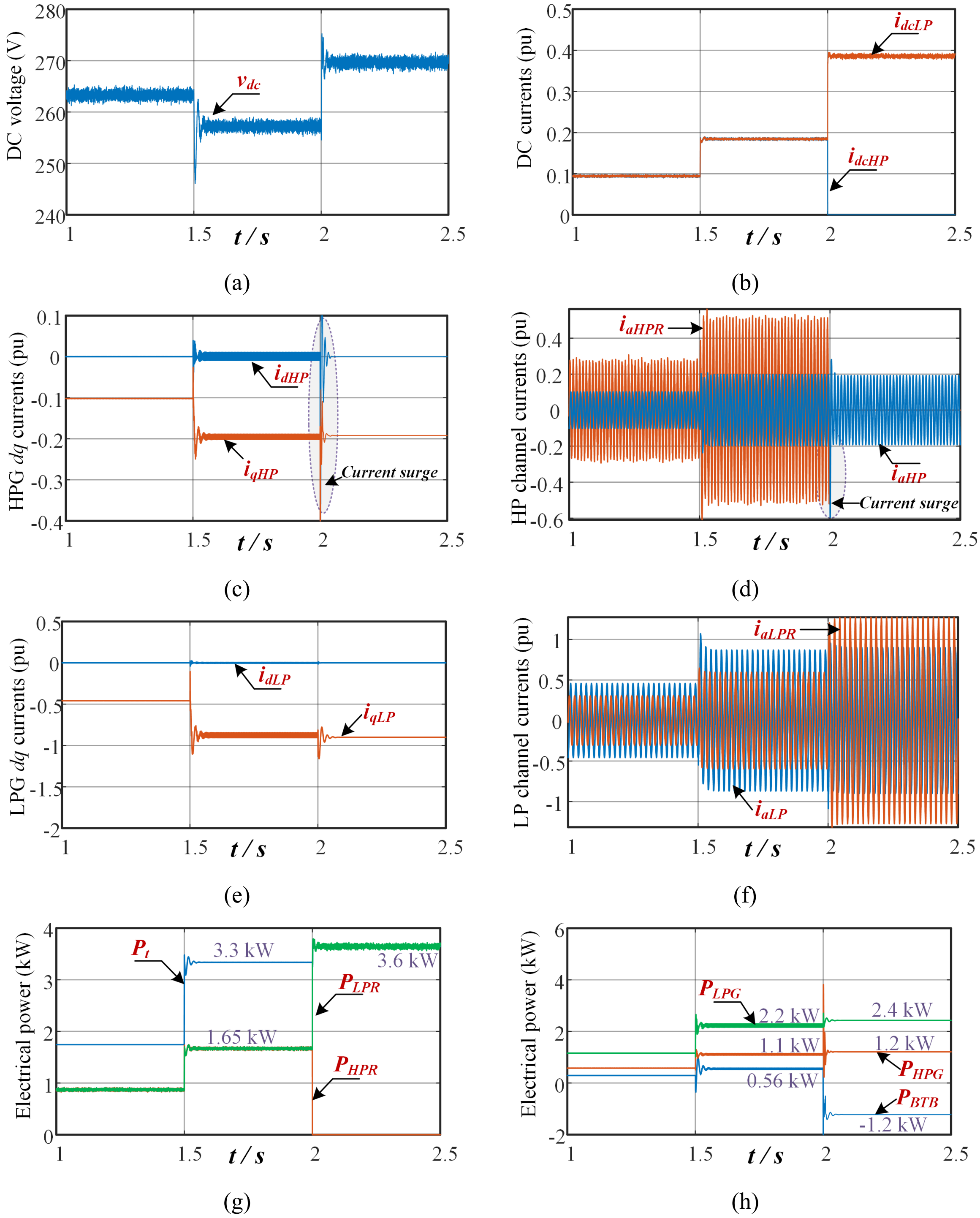

Figure 5.10. Simulation results in the scenario of disabling the HPR without voltage command initialization. (a) DC voltage v_{dc}. (b) DC currents of the rectifiers i_{dcLP} and i_{dcHP}. (c) dq currents of the HPG. (d) phase currents of the HPG and HPR. (e) dq currents of the LPG. (f) phase currents of the LPG and LPR. (g) Load power, powers of HPR and LPR. (h) Powers of the LPG, HPG, and BTB converter.

The *dq* currents of the LPG and phase currents of the LP channel are exhibited in Figure 5.10(e) and (f). From Figure 5.10(e) it can be concluded that operation of the LPG keeps the same as that in the healthy state. Figure 5.10(f) shows that before t=2s, the magnitude of i_{aLPR} is smaller than i_{aLP} because the BTB converter transfers power from the LP to HP channel. However, after t=2s, the HPG outputs power to the LP channel through the BTB converter, making the magnitude of i_{aLPR} larger than that of i_{aLP}. From Figure 5.10(c)-(f), the third point in the checklist Table 5-3 is validated, confirming that in the case of the HPR failure, the system reconfiguration and fault tolerant control in Section 5.4 can ensure that the two generators continue operating as normal.

Electrical powers are given in Figure 5.10(g) and (h). Before t=2s, P_{HPR} and P_{LPR} are 1.65kW, achieving an equal power sharing. At t=2s, the PWM driving signals for HPR are disabled, hence P_{HPR} =0 and P_{LPR} = P_t = 3.6kW. Power ratio between the LPG and the HPG is set as 2:1. Hence, power of the HPG is one-third of the total power P_t. The BTB converter carries all the 1.2kW power of the HPG. A negative power of P_{BTB} means that this power is transferred from the HP channel to the LP channel.

The voltage command initialization strategy proposed in Section 5.3 is tested to limit the current surge in the transition of disabling the HPR. As can be seen from the dashed lines in Figure 5.11(a), without initialization, the *dq* voltages of the HPG change to zero volts at t=2s and then oscillate because a new control scheme is applied to the BTB_H converter. These oscillated voltages lead to current surge in Figure 5.10(c) and (d). However, with the voltage initialization, the voltages of HPG transit smoothly at t=2s. Therefore, Figure 5.11(b) and (c) show much smoother current performance than those in Figure 5.10(c) and (d). This means that the voltage initialization method in Section 5.4 can effectively ensure a smooth transition, and hence the third point in the checklist Table 5-3 is validated.

The main advantages of the proposed solution that have been simulatively validated can be highlighted as follows:

- After the HPR or LPR failure, through system reconfiguration and fault tolerant control, the BTB converter can provide a power flow path to the generator of the failed channel. The generator associated with the faulty rectifier can supply continuous power through the BTB converter to the healthy rectifier and then to the

DC bus. In this way, the generator can provide power to the load without interruption, which ensures a reliable power supply capability and this is proved beneficial to the stability of the engine.

- To avoid the current surge of the generator's current during the transition from the normal operation to post-fault operation, a smooth transition strategy is proposed where the voltage command is properly initialized when switching to a new controller of the BTB converter.

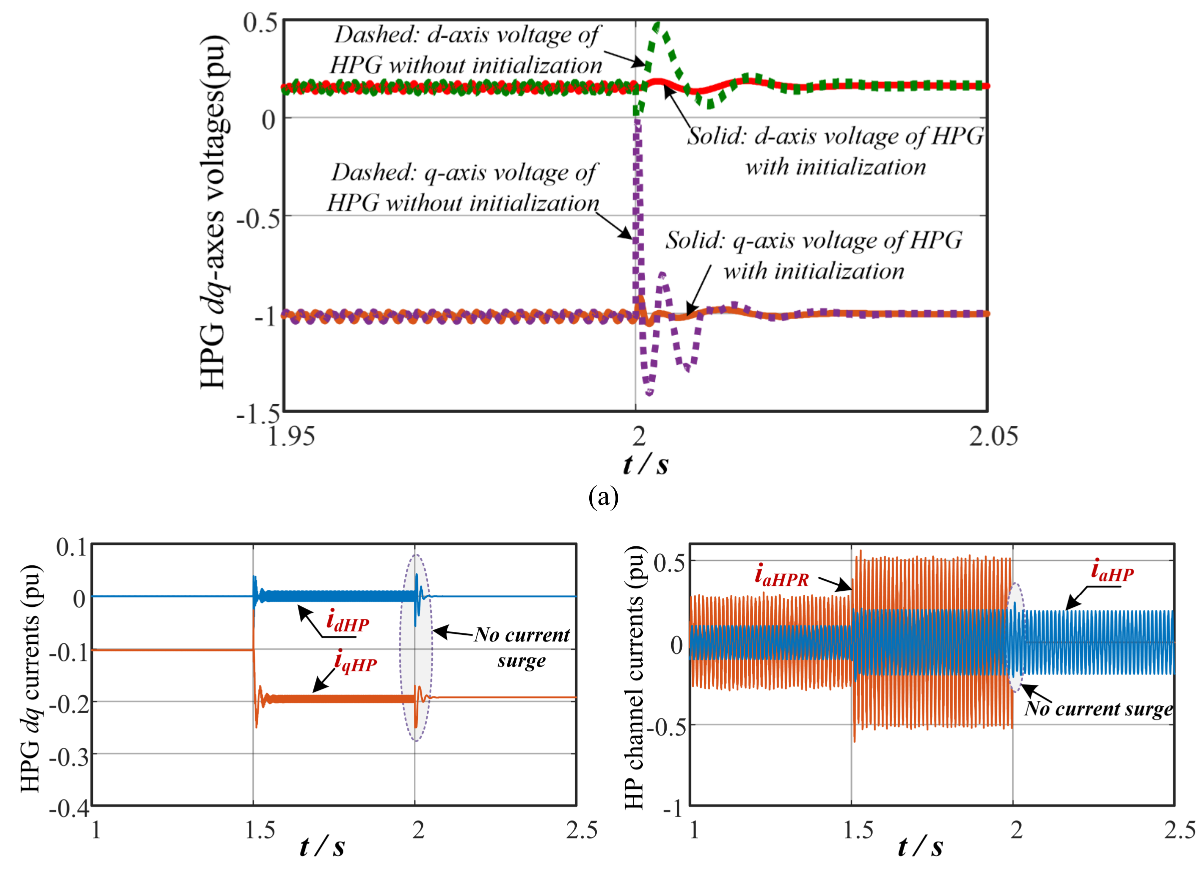

Figure 5.11. Simulation results with voltage command initialization. (a) comparison of *dq* voltages of the HPG with and without voltage command initialization. (b) *dq* currents of the HPG with initialization. (c) phase currents of the HPG and HPR with initialization.

5.5.3 Engine Performance Comparison using Different Power Generation Centre Architectures

To study the impact of main AC/DC rectifier failure on engine performances with both the PGC and the APGC, a multi-spool turbofan model has been developed using the intercomponent volume method and CFM56-3 engine maps [73], [74]. The cruise mode is studied because cruising usually takes most of a flight. The altitude is assumed 39kft and the Mach number is 0.79. The speed of LPS is fixed to provide a constant thrust. The operating points are shown in Figure 5.12, where points A and B indicate that the engine operates with the PGC and the proposed APGC, respectively. LPR is consdiered faulty and disabled.

As proved in the previous subsections, with the APGC, the operating states of the LPG and HPG are not affected when disabling the LPR. However, with the PGC, disabling the LPR will make the remnant HPR to feed all the load power. As a result, the HPG extracts more mechanical power from the HP spool of engine, decreasing the rotary speed of the HP spool. Since the high-pressure compressor (HPC) is coupled with HP spool, the speed of HPC is also reduced, leading to a decreased mass flow demand. In this case, HPC acts as a blockage for rear side of low-pressure compressor (LPC), pushing the LPC to decrease its mass flow. Consequently, the pressure ratio of the LPC will increase and the operating point will move close to the surge line on compressor map. This is the reason why the operating points in Figure 5.12 move from B to A.

Comparing point B with A, it can be seen that when LPR is faulty and disabled, the proposed APGC can provide a larger compressor surge margin than the PGC does. Larger surge margin means larger stability margin of engine. Therefore, the proposed APGC is a favourable option considering the safe operation of engine.

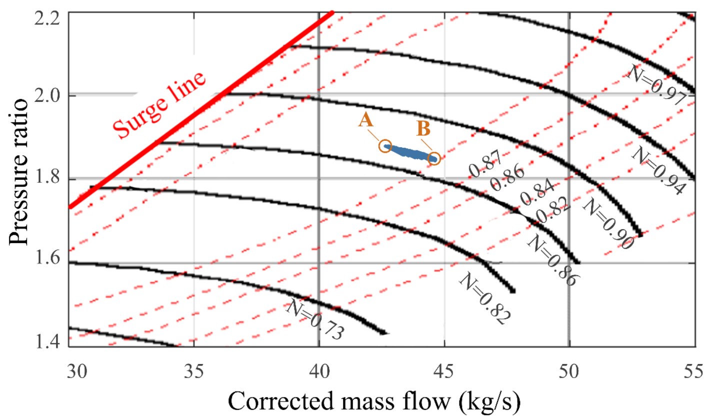

Figure 5.12. LPC map and operating points in the cruise mode (39kft, Mach number =0.79).

5.6 Chapter Summary

In this chapter the fault tolerance capability of the APGC dealing with the main AC/DC rectifier failure is investigated. The proposed APGC allows post-fault operation when one of the main rectifiers fails through reconfiguration of the system. The back-to-back converter provides an additional power flow path for the generators when the one of the main rectifiers is faulty. Fault tolerant control schemes for the APGC are tailored considering both cases of the HP rectifier and LP rectifier failure. Voltage command initialization strategies are proposed to avoid the abrupt change of generator current and current surge when the rectifiers become faulty and being disabled. Simulation results verify the fault tolerance improvement of the proposed APGC compared with the PGC and the effectiveness of proposed control schemes. Experimental verification will be carried out in Chapter 7.

Chapter 6. Enhancement of Stability of both the Onboard HVDC Grid and the Engine Using the Proposed APGC

In this chapter, the stability of HVDC grid with different power sharing ratios between the HPR and LPR is analysed in detail. Analytical findings reveal that the stability of the droop control based HVDC grid is related to the power sharing ratio between the HPR and the LPR. Increasing the proportion of the LP channel's power improves the HVDC grid stability. However, as it will be shown in this chapter, increasing the LP to HP power ratio degrades the engine stability in certain engine operation modes. The proposed APGC can address this conflict, improving the stability of both engine and HVDC grid by transferring some part of the HP power to the LP channel through the BTB converter. The theoretical ground and methodology on employing the APGC to enhance stability of both HVDC grid and engine are delivered by this chapter.

6.1 Introduction

The power flow diagram of PGC in the coordinated power offtake mode is shown in Figure 6.1. The electrical power that the HPR delivers to the DC bus is converted from the mechanical power of the HPS. The electrical power that the LPR delivers to the DC bus comes from the mechanical power of the LPS of the engine. In this configuration, in both LP and HP power generation channels the electrical power of the main AC/DC rectifiers is equivalent to the mechanical power (assuming negligible power losses) of engine spools is defined as "Power Coupling Effect", which is

HP Channel: Electrical Power of the HPR = Extracted Mechanical Power of the HPS

LP Channel: Electrical Power of the LPR = Extracted Mechanical Power of the LPS

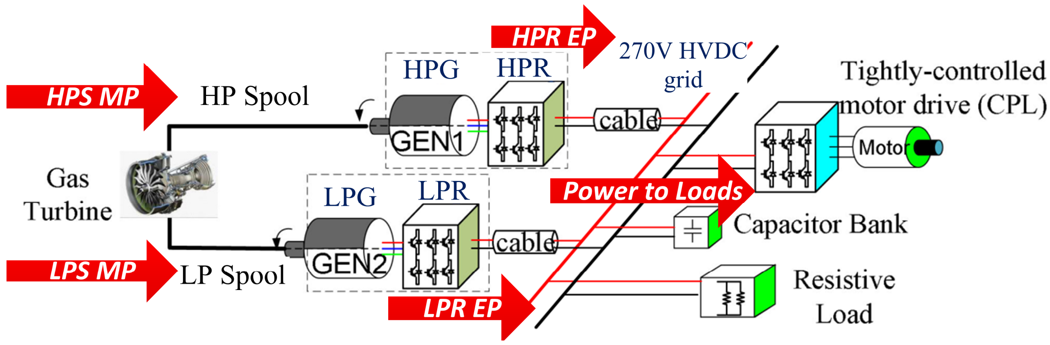

Figure 6.1. Power flow diagram of the PGC. MP: mechanical power; EP: electrical power.

The Power Coupling Effect makes the HVDC grid stability and the engine stability show the opposite trend. Improving one of the stabilities will degrade the other. For maintaining stability of the HVDC gird, this chapter proves that the LPR is expected to feed more electrical power than the HPR to the DC bus. In the PGC, this means that more mechanical power is extracted from the LPS than HPS. However, in the high-power settings of engine, such as maximum take-off and top of climb, more mechanical power needs to be extracted from the HPS than the LPS to avoid the overspeed and potential instability of the HPS [73], [74]. Apparently, the PGC in Figure 6.1 cannot handle this conflict.

The proposed APGC with an AC/AC bridging converter provides the flexibility to address the Power Coupling Effect and achieve stability improvement for both engine and HVDC grid simultaneously. The BTB converter connects the AC terminals of the LPG and HPG. It can transfer power between the HP and LP power generation channels. From the viewpoint of power, as can be seen from the arrows in Figure 6.2, the proposed APGC has the following feature (MP: mechanical power; EP: electrical power):

HP Channel: HPS's extracted MP = HPG's EP = HPR's EP +/- BTB's EP

LP Channel: LPS's extracted MP = LPG's EP = LPR's EP -/+ BTB's EP

From the relation it can be seen that the BTB converter can be regarded as a power decoupling bridge. More mechanical power can be extracted from the HPS than the LPS for preventing the overspeed of the HPS. On the other hand, the LPR can share more power than the HPR to improve the HVDC grid stability. This favourable feature makes this APGC more flexible in terms of power flow. The stability of both engine and HVDC gird can be enhanced simultaneously.

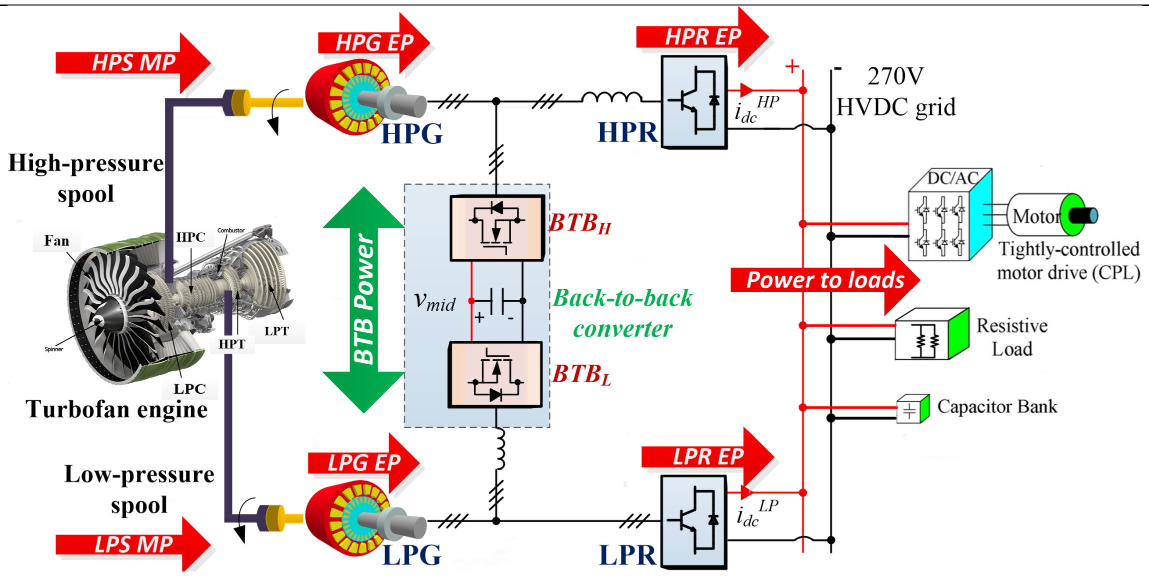

Figure 6.2. Power flow diagram of the APGC. MP: mechanical power; EP: electrical power.

6.2 HVDC Grid Stability Analysis with Different Power Sharing Ratios between the HPR and the LPR

To analyse the HVDC grid stability with different HPR/LPR power sharing ratios, a DC side equivalent circuit is built as shown in Figure 6.3. It includes the droop-controlled rectifiers, cables, DC capacitors, and loads. The superscripts *HP* and *LP* represent variables of the HP and LP power generation channels, respectively.

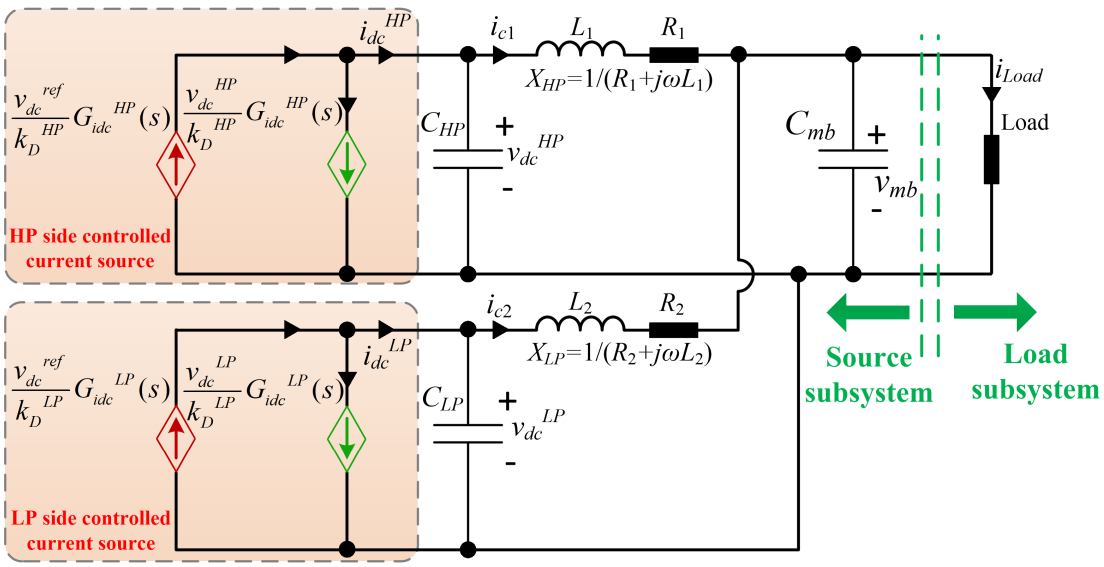

Figure 6.3. DC equivalent circuit with droop control.

Since a current mode droop control is implemented to regulate the DC currents (see (3-15)), the HP and LP channels can be regarded as current sources. In Figure 6.3, i_{dc}^{HP} and i_{dc}^{LP} are current sources controlled by the local DC voltages v_{dc}^{HP} and v_{dc}^{LP}, using droop gains k_D^{HP} and k_D^{LP}. The DC current dynamics $G_{idc}(s)$ (from i_{dc}^* to i_{dc}) derived in (3-24) is also considered. The DC currents can be expressed as follows:

$$i_{dc}^{HP} = \frac{v_{dc}^* - v_{dc}^{HP}}{k_D^{HP}} G_{idc}^{HP}(s) \quad i_{dc}^{LP} = \frac{v_{dc}^* - v_{dc}^{LP}}{k_D^{LP}} G_{idc}^{LP}(s) \tag{6-1}$$

In Figure 6.3, C_{HP} and C_{LP} are the capacitances of DC capacitors. The transmission cables are represented by RL branches and their admittances are denoted as X_{HP} and X_{LP}, respectively. v_{mb} and C_{mb} are voltage and capacitance of the global main HVDC bus, respectively.

6.2.1 Impedance Based Stability Analysis

Middlebrook proposed an impedance-based approach to analyse stability of a system with sources and loads, which allows definition of stability criterion for every individual subsystem through convenient impedance specifications [97]. Denoting the impedances of source and load subsystems as $||Z_s||$ and $||Z_L||$, respectively, the Middlebrook Criterion gives a sufficient stability criterion, which is:

$$\|Z_s\| \ll \|Z_L\| \tag{6-2}$$

From (6-2) the system stability can be assessed by $||Z_s||$. To obtain $||Z_s||$, the open-circuit voltage $v_{oc}(s)$ and short-circuit current $i_{sc}(s)$ of the source subsystem in Figure 6.3 in frequency domain are derived as follows. The derivation process is given in Appendix E.

$$\begin{cases} v_{oc}(s) = \dfrac{\displaystyle\sum_{j=LP}^{HP} \frac{X_j G_{idc}^{\ j}}{sC_j k_D^{\ j} + k_D^{\ j} X_j + G_{idc}^{\ j}} v_{dc}^*}{sC_{mb} + \displaystyle\sum_{j=LP}^{HP} \frac{sC_j k_D^{\ j} X_j + G_{idc}^{\ j} X_j}{sC_j k_D^{\ j} + k_D^{\ j} X_j + G_{idc}^{\ j}}} \\ i_{sc}(s) = \displaystyle\sum_{j=LP}^{HP} \frac{X_j G_{idc}^{\ j}}{sC_j k_D^{\ j} + k_D^{\ j} X_j + G_{idc}^{\ j}} v_{dc}^* \end{cases} \tag{6-3}$$

Therefore, the output impedance of the source subsystem can be derived as follows:

$$Z_s(s) = \frac{v_{oc}(s)}{i_{sc}(s)} = \frac{1}{\left(sC_{mb} + \sum_{j=LP}^{HP} \frac{sC_j k_D{}^j X_j + G_{idc}{}^j X_j}{sC_j k_D{}^j + k_D{}^j X_j + G_{idc}{}^j} \right)} \tag{6-4}$$

Figure 6.4 presents the Bode plot of the impedance $Z_s(s)$, where the system parameters are given in Table 6-1. It can be seen from Figure 6.4 that as the proportion of LPR's power increases, the peak magnitude of the source impedance at low-frequency region will decrease. According to the Middlebrook Criterion, the reduction in the magnitude of source subsystem impedance indicates that the system tends to be more stable [98], [99].

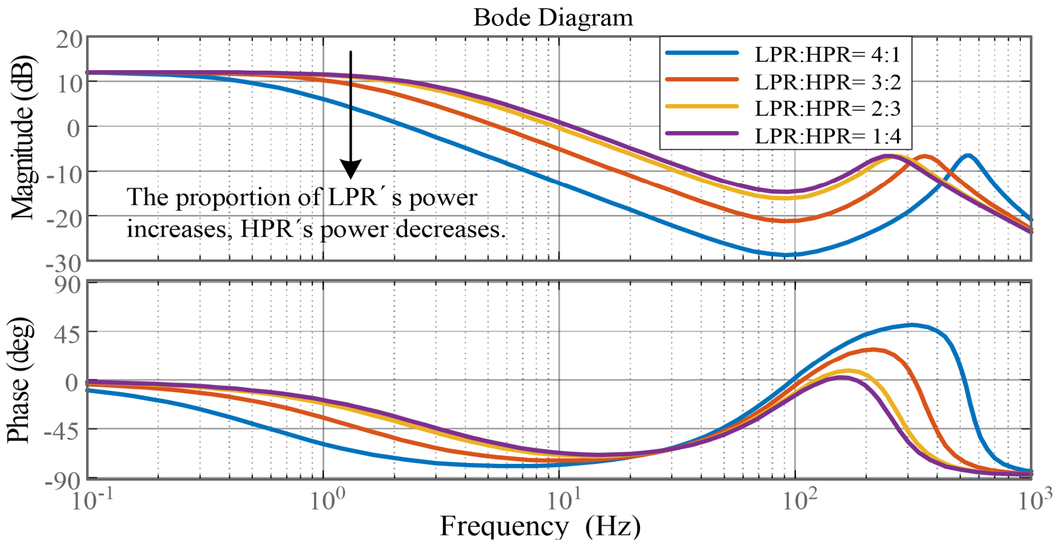

Figure 6.4. Bode plot of the source impedance $\|Z_s(s)\|$ in (6-4) at different power sharing ratios between the LPR and HPR.

6.2.2 Time Domain Analysis Using the State-Space Model

In order to verify whether the impedance analysis-based results are correct, in this section the equivalent circuit shown in Figure 6.3 is further analysed from a different angle using a state-space model. Then the outcomes of the state-space model and the impedance model are compared in the end of this section to see whether they are consistent.

The currents of inductors and voltages across capacitors are selected as state variables., and the state-space model can be expressed as follows:

$$\Delta \dot{x} = A \Delta x \tag{6-5}$$

where x=[$v_{dc}{}^{HP}$, $v_{dc}{}^{LP}$, i_{c1}, i_{c2}, v_{mb}] which is a state-space vector and A is the system matrix.

Considering the droop effect in (3-15), v_{dc}^{LP} can be written as

$$v_{dc}^{LP}(s) = \left[v_{dc}^{*}(s) - k_D{}^{LP} i_{dc}{}^{LP}(s) \right] G_{vdc}{}^{LP}(s) \tag{6-6}$$

where $G_{vdc}^{LP}(s)$ is the DC voltage transfer function of the LPR control system. It can be expressed as follows:

$$G_{vdc}{}^{LP}(s) = \frac{\Delta v_{dc}}{\Delta v_{dc}{}^{*}} = \frac{G_{idc}(s)}{G_{idc}(s) + k_D Cs} = \frac{z_2 s^2 + z_1 s + z_0}{p_3 s^3 + p_2 s^2 + p_1 s + p_0} \tag{6-7}$$

where the expressions of z_2, z_1, z_0, p_3, p_2, p_1 and p_0 can be found in Appendix F.

It can be seen in (6-7) that $G_{vdc}^{LP}(s)$ is a third-order transfer function, which will complicate the state-space model. Proper order reduction is required. This can be achieved by transforming the transfer function from s (the Laplace domain) into $j\omega$ (the frequency domain), and investigating the characteristics in the frequency domain. Substitute the s with $j\omega$, $G_{vdc}^{LP}(s)$ can be rewritten as

$$G_{vdc}{}^{LP}(j\omega) = \frac{z_2(j\omega)^2 + z_1(j\omega) + z_0}{p_3(j\omega)^3 + p_2(j\omega)^2 + p_1(j\omega) + p_0} = \frac{z_1(j\omega) + (z_0 - z_2\omega^2)}{(p_1 - p_3\omega^2)j\omega + (p_0 - p_2\omega^2)} \tag{6-8}$$

As shown in Table 6-1, the control bandwidth for the DC voltage is designed as 100Hz. Hence, the frequency range from 0Hz (ω= 0 rad/s) to 150Hz (ω= 942.5 rad/s) which covers the control bandwidth is focused to investigate the characteristic of $G_{vdc}^{LP}(j\omega)$ in (6-8). When the frequency component ω is within range of interest [0, 942.5 rad/s], the following relations are met:

$$z_2\omega^2 \ll \frac{z_0}{10} \quad p_3\omega^2 \ll \frac{p_1}{10} \quad p_2\omega^2 \ll \frac{p_0}{10} \tag{6-9}$$

Therefore, $G_{vdc}^{LP}(s)$ can be simplified into a first-order transfer function within the frequency range of the control bandwidth, given as follows:

$$G_{vdc}{}^{LP}(s) \approx \frac{z_1 s + z_0}{p_1 s + p_0} \tag{6-10}$$

Subsequently, applying (6-10) to (6-6) and transforming (6-6) into the time domain, the following relation can be derived

$$p_0 v_{dc}^{LP} + p_1 \frac{dv_{dc}^{LP}}{dt} = z_0 v_{dc}^* + z_1 \frac{dv_{dc}^*}{dt} - z_0 k_D^{LP} i_{dc}^{LP} - z_1 k_D^{LP} \frac{di_{dc}^{LP}}{dt} \tag{6-11}$$

(6-11) can be transferred into small-signal expression around some steady-state operating point and written as follows:

$$\Delta\dot{v}_{dc}^{LP} = -\frac{p_0}{p_1}\Delta v_{dc}^{LP} - \frac{z_0 k_D^{LP}}{p_1}\Delta i_{dc}^{LP} - \frac{z_1 k_D^{LP}}{p_1}\Delta\dot{i}_{dc}^{LP} \tag{6-12}$$

where v_{dc}^* is omitted because it is set as a fixed 270V in this study [35].

The voltage balance equation across the transmission cable can be expressed as follows:

$$v_{dc}^{LP} - v_{mb} = R_2 i_{c2} + L_2 \frac{di_{c2}}{dt} \tag{6-13}$$

where R_2 and L_2 are the equivalent resistance and inductance of the LP channel's cable, i.e., $X_{LP}=1/(R_2+j\omega L_2)$.

Hence, the state-space equation of i_{c2} in the small signal manner can be derived as follows:

$$\Delta\dot{i}_{c2} = \frac{1}{L_2}\Delta v_{dc}^{LP} - \frac{R_2}{L_2}\Delta i_{c2} - \frac{1}{L_2}\Delta v_{mb} \tag{6-14}$$

The voltage equation of the main DC capacitor is

$$i_{c1} + i_{c2} = C_{mb}\frac{dv_{mb}}{dt} + i_{Load} \tag{6-15}$$

In MEA many energy consuming loads, such as the thermal mats for wing ice protection system and the power converter driven compressors for environment control system, can be regarded as constant impedance load (CIL) and constant power load (CPL), respectively [2]. Hence, in this study the system is considered as loaded with CPL, whose power is P_{CPL}, and CIL, whose impedance is R_{CIL}. The current of load i_{Load} can be derived as follows

$$i_{Load} = \frac{P_{CPL}}{v_{mb}} + \frac{v_{mb}}{R_{CIL}} \tag{6-16}$$

Combing (6-15) and (6-16), the state-space equation of v_{mb} in the small signal manner can be written as follows:

$$\Delta\dot{v}_{mb} = \frac{1}{C_{mb}}\Delta i_{c1} + \frac{1}{C_{mb}}\Delta i_{c2} + \left(\frac{P_{CPL}}{C_{mb}\bar{v}_{mb}^{\,2}} - \frac{1}{C_{mb}R_{CIL}}\right)\Delta v_{mb} \tag{6-17}$$

where $\bar{v}_{mb}$ is the steady operating point of the main DC bus voltage.

With (6-12), (6-14) and (6-17), and considering the LP and HP channels are identical as shown in Figure 6.3, the system matrix A in equation (6-5) can be derived as follows:

$$A = \begin{bmatrix} -\frac{p_0^{HP}}{p_1^{HP}} & 0 & -\frac{z_0^{HP}k_D^{HP}}{p_1^{HP}} & 0 & 0 \\ 0 & -\frac{p_0^{LP}}{p_1^{LP}} & 0 & -\frac{z_0^{LP}k_D^{LP}}{p_1^{LP}} & 0 \\ \frac{1}{L_1} & 0 & -\frac{R_1}{L_1} & 0 & -\frac{1}{L_1} \\ 0 & \frac{1}{L_2} & 0 & -\frac{R_2}{L_2} & -\frac{1}{L_2} \\ 0 & 0 & \frac{1}{C_{mb}} & \frac{1}{C_{mb}} & \frac{P_{CPL}}{C_{mb}\bar{v}_{mb}^{\,2}} - \frac{1}{C_{mb}R_{CIL}} \end{bmatrix} \tag{6-18}$$

The matrix in (6-18) presents the system matrix A of the fifth-order state-space model in (6-5). Stability of the system can be assessed using the eigenvalues of A. Figure 6.5 shows the eigenvalues loci when the power ratio between the LPR and HPR changes from 0.5:1 to 2:1. It can be seen that as the LPR accounts for more power, the dominant eigenvalues will move far away from the right half-plane. It reveals that the system tends to be more stable.

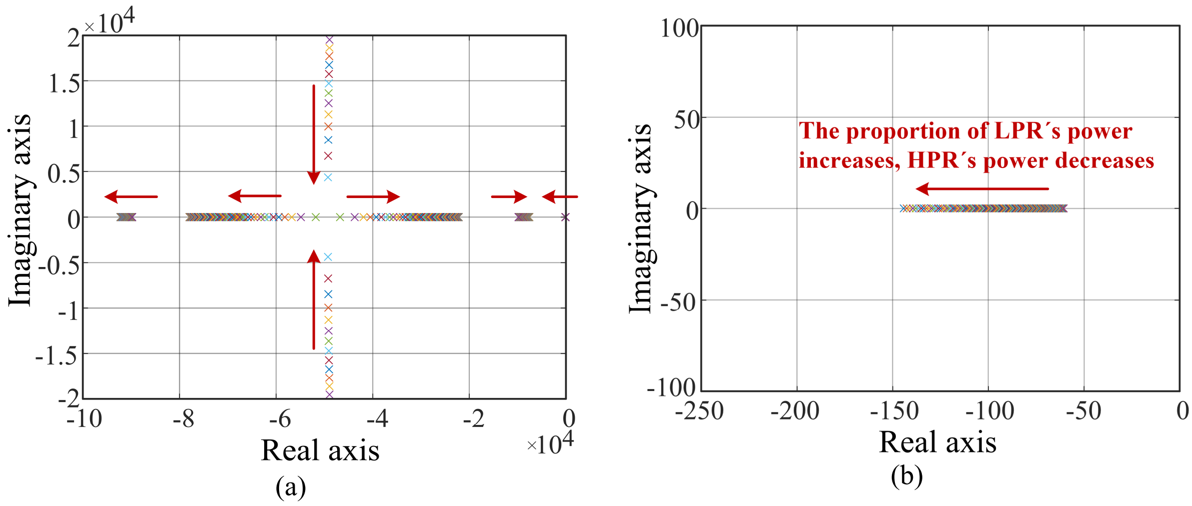

Figure 6.5. Eigenvalues of the DC equivalent circuit with the variation of power sharing ratio between the HPR and LPR. (a) Overall plot. (b) Zoomed area of the dominant eigenvalues. The arrows represent the direction that the proportion of the LPR's power increases.

Subsection 6.2.1 and 6.2.2 study the stability of DC grid from different angles. The results in Figure 6.4 derived from the Middlebrook approach and Figure 6.5 derived from the state-space model are aligned, both indicating that *increasing the proportion of the LPR's output power will contribute to a more stable HVDC gird*. This crucial conclusion will be validated through simulation and experiments. It can also be used as a criterion for researchers and engineers when designing onboard power generation centres and electrical power systems with a sufficient stability margin for the MEA application.

6.2.3 Effect of Power Sharing Ratio on the Line Losses

The above stability analysis reveals the relation between the LPR's power and HVDC grid stability, but it does not specify the HPR/LPR power ratio. To find the power sharing ratio range quantitively, other approaches or optimization objectives should be considered. In this subsection, the impact of power sharing ratio on the transmission line losses is further analysed, and the optimal power ratio is derived for minimizing the line losses.

Assume that n_1 and n_2 are the ratios of the DC side current of the HPR and LPR to the total load current. The current sharing ratio can be expressed as

$$\begin{cases} \dfrac{i_{dc}^{HP}}{i_{dc}^{LP}} = \dfrac{n_1 \cdot i_{Load}}{n_2 \cdot i_{Load}} = \dfrac{n_1}{n_2} \\ \text{s.t. } n_1 + n_2 = 1 \end{cases} \tag{6-19}$$

Typically, the geometry of power system onboard MEA is symmetrical [54]. Hence, the cable length can be assumed to be identical for the HP and LP channels. Denoting the cable resistance R_1 and R_2 in Figure 6.3 both as R_c, the line losses minimization problem (P_{Loss}) can be formulated as

$$\begin{cases} \min\left(P_{Loss}\right) = \min\left[\left(n_1^2 + n_2^2\right) \cdot i_{Load}^2 R_c\right] \\ \text{s.t. } n_1 + n_2 = 1 \end{cases} \tag{6-20}$$

To analytically solve the optimization problem formulated in (6-20), the Lagrange multiplier approach is applied to obtain the solution for (6-20), which can be shown as follows:

$$H\left(n_1,n_2,\lambda\right)=\left(n_1^{\ 2}+n_2^{\ 2}\right)\cdot i_{Load}^{\ \ 2}R_c+\lambda\left(n_1+n_2-1\right) \tag{6-21}$$

The partial derivative of (6-21) is expressed as follows:

$$\begin{cases} \dfrac{\partial H\left(n_1,n_2,\lambda\right)}{\partial n_1}=2i_{Load}^{\ \ 2}R_c n_1+\lambda=0 \\ \dfrac{\partial H\left(n_1,n_2,\lambda\right)}{\partial n_2}=2i_{Load}^{\ \ 2}R_c n_2+\lambda=0 \\ \dfrac{\partial H\left(n_1,n_2,\lambda\right)}{\partial \lambda}=\left(n_1+n_2-1\right)=0 \end{cases} \tag{6-22}$$

Eliminating the parameter λ in (6-22), the optimal power sharing ratio aiming for line losses minimization can be obtained as follows:

$$\frac{n_1}{n_2}=\frac{k_D^{\ LP}}{k_D^{\ HP}}=1 \tag{6-23}$$

Equation (6-23) indicates that for a MEA with symmetrical geometry of electrical power system, an equivalent power sharing between the HPR and LPR will help minimize the power losses on transmission cable.

6.2.4 Power Decoupling Characteristic of the Proposed APGC

Equation (6-23) shows that the LPR and HPR share power equally to minimize the line losses. The findings in Figure 6.4 and Figure 6.5 reveal that increasing the proportion of the LPR's power is beneficial to the HVDC grid stability. Summarizing these findings, it can be stated that *the LPR should deliver more power than the HPR to enhance the HVDC grid stability and reduce line losses*.

However, given the stability of engine, in engine operation modes such as maximum take-off and top of climb, more mechanical power needs to be extracted from the HPS than the LPS to avoid overspeed of the HPS and the potential instability [73], [74]. For the PGC, the Power Coupling Effect makes it impossible to extract more power from the HPS and meanwhile delivering more power to the DC bus through the LPR. However, with the APGC, the BTB converter can transfer power from the HP channel to LP channel, allowing the HPS shares more power than the LPS whilst the LPR feeds more power than the HPR. Hence, the proposed APGC presents a Power Decoupling characteristic.

6.3 Simulation Results

To verify the theoretical findings in this Chapter, a Simulink model of the PGC is built to test the HVDC grid stability under different power sharing ratios between the HPR and LPR. The nonlinear model is presented in Appendix D. As stated in section 6.2.3, the impedance of transmission cable of the HP and LP channels are assumed identical. The control scheme for both rectifiers has been presented in Chapter 3, Section 3.2.3, where the control bandwidths for voltage loop and current loop are set as 100Hz and 1kHz, respectively. The associated control parameters are also given in Table 6-1. Decoupling terms and anti-windup scheme presented in [52] are applied for current controller to achieve a better dynamic performance.

Table 6-1. Parameters of the studied power generation centre.

Category	Parameter	Value
Electrcial machines	Speed of the LP generator	7,000 rpm
	Speed of the HP generator	20,000 rpm
	Nominal speed	8,000 rpm
	Stator inductcne	0.1 mH
	Stator resistance	58 mΩ
	Number of pole pairs	3
DC Link	Rated voltage	270 V
	Local shunt capacitor	1 mF
	Main bus capacitor	1.2 mF
CPL (A buck converter)	Load power	From 10 kW to 30 kW
	Input resistance R_{ic}	$R_{ic} = -\frac{\bar{v}_{dc}}{\bar{\iota}_{Load}}$
	Resosnance frequency ω_o	$\omega_o = \frac{1}{\sqrt{L_f C_f}}$,
	Input filter inductance L_f	1.2 μH
	Input filter capacitance C_f	2 mF
	Quality factor Q_0	$Q_0 = \frac{1}{R_{cf}}\sqrt{\frac{L_f}{C_f}}$
	Input filter resistance R_{cf}	0.01 Ω
Cable impedance	Nominal cable resistance	0.16 mΩ/m
	Nominal cable inductance	0.11 μH/m

	Distance from the engine-driven generator-rectifier unit to the main DC bus	5 m
	Distance from the APU-driven generator-rectifier unit to the main DC bus	20 m
Other control paramters	Current loop control	1 kHz bandwidth
	Voltge loop control	100 Hz bandwidth
	Droop gains	g_{LP}=1/4, g_{HP}=1/4

The DC currents and DC bus voltage under different power sharing ratios between the HPR and LPR are presented in Figure 6.6. Figure 6.6(a) and (c) present the DC currents and voltage where the electrical power of the LPR (P_{LPR}) is triple of that of the HPR (P_{HPR}), i.e., $P_{HPR} : P_{LPR}$ = 1:3. It can be seen that as the increase of load power from 10kW to 30kW, the DC voltage decreases due the droop control effect. The i_{dc}^{LP} is tighltly controlled to be thriple of i_{dc}^{HP}, showing smooth performance in transient and steady states.

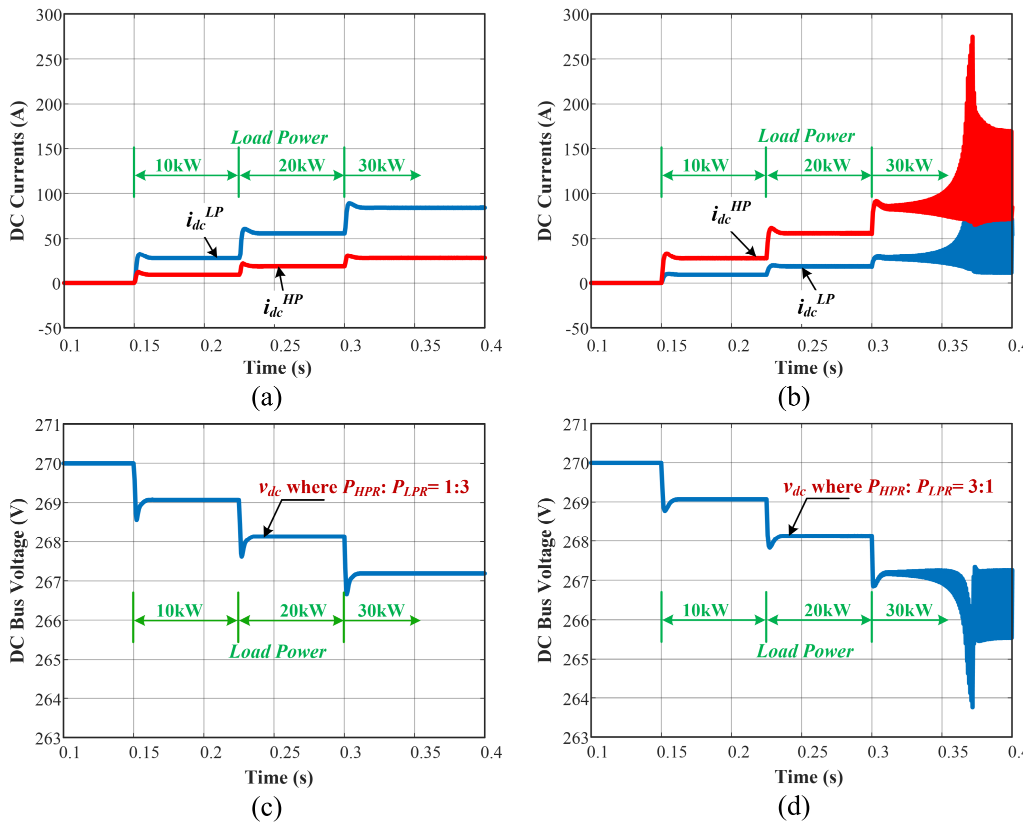

Figure 6.6. Simulation results of the HVDC grid stability under different power sharing ratios between the HPR and LPR. (a) DC currents where $P_{HPR} : P_{LPR}$ = 1:3. (b) DC currents where $P_{HPR} : P_{LPR}$ = 3:1. (c) Main DC bus voltage v_{dc} where $P_{HPR} : P_{LPR}$ = 1:3. (d) Main DC bus voltage v_{dc} where $P_{HPR} : P_{LPR}$ = 3:1.

Swapping the power sharing ratio between the HPR and LPR, i.e., $P_{HPR} : P_{LPR} = 3:1$, and keeping the rest of configurations unchanged, the system responses are exhibited in Figure 6.6(b) and (d). With 10kW and 20kW load power, the system remains stable, same as that in Figure 6.6(a) and (c). However, as the load power increases to 30kW, the system moves into a unstable state with severe oscillation in the DC currents and DC voltage. The comparative results in Figure 6.6 show that increasing the power sharing ratio of the LPR in the heavy load condition will contribute to a more stable HVDC grid.

According to the operating points in Figure 6.6 and the system parameters in Table 6-1, Bode plot of source and load impedances under different load powers and power sharing ratios between the HPR and LPR are presented in Figure 6.7. The expression of source impedance $Z_s(s)$ has been formulated in (6-4). A DC/DC buck converter is tightly controlled as a CPL. The input impedance $Z_L(s)$ of the buck converter can be expressed as follows [100]:

$$Z_L(s) = -R_{ic}\frac{\dfrac{s^2}{{\omega_o}^2} + \dfrac{s}{Q_0\omega_o} + 1}{\dfrac{s}{\omega_p} + 1} \tag{6-24}$$

where the definitions and values of R_{ic}, ω_o, ω_p and Q_0 are given in Appendix F.

It can be seen from Figure 6.7(a) that under 20kW load condition, the magnitude of $Z_s(s)$ at various power sharing ratios is much smaller than the magnitude of $Z_L(s)$. As shown in (6-2), according to the Middlebrook Criterion, this indicates a sufficient system stability margin. This result is consistent with the simulation results in Figure 6.6, where the system remains stable under 20kW load condition for both $P_{HPR} : P_{LPR} = 1:3$ and 3:1. However, Figure 6.7(b) presents that as the load power increases to 30kW, the magnitude of $Z_s(s)$ with $P_{HPR} : P_{LPR} =$ 3:1 and 1:1 is very close to the magnitude of $Z_L(s)$, showing no stability margin. This is consistent with the simulation results in Figure 6.6(b) and (d), where the system becomes unstable under 30kW load power condition. By decreasing the ratio $P_{HPR} : P_{LPR}$ to 1:3, the magnitude of $Z_s(s)$ decreases, meeting the requirement in (6-2). This is why in Figure 6.6(a) and (c) where at $P_{HPR} : P_{LPR} = 1:3$, the system operates in a stable state even though under 30kW load power.

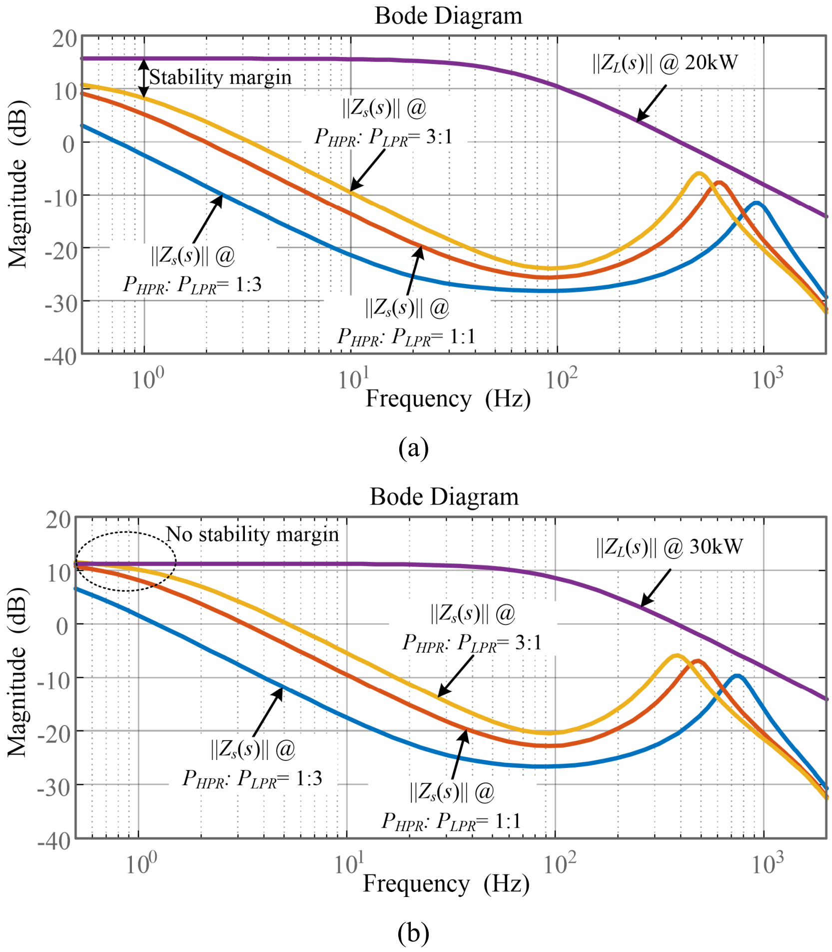

Figure 6.7. Bode plot of source and load impedances under different load powers and power sharing ratios between the HPR and LPR. (a) source and load impedances with 20kW load power. (b) source and load impedances with 30kW load power.

The line losses under 20kW and 30kW load conditions with different power sharing ratios are presented in Figure 6.8. Cable impedance has been demonstrated in Table 6-1. It can be seen that a minimal line losses is achieved at $P_{HPR} : P_{LPR} = 1{:}1$. This is consistent with the analysis in subsection 6.2.3. The increase of line losses caused by increased power ratio of the LPR is less than 5W, which is trivial compared with total load power. Hence, the HVDC grid stability should be the main consideration for selecting the power sharing ratio between the HPR and LPR. In other words, it is desired to deliver more electrical power through the LPR to the main DC bus than the HPR for a more stable HVDC grid.

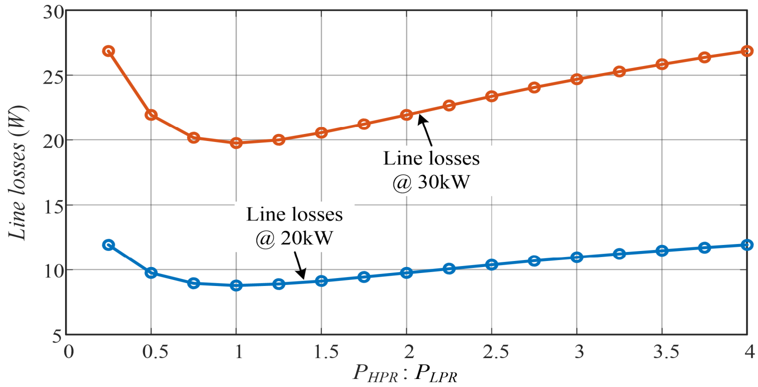

Figure 6.8. Line losses under 20kW and 30kW load conditions with different power sharing ratios.

6.4 Discussion of Benefits in Aircraft-level

Turbofans, as primary source of propulsion, are designed for cruise phase, which consumes most of an aircraft's fuel. Hence, the compressors and turbines are designed and assembled for optimizing the cruise operation. Since the aerodynamic point (ADP) is specifically designed for the cruise condition, while for the other engine operation modes, such as ground idle mode or maximum take-off mode, the engine may operate in a suboptimal condition.

In take-off and climb phases, the LPS operates in a high speed to generate excess thrust to increase lift to overcome other forces such as weight and drag. Since the speed of the HPS and LPS are thermodynamically coupled through airflow, this pushes the speed of the HPS to its limits and overspeed may occur. This degrades the stability of engine. A solution is to properly decrease the throttle, while the expense is a longer flight phase and lower lift.

As revealed in this chapter, the BTB converter inside the APGC establishes an electrical power path between the HPS and LPS. Therefore the speed of the HPS and LPS can be decoupled. By managing the power split ratio between the two spools, the issue of overspeed of the HPS at high engine power settings can be addressed without affecting the stability of the electrical power network. This provides a higher flexibility in terms of the engine design as well as brings potential benefits in aircraft-level. For example, the airplane can take off and climb with the maximum allowable thrust, which can shorten the take-off phase or carry a heavier airplane. The size of high-pressure turbine can be potentially reduced which makes the engine lighter. Also the HPS can be maintained at a reasonably high speed, which provides a higher core pressure ratio. This will be beneficial for the engine efficiency.

6.5 Chapter Summary

In this chapter, the Power Coupling Effect of the PGC has been studied. Due to this effect, it is difficult to enhance the stability of HVDC grid and engine simultaneously at the high-power settings of engine. In contrast, the proposed APGC removes the Power Coupling Effect by transferring power from the HP channel to the LP channel, allowing the extraction of more mechanical power from the HPS than the LPS, whilst the LPR delivers more electrical power than the HPR to the DC bus.

This paper also derives the source and load impedances and provides detailed stability analysis for the HVDC grid. The derived impedance model and analytical findings may be of interest for other researchers who are interested in the stability issue of the onboard DC microgrid. The theoretical findings of the HVDC grid stability and stability improvement using the proposed APGC will be verified in experiments in Chapter 7.

Chapter 7. Experimental Validations

7.1 Introduction

This chapter introduces the test platforms and provides experimental results to support the theoretical analysis and analytical findings of this Thesis Chapters. The key findings that were experimentally verified and reported in this chapter can be summarized as follows:

- The HPG can operate in a high-speed setting without field-weakening operation in the proposed APGC. Compared with the same operating point in the PGC, power losses in the APGC are reduced.
- A phase current synchronization strategy is proposed to control the BTB converter. The phase currents of the LPG, BTB_L converter and LPR should be synchronized in phase. The DC-link voltage of the BTB converter can be regulated based on the active control of the phase current magnitude.
- Fault tolerant control schemes for the APGC are proposed considering both cases of the HPR and LPR failure. To avoid the abrupt change and surge of generator's current when the rectifiers become faulty, an initialization strategy is proposed to initialize the voltage command in the new controller for the power converter which is connected with the generator. Control performances of these schemes are verified.
- Increasing the proportion of LPR's power to the HVDC grid enhances the stability of HVDC grid.

7.2 Experimental Setup

7.2.1 Engine Emulator Platform

To validate the foregoing theoretical analysis, an engine emulator platform consisting of two high speed drive systems to mimic the HP spool and LP spool behaviours was built in the laboratory. This engine emulator rig was developed in collaboration with my colleague Hossein B. Enalou whose was thanked in Acknowledgement. The configuration and key components are shown in Figure 7.1. It consists of one dSpace (used for hardware-in-the-loop simulation), two PMMs as generators, two three-level AC/DC rectifiers, two induction machines as prime movers and their drive systems.

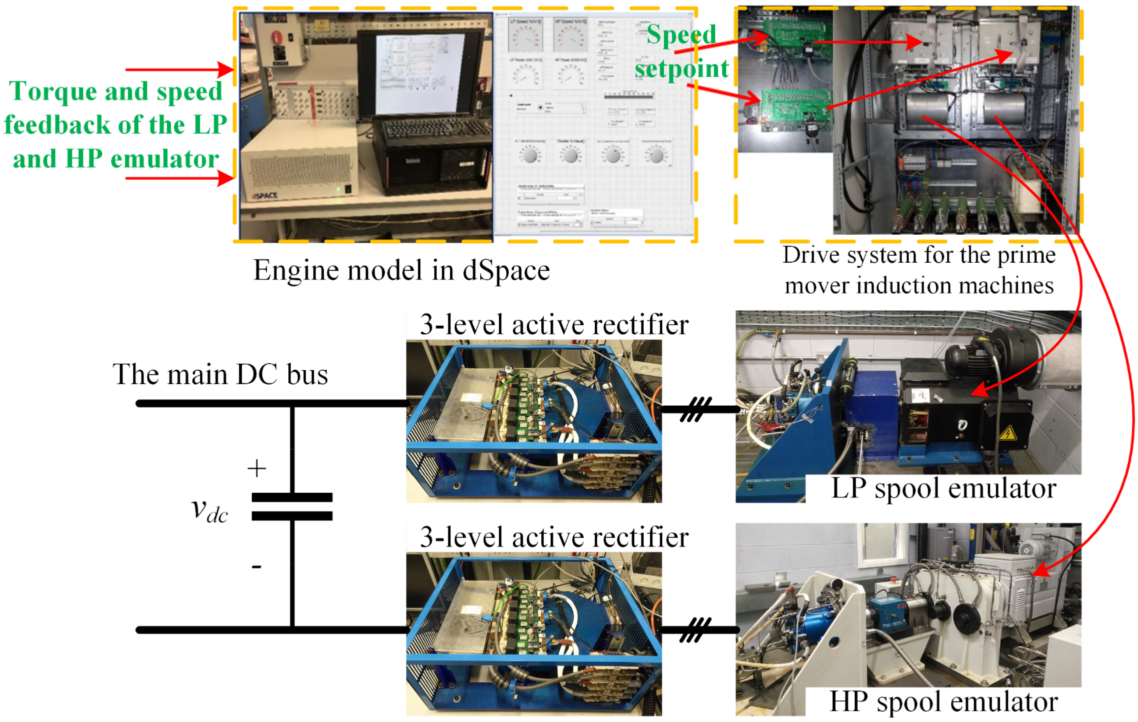

Figure 7.1. Configuration and key components of the engine emulator.

The dSPACE control system runs a real-time model of a dual-spool turbofan engine [11] to achieve a hardware-in-the-loop implementation. The engine model in the Simulink will be downloaded to dSpace for real-time calculation. The torque and speed measurements of the LP and HP shafts are provided to the engine model for a closed-loop calculation. The speed setpoints are generated by the engine model and sent to the prime mover induction machine drive system to mimic the speed-torque characteristic of the engine spools.

For the drive system of the prime mover induction machines, two bidirectional AC/DC power converters (SEMIKRON's IGBTS Power Stack-SEMIKUBE: SKM400GB12E4) are used. The SEMIKUBE power converter integrates circuits to sense the current through an external current sensor and sense the DC bus voltage through an external voltage sensor. The driver board also integrates overcurrent, overvoltage and over temperature protection. The SEMIKUBE is shown in Figure 7.2.

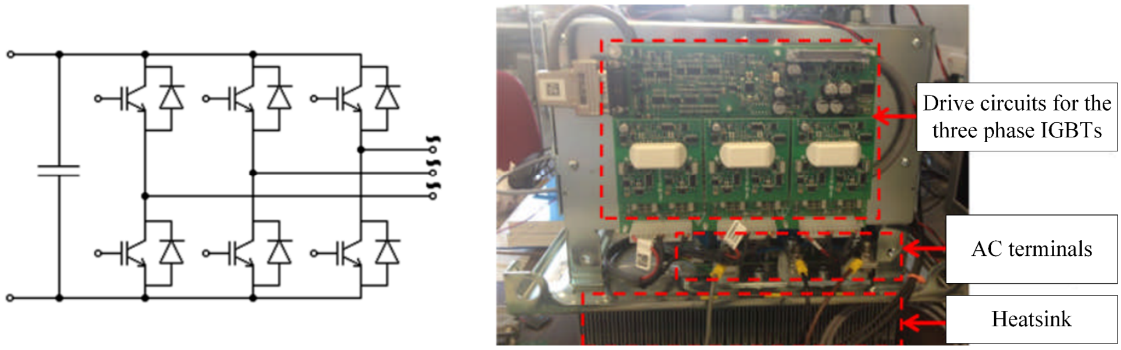

(a) (b)

Figure 7.2. SEMIKUBE power stack. (a) Main circuit schematic. (b) prototype.

The main AC/DC power converter connected with the DC bus, needs to feed the electrical machine in the starter mode. In generator mode it operates as a synchronous rectifier. To reduce the power losses of converter, to decrease dv/dt, and to achieve a high equivalent switching frequency, two neutral-point-clamped three-level power converters are designed as shown in Figure 7.1. The layout of main circuit is presented in Figure 7.3.

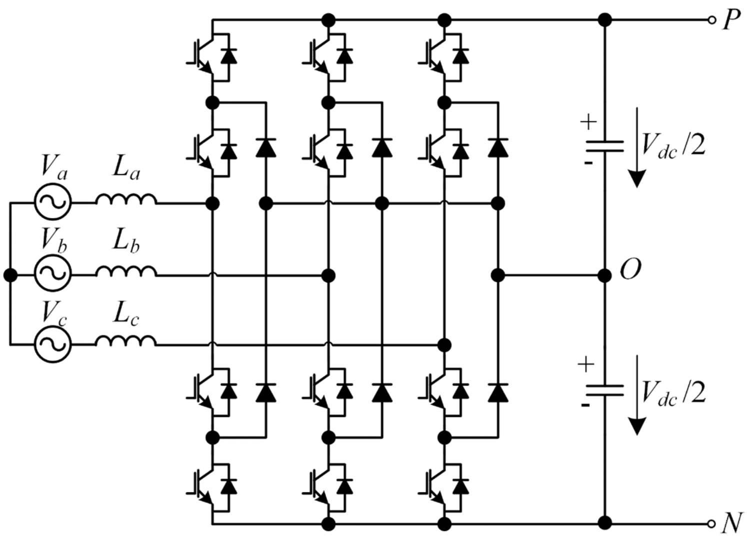

Figure 7.3. Main circuit layout the three-level power converter.

For the digital control platform, as shown in Figure 7.4, a TMS320C6713 floating-point DSP and a FPGA board are integrated, providing ten 12-bit A/D channels and ten fibre optics to drive power converters. A HPI daughter card, allows the program to be loaded into the DSP and enables a bi-directional data transfer between the host PC and the DSP via a USB connection. Matlab is used to monitor the variables of the control program in real time.

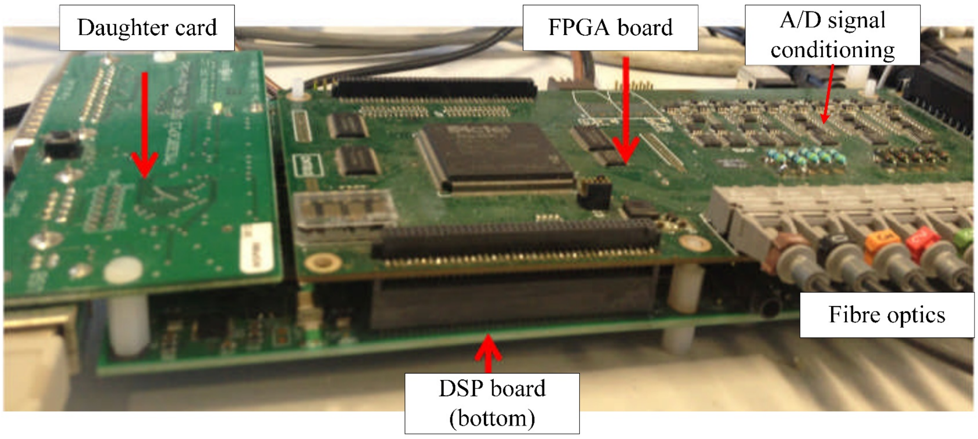

Figure 7.4. Digital control platform.

7.2.2 Downscaled Lab Prototype of the APGC

To facilitate the research of the APGC and verification of the key findings, a downscaled lab prototype consisting of two rectifiers and one BTB converter has been built as shown in Figure 7.5. An autotransformer (AF) whose primary side is connected with utility grid is used to emulate the LPG. Therefore, the voltage frequency of the LPG emulator is the same as the utility grid's voltage frequency, which is 50Hz. A Chroma QuadTech 31120 programmable AC source is used to emulate the HPG, and its voltage frequency is set as higher than 50Hz. In this study, the voltage frequency of the HPG emulator is set as 80Hz, hence the frequency ratio between the HPG and LPG is 1.6, which is similar to the speed ratio of correspondent engine spools. The TMDSCNCD28379D control card is used as the digital control platform. A resistive load bank and an APM electronic load (E-load) are connected to the DC bus, performing as CIL and CPL, respectively. Some other system parameters are listed in Table 7-1.

Table 7-1. Parameters of the downscaled lab prototype.

Parameter	Value
Rated DC bus voltage	270 V
Internal DC-link voltage of the BTB converter	400 V
Inductance of the AC filter	2.5 mH
Switching frequency	5 kHz
Current loop and voltage loop execution frequencies	5kHz / 1kHz
Voltage and current Sensors	LV25-P and LA200-P

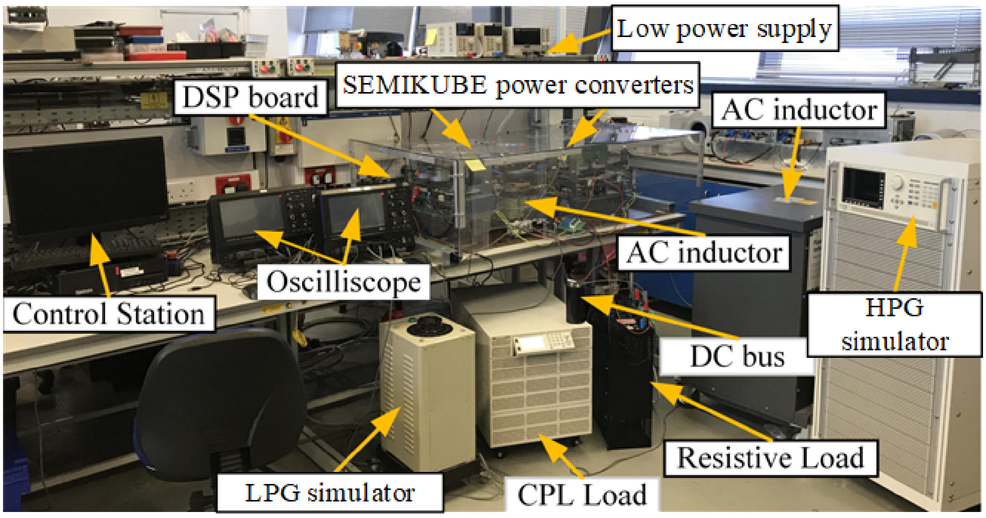

Figure 7.5. Experimental setup of the downscaled experimental prototype.

The schematic layout of the downscaled lab prototype is depicted in Figure 7.6. The power converters are all IGBT Power Stack-SEMIKUBE which has been described in Figure 7.2.

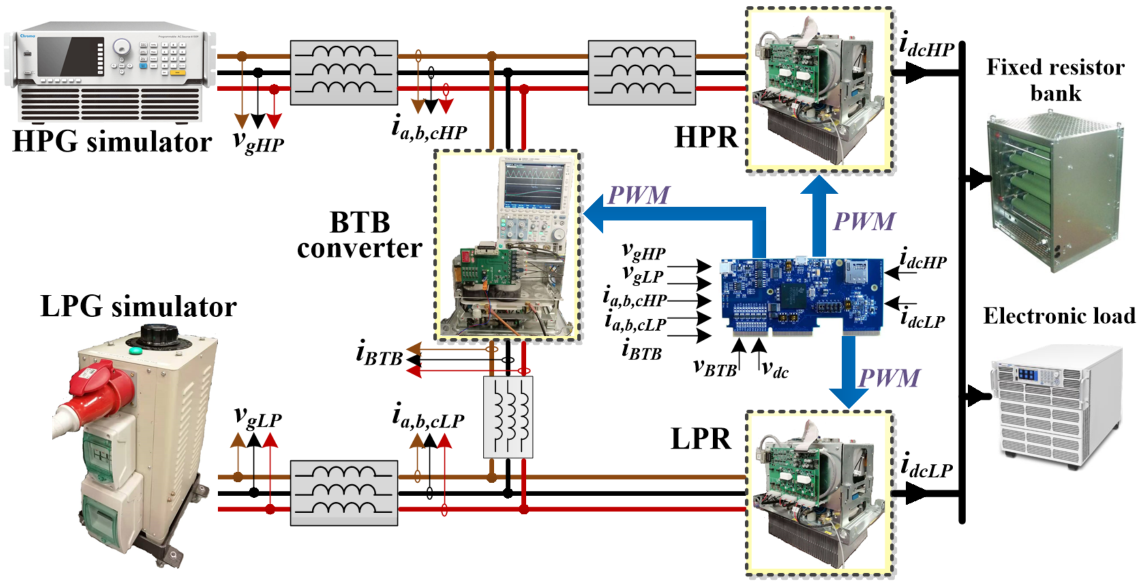

Figure 7.6. Schematic layout of the experimental prototype.

7.3 Experimental Results Overview

After reviewing the experimental platforms developed in the lab, this section summarizes the experimental results which will be shown in the following subsections.

- Section 7.4 demonstrates the essential functionalities of the APGC in normal operation regime, including the main DC bus voltage control, power sharing between rectifiers using droop control, the DC-link voltage control of the BTB converter, and phase current synchronization presented in Section 4.2.1.

- Section 7.5 proves the elimination of the HPG field-weakening control in the proposed APGC. Results are exhibited to support the analysis in Chapter 4. The HPG stator current and the power losses are shown to be reduced in the proposed APGC compared to the original PGC.
- Section 7.6 illustrates the effectiveness of the fault modes control in the case of main rectifiers failures in the APGC. Transitions from healthy to post-fault operation are investigated, validating the designed fault control and transition schemes studied in Chapter 5.
- Section 7.7 demonstrates the simultaneous stability improvement of both engine and HVDC grid offered by the proposed APGC. Results at different HP/LP power sharing ratios are investigated and presented, supporting the HVDC grid stability analysis in Chapter 6.

7.4 Control Performance of the APGC in Normal State

In this subsection, performances of the APGC in normal operation are presented. The main DC bus performance at various load powers is exhibited in Figure 7.7, where the whole process is divided into five phases. In phase 1 and 5, a CPL and CIL together consumes 1.85kW power. In phase 2 and 4, the CPL increases to 2.35kW. In phase 3, the CPL consumes more power, resulting in a 3.1kW total load power. Droop gains for the two rectifiers are set identical.

7.4.1 DC Bus Voltage and DC Currents under Droop Control

Results of the main DC bus voltage (v_{dc}), DC currents of the HPR and the LPR i_{dcHP} and i_{dcLP} are presented in Figure 7.7. It can be seen that as the increase of load power, v_{dc} deviates from the 270V rated value to 265V, 255V and 253V due to the droop control effect. i_{dcHP} is the same as i_{dcLP}, which means output power of the HPR and LPR are controlled as identical. The equivalent power sharing is achieved using droop control.

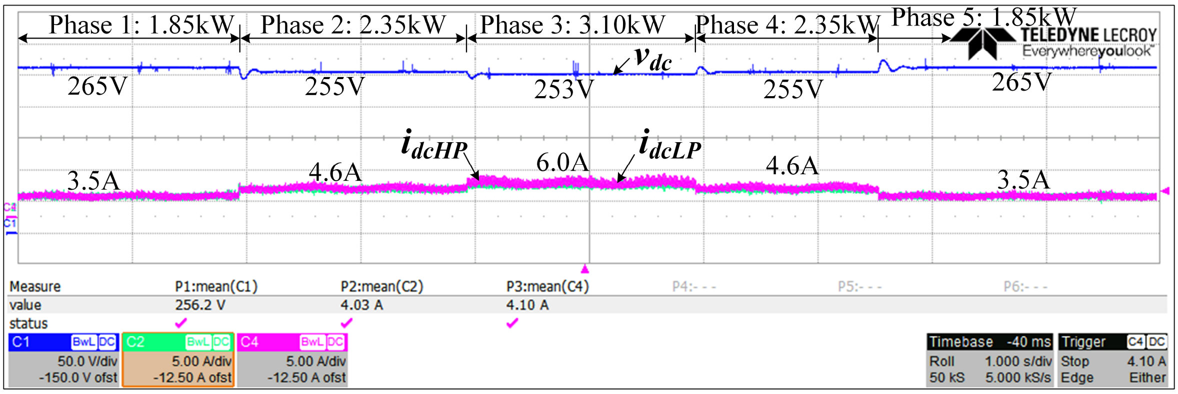

Figure 7.7. The DC voltage and currents at different load powers

7.4.2 Phase Current Synchronization Control

To verify the effectiveness of the phase current synchronization control shown in Figure 4.3, the steady-state results of the LPG's phase current i_{aLP}, BTB_L converter's phase current i_{aBTBL}, and the DC-link voltage of the BTB converter v_{BTB} are shown in Figure 7.8. It can be seen that i_{aLP} and i_{aBTBL} are synchronized in phase. The peak value of i_{aLP} is 13.1A, that of i_{aBTBL} is 8.8A. Thus, according to the relation in (4-1), ratio between power of the LPG and power through the BTB converter is 13.1/8.8=1.5. It means two third of LPG's power is transferred from the LP channel to the HP channel through the BTB converter, and one third of the LPG's power is delivered to the DC bus through the LPR. In Figure 7.8 it can be also seen that v_{BTB} is regulated to the designed value 400V. From the results, the proposed phase current synchronization scheme for the BTB converter shown in Figure 4.3 is verified.

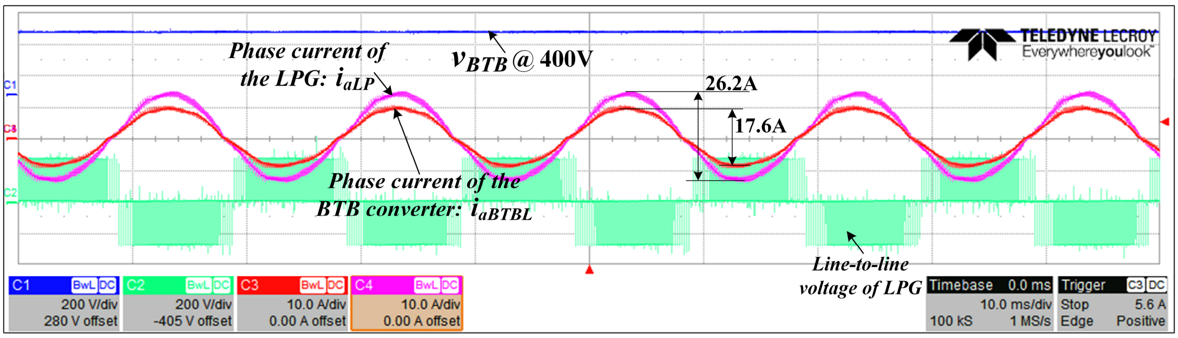

Figure 7.8. Steady-state results of the DC-link voltage of the BTB converter and phase currents of the LPG and BTB_L converter.

Dynamic experimental results when changing BTB converter's power are shown in Figure 7.9. In the experiments in Figure 7.9(a), the total load power (P_t) is 6kW. The LPR and HPR shares the same amount of power. Before the time instant t_1, the ratio between the LPG's power (P_{LPG}) and HPG's power (P_{HPG}) is 2:1, which means the amount of power transferred through the BTB converter (P_{BTB}) is P_{LPG} - P_{LPR} $=(2/3 - 1/2)P_t = 1/6\,P_t$. At the time instant t_1, the ratio between P_{LPG} and P_{HPG} increases to 3:1, which means that P_{BTB} increases to P_{LPG} - P_{LPR} $=(3/4 - 1/2)P_t = 1/4\,P_t$. Hence, according to the power relation in (4-1), in the steady state, the gain m can be derived as follows:

$$\begin{cases} Before\ \ t_1, m = \dfrac{P_{BTB}}{P_{LPG}} = \dfrac{\frac{1}{6}P_t}{\frac{2}{3}P_t} = 0.25 \\ After\ \ t_1, m = \dfrac{P_{BTB}}{P_{LPG}} = \dfrac{\frac{1}{4}P_t}{\frac{3}{4}P_t} = 0.33 \end{cases} \tag{7-1}$$

The DC-link voltage of the BTB converter v_{BTB}, the gain m, and the phase currents of the LPG simulator and BTB_L converter, i.e., i_{aLP} and i_{aBTBL}, are presented in Figure 7.9(a). It shows that as the increase of P_{BTB} at t_1 instant, the steady state value of the gain m increases from 0.25 to 0.33, which perfectly matches with the analytical results shown in (7-1). Figure 7.9(a) also shows that the phase currents i_{aBTBL} and i_{aLP} are synchronized in phase, and the ratio of magnitude between i_{aBTBL} and i_{aLP} increases from 0.25 to 0.33, which follows the change of the gain m.

The experimental results of decreasing P_{BTB} are demonstrated in Figure 7.9(b), where the P_{BTB} decreases from $\frac{1}{4}P_t$ to $\frac{1}{6}P_t$ at the time instant t_1. It can be seen from Figure 7.9(b) that a smooth control is achieved for the gain m. m decreases from 0.33 to 0.25, leading to the decrease of magnitude ratio between i_{aBTBL} and i_{aLP}. The phase currents are kept in phase in the whole process. The experimental results in Figure 7.9 confirm the effectiveness of the phase current synchronization method in power control and DC-link voltage control for the BTB converter.

Although in Figure 7.9 smooth control is realized for the gain m, i_{aLP} and i_{aBTBL}, it can be seen that the transient process from t_1 instant to the new steady state takes 40-60 ms, which presents a slow dynamic characteristic. This is due to the linear control effect of the inherent v_{BTB} PI controller as can be seen in Figure 4.3. To improve the dynamic performance, currently the author is investigating a direct power control based on the instantaneous power theory to replace the phase current synchronization method.

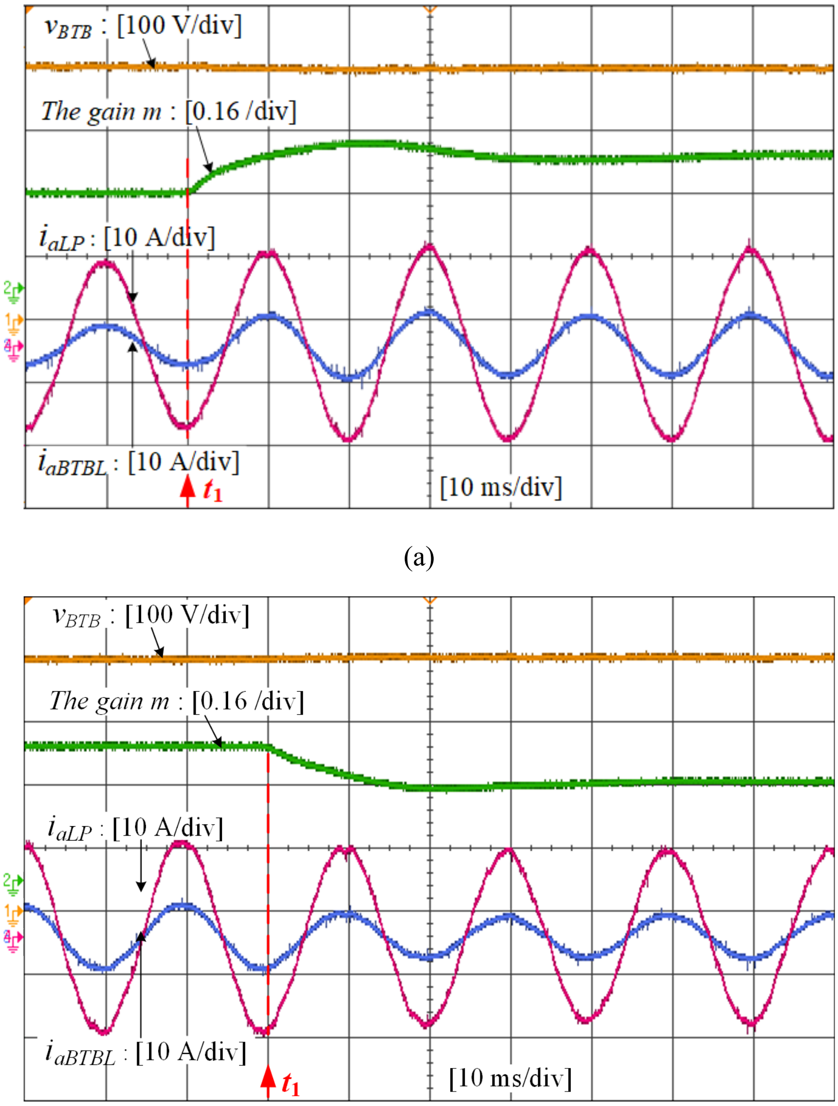

Figure 7.9. Dynamic results when changing BTB converter's power. (a) results of increasing BTB converter's power. (b) results of decreasing BTB converter's power.

7.5 Elimination of the Field-weakening Operation of the HPG

In this section, the elimination of field-weakening operation of the HPG in the APGC and effect on power losses is investigated. The engine emulator with the high-speed drive test bench is used to carry out relevant tests.

To compare the power losses in the PGC and APGC, system performances at a high speed, high power condition to emulate the cruise condition which takes the majority of a flight are demonstrated in Figure 7.10. In Figure 7.10 the speed setpoint generated from the engine model for the HPG is 15,000rpm, delivering 10.3kW power to the main DC bus.

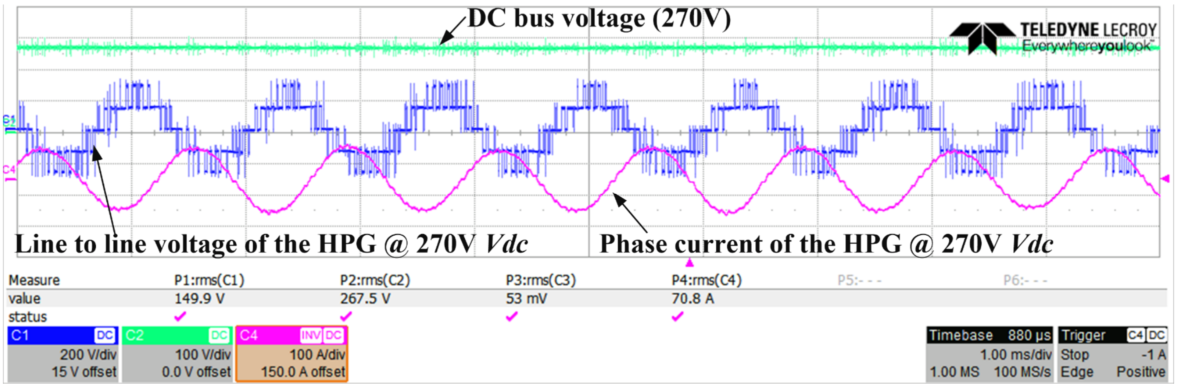

(a)

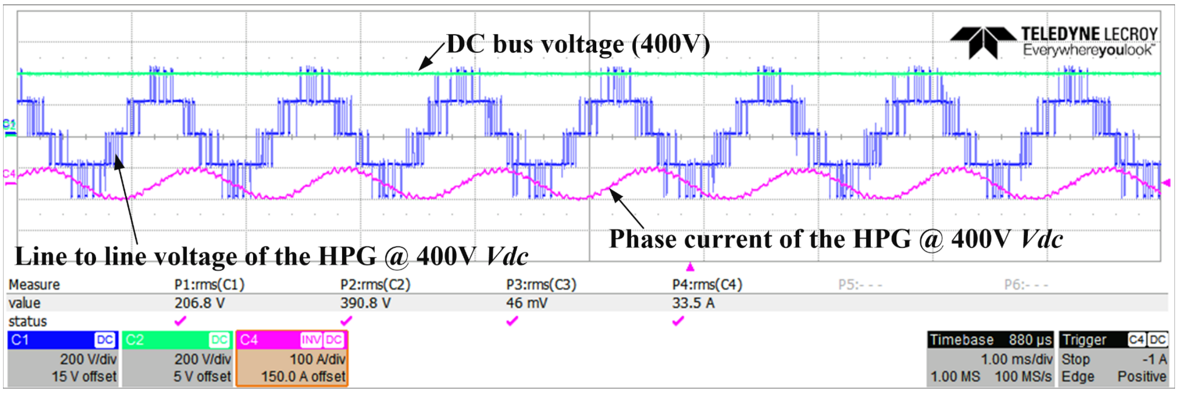

(b)

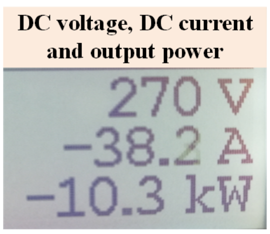

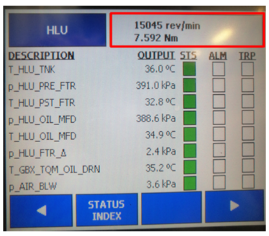

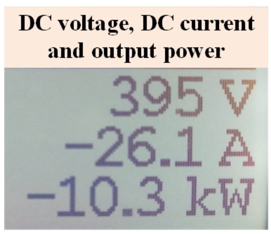

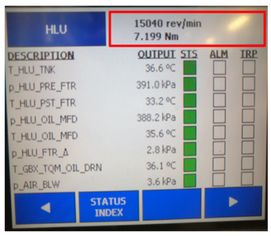

(c) (d) (e) (f)

Figure 7.10. Performance of the HP channel in cruise mode when the HPG operates at 15,000rpm and delivers 10.3kW active power. (a) voltages and phase current in the PGC. (b) voltages and phase current in the APGC. (c) Measured DC voltage, DC current and output power of the HPR in the PGC. (d) speed and torque (7.592Nm) of the prime mover in the PGC. (e) Measured DC voltage, DC current and output power of the HPR in the APGC. (f) speed and torque (7.199Nm) of the prime mover in the APGC.

In Figure 7.10, output power of the HP rectifier is 10.3kW for both PGC and APGC. The speed is fixed to be 15,000rpm to emulate the high-speed cruise mode. In the PGC, the torque of prime mover is 7.592Nm, while that of the APGC is 7.199Nm. Given the mechanical speed is 15,000rpm, this means the extracted mechanical power from the prime mover is 11.9kW and 11.3kW in the PGC and APGC, respectively. Hence, when generating the same active power, the prime mover needs to provide less power in the APGC than the PGC. The overall efficiency of HP power generation channel in the PGC is 10.3kW/11.9kW=86.5%, and that in the APGC is 10.3kW/11.3kW=91.1%. A 4.6% efficiency improvement is achieved at this operating point. As analysed in Chapter 4, this improvement comes from the elimination of field-weakening operation of the HPG. As can be seen in Figure 7.10(a), in PGC the magnitude of phase current is around 100A because of a high de-fluxing current component in *d*-axis. In Figure 7.10(b), the magnitude of phase current is only 50A since there is no de-fluxing component in the APGC.

Another relatively lower speed and lower power operating point is selected, where the speed of HPG is 13,000 rpm and delivered power to the main DC bus is 4.2kW, as exhibited in Figure 7.11. As can be seen in Figure 7.11(a), in the PGC, the magnitude of phase current is 58A. Figure 7.11(b) shows that the magnitude of phase current in the APGC is reduced to 30A because the *d*-axis current component for field-weakening purpose is removed. Thus, lower power losses of the HPG and HP rectifier can be expected.

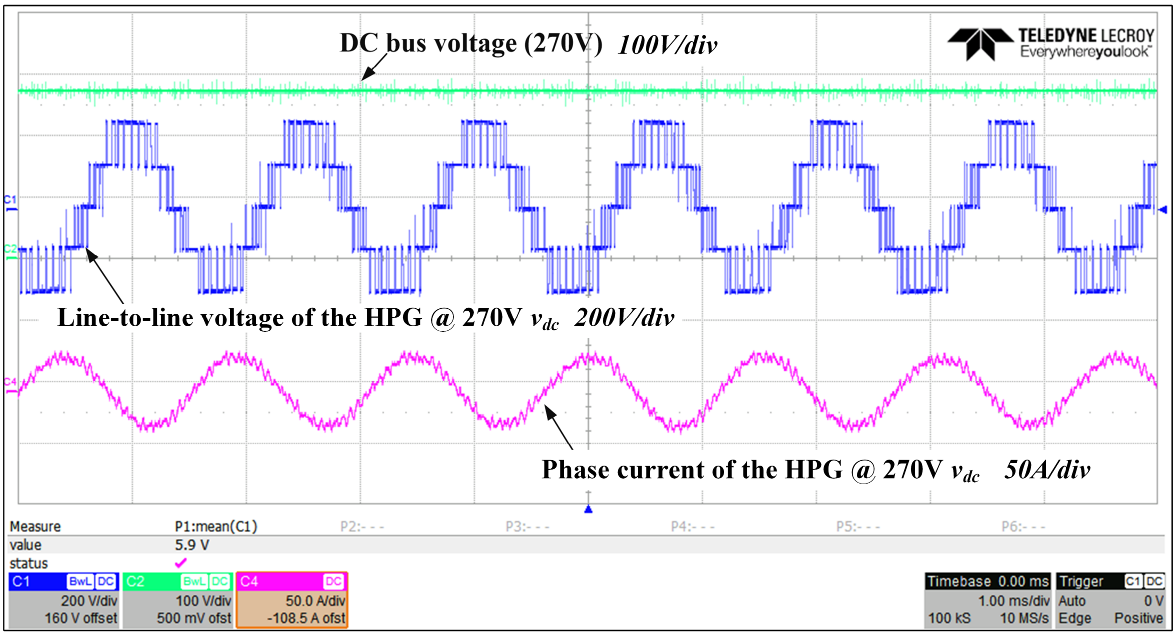

(a)

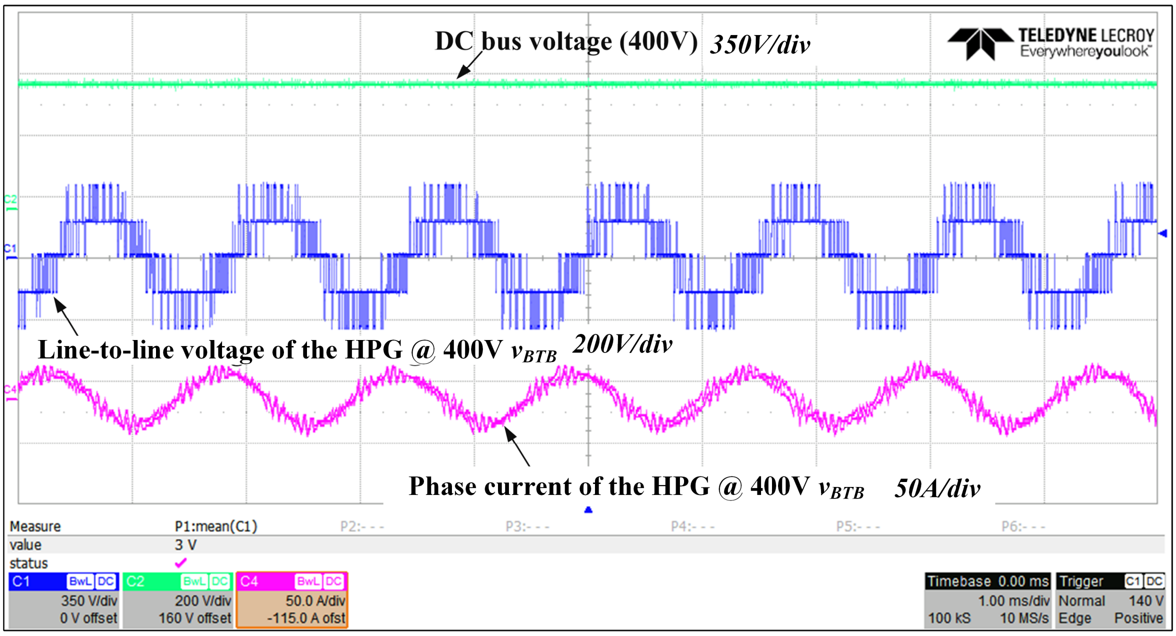

(b)

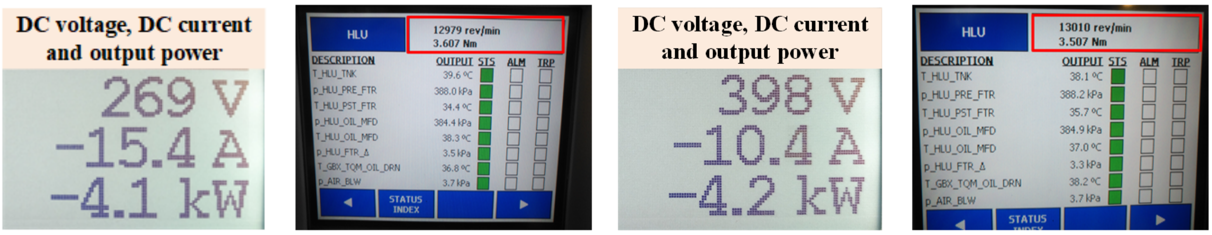

(c) (d) (e) (f)

Figure 7.11. Performance of the HP channel when the HPG operates at 13,000rpm and delivers 4.2kW active power. (a) voltages and phase current in the PGC. (b) voltage and phase current in the APGC. (c) Measured DC voltage, DC current and output power of the HPR in the PGC. (d) speed and torque (3.607Nm) of the prime mover in the PGC. (e) Measured DC voltage, DC current and output power of the HPR in the APGC. (f) speed and torque (3.507Nm) of the prime mover in the APGC.

Power losses in PGC and APGC are compared considering the entire HP power generation channel, including the HPG and HP rectifier. Results are given from Figure 7.11(c) to (f). The delivered active power to the main DC bus is 4.2kW for both PGC and APGC, as shown in Figure 7.11(c) and (e). The speed of prime mover is fixed to be 13,000rpm. As can be seen in Figure 7.11(d), in the PGC the torque of prime mover is 3.607Nm, while that of the APGC is 3.507Nm as shown in Figure 7.11(f). This means the extracted mechanical power from the prime mover is 4.9kW and 4.7kW in the PGC and APGC, respectively. Less power is consumed from the prime mover in the proposed APGC compared with PGC. Considering the identical generated active power (4.2kW), the overall efficiency of HP power generation channel in the PGC is 85.0%, and that in the APGC is 88.0%. A 3% efficiency improvement is achieved at this operating point.

It can be concluded that compared with the PGC, the proposed APGC reduces the HPG's stator current at a high speed. This is beneficial for improving efficiency and this has been achieved by eliminating of the field-weakening operation of the HPG in the APGC (due to an increased DC-link voltage in the BTB converter from a 270V v_{dc} to a 400V v_{BTB}).

A drawback brought by the increased available DC voltage is the increase of current harmonics. In a machine drive system, phase current ripple and harmonics increase with the increase of DC-link voltage [101]. To note, this issue can be addressed by adjusting the switching frequency or increasing the stator inductance of electrical machine.

7.6 Fault Tolerance Improvement of the APGC

In this section the results of fault tolerance improvement of the APGC in the case of either the LPR or HPR failure is presented. Results from healthy to post-fault operation are provided to support the designed fault control and transition scheme in Chapter 5.

7.6.1 Experimental Results for Cases with LPR Failure

To verify the fault tolerant control and seamless transition strategy from the healthy to post-fault operation state, experiments were carried out on the downscaled test rig described in Section 7.2.2, because it is too risky to perform the test in a high-power high-speed condition on the engine emulator.

Experimental results when the LPR fails without the proposed transition scheme are presented in Figure 7.12. There are three operating stages. In stage 1, a fixed resistor is connected to the DC bus, absorbing 1.2kW power. In stage 2, an electronic load performs as a CPL, consuming extra 550W power. In stage 3, PMW signals for the LPR is disabled to simulate the faulty scenario of the LPR. The droop gains for the HPR and LPR are set identical in the first two stages.

From Figure 7.12(a) one can see that i_{dcLP} and i_{dcHP} are equivalent in the first two stages due to identical droop gains. The DC bus voltage v_{dc} decreases from 268V in stage 1 to 265V in stage 2 because of increased power. After disabling the PWM for the LPR, i_{dcLP} drops to zero, while i_{dcHP} increases from 3.3A to 6.4A because the HPR delivers all the load power. v_{dc} restores to rated 270V in stage 3 as only the HPR is supplying power to the main DC bus, hence there is no need for power sharing using droop control. The results in Figure 7.12(a) are perfectly consistent with the simulation results in Figure 5.8(a) and (b) in Chapter 5.

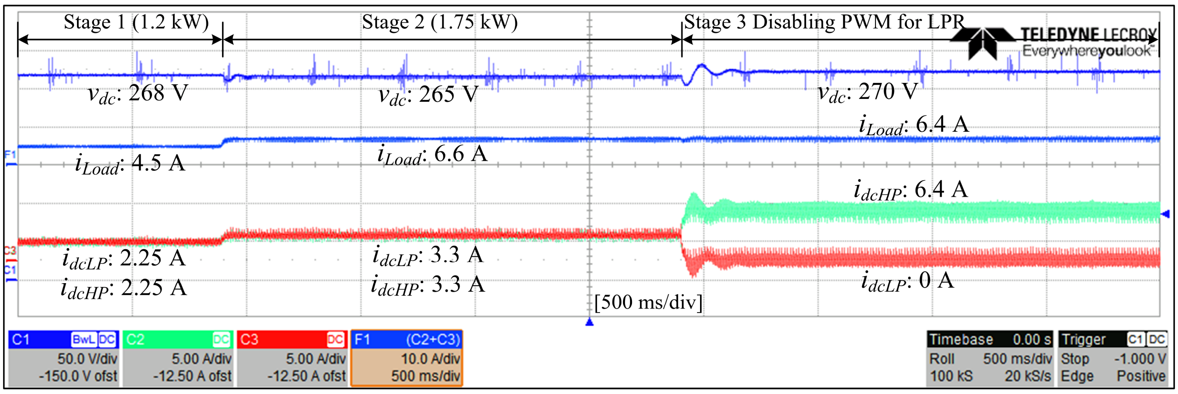

(a)

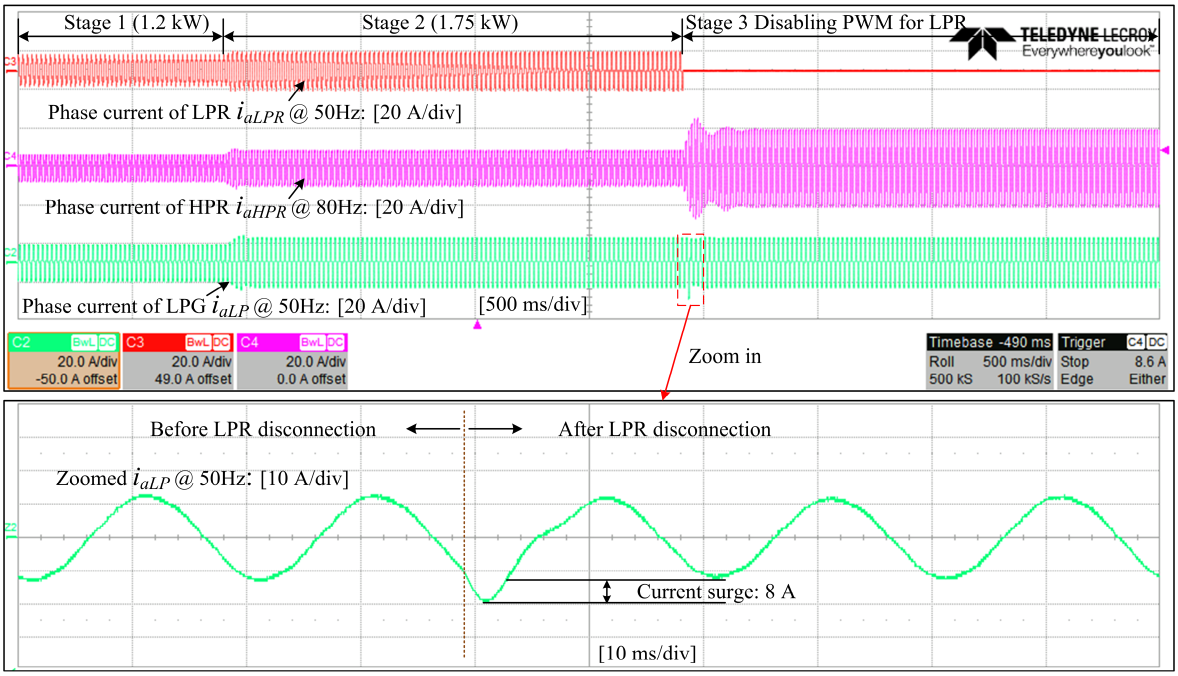

(b)

Figure 7.12. Experimental results in the scenario of disabling the LPR without voltage command initialization. (a) main DC bus voltage v_{dc}, rectifiers' DC side currents i_{dcLP} and i_{dcHP}, and total load current i_{Load}. (b) phase currents of the HPR, LPR, and LPG, and expanded figure of the LPG's phase current.

The experimental results of phase currents are exhibited in Figure 7.12(b). With the increase of power from 1.2kW to 1.75kW, the magnitude of all phase currents also increases. After disabling the PWM for the LPR, i_{aLPR} becomes zero. Power of the LPG is transferred to the

HP channel through the back-to-back converter and fed to the main DC bus through the HPR. i_{aHPR} boosts because the HPR carries all the load power. Evident current surge in the LPG's phase current i_{aLP} can be seen in the transient process of the LPR disconnection. As can be seen in the zoomed figure, the current surge is around 8A larger than the normal phase current. The results in Figure 7.12(b) are in accordance with the simulation results in Figure 5.8(d) and (f) in Chapter 5.

To remove the effect of disabling the LPR on the operation of the LPG and diminish the current surge in the LPG's phase current, the proposed voltage command initialization strategy in Section 5.3 is applied. Results are shown in Figure 7.13. Compared with Figure 7.12(b), the proposed method provides a much smoother transient performance in i_{aLP}. This can be attributed to the proper initialization of voltage command for the LPG when switching to a new control scheme from the healthy to post-fault operation. Overall, the results in Figure 7.12 and Figure 7.13 validates the proposed fault tolerance improvement and smooth transition when the LPR fails in the APGC.

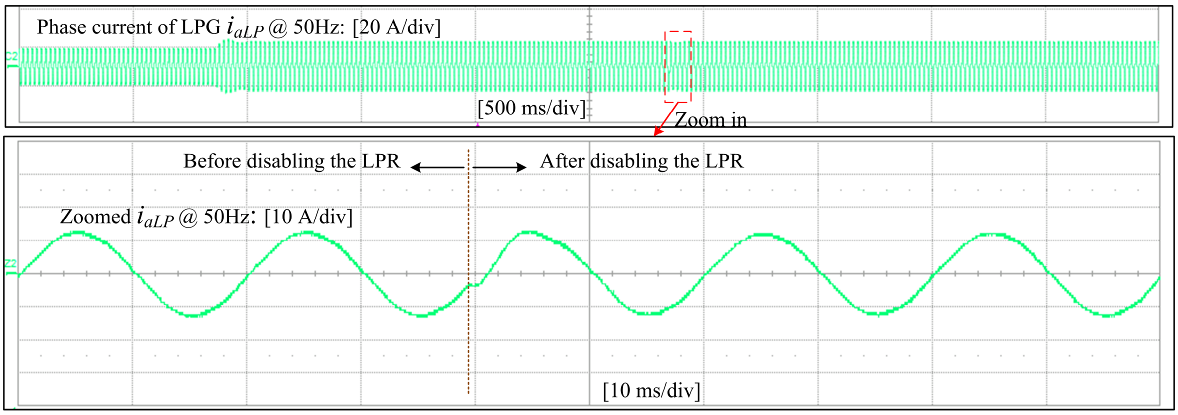

Figure 7.13. Experimental results in the scenario of disabling the LPR with the proposed voltage command initialization method.

7.6.2 Experimental Results for Cases with HPR Failure

Experimental results of the HPR failure without voltage command initialization are given in Figure 7.14. The operating stages and settings are the same as that in Figure 7.12. From Figure 7.14(a) it can be seen that the DC currents are same in the first two stages due to identical droop gains. The DC bus voltage drops with the increase of power. In the stage 3 where the PWM signals for the HPR are disabled, power of the HPG is transferred to the LP channel and fed to the main DC bus through the LPR. Hence, i_{dcHP} falls to zero and i_{dcLP} is doubled. The DC bus voltage restores to the rated value 270V because of the deactivation of droop control. The results in Figure 7.14(a) are consistent with the simulation results in Figure 5.10(a) and (b) in Chapter 5.

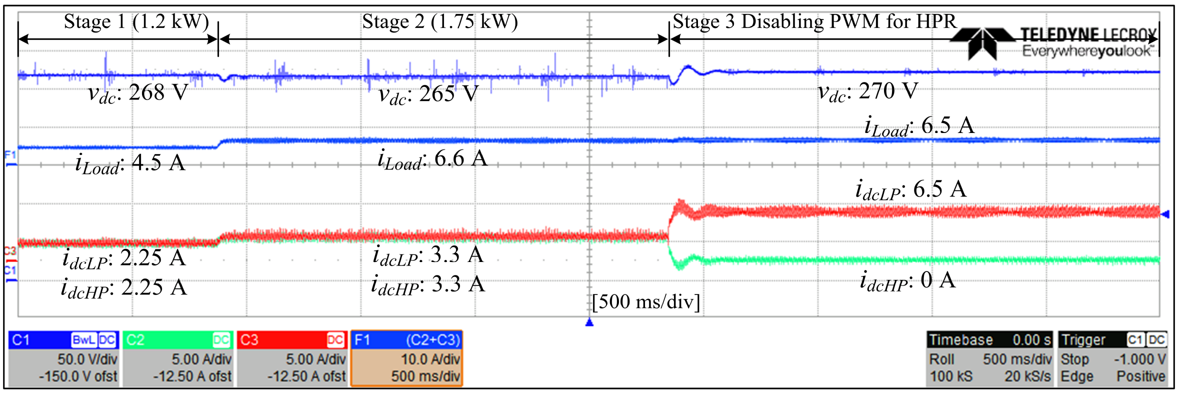

(a)

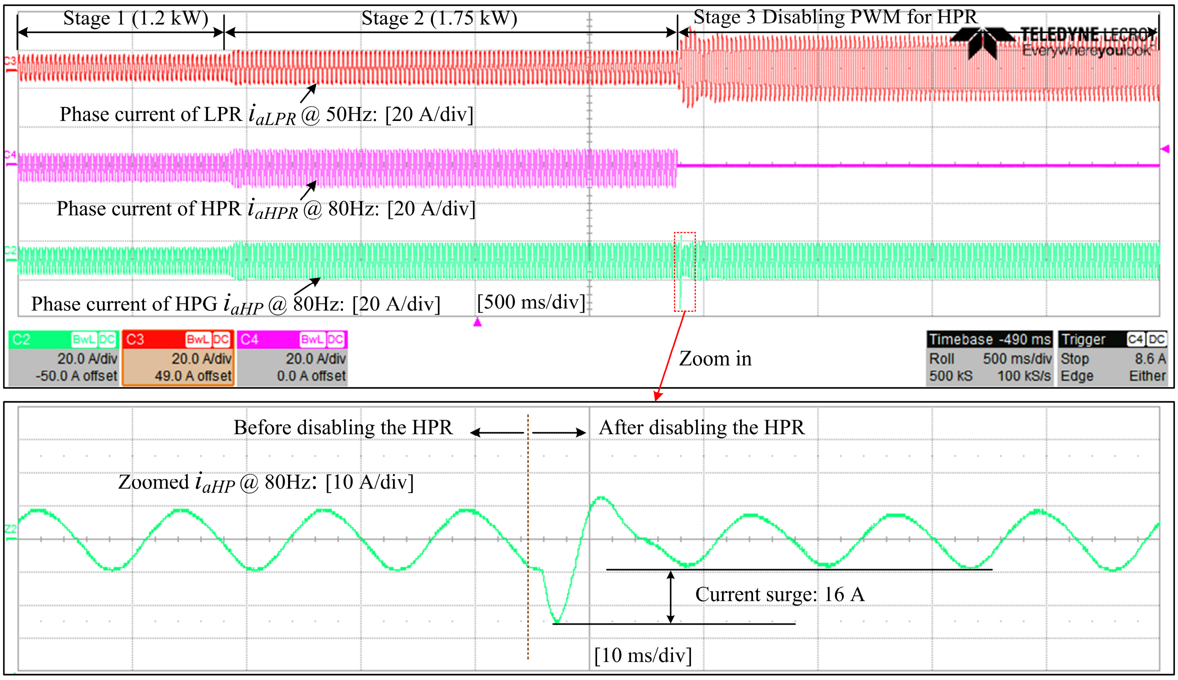

(b)

Figure 7.14. Experimental results in the scenario of disabling the HPR without voltage command initialization. (a) main DC bus voltage v_{dc}, rectifiers' DC side currents i_{dcLP} and i_{dcHP}, and total load current i_{Load}. (b) phase currents of the HPR, LPR, and HPG, and expanded figure of the HPG's phase current.

The experimental results of phase currents are shown in Figure 7.14(b). As the load power increases from 1.2kW to 1.75kW, the magnitude of all phase currents also increases. In the transient process when the PWM signals for the HPR are disabled, i_{aHPR} drops to zero, and

i_{aLPR} boosts significantly. Current surge of i_{aHP} is highlighted in a dash rectangular where 16A current surge is observed. The results in Figure 7.14(b) are consistent with the simulation results in Figure 5.10(d) and (f), showing that phase current surge occurs to the HPG if directly changing to the fault tolerant control without the proposed voltage command initialization.

The effectiveness of the voltage command initialization strategy proposed in Section 5.4.2 is tested as Figure 7.15 reports. Compared with Figure 7.14(b), transient performance of the HPG's phase current becomes smoother with limited current surge and recovery time. This is consistent with the simulation results shown in Figure 5.11 in Chapter 5, confirming that the proposed voltage command initialization strategy can provide a seamless transition from the normal operation to post-fault operation when disabling PWM for the HPR.

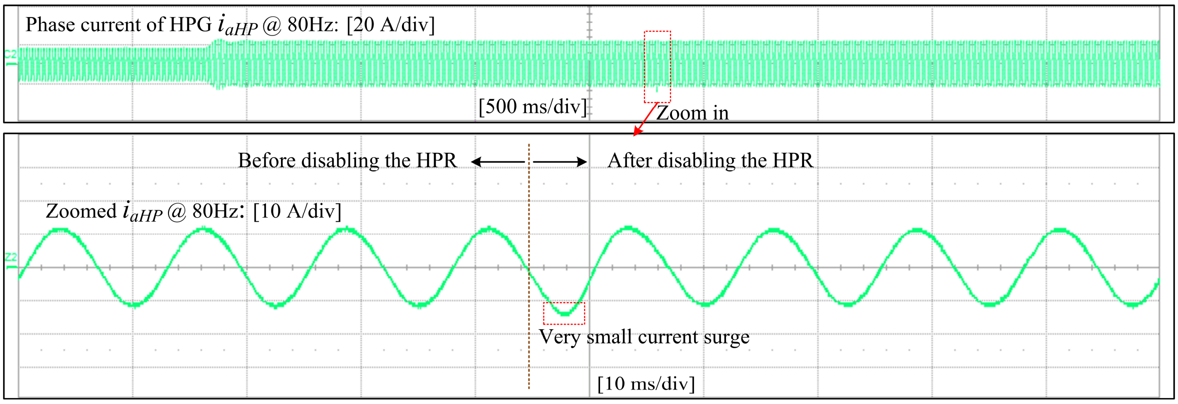

Figure 7.15. Experimental results in the scenario of disabling the HPR with the proposed voltage command initialization method.

7.7 Stability Enhancement

In this section the results of simultaneous stability improvement of both HVDC grid and engine in the APGC are presented. Experiments are carried out on the designed downscaled lab prototype in Figure 7.5. Results at different HPR/LPR power sharing ratios are presented, validating the theoretical analysis of HVDC grid stability in Chapter 6. The Power Coupling Effect (PCE) identified in Section 6.1 which hinders the simultaneous stability improvement of HVDC grid and engine in the PGC is solved by the APGC.

7.7.1 HVDC Grid Stability with Different HPR/LPR Power Sharing Ratios

In this subsection, the impact of power sharing ratio between the HPR and LPR on HVDC grid stability is examined. Experimental results are shown in Figure 7.16, where the DC bus voltage v_{dc}, DC currents of the HPR and LPR (i_{dc}^{HP} and i_{dc}^{LP}), and the phase current of the HPG i_a^{HP} are presented. Load power is set to be 3.0kW using the CPL.

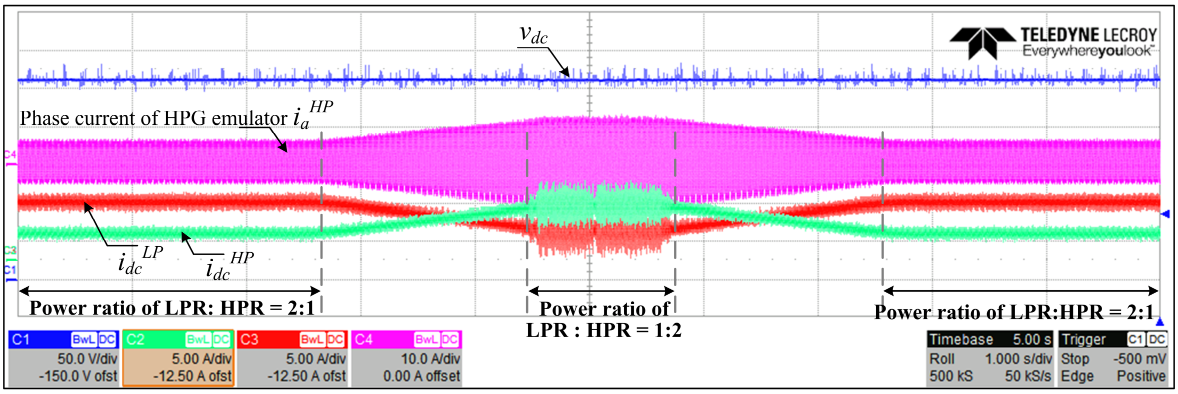

Figure 7.16. Experimental results for different power sharing ratios between the HPR and LPR under 3.0kW load power.

Initially, power sharing ratio between the LPR and HPR is 2:1, i.e., P_{LPR}: P_{HPR}= 2:1, It can be seen that the system is stable. Subsequently, power sharing ratio between the LPR and HPR gradually decreases to 1:2 (P_{LPR}: P_{HPR}= 1:2). It can be seen that the system tends to be unstable with severe oscillation in DC currents. Then, the power sharing ratio gradually restores to 2:1, and the system becomes stable again.

The operating points shown in Figure 7.16 are used to feed the source and load impedances in (6-4) and (6-24), and the magnitude of their impedances are shown in Figure 7.17. It can be seen that when P_{LPR}: P_{HPR}= 2:1, the source impedance $\|Z_s(s)\|$ is covered by the load impedance $\|Z_L(s)\|$ with around 6dB stability margin in the low frequency region. This indicates that the system can operate in a stable state according to the Middlebrook Criterion, which also matches with the experimental results in Figure 7.16. However, when the power ratio changes to P_{LPR}: P_{HPR}= 1:2, in the low frequency area shown by the red dashed rectangular, $\|Z_s(s)\|\approx \|Z_L(s)\|$, showing no stability margin. Therefore, this explains why the DC voltage and currents become distorted in Figure 7.16 when P_{LPR}: P_{HPR}= 1:2.

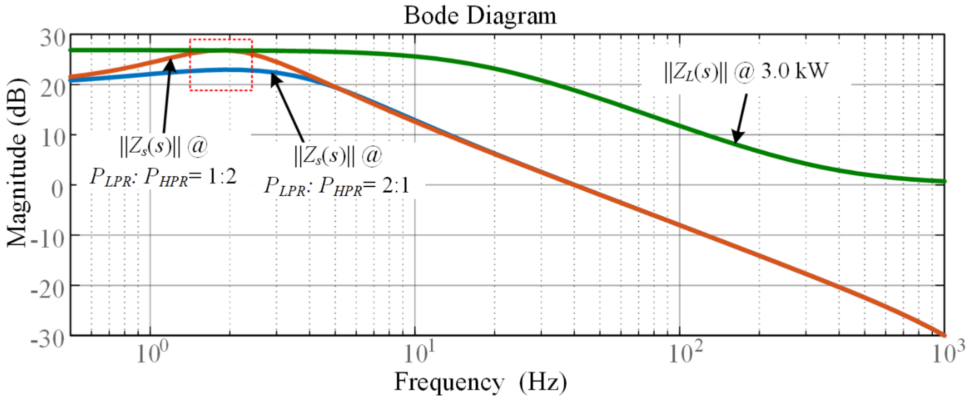

Figure 7.17. Bode plot of source and load impedances with different power sharing ratios under 3.0kW load power.

To quantitively analyse the system performance with different power sharing ratios, harmonic analysis of the *a*-phase current of the HPG (i_a^{HP}) is shown in Figure 7.18. From Figure 7.18(c) and (d) it can be seen that the total harmonic distortion (THD) of i_a^{HP} is 4.15% when P_{LPR}: P_{HPR}= 2:1, while it increases to 8.23% when P_{LPR}: P_{HPR}= 1:2. The results show that the LPR shares more power than HPR can improve system performance with reduced current ripple.

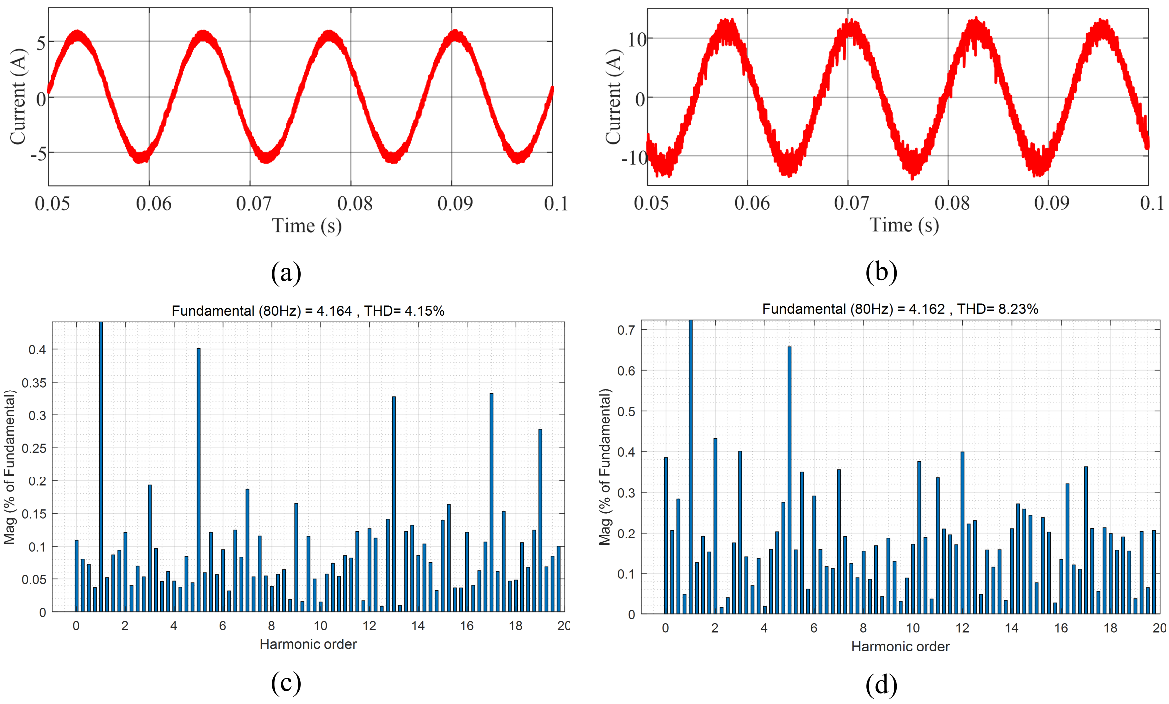

Figure 7.18. Wave spectrum of the phase current of the HPG with different power sharing ratios. (a) A-phase current of the HPG when P_{LPR}: P_{HPR}= 2:1. (b) A-phase current of the HPG when P_{LPR}: P_{HPR}= 1:2. (c) Harmonic spectrum of *a*-phase current of the HPG when P_{LPR}: P_{HPR}= 2:1. (d) Harmonic spectrum of *a*-phase current of the HPG when P_{LPR}: P_{HPR}= 1:2.

The results shown from Figure 7.16 to Figure 7.18 are in accordance with the theoretical analysis and simulation results in Chapter 6, confirming that increasing the proportion of the LPR's power contributes to a more stable HVDC grid.

7.7.2 Engine Performance with Different Power Offtake Ratios

The engine performance with different power offtake ratios between the HP spool and LP spool is investigated based on a multi-spool turbofan model [73], [74]. The maximum take-off (MTO) mode is selected as an example of the high-power settings of engine. Results are exhibited in Figure 7.19.

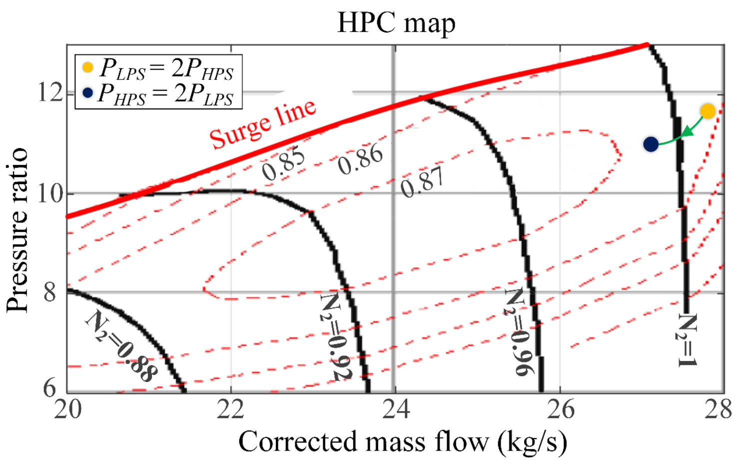

(a)

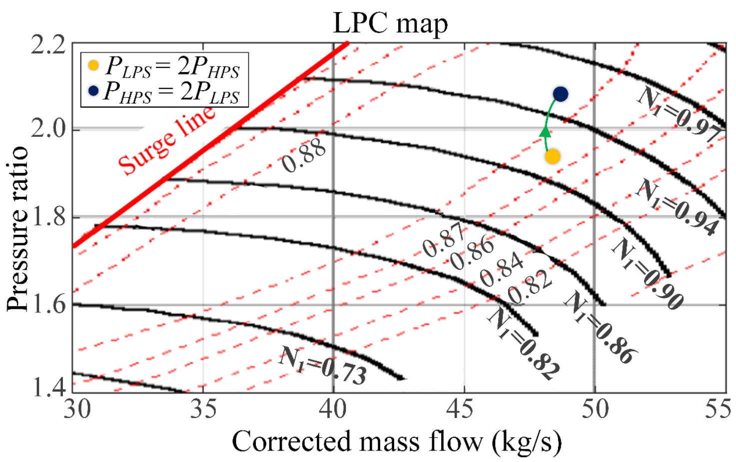

(b)

Figure 7.19. Compressor maps in the MTO mode. (a) HPC map. (b) LPC map. The arrow in green represents the direction that the proportion of HP spool's power increases.

Figure 7.19(a) presents the HPC map and operating points with different power ratios. It can be seen that when the mechanical power extracted from the LPS (P_{LPS}) is double than that of the HPS (P_{HPS}), i.e., P_{LPS}=2P_{HPS}, the speed of the HPS has exceeded the maximum allowable speed (N_2=1, where normally N_2 is an indicator is a cockpit gauge which presents the rotational speed of the high-pressure engine spool). Conventionally, to decrease the speed of the HPS, pilot needs to decrease the engine throttle. While with modern multi-generator topology within a more electric engine, overspeed of the HPS can be addressed by changing the powers ratios between the HPS and LPS. In Figure 7.19(a), when P_{HPS}=2P_{LPS}, i.e., extracting more mechanical power from the HPS than LPS, air mass flow and pressure ratio decrease back to the allowable region within N_2=1. And the operating point moves closer to the central efficiency contour with a higher operation efficiency.

From the viewpoint of the LPC's map, as shown in Figure 7.19(b), increasing the proportion of the LPS's power will lead to the decrease of the LPS's speed. Since the thrust is proportional to the speed of LPS, this will decrease the thrust. Moreover, the operating point moves to a lower efficiency contour.

The results in Figure 7.19 show that in the high-power settings of engine such as maximum take-off, extracting more mechanical power from the HPS than LPS can avoid the overspeed and potential instability of the HPS and maintain thrust, which is beneficial for engine stability and efficiency.

7.7.3 Stability Improvement of the HVDC Grid and Engine Using the APGC

From the analysis in Chapter 6 and the experimental results in Sections 7.7.1 and 7.7.2, it can be seen that more electrical power from the LPR is beneficial for the HVDC grid stability. However, in the high-power settings of engine, such as maximum take-off, extracting more mechanical power from the HPS than LPS can enable the HP compressor to operate within the allowable speed region.

In the PGC, as discussed above, these two goals cannot be met at the same time due to the lack of internal power exchange path. In contrast, in the proposed APGC, the BTB converter can transfer electrical power from the HP channel to LP channel. Hence, the stability improvement of the HVDC grid and engine can be expected. This point will be experimentally investigated in this section.

In the following experiments, power sharing ratio between the HPR and LPR is set as 1:2, i.e., P_{HPR}: P_{LPR}= 1:2. To simulate the situation that offtaking more mechanical power from the HPS than the LPS, power ratio between the HPG's power (P_{HPG}) and LPG's power (P_{LPG}) is set as 2:1. Thus, in this case, the BTB converter needs to transfer electrical power from the HP channel to the LP channel.

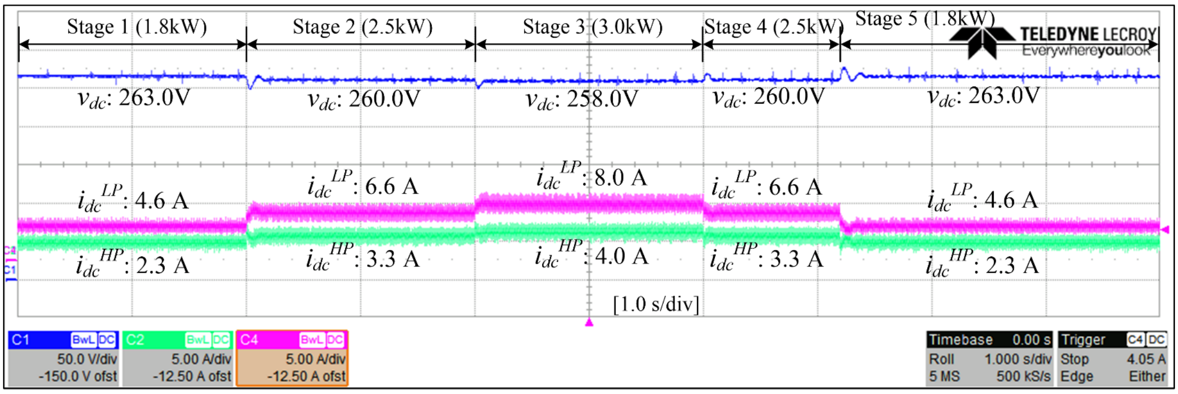

Figure 7.20. DC bus voltage and DC currents with 1.8kW, 2.5kW and 3.0kW load powers.

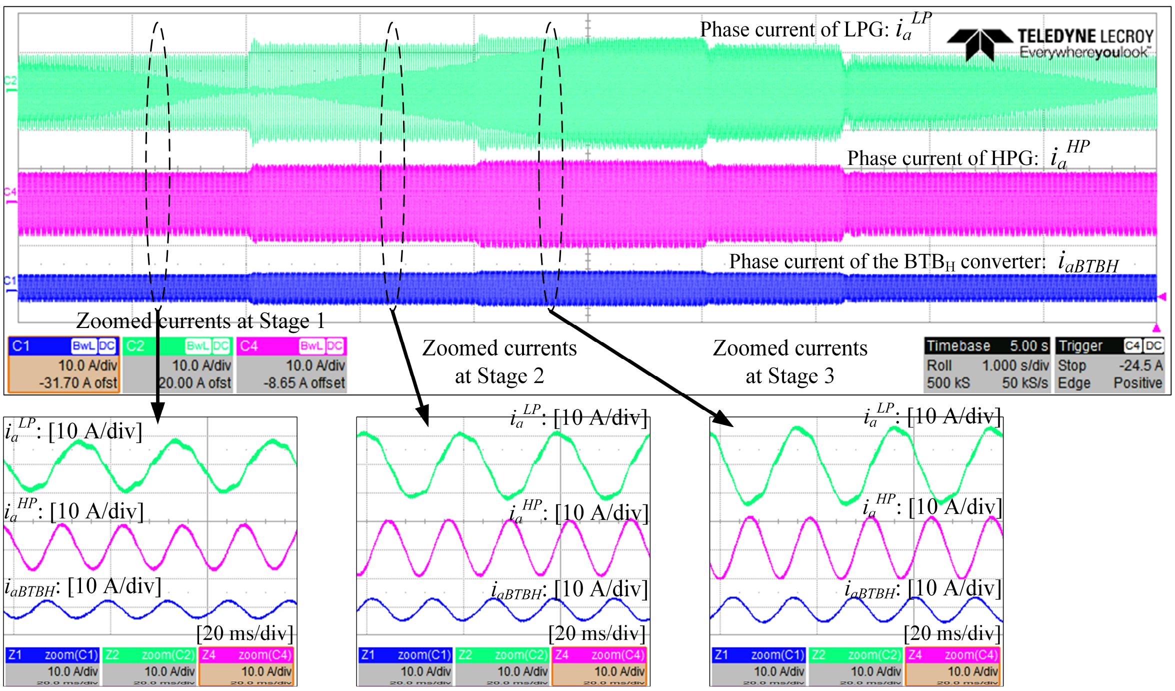

Figure 7.21. Phase currents of the HPG, LPG and BTB$_H$ converter.

Control performance of the APGC under various load power conditions is demonstrated in Figure 7.20 and Figure 7.21. The whole process is divided into five stages. At stage 1 and 5, the CPL is deactivated and only a 40Ω CIL consumes 1.8kW power. At stage 2 and 4, the CPL is activated and the total load power increases to 2.5kW. At stage 3, the CPL consumes more power, resulting in a 3.0kW total load power.

The results of DC bus voltage (v_{dc}), DC currents of the rectifiers (i_{dc}^{HP} and i_{dc}^{LP}) are presented in Figure 7.20. It can be seen that with the increase of load power, v_{dc} deviates from the rated value 270V to 263.0V, 260.0V and 258.0V due to the droop control effect. i_{dc}^{LP} is double of i_{dc}^{HP} in the whole process (4.6A/2.3A, 6.6A/3.3A, 8.0A/4.0A), which means the output power of the LPR is successfully controlled to twice that of the HPR. The phase currents of the HPG, LPG and BTB_H converter are exhibited in Figure 7.21. It can be seen that as the load power increases, phase currents of the HPG and LPG increase as they need to supply more power. Phase current of the BTB_H converter also increases because the BTB converter transfers more power from the HP channel to LP channel. It should be noted that the phase current of the LPG distorts, this is due to the inherent distortion of the utility grid voltage. Based on the above-mentioned power sharing ratios, the relations of power flow at different stages are summarized in Table 7-2.

Table 7-2. Relationships of power flow at different operating stages.

	Total load power	Power of the HPR (P_{HPR})	Power of the LPR (P_{LPR})	Extracted power from the HPS (P_{HPG})	Extracted power from the LPS (P_{LPG})	Power through the BTB converter
	P_t	$\frac{1}{3}P_t$	$\frac{2}{3}P_t$	$\frac{2}{3}P_t$	$\frac{1}{3}P_t$	$P_{HPG} - P_{HPR} = \frac{1}{3}P_t$
Stage 1 & 5	1.8 kW	0.6 kW	1.2 kW	1.2 kW	0.6 kW	0.6 kW
Stage 2 & 4	2.5 kW	0.83 kW	1.67 kW	**1.67 kW**	0.83 kW	0.83 kW
Stage 3	3.0 kW	1.0 kW	2.0 kW	**2.0 kW**	1.0 kW	1.0 kW

To verify the values of power flow in Table 7-2, the operating status of the HPG simulator is recorded as shown in Figure 7.22. As shown in Table 7-2, ideally the HPG's power P_{HPG} should be 1.67kW and 2.00kW at stage 2 and 3, respectively. The actual results in Figure

7.22 are 1.78kW and 2.10kW, which are well matched with the designed values considering the inevitable power losses.

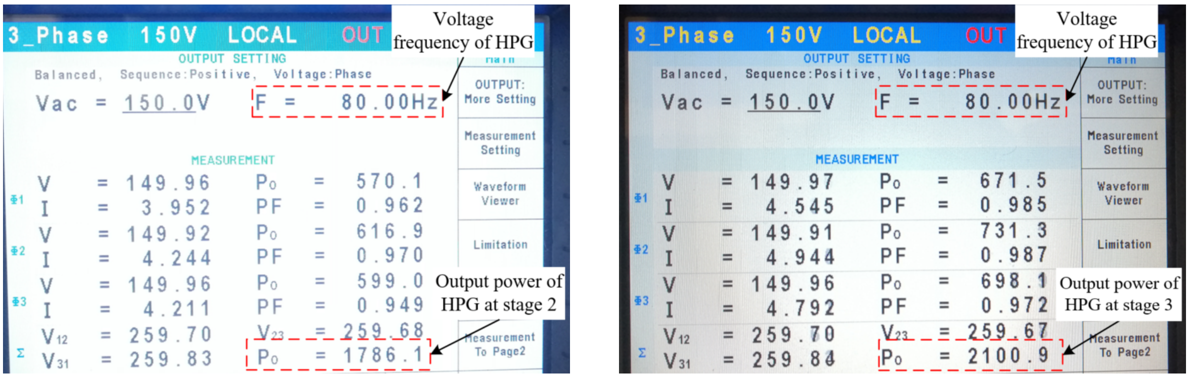

(a) (b)

Figure 7.22. Output power of HPG simulator at (a) Stage 2. (b) Stage 3.

From the results in Figure 7.20 to Figure 7.22**,** it can be seen that the LPR delivers two third of total power to the main DC bus and the HPG extracts two third of total power from the HPS of the engine. The BTB converter transfers one third of total power from the HP channel to the LP channel. The flexibility in power flow is attributed to the BTB converter, which provides a power flow path between the HP and LP power generation channel. Hence, the inherent Power Coupling Effect of the PGC identified in Section 6.1 can be removed using the APGC by transferring power from the HP to LP channel through the BTB converter. Compared with the PGC, the proposed APGC can enhance stability for both HVDC grid and engine in the high-power settings of engine.

7.8 Potential Challenges from the Down-scale Lab Prototype to a Practical Full-scale System

In the above subsections, the effectiveness of the postfault reconfiguration, fault tolerant control, and power decoupling effects of the APGC has been verified on the downscaled lab prototype. However, there are still some challenges in implementing the proposed method to a practical full-scale system. Although this is not the main focus of this research, it is still valuable to find out the differences and pave the way for a potential application in real full-scale system. The potential challenges may include:

- The scaling of essential variables such as generator's speed and torque used for feedback control. In [126], [127], the power-level adjustment between the down-scale and full-scale systems is achieved through adaptation of coefficients for the torque and speed between the simulation and real equipment. Different operating limitations for speed and torque should be set for the down-scale and full-scale systems. A major drawback of this method is that it is only valid for the steady-state analysis since the dynamic similitude of the down-scale and full-scale systems are very different.
- To investigate the dynamic performance of a full-scale system through an available down-scale system, time should be scaled as well. The author's research team has studied the time-scaling issue in depth, and relevant research outcomes have been published in [11]. A novel time-scaling method was proposed in to implement data exchange between the simulation model and the generator drive stand for nonlinear system transient emulation. In this scheme, all variables are scaled in the hardware, while time is scaled in the simulation to realize flexible real-time hardware-in-the-loop experimentation. Based on the time-scaling method, a criterion for scaled shaft emulation is introduced where not only the shaft inertia but also the gear ratio, speed- and time-scaling factors are involved in determining if the shaft emulation is valid or need mitigation.

Moreover, in the lab prototype an autotransformer and a programable AC source are used as the LPG and HPG simulator, respectively. There are some differences between the generator simulators and the actual generators. To be specific:

- The actual generators have shaft inertia while the generator simulators do not. The shaft inertia determines the rate of change of speed, which correlates to the back EMF and fundamental frequency of the actual generators. As a contrast, for the generator simulator, there is no back EMF, and the fundamental frequency is manually changed.
- Another difference is related to the control issues. For an electrical generator for high-speed applications, the electrical parameters are relatively small. For example, for the AEGART electrical machine developed under the frame of the Clean Sky project [128], the stator resistance and inductance are 1.058 mΩ and 100 μH, respectively [129]. Such a small impedance causes the motor current to change quickly, resulting in difficulty for discrete digital control. Moreover, the machine parameters depend on operating conditions, such as stator current, fundamental frequency, and temperature

[130]. All these issues cause difficulty in control. As a contrast, these nonlinearities do not exist in the generator simulator, which ease the control design.

Although there are some differences between the actual system and the lab prototype, from the perspective of fault-tolerant control and power control that this Thesis focuses, these differences do not cause significant impact. The idea of system reconfiguration, fault tolerant control, and power control are the same, while the control gains and control bandwidth should be adjusted for a larger scale system.

7.9 Chapter Summary

This chapter dealt with the experimental validation of the theoretical results accumulated from the previous Chapters. An engine emulator integrated with high-speed test platform and a downscaled lab prototype of the APGC are described. The experimental findings can be summarised as follows:

- The essential functionalities of the APGC in normal operation state are verified, including the main DC bus voltage control, power sharing between rectifiers, the DC-link voltage control of the BTB converter, and phase current synchronization of the LP channel's phase currents.
- Field-weakening operation of the HPG is eliminated in the high-speed region in the APGC. This helps to significantly reduce the power losses compared with the PGC.
- The fault tolerance capability in the case of rectifier failure is improved in the APGC compared with the PGC. The generators can normally operate even the main rectifier is disabled. This is achieved through system reconfiguration using the BTB converter and fault tolerant control.
- Compared with the PGC, stability of both engine and HVDC grid can be enhanced simultaneously in the APGC. This is achieved by delivering more electrical power through the LP rectifier than the HP rectifier to the DC bus, whilst extracting more mechanical power from the HP spool than the LP spool.

Summarising, the reported experimental results in this chapter have confirmed all the key theoretical findings of this Thesis

Chapter 8. Conclusion and Future Work

8.1 Conclusion and Discussion

The Thesis proposes a novel advanced power generation centre (APGC) architecture for the More-Electric Aircraft application. Compared with the single DC-bus topology PGC, the proposed APGC integrates an additional AC/AC bridging converter to establish a bidirectional power flow bridge between the HP power generation channel and the LP channel. In this Thesis, the bridging converter is specifically selected as a back-to-back (BTB) converter due to the maturity of control and modulation schemes, and high reliability compared with other AC/AC candidates such as the matrix converter. The BTB converter makes the APGC much more flexible than the PGC in terms of power flow and generator control. Compared with the PGC, the main contributions brought by the APGC can be highlighted as follows:

- Allowing the permanent magnet machine-based HPG operate at a high speed without field-weakening operation. This helps to reduce power losses caused by the significant de-fluxing current of the HPG and improve efficiency.
- Allowing post-fault operation and uninterruptible power supply of generators to the onboard loads in the case of main rectifier failure.
- Improving stability of the onboard HVDC grid and the engine in the high-power settings of engine.

In Chapter 2, the state-of-the-art technologies of aircraft electrical power systems including power generation, distribution, and utilization were reviewed. For power generation centres embedded in a more electric engine, the dual-channel single HVDC bus PGC is a competitive candidate in terms of no need for reactive power compensation equipment and for reduction of power losses in cables. However, the requirement of field-weakening operation of the HPG, no fault tolerance to rectifier failure, and incapability to enhance stability of HVDC grid and engine, makes this PGC in need of revision. An APGC integrated with an AC/AC bridging converter between the HP and LP power generation channel is proposed to cope with these issues. Details of realization have been presented in the subsequent chapters.

In Chapter 3, the single HVDC bus PGC is studied. Control schemes for the PGC are developed, including current-loop control, power sharing between rectifiers, field-weakening control, and DC bus voltage control. These contents lay essential foundation in terms of control for the proposed APGC. The concept of electrical power transfer (EPT) has been presented. Some amount of power can be exchanged between the LP and HP spool through the electrical path. The case that EPT from the LP spool to HP spool is studied, where the LP generator supplies power for both HP machine and onboard loads. The simulation results of engine performances confirm the improvement of fuel efficiency and compressor surge margin.

In Chapter 4, an APGC with a BTB converter is proposed. The BTB converter can transfer power between the LP and HP power generation channels and between engine shafts. A phase current synchronization strategy is reported to regulate the BTB converter. By applying this method, DC-link voltage of the BTB converter can be stabilized and the phase currents of the LPG, LPR and BTB converter can be controlled in phase. The magnitude ratio between phase currents is equivalent to the power ratio. Passive components are designed as well considering the overall operating range. Compared with the PGC, the APGC can allow the HPG operate at a high speed without field weakening operation. All the stator currents of the HPG can be distributed on the q axis without the need for de-fluxing current on the d axis. Hence, at a given torque, stator current of the HPG is significantly reduced in the APGC. At the selected operating point (HPG @ 20,000 rpm, LPG @ 7,000 rpm, load power 20 kW), the overall efficiency is improved from 94.0% in the case of the PGC to 95.0% in the APGC in simulation.

In Chapter 5, the fault tolerance capability of the APGC to deal with the main AC/DC rectifiers failure is investigated. In the PGC, the generator has to be stopped if the associated rectifier is detected. However, the APGC allows generators to continue normal operation to supply continuous power when one of the main rectifiers fails through reconfiguration of the system. The BTB converter provides an additional power flow path for the generators when the original rectifier is disconnected. System reconfiguration and fault tolerant control schemes are tailored considering both cases of the HPR and LPR failure. To avoid the abrupt change of generator current and current surge in the transient of disconnecting the faulty rectifiers, a seamless transition strategy is proposed by voltage command initialization when switching to a new controller. Simulation results verify the fault tolerance improvement of the APGC and the effectiveness of the proposed control schemes.

In Chapter 6, a detailed stability analysis for the HVDC grid is carried out using a transfer function-based impedance model and a state-space model. The analytical findings reveal that increasing the proportion of the LPR’s electrical power over the HPR can lead to a more stable HVDC grid. However, due to the Power Coupling Effect of the PGC identified in this chapter, it means increasing the proportion of power offtake from the LPS. This will lead to overspeed and potentially instability of the HPS at high power settings of engine. In contrast, the proposed APGC removes the Power Coupling Effect by transferring power from the HP channel to the LP channel, allowing the extraction of more mechanical power from the HPS than the LPS, whilst the LPR delivers more electrical power than the HPR to the DC bus. As a result, the stability of HVDC grid and engine can be ensured simultaneously.

Finally, experimental validation of the theoretical results accumulated from the previous chapters has been performed in Chapter 7.

8.2 Future Works

Although the work in this Thesis has addressed several research points of the proposed APGC in terms of power management, control, post-fault operation and stability analysis, there are possible points which could be investigated further.

- **Coordinated control and integration of energy storage system**

Energy storage system (ESS) is of interest which may help reduce the generator ratings, improve dynamics performance of the main DC bus voltage, provide a back-up electrical power supply and adjust the power flow such as peak shaving to meet the load demand [102], [103]. A coordinated control strategy needs to be developed to deal with the power balance between main generators in the APGC and ESS. When the load power demand exceeds the generator capacity, the ESS can operate in the discharging mode and supply power to the loads. If more than one set of ESS is deployed onboard, the ESS with higher state of charge is supposed to supply more power to the load.

- **Active current injection for the generators to reduce current harmonics**

The BTB converter in the APGC can be regarded as a static synchronous compensator (STATCOM) [105], behaving as a source or sink of both active power and reactive power. Thus, the required reactive power of generators can be provided by the BTB converter, and the main AC/DC rectifiers only need to deliver active power to the DC bus. This could help reduce the required power rating of the main rectifiers. Moreover, the BTB converter can be controlled to injected certain order current harmonics through pulse width modulation technique, this can be used to counter the current harmonics in generators and reduce THD in stator currents.

- **Instantaneous power control for the BTB converter to improve power control accuracy and dynamic response**

In Chapter 4, a phase current synchronization (PCS) strategy was introduced to regulate the transferred power through the BTB converter. By synchronizing the phase currents of the LPG and BTB_L converter (the BTB_L converter is the AC/DC converter connected to the LPG within the BTB converter), electrical power transferred from the LPG to the BTB converter can be determined by the magnitude ratio of phase currents. Although this PCS method is proved to be effective, the transferred power through the BTB converter using this method is not directly controlled and it suffers from low power control dynamics. Moreover, the PCS control performance is very sensitive to controller parameters, which means it is hard to achieve optimal performance. Once the control parameters are not well tuned, the system will tend to be unstable. Besides, the PCS method cannot control the transferred active power and reactive power independently.

To achieve a fast and accurate power control, in recent years the instantaneous power control (IPC) emerges as a preferrable solution. The concept of IPC was firstly proposed by Akagi *et. al.* based on the *pq* theory to compensate the reactive power in a balanced three phase system with an ideal voltage source [117]. Then it was further successfully developed for power control in more complex applications such as unbalanced grid and load [118], advanced electrical machine drives [119], and pulse-width modulated (PWM) rectifier with phase delays [120]. To address these issues with the PCS method, in our future work, we aim to develop an IPC method to control the power flow of the BTB converter.

Appendix A Reference Frame Transformation

A three phase quantities (in *abc* frame) can be transformed into a two-axis frame (*dq* frame) rotating at a synchronous speed denoted by ω. This is called *dq* transformation. The *dq* transformation equation is given by [104]:

$$f_{dq} = T\left[\omega t\right] f_{abc} \tag{A-1}$$

where f is a lumped variable of voltage, current, or flux linkage of an electrical machine.

The *dq* transformation matrix is defined as:

$$\mathbf{T}[\omega t] = K \begin{bmatrix} \cos(\omega t) & \cos(\omega t - \frac{2\pi}{3}) & \cos(\omega t + \frac{2\pi}{3}) \\ -\sin(\omega t) & -\sin(\omega t - \frac{2\pi}{3}) & -\sin(\omega t + \frac{2\pi}{3}) \end{bmatrix} \tag{A-2}$$

K is a constant coefficient depending on the type of transformation conventions. K is equal to 2/3 for peak conventions and $\sqrt{\frac{2}{3}}$ for power convention [104]. ω is the synchronous electrical speed in rad/s. ωt is the rotor angle position in degree. The diagram of *dq* transformation is shown in Figure A.1.

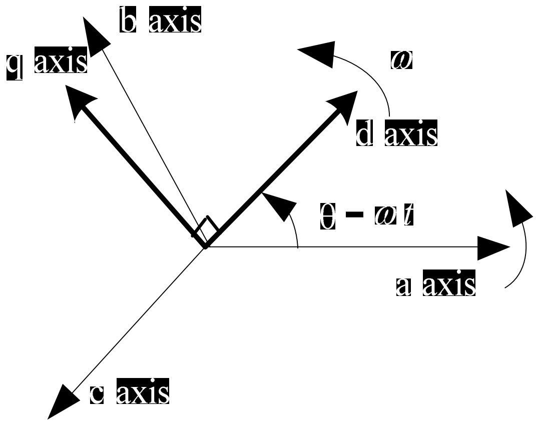

Figure A.1: The vector diagram of *dq* transformation

Similarly, a two-axis frame (*dq* frame) can be transformed into a three-phase frame. This is called inverse *dq* transformation. An inverse *dq* transformation is given by:

$$f_{abc} = T^{-1}[\omega t] f_{dq} \tag{A-3}$$

where the inverse *dq* transformation matrix is defined as:

$$\mathbf{T}^{-1}[\omega t] = \begin{bmatrix} \cos(\omega t) & -\sin(\omega t) \\ \cos(\omega t - \frac{2\pi}{3}) & -\sin(\omega t - \frac{2\pi}{3}) \\ \cos(\omega t - \frac{2\pi}{3}) & -\sin(\omega t + \frac{2\pi}{3}) \end{bmatrix} \tag{A-4}$$

Appendix B Stator Winding Voltage Equations of a PMM in the DQ Frame

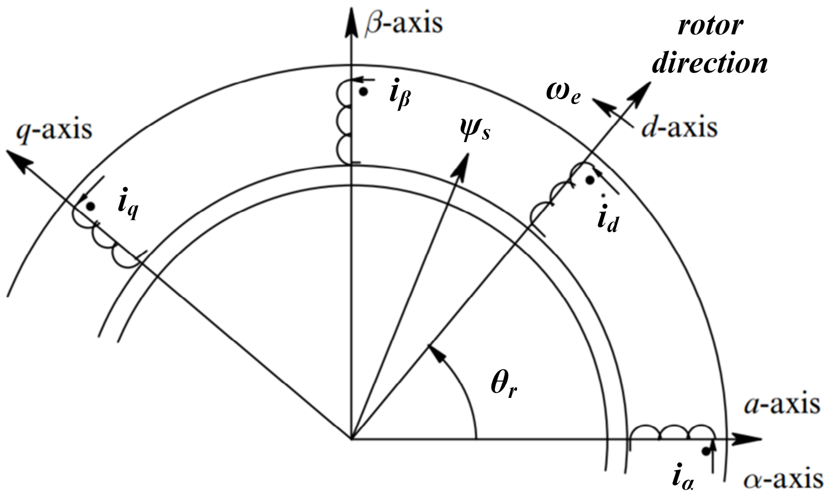

Figure B.1. Diagram of stator windings in $\alpha\beta$ and dq frame.

To derive the dq stator winding voltages, firstly considering a set of orthogonal $\alpha\beta$ stator windings which are affixed to the stator, as shown in Figure B.1, where the α-axis is aligned with the stator a-axis. In $\alpha\beta$ stator windings, the voltage equations can be expressed as follows:

$$\begin{cases} v_\alpha = R_s i_\alpha + \dfrac{d}{dt}\psi_\alpha \\ v_\beta = R_s i_\beta + \dfrac{d}{dt}\psi_\beta \end{cases} \tag{B-1}$$

where v_α and v_β are the stator winding voltages in $\alpha\beta$ frame. i_α and i_β are the stator winding currents in $\alpha\beta$ frame. ψ_α and ψ_β are the stator winding flux linkage in $\alpha\beta$ frame. R_s is the stator winding resistance.

The two equations in (B-1) can be combined by multiplying both sides of the β-axis voltage equation by the operator j and then adding to the α-axis voltage equation. Then the stator winding voltage can be written in space vectors as follows:

$$\vec{V}_{\alpha\beta} = R_s \vec{I}_{\alpha\beta} + \frac{d}{dt}\vec{\psi}_{\alpha\beta} \tag{B-2}$$

where $\vec{V}_{\alpha\beta} = v_\alpha + jv_\beta$, $\vec{I}_{\alpha\beta} = i_\alpha + ji_\beta$, $\vec{\psi}_{\alpha\beta} = \psi_\alpha + j\psi_\beta$.

As can be seen from Figure B.1, the current, voltage, and flux linkage space vectors with respect to the α-axis are related to those with respect to the d-axis:

$$\begin{cases} \vec{V}_{\alpha\beta} = \vec{V}_{dq} \cdot e^{j\theta_r} \\ \vec{I}_{\alpha\beta} = \vec{I}_{dq} \cdot e^{j\theta_r} \\ \vec{\psi}_{\alpha\beta} = \vec{\psi}_{dq} \cdot e^{j\theta_r} \end{cases} \tag{B-3}$$

where $\vec{V}_{dq} = v_d + jv_q$, $\vec{I}_{dq} = i_d + ji_q$, $\vec{\psi}_{dq} = \psi_d + j\psi_q$. They are space vectors of stator voltages, stator currents, and flux linkage in the dq frame, respectively.

Applying (B-3) into (B-2), yielding:

$$\vec{V}_{dq} \cdot e^{j\theta_r} = R_s \vec{I}_{dq} \cdot e^{j\theta_r} + \frac{d}{dt}\left(\vec{\psi}_{dq} \cdot e^{j\theta_r}\right) \tag{B-4}$$

(B-4) can be rearranged as follows:

$$\vec{V}_{dq} \cdot e^{j\theta_r} = R_s \vec{I}_{dq} \cdot e^{j\theta_r} + \frac{d\vec{\psi}_{dq}}{dt} \cdot e^{j\theta_r} + j\underbrace{\frac{d\theta_r}{dt}}_{\omega_e} \cdot e^{j\theta_r} \cdot \vec{\psi}_{dq} \tag{B-5}$$

Removing the common term $e^{j\theta r}$ from the both sides in (B-5), the stator winding voltages equations can be rewritten as:

$$\vec{V}_{dq} = R_s \vec{I}_{dq} + \frac{d\vec{\psi}_{dq}}{dt} + j\omega_e \vec{\psi}_{dq} \tag{B-6}$$

The flux linkages in the dq frame are given as:

$$\begin{cases} \psi_d = L_d i_d + \psi_m \\ \psi_q = L_q i_q \end{cases} \tag{B-7}$$

where L_d and L_q are the stator inductances in the dq frame, respectively. ψ_m is the flux linkage in the airgap generated by the permanent magnets mounted on the rotor.

Substituting (B-7) into (B-6) and separating the real and imaginary components in (B-6), the stator winding voltage equations of a PMM in the dq frame can be obtained as follows:

$$\begin{cases} v_d = R_s i_d + L_d \dfrac{d}{dt} i_d - \omega_e L_q i_q \\ v_q = R_s i_q + L_q \dfrac{d}{dt} i_q + \omega_e L_d i_d + \omega_e \psi_m \end{cases} \tag{B-8}$$

Appendix C Simulation Models of the PGC

Simulation analysis in Chapter 3 was primarily conducted in the Matlab®/Simulink® environment. The following are the nonlinear equivalent models of the PGC created in the Simulink to support the study in Chapter 3.

The overall model of the PGC is demonstrated in Figure C.1.

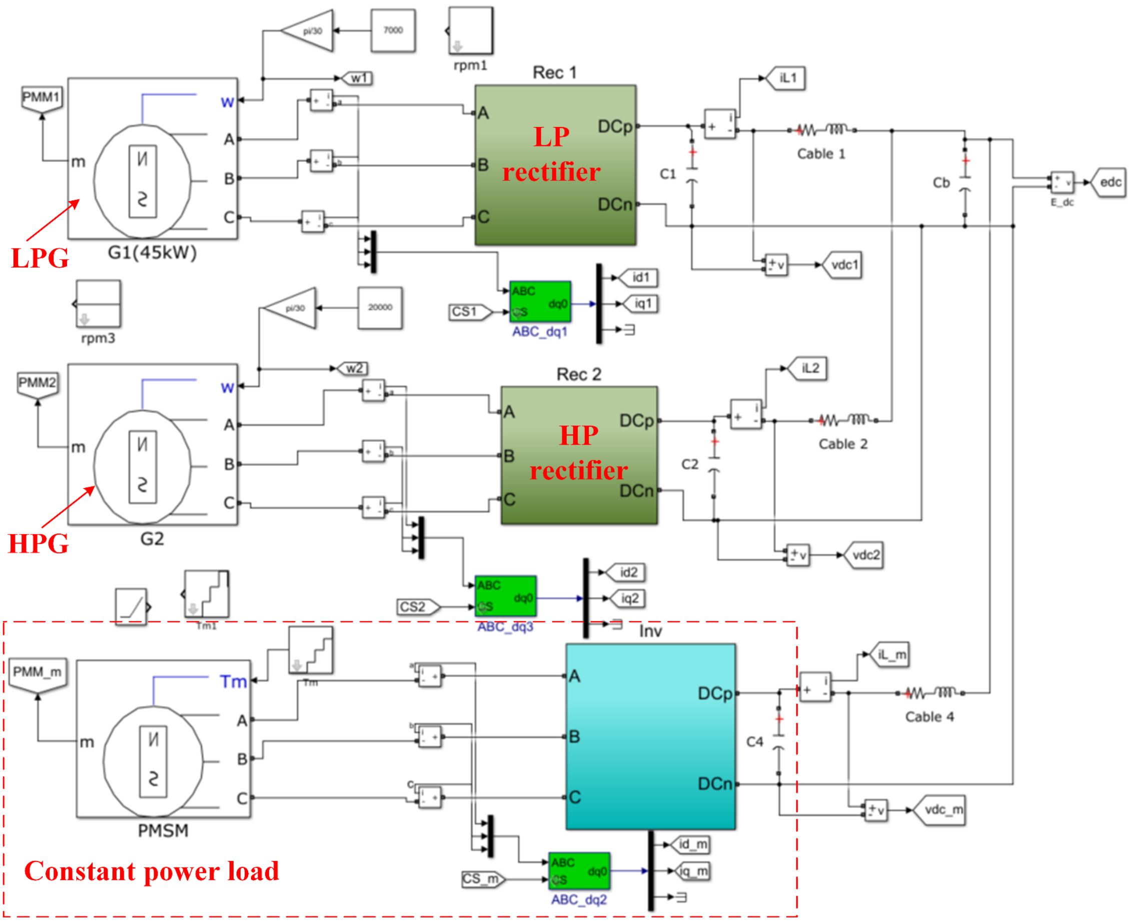

Figure C.1. The PGC simulation model.

The control structure for the LP and HP rectifiers is shown in Figure C.2. The functionalities of core blocks are highlighted. The schematic diagram of the control structure has been shown in Figure 3.15. To be specific, the error between the voltage reference and actual voltage is amplified through a droop gain, giving the DC current reference. Then through a closed-loop calculation of the DC currents, the *q*-axis current reference is generated. It is correlates to the *d*-axis current, to make sure that the current references are within the current limits. Then through the inner current loop calculation, voltage references are generated and also limited within the voltage limits. The voltage references are transformed into gate drive signals to drive the HPR and LPR.

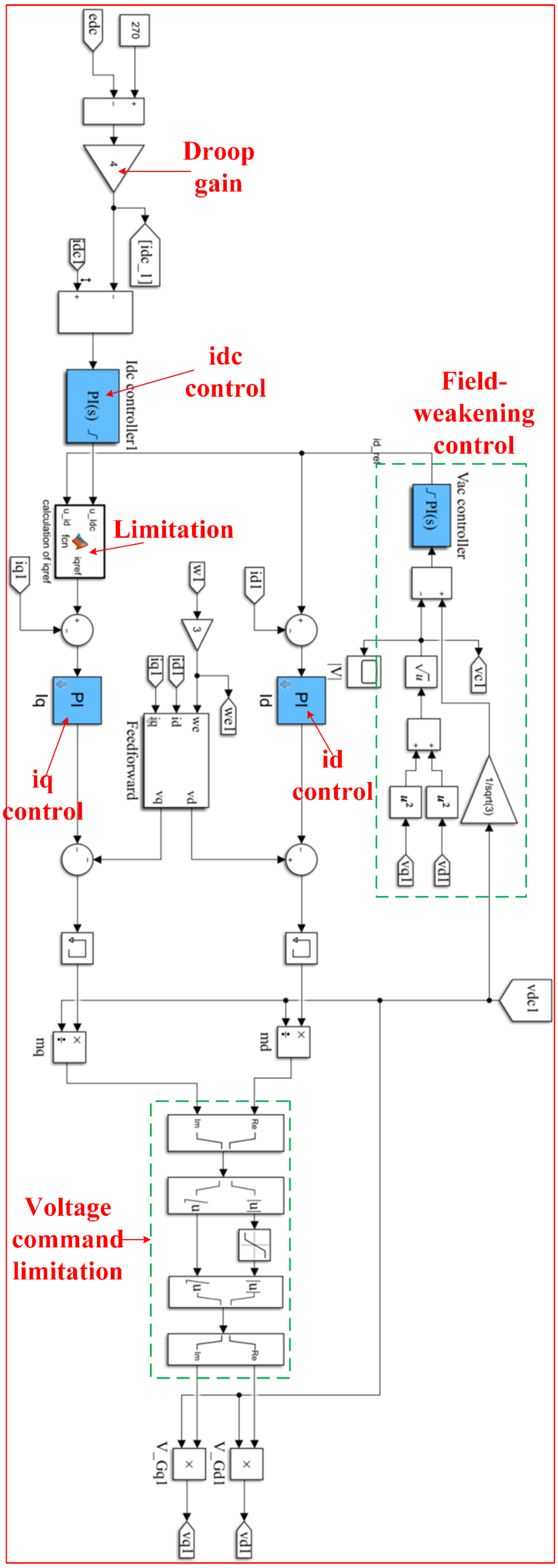

Figure C.2: Control structure for the rectifiers.

Appendix D Simulation Models of the APGC

Simulation analysis was primarily conducted in the Matlab®/Simulink® environment. The following are the nonlinear equivalent models of the APGC created in the Simulink to support the study in Chapter 4-7.

The overall model of the APGC is demonstrated in Figure D.1.

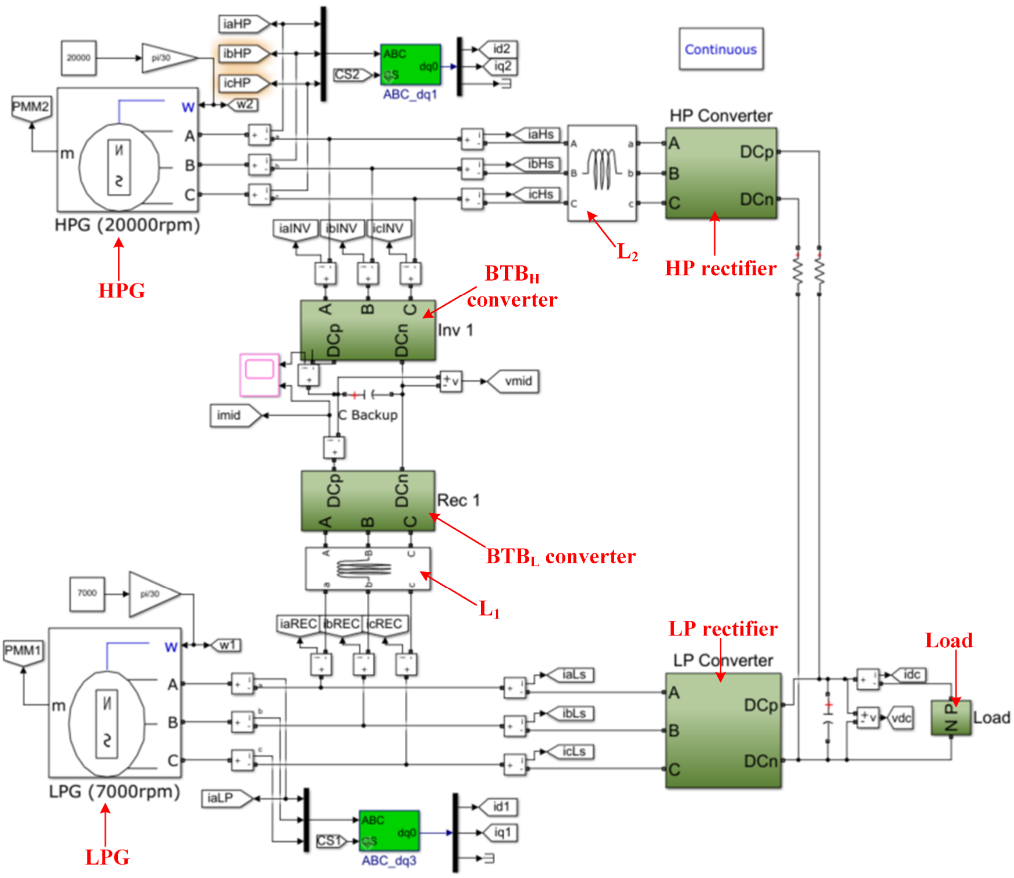

Figure D.1. The APGC simulation model consisting of the HPG, LPG, HPR, LPR, BTB converter and passive components.

The control structure for rectifiers is presented in Figure D.2.

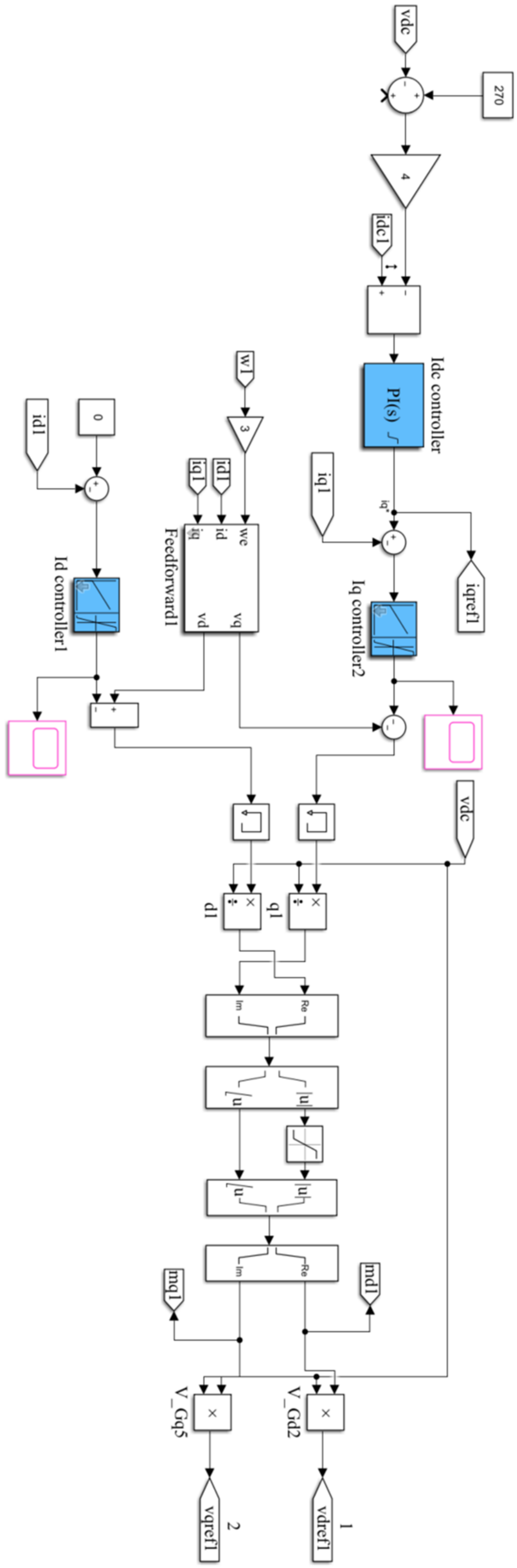

Figure D.2. Control structure for the rectifiers.

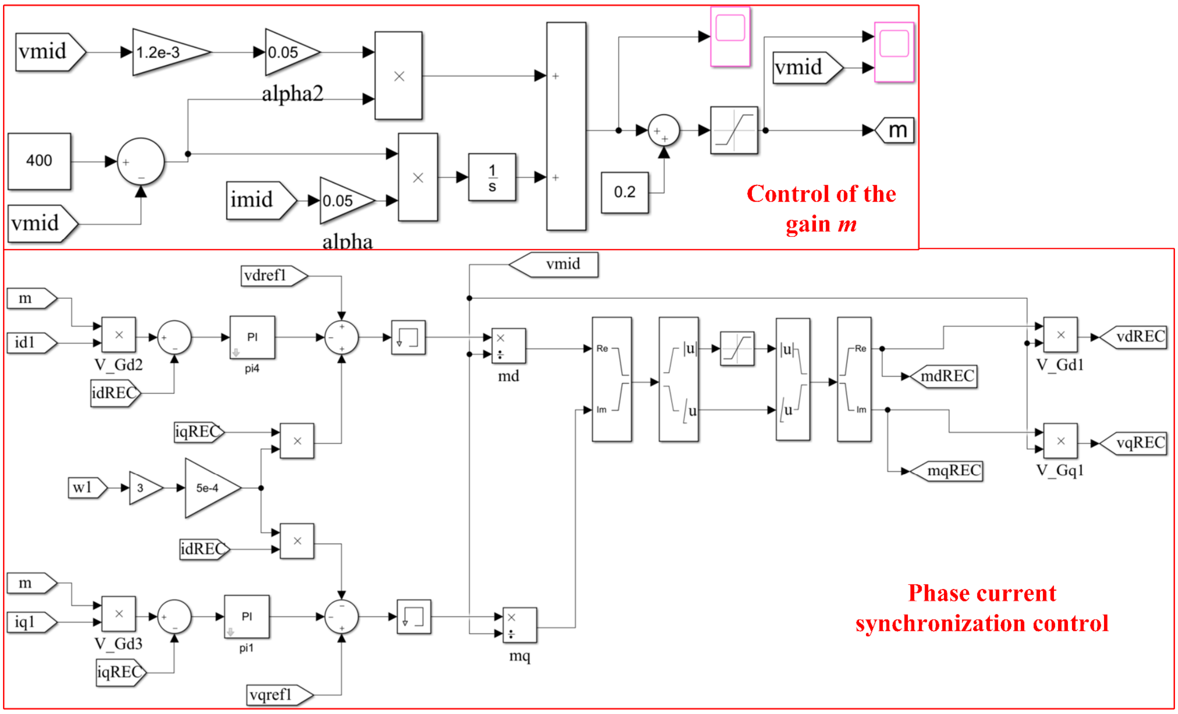

Figure D.3. Control scheme for the BTB_L converter.

Control scheme for the BTB_L converter is presented in Figure D.3. The upper one is used to control the gain *m*. The DC-link voltage reference of the BTB converter is 400V. A PI control structure is used to control the gain *m*, where the control parameters are adaptively tuned based on the derived relation shown in (4-12). The gain *m* is further used in the phase current synchronization control as shown in the lower subfigure in Figure D.3, where *m* is multiplied with the *dq* currents of the LPG. The product serves as the current references for the BTB_L converter.

Appendix E

Derivation of the Source Impedance $Z_s(s)$ in (6-4) in Section 6.2.1

According to the Kirchhoff Current Law, current through the HP channel's cable in Figure 6.3 can be derived as follows:

$$i_{c1}(s) = \frac{v_{dc}^{*} - v_{dc}^{HP}}{k_D^{HP}} G_{idc}^{HP}(s) - v_{dc}^{HP} \cdot sC_{HP} \tag{E-1}$$

The current can also be derived from the voltage across cable and cable admittances, given as:

$$i_{c1}(s) = \left(v_{dc}^{HP} - v_{mb}\right) X_{HP} \tag{E-2}$$

Combing (E-1) and (E-2), the following relationship can be derived

$$v_{dc}^{HP} = \frac{G_{idc}^{HP} v_{dc}^{*} + k_D^{HP} X_{HP} v_{mb}}{sC_{HP} k_D^{HP} + k_D^{HP} X_{HP} + G_{idc}^{HP}} \tag{E-3}$$

Due to the LP channel circuit is identical to that of the HP channel, the local DC voltage of the LP channel can also be written as follows:

$$v_{dc}^{LP} = \frac{G_{idc}^{LP} v_{dc}^{*} + k_D^{LP} X_{LP} v_{mb}}{sC_{LP} k_D^{LP} + k_D^{LP} X_{LP} + G_{idc}^{LP}} \tag{E-4}$$

Under the short circuit condition, the main DC bus voltage is zero, i.e., v_{mb}=0. Hence, based on (E-3) and (E-4), the short circuit current of source subsystem can be expressed as follows:

$$\begin{aligned} i_{sc}(s) &= v_{dc}^{HP} X_{HP} + v_{dc}^{LP} X_{LP} \\ &= \frac{G_{idc}^{HP} X_{HP} v_{dc}^{*}}{sC_{HP} k_D^{HP} + k_D^{HP} X_{HP} + G_{idc}^{HP}} + \frac{G_{idc}^{LP} X_{LP} v_{dc}^{*}}{sC_{LP} k_D^{LP} + k_D^{LP} X_{LP} + G_{idc}^{LP}} \\ &= \sum_{j=LP}^{HP} \frac{G_{idc}^{j} X_j}{sC_j k_D^{j} + k_D^{j} X_j + G_{idc}^{j}} v_{dc}^{*} \end{aligned} \tag{E-5}$$

In the open circuit condition, the open circuit voltage can be expressed as follows:

$$\left(v_{dc}^{LP} - v_{oc}\right) X_{LP} + \left(v_{dc}^{HP} - v_{oc}\right) X_{HP} = v_{oc} \cdot sC_{mb} \tag{E-6}$$

Applying (E-3) and (E-4) into (E-6), the open circuit voltage can be derived as follows:

$$v_{oc}(s) = \frac{\displaystyle\sum_{j=LP}^{HP} \frac{G_{idc}^{j} X_j}{sC_j k_D^{j} + k_D^{j} X_j + G_{idc}^{j}} v_{dc}^{*}}{sC_{mb} + \displaystyle\sum_{j=LP}^{HP} \frac{sC_j k_D^{j} X_j + G_{idc}^{j} X_j}{sC_j k_D^{j} + k_D^{j} X_j + G_{idc}^{j}}} \tag{E-7}$$

Hence, the output impedance of the source subsystem can be derived by dividing (E-7) by (E-5):

$$Z_s(s) = \frac{v_{oc}(s)}{i_{sc}(s)} = \frac{1}{sC_{mb} + \displaystyle\sum_{j=LP}^{HP} \frac{sC_j k_D^{j} X_j + G_{idc}^{j} X_j}{sC_j k_D^{j} + k_D^{j} X_j + G_{idc}^{j}}} \tag{E-8}$$

The relation in (E-8) is the source subsystem impedance which has been presented in (6-4).

Appendix F

The coefficients in (6-7) are presented in the following:

$$a_2 = K_{vP} L_q \bar{i}_{qLP},\ a_1 = \left[K_{vP}(\bar{v}_q + R_s \bar{i}_{qLP}) + K_{vI} L_q \bar{i}_{qLP} \right],\ a_0 = K_{vI}(\bar{v}_q + R_s \bar{i}_{qLP}).$$

$$b_2 = K_{vP} L_q \bar{i}_{qLP},\ b_1 = \left[K_{vP}(\bar{v}_q + R_s \bar{i}_{qLP}) + K_{vI} L_q \bar{i}_{qLP} + \frac{2}{3}\bar{v}_{dc} \right],\ b_0 = K_{vI}(\bar{v}_q + R_s \bar{i}_{qLP}).$$

$z_2 = a_2$, $z_1 = a_1$, $z_0 = a_0$.

$$p_3 = b_2 k_D C,\ p_2 = a_2 + \frac{b_2 k_D \bar{P}}{\bar{v}_{dc}^{\ 2}} + b_1 k_D C,\ p_1 = a_1 + \frac{b_1 k_D \bar{P}}{\bar{v}_{dc}^{\ 2}} + b_0 k_D C,\ p_0 = a_0 + \frac{b_0 k_D \bar{P}}{\bar{v}_{dc}^{\ 2}}.$$

The parameters used in the (6-24) are presented in the following:

R_{ic} is the negative resistance of buck converter, written as $R_{ic} = -\frac{\bar{v}_{dc}}{\bar{\imath}_{Load}}$, where $\bar{v}_{dc}$ and $\bar{\imath}_{Load}$ depend on load power and droop gains. $\omega_o = \frac{1}{\sqrt{L_f C_f}}$, where L_f and C_f are the inductance and capacitance of the input LC filter. In Section 6.3, L_f =1.2 μH and C_f = 2 mF. Thus, ω_o= 20412 rad/s. $Q_0 = \frac{1}{R_{lf}+R_{cf}}\sqrt{\frac{L_f}{C_f}}$, where R_{lf} and R_{cf} are the equivalent resistances of inductor and capacitor of the LC filter. In Section 6.3, R_{lf}= 8 mΩ, R_{cf}= 0.01 Ω. Hence, Q = 13.6. $\omega_p = -\frac{1}{C_f R_{ic}}$.

Appendix G

System Weight Due to the Extra BTB Converter and Fuel Efficiency Analysis

Compared with the PGC, there is an additional BTB converter (including two AC/DC power converters), capacitor bank, and filtering inductors in the APGC. These components bring extra weight and size, which will cost more fuel burn. However, as revealed in [18], the APGC offers a higher power generation efficiency than the PGC. This appendix will investigate how the actual fuel efficiency will change with the APGC architecture.

A. Fuel Consumption Increase due to the Additional Back-to-back Converter System

The B787 Dreamliner is considered as the targeted MEA. The essential characteristic of the B787 is listed in Table G-1. It can be seen that the total power rating of the main generators is 1000kVA. For the state-of-the-art power electronics technologies, the power density is considered as 14.3 kW/kg and the power conversion efficiency is 97.5% [123], [124]. Hence, given the requirement to handle all the 1000kVA power in the postfault operation mode, the weight of the power electronics of the BTB converter can be assumed to be: $W_{PE} = W_{BTBL} + W_{BTBH} = 2\times[1000\text{kW}/(97.5\%\times14.3\ \text{kW/kg})] = 143.3$ kg. The power density of the cooling system is considered as 15 kW/kg [74], hence the weight can be assumed to be $W_{Cool} = 2\times(1000\text{kW}/15\ \text{kW/kg}) = 133.3$ kg. Some state-of-the-art inductors for high-current high-frequency applications with acceptable weight (W_L = 23.5kg [125]) are suitable to be applied in the APGC. Hence the total weight increase is $W_{Total} = W_{PE} + W_{Cool} + 2\times2\times W_L = 370.6$ kg.

A rule-of-thumb is that an 1% increase in weight results in an 0.75% increase in fuel consumption (FC) [50]. Considering the maximum landing weight in Table G-1 and the total FC of a typical 4-hour flight mission using the CFM56-3 engine in Table G-2 [11], the extra FC due to added weight is:

$$\text{Extra FC} = \frac{W_{Total}}{201,000\text{kg}} \times \frac{0.75\%}{1\%} \times 3964\text{kg} = 5.5\,\text{kg} \tag{G1}$$

Table G-1. Characteristic of the B787.

Parameter	Value	Parameter	Value
Number of engines	2	Power rating of the generators in each engine	2×250 kVA
Maximum landing weight	201,000 kg	Aviation fuel energy density	12.5 kW·h/kg

Table G-2. Average fuel consumption of a CFM56-3 engine for a 4-hour flight mission [11].

Flight phase	Time	FC per unit time	Total FC
Taxiing	5 min	9.9 kg/min	49.5 kg
Climb	30 min	42.11 kg/min	1263.3 kg
Cruise	180 min	13.39 kg/min	2410.2 kg
Descent	25 min	7.66 kg/min	191.5 kg
Taxiing	5 min	9.9 kg/min	49.5 kg
Total flight mission	245 min	-	3964 kg

B. Fuel Consumption Decrease due to the Higher Power Generation Efficiency

As indicated in [18], a 5% power generation efficiency improvement can be achieved using the APGC compared with the PGC. Therefore, the total energy saving with the APGC can be calculated with the flight mission data in Table G-2:

$$\text{Energy saving} = 1000\text{kW} \times 5\% \times 245\,\text{min}/\,60\,\text{min}/\,\text{h} = 204\text{kW} \cdot \text{h} \tag{G2}$$

Considering the aviation fuel energy density in Table G-1, the saved FC is 204 kW·h/12.5 kW·h/kg = 16.32 kg. Consequently, the saved FC (16.32 kg) is larger than the extra consumed FC (5.5 kg), which means a higher fuel efficiency is achieved by using the APGC architecture for the studied B787 aircraft in a 4-hour flight mission scenario.

References:

[1] Atılgan, Ramazan, *et. al*. "Environmental impact assessment of a turboprop engine with the aid of exergy." *Energy*, 58 (2013): 664-671.

[2] V. Madonna, P. Giangrande and M. Galea, "Electrical Power Generation in Aircraft: Review, Challenges, and Opportunities," *IEEE Trans. Transport. Electrific.*, vol. 4, no. 3, pp. 646-659, Sept. 2018.

[3] Nasa.gov. 2020. *Why Build An Electric Airplane?* [online] Available at: <https://www.nasa.gov/specials/X57/electricairplane.html> [Accessed 05 January 2020].

[4] S. Finlayson and G. S. Gupta, "Instrumentation and automated control of aircraft leading edge temperature," *2013 IEEE Sensors Applications Symposium Proceedings*, Galveston, TX, 2013, pp. 182-187.

[5] Mahdi Pourbagian, Wagdi G. Habashi, "Aero-thermal optimization of in-flight electro-thermal ice protection systems in transient de-icing mode", *International Journal of Heat and Fluid Flow*, volume 54, 2015.

[6] B. Sarlioglu and C. T. Morris, "More electric aircraft: Review, challenges, and opportunities for commercial transport aircraft," *IEEE Trans. Transport. Electrific.*, vol. 1, no. 1, pp. 54–64, Jun. 2015.

[7] D. R. Trainer and C. R. Whitley, "Electric actuation–Power quality management of aerospace flight control systems," *in Proc. IET Int. Conf. Power Electron. Mach. Drives*, 2002, pp. 229–234.

[8] J. S. Ngoua Teu Magambo *et al.*, "Planar Magnetic Components in More Electric Aircraft: Review of Technology and Key Parameters for DC–DC Power Electronic Converter," *IEEE Trans. Transport. Electrific.*, vol. 3, no. 4, pp. 831-842, Dec. 2017.

[9] P. W. Wheeler, J. Clare, A. Trentin, and S. Bozhko, "An Overview of the More Electrical Aircraft," *Proceedings of the Institution of Mechanical Engineers, Part G: Journal of Aerospace Engineering*, vol. 227, pp. 578-585, 2013.

[10] Karimi, Kamiar J. "Future aircraft power systems-integration challenges." *The Boeing Company*, 2007.

[11] H. B. Enalou, X. Lang, M. Rashed and S. Bozhko, "Time-Scaled Emulation of Electric Power Transfer in the More Electric Engine," *IEEE Trans. Transport. Electrific.*, vol. 6, no. 4, pp. 1679-1694, Dec. 2020.

[12] H. B. Enalou, M. Rashed, P. Kulsangcharoen, C. I. Hill and S. Bozhko, "Nonlinear aircraft engine model for future integrated power center development," *in Proc. Electrical Systems for Aircraft, Railway, Ship Propulsion and Road Vehicles Int. Transportation Electrification Conf. (ESARS-ITEC),* 2016, pp. 1-5.

[13] E. Astfalk, “Konzepterstellung einer Generator Management Unit für ein Unmanned Aerial Vehicle,“ Diplom Thesis, University of Federal Defence Munich, 2009.

[14] G. C. Lemmers, Jr. and D.S. Behling, “High to low pressure spool summing gearbox for accessory power extraction and electric start,” U.S. Patent 7 882 691, Feb. 8, 2011.

[15] M. Sinnett, “787 No-bleed systems: saving fuel and enhancing operational efficiencies”, *Boeing Aero Mag*., vol. 4, pp. 6–11, 2007.

[16] J.C. Swierczek, F. Moller, C. Saudemont, R. Meuret, and B. Robyns, “Power management of a regenerative local HVDC aircraft network using supercapacitors,” in *Proc. of the 15th International Power Electronics and Motion Control Conference, EPE-PEMC 2012 ECCE Europe*, Novi Sad, Serbia, 2012.

[17] MOET EU Project, (2006). [Online]. Available: http://www.eurtd.com/moet

[18] X. Lang, T. Yang, C. Li, H. B. Enalou, S. Bozhko and P. Wheeler, "A Dual-Channel-Enhanced Power Generation Architecture With Back-to-Back Converter for MEA Application," *IEEE Trans. Industry Appl.*, vol. 56, no. 3, pp. 3006-3019, May-June 2020.

[19] X. Lang, T. Yang, H. B. Enalou, S. Bozhko and P. Wheeler, "An Enhanced Power Generation Centre for More Electric Aircraft Applications," *2018 IEEE International Conference on Electrical Systems for Aircraft, Railway, Ship Propulsion and Road Vehicles & International Transportation Electrification Conference (ESARS-ITEC)*, Nottingham, 2018, pp. 1-6.

[20] F. Gao, S. Bozhko, A. Costabeber, G. Asher and P. Wheeler, "Control Design and Voltage Stability Analysis of a Droop-Controlled Electrical Power System for More Electric Aircraft," *IEEE Trans. Ind. Electron*., vol. 64, no. 12, pp. 9271-9281, Dec. 2017.

[21] F. Gao *et al*., "Comparative Stability Analysis of Droop Control Approaches in Voltage-Source-Converter-Based DC Microgrids," *IEEE Transactions on Power Electronics*, vol. 32, no. 3, pp. 2395-2415, March 2017.

[22] K. Sun, L. Zhang, Y. Xing, and J. M. Guerrero, “A distributed control strategy based on DC bus signaling for modular photovoltaic generation systems with battery energy storage,” *IEEE Trans. Power Electron.*, vol. 26, no. 10, pp. 3032–3045, Oct. 2011.

[23] L. Xu and D. Chen, “Control and operation of a DC microgrid with variable generation and energy storage,” *IEEE Trans. Power Electron*., vol. 26, no. 4, pp. 2513– 2522, Oct. 2011.

[24] X. Yu, A. M. Khambadkone, H. Wang, and S. T. S. Terence, “Control of parallel connected power converters for low-voltage microgrid-Part I: A hybrid control architecture,” *IEEE Trans. Power Electron.*, vol. 25, no. 12, pp. 2962–2970, Dec. 2010.

[25] K. Rajashekara, "Parallel between More Electric Aircraft and Electric\/Hybrid Vehicle Power Conversion Technologies," *IEEE Electrification Magazine*, vol. 2, no. 2, pp. 50-60, June 2014.

[26] K. Fischer et al., “Field-Experience based root-cause analysis of powerconverter failure in wind turbines,” *IEEE Trans. Power Electron*., vol. 30, no. 5, pp. 2481–2492, May 2015.

[27] U. M. Choi, H. G. Jeong, K. B. Lee, and B. F. Blaabjerg, “Method for detecting an open-switch fault in a grid-connected NPC inverter system,” *IEEE Trans. Power Electron.,* vol. 27, no. 6, pp. 2726– 2739, Jun. 2012.

[28] K. Ni, Y. Hu, G. Chen, C. Gan and X. Li, "Fault-Tolerant Operation of DFIG-WT With Four-Switch Three-Phase Grid-Side Converter by Using Simplified SVPWM Technique and Compensation Schemes," *IEEE Trans. Indus. Appl.*, vol. 55, no. 1, pp. 659-669, Jan.-Feb. 2019.

[29] X. Lang, T. Yang, Z. Huang, C. Wang, Z. Wang, S. Bozhko, P. Wheeler, “Stability Improvement of Onboard HVDC Grid and Engine Using an Advanced Power Generation Center for the More-Electric Aircraft”, *IEEE Trans. Transport. Electrific*., in press.

[30] Q. Xiao, L. Chen, H. Jia, P. W. Wheeler and T. Dragičević, "Model Predictive Control for Dual Active Bridge in Naval DC Microgrids Supplying Pulsed Power Loads Featuring Fast Transition and Online Transformer Current Minimization," *IEEE Trans. Ind. Electron.,* vol. 67, no. 6, pp. 5197-5203, June 2020.

[31] A. Eid, H. El-Kishky, M. Abdel-Salam, and T. El-Mohandes, “Modeling and characterization of an aircraft electric power system with a fuel cell equipped APU paralleled at main ac bus,” in *Proc. IEEE Conf. Int. Power Modulator High Voltage,* 2010, pp. 229–232.

[32] I. Moir and A. Seabridge, *Aircraft Systems: Mechanical, Electrical and Avionics Subsystems Integration*: Wiley, 2008.

[33] X. Roboam, B. Sareni, and A. D. Andrade, “More electricity in the air: toward optimized electrical networks embedded in more-electrical aircraft,” *IEEE Ind. Electron. Mag.*, vol. 6, no. 4, pp. 6–17, Dec. 2012.

[34] M. Olaiya and N. Buchan, “High power variable frequency generator for large civil aircraft,” in *Proc. IET Elect. Mach. Syst. More Elect. Aircr.,* 1999, pp. 1–4.

[35] "MIL-STD-704F," in *Aircraft Electric Power Characteristics*, ed. United States of America: Department of Defence Interface Standard.

[36] Shoujun, S., Weiguo L., Peitsch D., Schaefer. U, *Detailed Design of a High Speed Switched Reluctance Starter/Generator for More/All Electric Aircraft*. Chinese Journal of Aeronautics, 2010. 23: p. 216-226.

[37] C. Li *et al.*, "A Modified Neutral Point Balancing Space Vector Modulation for Three-Level Neutral Point Clamped Converters in High-Speed Drives," *IEEE Trans. Ind. Electron.*, vol. 66, no. 2, pp. 910-921, Feb. 2019.

[38] J. M. Guerrero, J. C. Vasquez, J. Matas, L. G. de Vicuna and M. Castilla, "Hierarchical Control of Droop-Controlled AC and DC Microgrids—A General Approach Toward Standardization," *IEEE Trans Ind. Electron.*, vol. 58, no. 1, pp. 158-172, Jan. 2011.

[39] Z. Yang, F. Shang, I. P. Brown, and M. Krishnamurthy, “Comparative study of interior permanent magnet, induction, and switched reluctance motor drives for EV and HEV applications,” *IEEE Trans. Transp. Electrific.,* vol. 1, no. 6, pp. 245–254, Oct. 2015.

[40] Y. Jia and K. Rajashekara, "An Induction Generator-Based AC/DC Hybrid Electric Power Generation System for More Electric Aircraft," *IEEE Trans. Indus. Appl.*, vol. 53, no. 3, pp. 2485-2494, May-June 2017.

[41] R. Bojoi, A. Cavagnino, A. Tenconi, and S. Vaschetto, “Control of shaft-lineembedded multiphase starter/generator for aero-engine,” *IEEE Trans. Ind. Electron.,* vol. 63, no. 1, pp. 641–652, Jan. 2016.

[42] *Basic construction of 3-phase AC induction motors you should know*. Access on 19th May, https://electrical-engineering-portal.com/construction-of-3-phase-ac-induction-motors.

[43] E. Richter and C. Ferreira, "Performance evaluation of a 250kW switched reluctance starter generator," *Industry Applications Conference, 1995. Thirtieth IAS Annual Meeting, IAS '95.*, 1995, pp. 434-440 vol.1.

[44] S. Bozhko, M. Rashed, C. I. Hill, S. S. Yeoh and T. Yang, "Flux-Weakening Control of Electric Starter–Generator Based on Permanent-Magnet Machine," *IEEE Trans. Transport Electrific.*, vol. 3, no. 4, pp. 864-877, Dec. 2017.

[45] Cleansky. AEGART Project Summary. Available: https://cordis.europa.eu/project/id/296090/reporting. Accessed: 26/01/2021.

[46] M. Degano, *et. al.*, "An optimized bi-directional, wide speed range electric starter-generator for aerospace application," *Power Electronics, Machines and Drives (PEMD 2014)*, 2014, pp. 1-6.

[47] F. Guo, T. Yang, C. Li, S. Bozhko and P. Wheeler, "Active Modulation Strategy for Capacitor Voltage Balancing of Three-Level Neutral-Point-Clamped Converters in High-Speed Drives," *IEEE Trans. Ind. Electron.*, early access.

[48] Enalou, Hossein Balaghi, *et al.* "A preliminary study into turbofan performance with LP-HP power exchange." *Proceedings of Montreal 2018 Global Power and Propulsion Forum.* 2018.

[49] Enalou, Hossein Balaghi, *et al.* “Potential improvements in turbofan’s performance by electric power transfer”, No. 2018-01-1962. *SAE Technical Paper*, 2018.

[50] Balaghi Enalou, Hossein, and Serhiy Bozhko. "Performance Improvement of Turbofans by Electric Power Transfer." *Journal of Turbomachinery* 142.11 (2020).

[51] Y. Ye, M. Kazerani and V. H. Quintana, "A novel modeling and control method for three-phase PWM converters," *2001 IEEE 32nd Annual Power Electronics Specialists Conference*, Vancouver, BC, 2001, pp. 102-107 vol. 1.

[52] R. Burgos, P. Kshirsagar, A. Lidozzi, F. Wang, and D. Boroyevich, “Mathematical model and control design for sensorless vector control of permanent magnet synchronous machines,” in *Proc. IEEE Workshops COMPEL*, Jul. 2006, pp. 76–82.

[53] S. Bolognani, S. Calligaro, R. Petrella, and F. Pogni, “Flux-weakening in ipm motor drives: Comparison of state-of-art algorithms and a novel proposal for controller design,” in *Proc. 2011-14th Eur. Conf. Power Electron. Appl. (EPE 2011)*, 2011, pp. 1–11.

[54] F. Gao, S. Bozhko, G. Asher, P. Wheeler, and C. Patel, “An improved voltage compensation approach in a droop-controlled DC power system for the more electric aircraft,” *IEEE Trans. Power Electron.,* vol. 31, no. 10, pp. 7369–7383, Oct. 2016.

[55] “*CFM International CFM56*,” Oct. 17, 2020. Accessed on: Nov. 07, 2020. Available: https://en.wikipedia.org/wiki/CFM_International_CFM56

[56] Q. Xiao, *et. al.*, "Model Predictive Control for Dual Active Bridge in Naval DC Microgrids Supplying Pulsed Power Loads Featuring Fast Transition and Online Transformer Current Minimization," *IEEE Trans. Ind. Electron.*, vol. 67, no. 6, pp. 5197-5203, June 2020.

[57] Yeoh, Seang Shen. Control strategies for the More Electric Aircraft starter-generator electrical power system. *PhD Dissertation, University of Nottingham*, 2016. Page 110.

[58] N. Fernando, P. Arumugam and C. Gerada, "Design of a Stator for a High-Speed Turbo-Generator with Fixed Permanent Magnet Rotor Radius and Volt–Ampere Constraints," *IEEE Trans. Energy Conver.*, vol. 33, no. 3, pp. 1311-1320, Sept. 2018.

[59] W. Fernando, P. Arumugam and C. Gerada, "Volt-ampere constrains and its influence on inductance limits in high speed PM machine design," *8th IET International Conference on Power Electronics, Machines and Drives (PEMD 2016),* Glasgow, 2016, pp. 1-6.

[60] D.-C. Lee, G.-M. Lee, and K.-D. Lee, "DC-bus voltage control of three phase ac/dc PWM converters using feedback linearization*," IEEE Trans. Ind. Appl.,* vol. 36, no. 3, pp. 826–833, May 2000.

[61] K. Jalili and S. Bernet, "Design of LCL Filters of Active-Front-End Two-Level Voltage-Source Converters," *IEEE Trans. Indus. Electron.,* vol. 56, no. 5, pp. 1674-1689, Jan. 2009.

[62] X. Zhang and J. Yang, " A DC-Link Voltage Fast Control Strategy for High-Speed PMSM/G in Flywheel Energy Storage System," *IEEE Trans. Indus. Appl.,* vol. 54, no. 2, pp. 1671-1679, Dec. 2017.

[63] M. Salcone and J. Bond, "Selecting film bus link capacitors for high performance inverter applications," *Proc. IEEE Elect. Mach. Drives Conf.,* Miami, FL, USA, 2009, pp. 1692–1699.

[64] Z. Xu, D. Zhang, F. Wang, and D. Boroyevich, "A unified control for the combined permanent magnet generator and active rectifier system," *IEEE Trans. Power Electron.,* vol. 29, no. 10, pp. 5644–5656, Oct. 2014

[65] J. W. Kolar, T. M. Wolbank and M. Schrodl, "Analytical calculation of the RMS current stress on the DC link capacitor of voltage DC link PWM converter systems," *1999. Ninth International Conference on Electrical Machines and Drives (Conf. Publ. No. 468)*, Canterbury, UK, 1999, pp. 81-89.

[66] Tianrui Luan, Ming Yang, Xiaoyu Lang, Zhi Lang and Dianguo Xu, "A novel Active Disturbance Rejection Control speed controller for PMSM drive," *2016 IEEE 8th International Power Electronics and Motion Control Conference (IPEMC-ECCE Asia)*, Hefei, China, 2016, pp. 116-120.

[67] B. C. Kuo, *Automatic Control System*. London, U.K.: Prentice-Hall, 1962.

[68] A. M. Diab *et al.*, "Fast and Simple Tuning Rules of Synchronous Reference Frame Proportional-Integral Current Controller," *IEEE Access*, vol. 9, pp. 22156-22170, 2021.

[69] S. Bolognani, S. Calligaro, R. Petrella, and F. Pogni, "Flux-weakening in ipm motor drives: Comparison of state-of-art algorithms and a novel proposal for controller design," *in Proc. 2011-14th Eur. Conf. Power Electron. Appl. (EPE 2011)*, 2011, pp. 1–11.

[70] Matthias Preindl, Silverio Bolognani, "Model Predictive Direct Torque Control with Finite Control Set for PMSM Drive Systems Part 2: Field Weakening Operation", *IEEE Trans. Indus. Informatics*, vol. 9, no. 2, pp. 648-657, 2013.

[71] S. D. Phillips, T. M. NEUMAN, and M. Armstrong, "Engine health monitoring and power allocation control for a turbine engine using electric generators," *US Patent US9593591B2*, 2013.

[72] A. A. Belokon, M. V. Senkevich, and G. L. Touchton, "Multi-spool turbogenerator system and control method," *US Patent US6931856B2*, 2003.

[73] Balaghi Enalou, Hossein, and Serhiy Bozhko. "Performance Improvement of Turbofans by Electric Power Transfer." *Journal of Turbomachinery*, 142.11 (2020).

[74] Balaghi Enalou, Hossein, and Serhiy Bozhko. "Electric Power Transfer Concept for Enhanced Performance of the More Electric Engine." *Journal of Engineering for Gas Turbines and Power*, (2021).

[75] A. Emadi, and M. Ehsani, "Aircraft power systems: Technology, state of the art, and future trends," *IEEE Aerosp. Electron. Syst. Mag.*, vol. 15, no. 1, pp. 28–32, Jan. 2000.

[76] K. W. E. Cheng, "Comparative study of ac/dc converters for more electric aircraft," in *Proc. IEE Conf. Power Electron. Variable Speed Drives*, 1998, pp. 21–23.

[77] D. Izquierdo, R. Azcona, F. J. L. Cerro, C. Fernández, and B. Delicado, "Electrical power distribution system (HV270DC), for application in more electric aircraft," in *Proc. IEEE Appl. Power Electron. Conf. Exhib.*, 2010, pp. 1300–1305.

[78] T. Jomier, "More open electrical technologies," EU FP6 Project, 2009.

[79] S. Bozhko, "Modern trends in aircraft electric power systems and in onboard electric power generation," presented at the IQPC Conf. More Electric Aircraft USA, Seattle, WA, USA, 2017.

[80] N. Fritz, M. Rashed, S. Bozhko, F. Cuomo, and P. Wheeler, “Analytical modeling and power density optimization of a single phase dual active bridge for aircraft application,” *Int. Conf. Power Electronics Machines Drives* (*PEMD*), Liverpool, U.K., 2018.

[81] K. Xu, N. Xie, C. Wang, J. Deng, and X. Shi, “Static modeling and power flow of the more electric aircraft power system,” *in Proc. 3rd Int. Conf. Syst. Inform*., 2016, pp. 193–198.

[82] C. Spagnolo, S. Sumsurooah, C. I. Hill, and S. Bozhko, “Finite state machine control for aircraft electrical distribution system,” *J. Eng.*, vol. 2018, pp. 506–511, 2018.

[83] Papadimitriou, C. N., E. I. Zountouridou, and N. D. Hatziargyriou. "Review of hierarchical control in DC microgrids." *Electric Power Systems Research*, 122 (2015): 159-167.

[84] AL-Nussairi, Mohammed Kh, *et al.* "Constant power loads (cpl) with microgrids: Problem definition, stability analysis and compensation techniques." *Energies*,10.10 (2017): 1656.

[85] S. Bozhko, S. Shen, G. Fei, and C. Hill, “Aircraft starter-generator system based on permanent-magnet machine fed by active front-end rectifier,” in *Proc. 40th Annu. Conf. IEEE Ind. Electron. Soc. (IECON),* Nov. 2014, pp. 2958–2964.

[86] Z. Zhang, J. Huang, Y. Jiang, W. Geng and Y. Xu, "Overview and analysis of PM starter/generator for aircraft electrical power systems," in *CES Transactions on Electrical Machines and Systems*, vol. 1, no. 2, pp. 117-131, 2017.

[87] J. Pakdeeto, K. Areerak, S. Bozhko and K. Areerak, "Stabilization of DC Micro-Grid Systems by Using the Loop-Cancellation Technique," in *IEEE Journal of Emerging and Selected Topics in Power Electronics*.

[88] D. N. Taneja, "Method and apparatus for extracting electrical power from a gas turbine engine," *US patent* US20130062885A1, 2011.

[89] G. Buticchi, S. Bozhko, M. Liserre, P. Wheeler and K. Al-Haddad, "On-Board Microgrids for the More Electric Aircraft—Technology Review," *IEEE Trans. Ind. Electron.*, vol. 66, no. 7, pp. 5588-5599, July 2019.

[90] M. D. Talan, "Two-shaft engine for aircraft with high electric power demand," *US patent* US8522526B2, 2006.

[91] K. A. Dooley, "Gas turbine engine including apparatus to transfer power between multiple shafts," *US patent* US7690186B2, 2005.

[92] P. M. Hield, J. M. Cundy, R. A. Midgley, A. C. Newton, and A. L. Rowe, "Shaft power transfer in gas turbine engines with machines operable as generators or motors," *US Patent* US5694765A, 1993.

[93] Begum, K. Ghousiya, A. Seshagiri Rao, and T. K. Radhakrishnan. "Enhanced IMC based PID controller design for non-minimum phase (NMP) integrating processes with time delays." *ISA transactions,* vol. 68 pp. 223-234, 2017.

[94] Holmes D G, Lipo T A. Pulse width modulation for power converters: principles and practice[M]. *John Wiley & Sons*, 2003.

[95] T. Kwon and S. Sul, "Novel Antiwindup of a Current Regulator of a Surface-Mounted Permanent-Magnet Motor for Flux-Weakening Control," *IEEE Trans. Industry Appli.*, vol. 42, no. 5, pp. 1293-1300, Sept.-Oct. 2006.

[96] J. Kim, I. Jeong, K. Nam, J. Yang and T. Hwang, "Sensorless Control of PMSM in a High-Speed Region Considering Iron Loss," *IEEE Trans. Ind. Electron.*, vol. 62, no. 10, pp. 6151-6159, Oct. 2015.

[97] R.D. Middlebrook, “Input filer consideration in design and application of switching regulators,” in *Proc. IEEE IAS Annu. Meet.*, Chicago, USA, Oct. 1976, pp. 336–382.

[98] A. Riccobono and E. Santi, "Comprehensive Review of Stability Criteria for DC Power Distribution Systems," *IEEE Trans. Indus. Appl.*, vol. 50, no. 5, pp. 3525-3535, Sept.-Oct. 2014.

[99] J. Yang, G. Buticchi, C. Gu, S. Günter, H. Zhang and P. Wheeler, "A Generalized Input Impedance Model of Multiple Active Bridge Converter," *IEEE Trans. Transport. Electrific.*, vol. 6, no. 4, pp. 1695-1706, Dec. 2020.

[100] S. K. Pidaparthy, B. Choi and Y. Kim, "A Load Impedance Specification of DC Power Systems for Desired DC-Link Dynamics and Reduced Conservativeness," *IEEE Trans. Power Electron.*, vol. 34, no. 2, pp. 1407-1419, Feb. 2019.

[101] Tian-Hua Liu, Chih-Chien Tseng, Jui-Ling Chen, Jian-Feng Tsai and Chien-Hsun Wu, "A wide-range adjustable speed control method for multi-motor drive systems," *IECON 2013 - 39th Annual Conference of the IEEE Industrial Electronics Society*, Vienna, Austria, 2013, pp. 2584-2589.

[102] K. Jong-Yul *et al.*, “Cooperative control strategy of energy storage system and micro sources for stabilizing the microgrid during islanded operation,” *IEEE Trans. Power Electron.*, vol. 25, no. 12, pp. 3037–3048, Dec. 2010

[103] H. Zhang, F. Mollet, C. Saudemont and B. Robyns, “Experimental validation of energy storage system management strategies for a local dc distribution system of more

electric aircraft,” *IEEE Trans. Ind. Electron.*, vol. 57, no. 12, pp. 3905–3916, Dec. 2010.

[104] Mohan N. *Advanced electric drives*. 2001 Oct.

[105] H. Akagi, S. Inoue and T. Yoshii, "Control and Performance of a Transformerless Cascade PWM STATCOM With Star Configuration," *IEEE Trans. Ind. Appl.*, vol. 43, no. 4, pp. 1041-1049, July-Aug. 2007.

[106] Y. Liu *et al.*, "LCL Filter Design of a 50-kW 60-kHz SiC Inverter with Size and Thermal Considerations for Aerospace Applications," *IEEE Trans. Ind. Electron.*, vol. 64, no. 10, pp. 8321-8333, Oct. 2017.

[107] K. Hu, Z. Liu, Y. Yang, F. Iannuzzo and F. Blaabjerg, "Ensuring a Reliable Operation of Two-Level IGBT-Based Power Converters: A Review of Monitoring and Fault-Tolerant Approaches," *IEEE Access*, vol. 8, pp. 89988-90022, 2020.

[108] K. Fischer *et al.*, “Field-Experience based root-cause analysis of powerconverter failure in wind turbines,” *IEEE Trans. Power Electron*., vol. 30, no. 5, pp. 2481–2492, May 2015.

[109] J. S. Lee and K. B. Lee, "Open-Switch Fault Tolerance Control for a Three-Level NPC/T-Type Rectifier in Wind Turbine Systems," *IEEE Trans. Industrial Electron*., vol. 62, no. 2, pp. 1012-1021, Feb. 2015.

[110] A. Kersten *et al.*, "Fault Detection and Localization for Limp Home Functionality of Three-Level NPC Inverters With Connected Neutral Point for Electric Vehicles," *IEEE Trans. Transport. Electrific.*, vol. 5, no. 2, pp. 416-432, June 2019.

[111] J. Zhang, L. Hu, S. Xu, and F. Deng. "Fault-tolerant compensation control for T-type three-level inverter with zero-sequence voltage injection.” *IET Power Electronics*, no. 14, pp. 3774-3781, 2019.

[112] F. Chai, L. Gao, Y. Yu and Y. Liu, "Fault-Tolerant Control of Modular Permanent Magnet Synchronous Motor Under Open-Circuit Faults," *IEEE Access*, vol. 7, pp. 154008-154017, 2019.

[113] R. R. Errabelli and P. Mutschler, “Fault-tolerant voltage source inverter for permanent magnet drives,” *IEEE Trans. Power Electron*., vol. 27, no. 2, pp. 500–508, Feb. 2012.

[114] G. Chen and X. Cai, “Reconfigurable control for fault-tolerant of parallel converters in PMSG wind energy conversion system,” *IEEE Trans. Sustain. Energy*, vol. 10, no. 2, pp. 604–614, Apr. 2019.

[115] X. Zhang, T. Wang, X. Wang, G. Wang, Z. Chen, and D. Xu, “A coordinate control strategy for circulating current suppression in multiparalleled three-phase inverters,” *IEEE Trans. Ind. Electron*., vol. 64, no. 1, pp. 838–847, Jan. 2017.

[116] Z. Wen, G. Valente, A. Formentini, L. Papini, C. Gerada and P. Zanchetta, "Open Circuit Fault Control Techniques for Bearingless Multi-Sector Permanent Magnet Synchronous Machines," *IEEE Trans. Indus. Appl*., doi: 10.1109/TIA.2021.3060368.

[117] H. Akagi, Y. Kanazawa, and A. Nabae, “Instantaneous reactive power compensators comprising switching devices without energy storage components,” *IEEE Trans. Ind. Appl*., vol. IA-20, no. 3, pp. 625–630, May 1984.

[118] Y. Zhang, J. Jiao, J. Liu and J. Gao, "Direct Power Control of PWM Rectifier With Feedforward Compensation of DC-Bus Voltage Ripple Under Unbalanced Grid Conditions," *IEEE Trans. Indus. Appl.,* vol. 55, no. 3, pp. 2890-2901, May 2019.

[119] F. Bu, Y. Hu, W. Huang, S. Zhuang and K. Shi, "Wide-Speed-Range-Operation Dual Stator-Winding Induction Generator DC Generating System for Wind Power Applications," *IEEE Trans. Power Electron*., vol. 30, no. 2, pp. 561-573, Feb. 2015.

[120] C. Zhang, S. Yu, K. Jiang, X. Ge and J. Ma, "A Fast Instantaneous Power Calculation Algorithm for Single-Phase Rectifiers Based on Arbitrary Phase-Delay Method*," IEEE Trans. Indus. Appl*., vol. 55, no. 4, pp. 3935-3945, July-Aug. 2019.

[121] H. B. Enalou. Electric Power Transfer Concept for Improved Performance of Multi-spool Turbofan Jet Engine. *PhD Dissertation*, University of Nottingham, 2020.

[122] H. B. Enalou, S. Bozhko, M. Rashed, and P. Kulsangcharoen, "A Preliminary Study into Turbofan Performance with LP-HP Power Exchange," in *GPPS Global Power & Propulsion Society*, Montreal, 2018.

[123] Sahoo, S., Zhao, X., and Kyprianidis, K., 2020, "A Review of Concepts, Benefits, and Challenges for Future Electrical Propulsion-Based Aircraft," *Aerospace*, 7(4), p. 44.

[124] N. Swaminathan and Y. Cao, "An Overview of High-Conversion High-Voltage DC–DC Converters for Electrified Aviation Power Distribution System," *IEEE Trans. Transport. Electrific*., vol. 6, no. 4, pp. 1740-1754, Dec. 2020.

[125] HCS-601M-500AG inductor. Accessed: May. 2021. [Online]. Available https://www.coilws.com/images/HCS-601M-500AG%20REV.A.pdf.

[126] A.-L. Allegre, A. Bouscayrol, J.-N. Verhille, P. Delarue, E. Chattot, and S. El-Fassi, “Reduced-scale-power hardware-in-the-loop simulation of an innovative subway,” *IEEE Trans. Ind. Electron*., vol. 57, no. 4, pp. 1175–1185, Apr. 2010.

[127] M. Cheah-Mane, O. D. Adeuyi, J. Liang, and N. Jenkins, “A scaling method for a multi-terminal DC experimental test rig,” in *Proc. 17th Eur. Conf. Power Electron. Appl. (EPE ECCE-Europe),* Sep. 2015, pp. 1–9.

[128] *Final Report Summary - AEGART (AIRCRAFT ELECTRICAL GENERATION SYSTEM WITH ACTIVE RECTIFICATION AND HEALTH MONITORING).* Accessed: Apr. 2021. [Online]. Available: https://cordis.europa.eu/project/id/296090/reporting

[129] A. M. Diab, S. Bozhko, M. Galea and C. Gerada, "Stable and Robust Design of Active Disturbance-Rejection Current Controller for Permanent Magnet Machines in Transportation Systems," *IEEE Trans. Transport. Electrific.*, vol. 6, no. 4, pp. 1421-1433, Dec. 2020.

[130] X. Lang, T. Yang, C. Li, S. Yeoh, S. Bozhko, and P. Wheeler, " An Enhanced Feedforward Flux Weakening Control for High-Speed Permanent Magnet Machine Drive Applications," *IET Power Electronics*, 00: 1-15. (2021) doi: 10.1049/pel2.12170.

[131] Kern, John Michael, and Herman Lucas Norbert Wiegman. "Integrated electrical power extraction for aircraft engines." *U.S. Patent,* No. 7,468,561. 23 Dec. 2008.

[132] H. Akagi, Y. Kanazawa, and A. Nabae, “Instantaneous reactive power compensators comprising switching devices without energy storage components,” *IEEE Trans. Ind. Appl.*, vol. IA-20, no. 3, pp. 625–630, May 1984.

[133] Y. Zhang, J. Jiao, J. Liu and J. Gao, "Direct Power Control of PWM Rectifier With Feedforward Compensation of DC-Bus Voltage Ripple Under Unbalanced Grid Conditions," *IEEE Trans. Ind. Appl.*, vol. 55, no. 3, pp. 2890-2901, May 2019.

[134] S. Jiao, K. R. Ramachandran Potti, K. Rajashekara and S. K. Pramanick, "A Novel DROGI-Based Detection Scheme for Power Quality Improvement Using Four-Leg Converter Under Unbalanced Loads," *IEEE Trans. Indus. Appl.*, vol. 56, no. 1, pp. 815-825, Jan.-Feb. 2020.

[135] H. Liu, F. Bu, W. Huang, H. Xu, M. Degano and C. Gerada, "Control-Winding Direct Power Control Strategy for Five-Phase Dual-Stator Winding Induction Generator DC Generating System," *IEEE Trans. Transport. Electrific.*, vol. 6, no. 1, pp. 73-82, March 2020.

[136] F. Bu, Y. Hu, W. Huang, S. Zhuang and K. Shi, "Wide-Speed-Range-Operation Dual Stator-Winding Induction Generator DC Generating System for Wind Power Applications," *IEEE Trans. Power Electron.*, vol. 30, no. 2, pp. 561-573, Feb. 2015.

[137] C. Zhang, S. Yu, K. Jiang, X. Ge and J. Ma, "A Fast Instantaneous Power Calculation Algorithm for Single-Phase Rectifiers Based on Arbitrary Phase-Delay Method," *IEEE Trans. Ind. Appl.*, vol. 55, no. 4, pp. 3935-3945, July-Aug. 2019.

[138] L. Wang, C. Lam and M. Wong, "A Hybrid-STATCOM with Wide Compensation Range and Low DC-Link Voltage," *IEEE Trans. Ind. Electron.*, vol. 63, no. 6, pp. 3333-3343, June 2016.